Investigation of Multiphase Reactor Hydrodynamics Using Magnetic Resonance Imaging

A dissertation submitted for the degree of Doctor of Philosophy

UNIVERSITY OF CAMBRIDGE

Department of Chemical Engineering and Biotechnology

Nicholas Paul Rice
Magdalene College

September 2018

Per aspera ad astra

PREFACE

The work presented in this thesis was carried out in the Department of Chemical Engineering and Biotechnology at the University of Cambridge between October 2014 and May 2018. The work in this dissertation is the original and independent work of the author, except where specifically acknowledged within the text. No portion of this thesis has been previously submitted at any other university. This thesis contains fewer than 65,000 words and 150 figures.

N. P. R.

Cambridge, UK, 2018

ACKNOWLEDGEMENTS

I'd foremost like to acknowledge and thank my supervisor, Prof Lynn Gladden, for the guidance, assistance and instruction on so many of the theoretical and practical aspects of this project. I'd secondly like to thank my advisor Dr Andy Sederman, for his persistent help and direction on a day-to-day basis on topics including NMR theory, the practical operation of pilot-scale plants to departmental administrative procedures and scientific writing. Thirdly to Dr Mick Mantle, who is an invaluable presence at the MRRC in the office and laboratory. He is truly the master of shimming, and his advice and skills experimentally were of critical importance for my understanding of magnetic resonance and laboratory work.

I'd additionally like to extend thanks to Dr Dan Holland for the assistance on the material for chapters six and seven. Our conversations on Skype were crucial for developing the experimentation and theoretical aspects of this work. I'd also like to thank Dr Chris Boyce for his assistance on this work, and for the work in my master's project. Together they taught me practically all I know regarding using the NMR instrumentation and fluidisation rigs. I would like to thank Dr Nick Ramskill for additional assistance and support regarding many aspects of laboratory work, and theory on compressed sensing methods. On the practical front I would also like to thank Wei-Yao and the electronics section at the Department for assisting in the design and construction of the single bubble injector. A thank you must also be given to Andy Hubbard and the workshop team for many aspects of my apparatus construction. Additionally, I thank Jon and Iain and the computing section for assistance with the laboratory computing equipment.

I must formally acknowledge and thank Ms Christine Schmaus, who was responsible for acquiring the data used in chapters 4 and 5. These data were acquired at the MRRC in September 2010. The processing, analysis, calculations and presentation are all a result of my own work.

I would finally like to heartily thank the Gates Cambridge Trust, who funded this work and my master's degree. Without this financial support, none of this work would have been possible. I'd also like to thank the Gates Cambridge community for providing a welcoming and stimulating environment for research students in Cambridge. I would also like to thank Dr Stuart Martin, Dr Rowan Burnstein and Prof Paul Dupree, all tutors of Magdalene College, for their personal and financial support of my research. Finally, I would like to thank my parents and my brother for their permanent personal support and guidance. Without their enduring support, I would not have been able to undertake anything remotely ambitious as this thesis.

ABSTRACT

This thesis presents an investigation on multiphase reactor hydrodynamics using magnetic resonance imaging (MRI). The study demonstrates experimental techniques by which computational and quasi-analytical fluid models may be validated. Three types of industrially-important multiphase reaction vessels are considered: a co-current upflow gas-liquid-solid bed, a co-current downward trickle bed (gas, liquid, solid), and a gas-solid fluidised bed. These reactors were selected as they commonly demonstrate local hydrodynamic anisotropy which affects the global performance of industrial units. MRI was used to obtain 2D velocity images of the gas and liquid phases in the packed beds, and of the gas and the solid phases in the fluidised bed. This study reports the first spatially resolved velocity measurements of both the gas and liquid phases in a co-current upflow bed, and the gas and solid phases of an isolated bubble in a fluidised bed. The experimental vessels were: 52 mm in diameter using 5 mm glass spheres in the upflow bed at 8 bara, 27 mm with 5 mm glass spheres in the trickle bed at 6.75 bara, and 52 mm using 1.2 mm poppy seeds as the fluidised particles at 8.5 bara. The experiments were conducted at a laboratory temperature of 25.0 ± 3.0 °C.

In the upflow bed, time-averaged velocity images were acquired over a 2.5 h experimental time. This was done to capture the steady state behaviour of the vessel operating in the pulsing flow regime. The temporally-stable trickle flow state in the trickle bed was imaged over 15-100 minutes. In both packed beds, severe spatial anisotropy in the distribution of flow between pores was revealed. Furthermore, the data were used to determine classical design features such as catalyst wetting and liquid holdup which compared well with literature models. The trickle bed data were further analysed using a morphological algorithm which unambiguously identified the gas-liquid and liquid-solid interfaces. The interfacial flow fields were found to be similar to the bulk flow, with most voxels exhibiting static behaviour. The amount of interaction between the phases was found to be minimal, which is typical of the low interaction regime.

A single bubble injection system was employed in the fluidised bed which allowed the injection of isolated bubbles into the incipiently fluidised bed. It also enabled the triggered acquisition of NMR data at precise time intervals. The bubble was found to be an indented ellipsoidal shape, which rose with atypical behaviour which caused it to collapse. Rise velocity was found to be consistent with theory, and the injected bubbles were sufficiently spatially reproducible to acquire 2D velocity images using single-point imaging. These velocity images showed flow behaviour characteristic of a ‘fast’ rising bubble, with a gas recirculation cloud 37 mm in diameter. The particle field was shown to have very high flow in the bubble wake, revealing the mechanism of bubble collapse. The flow data were compared to classical two-phase fluidisation theory, which revealed noteworthy differences in the division of flow between the particulate and bubbling regions.

CONTENTS

CHAPTER 1 – INTRODUCTION

Solid-fluid contacting is a universally important phenomenon in nature and the process industries. The performance of both non-reacting operations such as drying, filtration and chromatography, and reacting systems such combustion, and solid-fluid reactions using solid catalysts or solid reagents depends on the effectiveness of solid-fluid contacting steps. Of the most commercial interest are reactor vessels in which multiphase flow interactions occur. Two of the most popular equipment choices for many of these operations include the fixed bed and the fluidised bed. The multiphase behaviour of these units is very complex and has been the topic of much research for decades. Despite the vast corpus of experimental knowledge, much remains to be understood about their fundamental fluid dynamics. The complexity of the fluid behaviour is typically simplified in design using empirical models and correlations. This sometimes leads to overdesign, and less-than-optimal use of materials, which is highly undesirable from a sustainability perspective.

A deeper knowledge of the hydrodynamics of these units will facilitate optimised design, scale-up and improve the operation of existing units and processes. Our understanding of multiphase reactor hydrodynamics is limited in part by the lack of detailed experimental measurements within these units. Few experimental techniques can probe the behaviour of fluids in optically-opaque systems of industrially relevant geometries. This project aims to use nuclear magnetic resonance (NMR) and magnetic resonance imaging (MRI) to study multiphase reactor hydrodynamics, focussing on co-current upflow beds, trickle-beds and fluidised bed reactors.

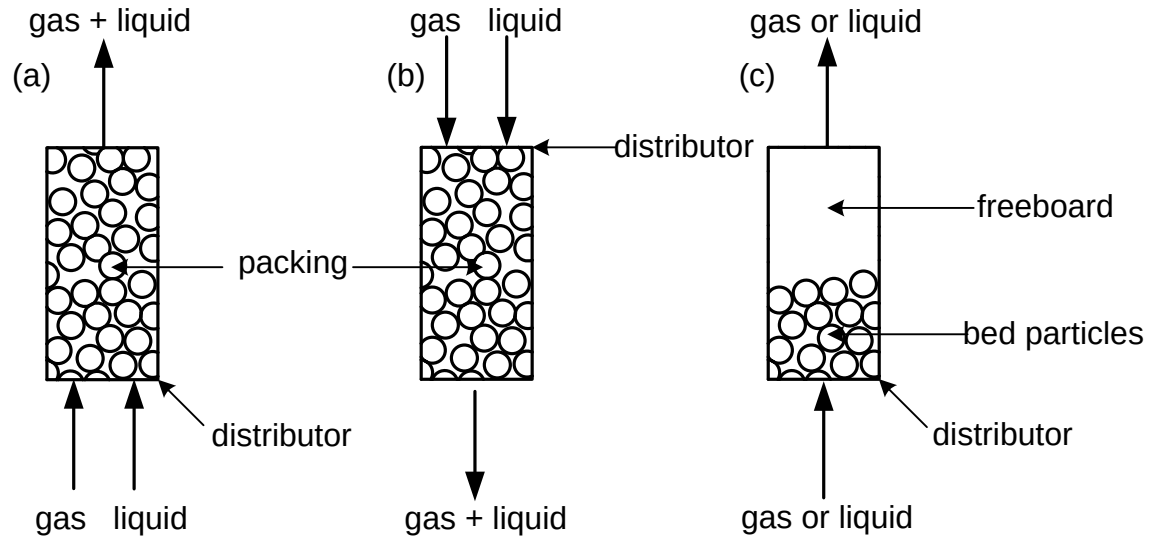

Figure 1.1: Schematic representations of the three configurations of multiphase reactor vessel presented in this thesis: (a) co-current upflow packed bed, (b) trickle bed and (c) fluidised bed.

The configuration of flow and basic structure of these reactor vessels is given schematically in Figure 1.1.

1.1. CO-CURRENT UPFLOW BEDS

Packed beds in co-current upflow configuration, in which a gas and liquid are passed mutually in the vertical upward direction, are used when a physicochemical transformation is required which benefits from large liquid residence times or from large liquid-to-gas volume ratios [1]. A co-current upflow arrangement is schematically depicted in Figure 1.1 (a). They are therefore sometimes called 'bubble columns', because in typical operation they consist of a continuous or semicontiguous liquid phase through which a dispersed gas phase is passed between the particle interstices. They are therefore also widely used for treating small amounts of gas in packed inert-solid absorption columns, in which the solid material serves only to promote contact between the gas and liquid phases [2]. The hydrodynamic behaviour and design considerations of upflow beds has been reviewed in several extensive reviews [1–4]. Despite being employed widely in industry, they remain relatively under-researched when compared with trickle-bed reactors which are run in co-current downward flow. A table summarising the noteworthy differences between co-current upflow and downflow (trickle flow) is given in Table 1.1.

Table 1.1: Comparison of key design differences between three phase upflow and trickle bed downflow reactors

	Upflow reactor	**Trickle bed reactor**
Liquid holdup	Higher, continuous phase	Lower, semi-continuous
Gas holdup	Disperse bubbles	Continuous, larger
Back mixing	Significant back mixing	Back mixing minimal
Side reactions	Homogeneous reactions possible	Liquid phase reactions minimised
Heat and mass transfer	Higher than trickle flow	Lower owing to poor catalyst wetting

For these reasons, co-current upflow beds are the favoured choice for processes involving gas absorption followed by catalytic reaction. Examples of industrially significant processes employing upflow reactors include hydrodesulfurisation [5], liquid phase catalytic

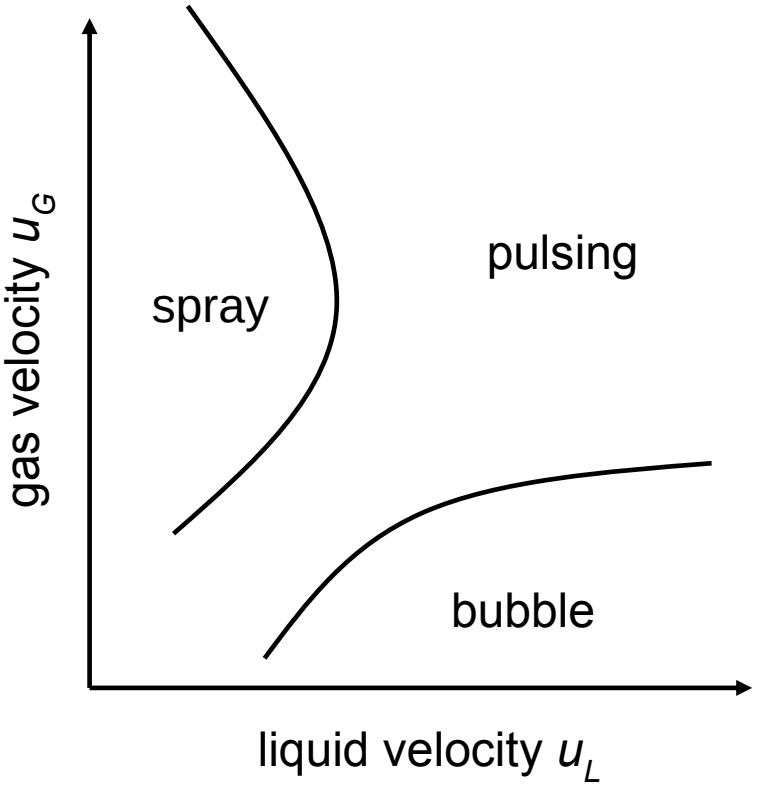

Figure 1.2: Three fundamental flow regimes for co-current upflow packed beds as a function of the liquid and gas superficial velocities. More complex flow regimes have been identified and are covered in Chapter 3. Adapted from Shah [3].

hydrocracking [1], amination of alcohols [6] and waste liquid treatment processes [7]. Recently, the use of upflow beds with structured packing has attracted interest because of their possible use in the reactive absorption of CO_2 from flue gas streams in carbon capture and storage schemes [8]. The complexity of the flow dynamics in upflow beds is summarised by studying their behaviour under broadly identifiable flow regimes and empirical correlations.

A typical flow regime map for co-current upflow beds is shown in Figure 1.2. At mutually high gas and liquid rates, a pulsing regime is encountered which consists of plugs of alternatively liquid-rich and gas-rich regions which rise through the fixed bed. At high gas rates with low liquid flow, the spray regime is encountered. This is characterised by two-phase flow within the bed pores which resembles a mist, with small liquid droplets entrained in the higher gas flow. At high liquid and low gas rates, the bubbling regime is encountered. Here small bubbles of gas rise within the bed pores with behaviour governed by the buoyant forces. Recently, Pokusaev *et al.* [9,10] showed that the bubbles can behave as either bubble 'trains' or as 'amoeboid'-type structures. This behaviour is illustrated in Figure 1.3. Trains of bubbles exist within liquid-rich pores and rise as bubbles which do not change in size (i.e. do not coalesce or break apart). Amoeboid bubbles rise and move through the packing, either encompassing packing elements or splitting apart. Bubbles may also coalesce in this regime. Each flow regime

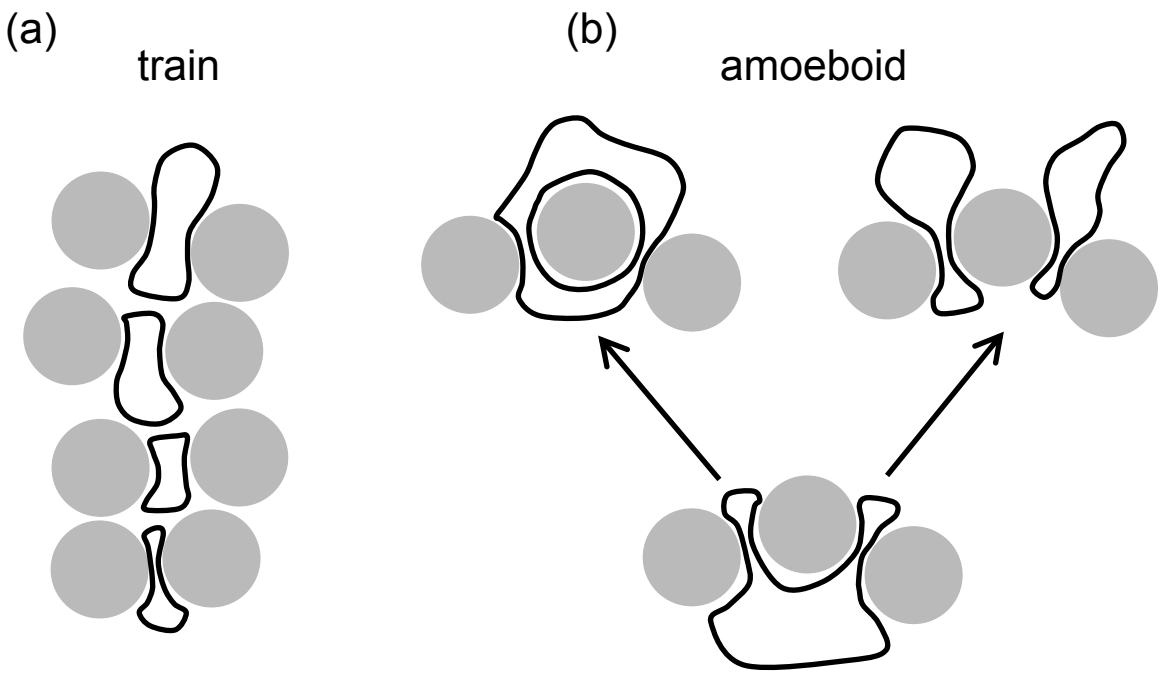

Figure 1.3: Observations of bubbling behaviour in co-current upflow packed bed reactors. In (a) the bubbles rise as a 'train' of successively liquid rich and lean pulses. In (b) larger bubbles move around particles, sometimes enveloping them and coalescing and sometimes splitting into more bubbles. Particles are indicated by the grey circles and the bubbles are outlined in black.

has different mass and heat transfer characteristics which must be tailored for the application. The energy requirements of the reactor also depend on the flow regime.

1.2. TRICKLE BEDS

Trickle bed reactors (TBRs) are the preferred choice of reactor vessel when a three-phase reaction (gas, liquid, solid) is required [11]. They are used for hydrotreating (hydrodesulphurisation and hydrodenitrogenation) and hydrocracking in the petrochemical industry. In these reactions gaseous hydrogen is reacted with liquid petroleum fractions over solid catalysts. They are also employed for hydrogenation, oxidation and Fischer-Tropsch reactions [3,12]. The total production output from trickle beds is worth more than £600 billion per year, and they are predicted to become increasingly important for the drive towards process intensification and sustainable processing [12]. Trickle beds consist of a static solid phase bed of particles which is packed in a usually cylindrical vessel. The packing is very often in the form of random, unstructured catalyst pellets, but it can also be structured. The reactive fluid phases are then passed through the vessel over the solid phase. A schematic diagram is provided in Figure 1.1 (b). The fluid phases are frequently passed co-currently downwards through the bed, but other counter-current configurations have been used in industry.

Trickle beds are favourable over many reactors due to their simplicity of operation and lack of moving parts. Maintenance is therefore straightforward, and they are relatively robust to varying process conditions. They do however suffer from a lack of adjustable parameters. They are used for catalytic liquid-phase reactions because of their high catalyst-to-liquid volume ratios.

The performance of the reactor is inherently related to the hydrodynamic behaviour of the bed. Most of the reaction between fluids occurs within the extensive porous network of the solid catalyst. Therefore, the degree of wetting of the catalyst has a severe effect on the behaviour and rate of chemical reaction. The fluid flow fields are affected by the bed structure, and recent studies have highlighted great anisotropy of bed structure and therefore fluid maldistribution in TBRs [12–15].

Modelling of the multiple phases in trickle bed reactors requires the independent equations describing the phases to have 'closure'. The precise nature of this closure is not yet established. The conservation balances for each fluid phase is known, but additional information regarding the interaction of the phases is required for a unique solution [16]. Closure models often take the form of phenomenological or empirical correlations, but a better physical understanding will improve the quality of computational modelling.

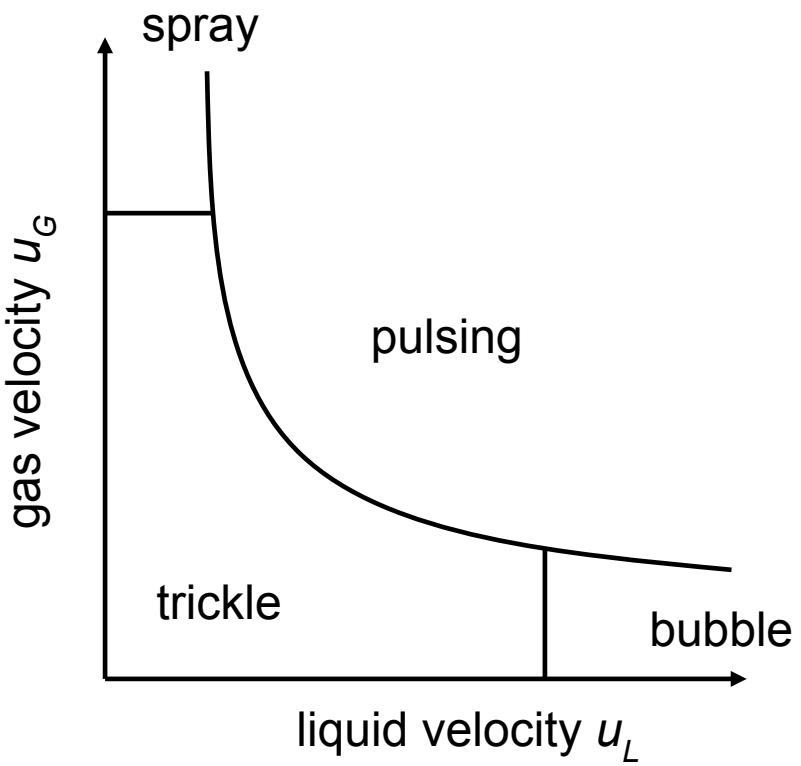

Figure 1.4: Flow regimes commonly encountered in trickle beds (co-current downward flow) as a function of the liquid and gas superficial velocities. Adapted from Tsochatzidis and Karabelas [13].

In a similar way to co-current upflow reactors, the overall hydrodynamic behaviour of TBRs is plotted as a broad function of liquid and gas superficial flow rate in regime maps, such as that shown in Figure 1.4. Similar pulsing behaviour to co-current upflow is seen at mutually high gas and liquid rates, with pulses of liquid- and gas-rich regions moving downwards through the bed in this case. A bubbling regime is also encountered at low gas and high liquid rates. Additionally, a spray flow regime with entrained liquid droplets is encountered at high gas and low liquid flows. However, a temporally stable regime known as trickle-flow which exists between the spray and bubbling behaviour. In this regime, the liquid flows as a stable continuum over the solid particles and the gas occupies the space between the liquid and solid regions of the pore space. The trickle regime belongs to the low-interaction-regime (LIR) whilst other more vigorous regimes are broadly classified as high-interaction regimes (HIR).

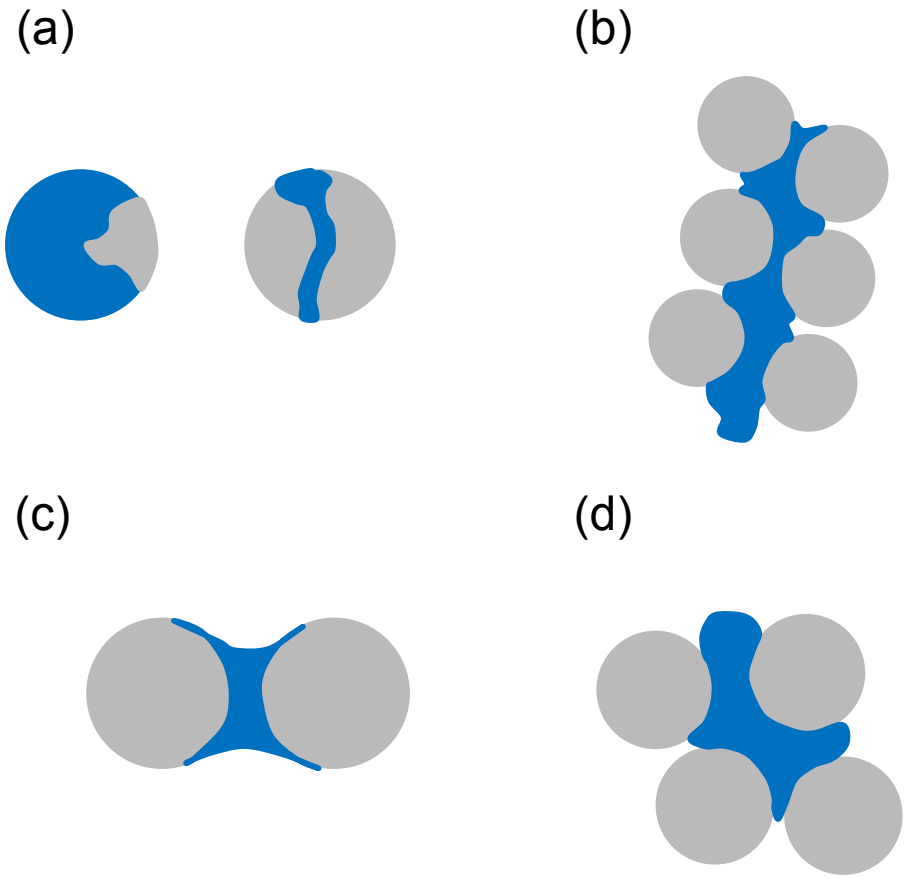

Figure 1.5: Several temporally stable local hydrodynamic phenomena commonly encountered in trickle beds. (a) shows partially-wetted particles including liquid films and rivulets over particles, b) shows a liquid filamant which spans several particles, (c) shows a pendular liquid structure and (d) shows a stagnant liquid pocket. Particles are shown by the grey circles and the liquid is represented in blue.

Several local hydrodynamic phenomena which have been observed experimentally in the low-interaction regime are depictured in Figure 1.5. These phenomena all contribute to phase maldistribution and loss of catalytic efficiency in trickle bed reactors. Figure 1.5 (a) shows two

aspects of partial catalyst wetting in the form of liquid films or rivulets over particles leaving some of their surface area dry. In (b) a stable liquid filament is shown, where different local flow regimes may exist over several particle lengths due to different local liquid behaviour. (c) shows a liquid pendular structure which consists of a pocket of liquid with films which may have different local hydrodynamics. When stagnant liquid exists between particles a pocket like that in (d) may form. Evidence suggests that these phenomena exist despite the full interior surface area of porous catalyst particles being wetted. Partial wetting and stagnant liquid cause variations in the reaction rate, which is difficult to predict using modern modelling. Enhanced experimental evidence will aid these approaches in allowing more quantitative local information to be obtained.

1.3. FLUIDISED BEDS

A typical fluidised bed consists of a cylindrical vessel filled with a bed of particulate solids which rest atop a fluid distributor. This structure is illustrated schematically in Figure 1.1 (c). When a fluid flows upwards through the bed, the pressure drop across the bed is initially governed by the same physics of a fixed bed, but as the flow is increased the upwards drag force on the particles becomes equal to their apparent weight at a certain flow rate. At this point the bed is said to be *fluidised*. A further increase in velocity results in bed expansion, an increase in solid void fraction and the formation of bubbles. Sufficiently high rates of flow will eventually cause transport of the solid material out of the vessel. This behaviour is illustrated in Figure 1.6 which shows the arrangement of solid particles together with the logarithmic pressure drop curve for a typical fluidised bed.

Due to characteristically high rates of heat and mass transfer, fluidised beds are a common choice for fast gas-solid catalytic reactions which require vigorous mixing to overcome diffusion limitations. As their particles mix continuously, they are nearly isothermal under chemical reaction making them a favourable choice when the temperature of reaction needs to be controlled precisely. Their isothermal nature is frequently exploited for high-temperature exothermic reactions and catalytic reactions which result in sintering or coking. Fluidised beds have been successfully used for the gasification of coal, fluidised catalytic cracking, drying and the Fischer-Tropsch synthesis of gasoline products from syngas [17].

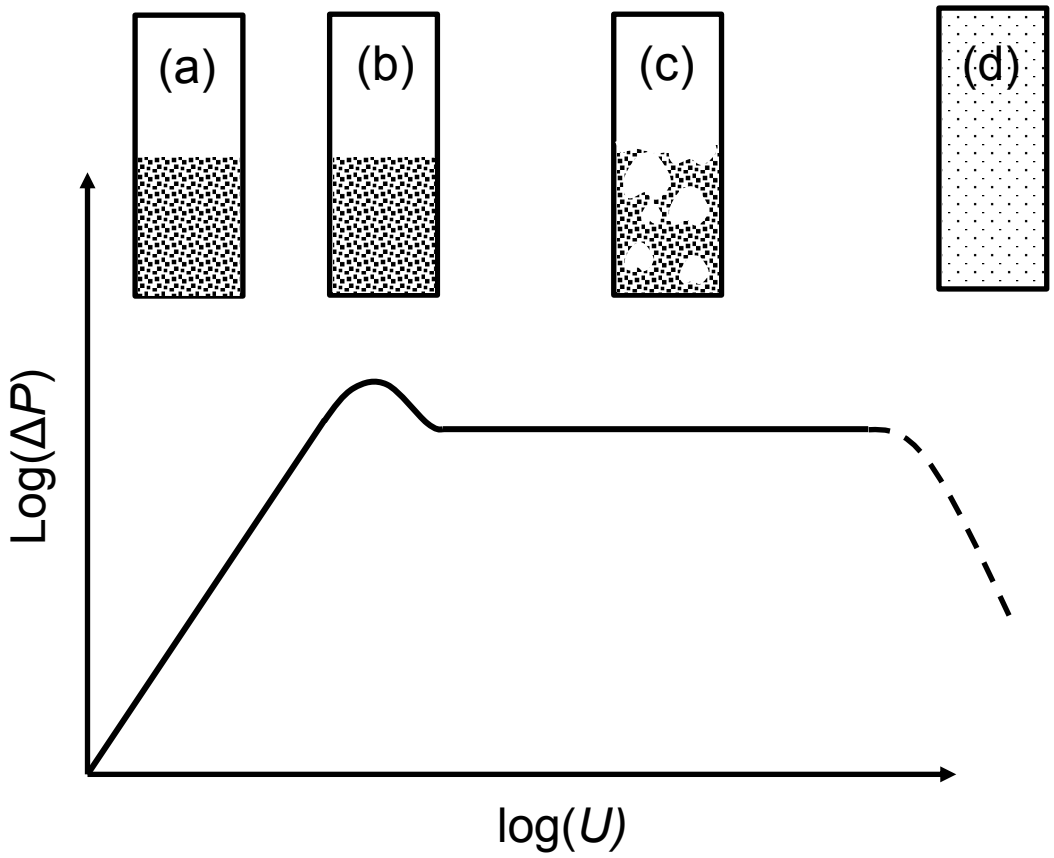

Figure 1.6: The behaviour of a fluidised bed as a function of the fluid velocity shown above the logarithm of pressure drop as a function of the logarithm of the fluid superficial velocity. (a) shows packed bed behaviour with static particles, (b) is the shown at U_{mf} and no macroscopic changes are observed but a maximum in the pressure drop curve is caused by particle jamming; after the point of minimum fluidisation the pressure drop is constant, and, in most beds, bubbling is encountered as in seen in (c). At sufficiently high velocities the solid material is transported out of the reactor as in (d).

Lately, attention has been shifted towards fluidised beds for the production synthesis gas from biomass. Biomass-derived syngas, such as that from wood, bagasse and agricultural or industrial residues can be produced catalytically but it tends to contain significant amounts of impurities. These impurities, primarily tars and alkali metals, have enormously detrimental effects on downstream processing equipment [18]. Due to the exothermic nature of the reaction and the importance of impurity removal, many studies [19–21] demonstrate the favourable characteristics of fluidised bed reactors for this use. Systems such as the circulating fluidised bed can successfully integrate gasification and tar-cracking catalysis in the same bed. Additionally, solid chemical looping agents such as calcium oxide can be added to the bed for carbon capture. Fluidised beds are also flexible in their performance with respect to changing feedstock conditions such as solids size distribution.

A phenomenon present in fluidised beds which challenged researchers for years was the emergence and motion of visible bubbles (lean regions consisting of mostly fluid) through the

bed which rise analogously to bubbles in liquids. The conceptual task was in understanding their existence despite the lack of a surface tension force in granular media. A theoretical stride forward came in the form of the seminal work by John Davidson [22] which described the fluid and particle motion around individual bubbles in granular media. These authors exploited similarities between the rise behaviour and geometry of fluidised bed bubbles and classical spherical cap gas bubbles rising through quiescent liquids. Figure 1.7 shows the geometry of an ideal bubble alongside an X-ray photograph from a real bubble rising through a fluidised bed.

In Figure 1.7 (a) the bubble geometry is that of a spherical cap which is the intersection of two spheres. A sphere of radius R_b forms the bubble region itself (region of reduced particle fraction) and from it is subtracted a spherical region of radius R which is the wake radius. The wake of the bubble is caused by the flow of particles into the rear of the bubble as it rises. The x-ray image in (b) by Yates and Simons [23] confirms this type of shape for certain particles. The onset of this type of behaviour for different materials can be predicted by the classification of powders and fluids by Geldart [24]. As the bubbling behaviour strongly influences the bed heat and mass transfer, for optimised design it is critical that a more fundamental understanding of the geometry and fluid flow of fluidised bed bubbles is obtained experimentally.

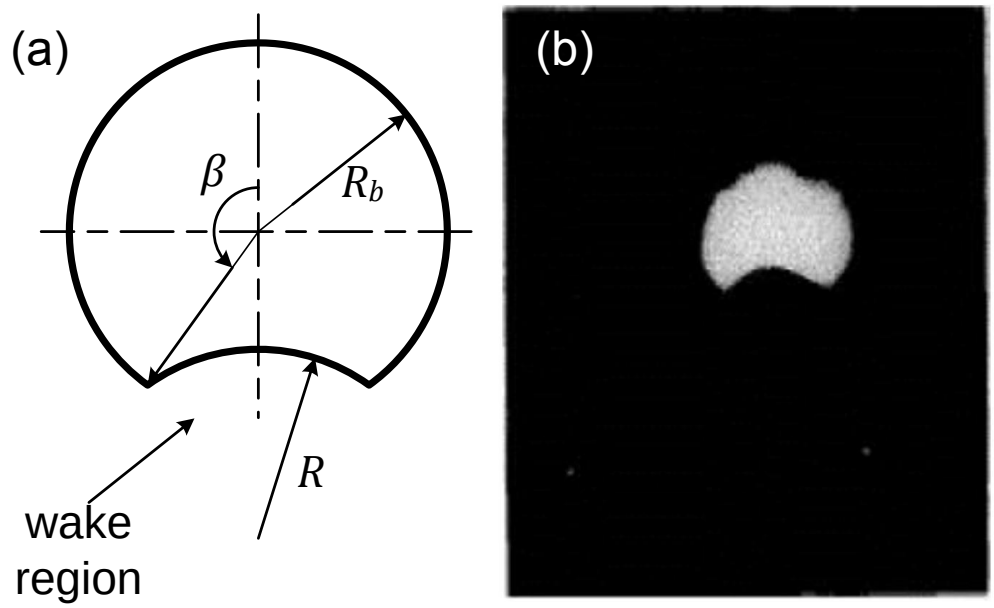

Figure 1.7: An isolated single bubble in a fluidised bed. (a) shows the ideal spherical cap shape for fluidised bed bubbles where R is the wake radius, R_b is the bubble radius and β is the wake angle. (b) shows a real fluidised bed bubble captured in an x-ray photograph by Yates and Simons [23] in a 3D fluidised bed.

1.4. AIM AND SCOPE OF THESIS

The aim of this thesis is to report on the use of magnetic resonance imaging techniques for the investigation of multiphase hydrodynamic behaviour in reactor vessels. Specifically, the study aims to advance the fundamental understanding of particle-scale local hydrodynamics in co-current upflow, trickle and fluidised beds. This is done principally through the application of thermally-polarised gas-phase velocity imaging which has not yet been applied for this purpose in the open literature in all three types of systems.

Gas phase imaging of each system was undertaken using an MRI pulse sequence designed specifically for use in systems with poorly-matched magnetic susceptibilities which traditionally negates the use of the pulsed field gradient technique. Time averaging and the use of controlled injections of bubbles is used to acquire quantitative, spatially-resolved maps of gas velocity in these complex multiphase systems for the first time. These maps are obtained in an experimental system with geometric characteristics which are industrially-relevant, under elevated pressure conditions. The quantitative information obtained is thus compared with traditional design metrics (such as pressure drop, catalyst wetting, fluidised bubble through-flow) and comments are made regarding the differences uncovered considering the use of more realistic experimental conditions and a non-intrusive measurement technique. Specifically, the multiple aims of the present study are therefore to:

- obtain the first spatially resolved velocity measurements of both the gas and liquid fields in a co-current upflow bed
- apply MRI velocimetry techniques to obtain the temporally stable velocity fields in a trickle bed to elucidate interactions at the phase interface
- characterise controlled bubble injections into an incipiently fluidised bed using MRI
- obtain the first quantitative flow maps of gas and particle flow around an isolated fluidised bed bubble and compare these to two-phase theory.

This information is gathered for the benefit of improved design of industrial multiphase reaction vessels. The sophistication of the techniques enables the interaction between gas, liquid and solid to be assessed in three different reactor vessels. These interactions are at present an open-ended problem in computational modelling, with no unified theory regarding how to describe phase interactions in different flow regimes. It is hoped that a more quantitative

description of reactor multiphase physics will validate modelling, improve design and inform the operation of these units across industry.

1.5. OUTLINE OF THESIS CHAPTERS

CHAPTER ONE introduces the content covered in this thesis, giving short theoretical descriptions of the reactor systems of interest and highlighting some important studies in the literature. An outline of the thesis structure is also given.

CHAPTER TWO gives a rudimentary description of NMR and MRI theory which is required for the correct comprehension of the experimental results.

CHAPTER THREE presents the experimental results obtained on the co-current upflow system. Here the spatially resolved phase density and velocity images are shown and the results discussed in terms of existing design theory. The chapter also contains a section on single-phase pipe flow.

CHAPTER FOUR discusses the first results obtained for (co-current downward) trickle flow. It presents a pore-scale discussion of the degree of anisotropy present in the flow fields and compares standard design metrics against the experimentally-obtained values.

CHAPTER FIVE describes a detailed investigation of the phase interfaces in trickle flow. The interfacial velocity and shear stress is determined in both the gas and liquid phases, to assess the extent of interaction present.

CHAPTER SIX illustrates the use of 1D MRI to characterise and study the injection of single controlled bubbles into an incipiently fluidised bed. The bubble rise velocity and injection reproducibility are assessed.

CHAPTER SEVEN presents the results of using controlled reproducible bubbles to produce images of the gas and particle flow fields around an isolated bubble rising in a gas-solid fluidised bed. The results are quantitatively compared with existing theories of fluidisation, and the vector maps are qualitatively discussed in terms of literature models.

CHAPTER EIGHT gives the primary conclusions from each of the chapters and the overall deductions from this study regarding the application of MRI techniques for the study of multiphase reactor hydrodynamics. The chapter also presents recommendations on each set of experiments for improved investigation in the future.

NOMENCLATURE

ABBREVIATIONS

MRI	magnetic resonance imaging
NMR	nuclear magnetic resonance
TBR	trickle bed reactor

SYMBOLS

P	pressure	bar
R	wake radius	m
R_b	bubble radius	m
U	fluid superficial velocity	m s^{-1}
U_{mf}	fluid superficial velocity at minimum fluidisation	m s^{-1}
u_L	liquid superficial velocity	m s^{-1}
u_G	gas superficial velocity	m s^{-1}

GREEK LETTERS

β	wake angle	rad

REFERENCES

[1] Hofmann, H.P. Multiphase Catalytic Packed-Bed Reactors. *Catal. Rev.* 1978;17: pp. 71–117.

[2] Ramachandran, P.A., Chaudhari, R. Three-phase catalytic reactors. vol. 2. New York: Gordon & Breach Science Pub; 1983.

[3] Shah, Y.T. Gas-liquid-solid reactor design. McGraw-Hill; 1979.

[4] Duduković, M.P., Larachi, F., Mills, P.L. Multiphase catalytic reactors: a perspective on current knowledge and future trends. *Catal. Rev.* 2002;44: pp. 123–246.

[5] Montagna, A., Shah, Y.T. Backmixing effect in an upflow cocurrent hydrodesulfurization reactor. *Chem. Eng. J.* 1975;10: pp. 99–105.

[6] Dai, P.S.E., Renken, T.L., Neff, L.D. Supported catalysts for amination. US5352835A, 1994.

[7] Jong, T., Parry, D.L. Removal of sulfate and heavy metals by sulfate reducing bacteria in short-term bench scale upflow anaerobic packed bed reactor runs. *Water Res.* 2003;37: pp. 3379–89.

[8] Khan, F.M., Krishnamoorthi, V., Mahmud, T. Modelling reactive absorption of CO2 in packed columns for post-combustion carbon capture applications. *Chem. Eng. Res. Des.* 2011;89: pp. 1600–8.

[9] Pokusaev, B.G., Karlov, S.P., Shreiber, I. Immersion Tomography of a Gas – Liquid Medium in a Granular Bed 2004;38: pp. 5795.

[10] Pokusaev, B.G., Kazenin, D.A., Karlov, S.P. Immersion Tomographic Study of the Motion of Bubbles in a Flooded Granular Bed 2004;38: pp. 561–8.

[11] Al-Dahhan, M.H., Larachi, F., Dudukovic, M.P., Laurent, A. High-Pressure Trickle-Bed Reactors: A Review. *Ind. Eng. Chem. Res.* 1997;36: pp. 3292–314.

[12] Ranade, V., Chaudhari, R., Gunjal, P. Trickle Bed Reactors: Reactor Engineering & Applications. 2011.

[13] Tsochatzidis, N.A., Karabelas, A.J., Giakoumakis, D., Huff, G.A. An investigation of liquid maldistribution in trickle beds. *Chem. Eng. Sci.* 2002;57: pp. 3543–55.

[14] Lopes, R.J.G., Quinta-Ferreira, R.M. CFD modelling of multiphase flow distribution in trickle beds. *Chem. Eng. J.* 2009;147: pp. 342–55.

[15] Gunjal, P.R., Ranade, V., Chaudhari, R. Liquid Distribution and RTD in Trickle Bed Reactors : Experiments and CFD Simulations. *Can. J. Chem. Engneering* 2003;81: pp. 821–30.

[16] Jiang, Y., Khadilkar, M.R., Al-Dahhan, M.H., Dudukovic, M.P. CFD of multiphase flow in packed-bed reactors: I. k-fluid modeling issues. *AIChE J.* 2002;48: pp. 701–15.

[17] Kunii, D., Levenspiel, O. Fluidization Engineering. 2nd ed. Stoneham: Butterworth-Heinemann; 1991.

[18] Richardson, Y., Blin, J., Julbe, A. A short overview on purification and conditioning of syngas produced by biomass gasification: Catalytic strategies, process intensification and new concepts. *Prog. Energy Combust. Sci.* 2012;38: pp. 765–81.

[19] McKendry, P. Energy production from biomass (part 3): gasification technologies. *Bioresour. Technol.* 2002;83: pp. 55–63.

[20] Corella, J., Aznar, M.P., Delgado, J., Aldea, E. Steam gasification of cellulosic wastes in a fluidized bed with downstream vessels. *Ind. Eng. Chem. Res.* 1991;30: pp. 2252–62.

[21] Rapagna, S., Jand, N., Kiennemann, A., Foscolo, P.U. Steam-gasification of biomass in a fluidised-bed of olivine particles. *Biomass and Bioenergy* 2000;19: pp. 187–97.

[22] Davidson, J.F. Symposium on fluidization - discussion. *Trans. Inst. Chem. Eng.* 1961;39: pp. 230–2.

[23] Yates, J.G., Simons, S.J.R. Experimental methods in fluidization research. *Int. J. Multiph. Flow* 1994;20: pp. 297–330.

[24] Geldart, D. Types of gas fluidization. *Powder Technol.* 1973;7: pp. 285–92.

CHAPTER 2 – NMR AND MRI THEORY

The principle of nuclear magnetic resonance (NMR) was discovered almost simultaneously by Felix Bloch [1] and Edward Purcell [2] in 1946. They showed that given certain conditions, atomic nuclei placed in a magnetic field can absorb and re-emit radiofrequency energy at frequencies which are specific to the nucleus in question. This work was awarded the Nobel Prize in 1952, and it was soon apparent that it could be used for chemical and structural analysis of molecules. Recognising the sensitivity of the technique to magnetic field strength, the same resonance principle was extended by Paul Lautebur [3] and Mansfield and Grannel [4] who produced ^{1}H density images using spatially-varying magnetic fields. These were the first experiments in magnetic resonance imaging (MRI), which has since become a fundamental technique in medicine for non-invasive diagnosis. MRI has recently been shown to be a powerful diagnostic technique in many other sciences, including engineering and materials science. In this chapter, the elementary principles of NMR and MRI are presented, along with the theory regarding the measurement of motion and compressed sensing in MRI. For a more detailed description of these theories and studies, the reader is referred to the standard texts [5–7] from which the following summary is largely adapted.

2.1. NUCLEAR SPIN AND THE ZEEMAN INTERACTION

Nuclear magnetic resonance is the physical phenomenon in which the quantum mechanical spins of nuclei resonate at a specific frequency which can be excited by an oscillating external magnetic field. Spin (designated I) is a fundamental quantum mechanical property belonging to elementary particles. Protons and neutrons, as comprised of elementary fermions, are both spin-1/2 particles. The spin of a nucleus is a function of the individual number of protons and neutrons it is comprised of. Simplistically, when the number of protons and neutrons in a nucleus is even, the net spin of the nucleus is zero. When there is an odd number, the spin will take an integer value. When, however, the sum of nucleons is odd, the value of the spin will be a half-integer value. Nuclei with net non-zero spin numbers possess a spin angular momentum (designated **P**), which is analogous to the classical idea of angular momentum. The spin angular momentum is quantised and related to the spin quantum number through:

$$\mathbf{P} = \hbar[I(I+1)]^{1/2}, \tag{2.1}$$

where $\hbar$ is the reduced Planck's constant $\hbar = h/2\pi$. The component of the angular momentum P_z in the vertical (z) direction is given by:

$$P_z = m_s\hbar, \tag{2.2}$$

where m_s is the magnetic quantum number restricted to values $m_s = I, I-1, I-2, \ldots, 0, \ldots, -I+1, -I$. Therefore, the z-component of spin-1/2 nuclei such as ^{1}H and ^{19}F have two allowable quantum states of $P_z = \pm\hbar/2$ for $m_s = \pm 1/2$.

Furthermore, these nuclei possess a net magnetic dipole moment which is related to the spin angular momentum through the following:

$$\boldsymbol{\mu} = \gamma \mathbf{P}. \tag{2.3}$$

Here, $\boldsymbol{\mu}$ is the magnetic dipole moment and γ is a property known as the gyromagnetic ratio, which is specific to a particular nucleus. Individual nuclei can exist in different spin states. Under standard thermal equilibrium and without the presence of an external magnetic field, the spin states are all degenerate in energy. This degeneracy can be removed, and the spin states split in energy if a collection of spins is placed in an external magnetic field. This phenomenon is termed the Zeeman interaction. The energy of each level is given by:

$$E = -\boldsymbol{\mu} \cdot B_0 = -\gamma P_z B_0 = -\gamma m_s \hbar B_0. \tag{2.4}$$

In Figure 2.1, the splitting process is illustrated for nuclear magnetic dipole moments of a spin-1/2 nucleus in the presence of an external magnetic field B_0. The difference in energy (ΔE) between the two levels $\alpha = m = 1/2$ and $\beta = m = -1/2$ is given by:

$$\Delta E = h\nu_0 = \hbar\gamma B_0, \tag{2.5}$$

where energy of the appropriate radiofrequency ν_0 can cause transitions from the lower energy state α to the higher energy state β. Clearly the energy difference is proportional to the strength of the external magnetic field B_0.

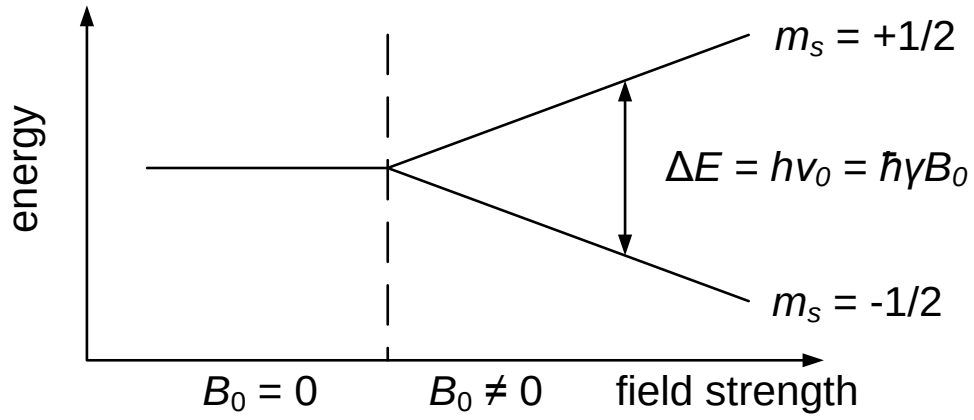

Figure 2.1: Simple schematic illustration of the Zeeman interaction splitting of a spin-1/2 nucleus in the presence initially of no magnetic field ($B_0 = 0$) then with an increasing magnetic field strength.

2.2. THE BLOCH VECTOR MODEL

It becomes useful in NMR to make use of the Bloch vector model, which is a description of the net nuclear magnetic dipole vector. There will be a distribution of nuclei in either the higher or lower energy state which can be described the following Boltzmann distribution:

$$\frac{N_\beta}{N_\alpha} = \exp\left(-\frac{\Delta E}{k_B T}\right) = \exp\left(\frac{\hbar\gamma B_0}{k_B T}\right). \tag{2.6}$$

In Equation 2.6 N_β and N_α are the number of spins in the high and low energy states respectively, k_B is the Boltzmann constant and T is the temperature. The difference in populations is typically very small, for example using ^{1}H in a 4.7 T magnetic field results in a splitting of the order of 10^{-5}, thus large magnetic fields are used to increase sensitivity to this inherently low energy difference. The spins can be viewed as aligned either "with" (low energy) or "against" (high energy) the magnetic field. If all the vectors are summed, this will give the bulk magnetisation vector **M**. Making use of a classical similarity to torque and the rate of change of angular momentum, we can derive:

$$\frac{d\mathbf{M}}{dt} = \mathbf{M} \times \gamma\mathbf{B}. \tag{2.7}$$

The solution of this equation gives the fundamental equation in NMR:

$$\omega_0 = \gamma B_0. \tag{2.8}$$

Here the precession frequency ω_0, the frequency at which the magnetisation vector will gyroscopically precess around the magnetic field is the fundamental frequency which will be excited and recorded in MRI and is termed the Larmor frequency. The position of this magnetisation vector can be disturbed at the resonance frequency by a secondary magnetic field B_1, applied perpendicularly to the main field and transitions between the two energy levels can be recorded.

In a standard NMR experiment, the static strong magnetic field B_0 is oriented so it is aligned vertically parallel with the *z*-axis to achieve polarisation in the vertical axis. The sample is excited using a radiofrequency (r.f.) coil which is placed around the sample. This coil is responsible for the application of the orthogonal secondary time-varying magnetic field B_1 and for signal detection. B_1 is applied to the sample using a sinusoidally varying current through the coil controlled by a signal generator. Signal detection is accomplished through electromagnetic induction of the spin population (which possesses a net magnetic moment) inside the coil. It is necessary therefore that the magnetisation vector be manipulated to have a transverse component with respect to the r.f coil. The spins are excited to the high energy state using timed 'pulses' of r.f. energy from the coil. These pulses are applied at the resonance frequency of the spins such that the combined precession of the vector around the effective field of B_0 + B_1 'tips' the net magnetisation vector into the transverse plane. The timed applications of B_1 are colloquially called 'r.f. pulses' and a series of pulses is called a 'pulse sequence'.

It is mathematically elegant to consider the motion of the vector **M** in the rotating frame of reference. If this is not done, the motion of the vector around the effective magnetic field B_0 + B_1 is complex. This process is best explained using the Bloch sphere for illustration in Figure 2.2. In Figure 2.2 (a) the pure precession of the magnetisation vector is seen about the static polarisation field. In (b), the secondary field B_1 has been applied as an r.f. pulse and the vector is seen traversing a complex 2D motion within the sphere. In (c), The vector is viewed in a frame of reference which is rotating at the Larmor frequency ω_0 about the *z*-axis. The motion of the vector is greatly simplified and is seen to tip into the horizontal plane. The final angle of the magnetisation vector can be controlled using the duration of the r.f. pulse applied according to $\theta = \gamma B_1 t_{pulse}$. This process is illustrated in Figure 2.3 where the vector undergoes a flip angle of 180°.

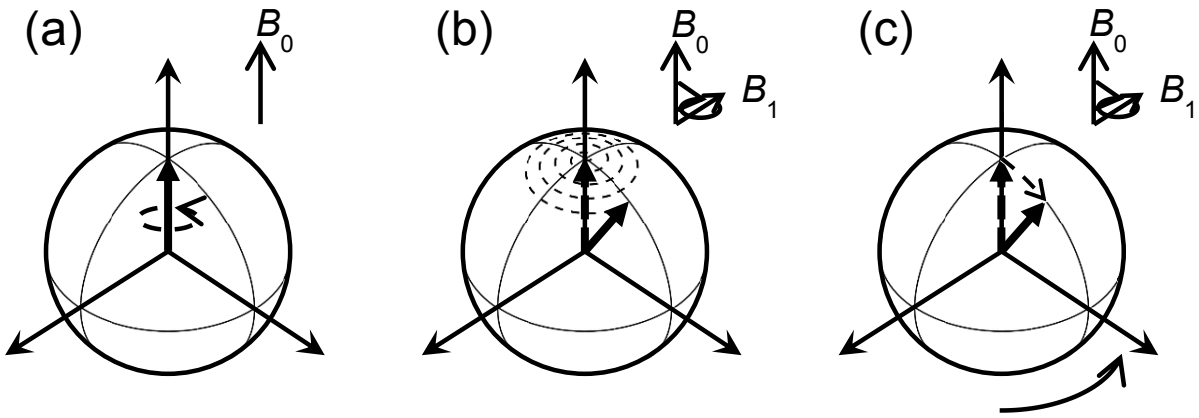

Figure 2.2: Illustration of the Bloch vector model of the net magnetisation **M** vector in NMR. (a) shows the net vector precessing around the *z*-axis in the laboratory frame of reference, (b) illustrates the path of the vector upon the application of the secondary orthogonal magnetic field B_1 applied at the resonance frequency of the nuclei which causes it to tip towards the horizontal plane as more spins become excited to the high energy state. **M** is seen precessing simultaneously around the effective vector sum of the applied magnetic fields. (c) shows this same process when the vector is viewed in the rotating frame of reference in which the precession is isolated to only that around B_1.

2.3. SIGNAL DETECTION

The r.f. coil detects the transverse component of the magnetisation vector as it returns to the equilibrium position. The signal arises as a time-varying induced electrical signal in the coil, $S(t)$ which is called the free induction decay (FID). The induced signal is inherently complex, and is detected in quadrature as a complex signal which is proportional to the magnitude of the transverse magnetisation component as follows:

$$M_{x,y}(t) = M_0 \cos(\omega_0 t) + iM_0 \sin(\omega_0 t), \tag{2.9}$$

or rewritten in complex notation as:

$$M_{x,y}(t) = M_0 \mathrm{e}^{i\omega_0 t}\,. \tag{2.10}$$

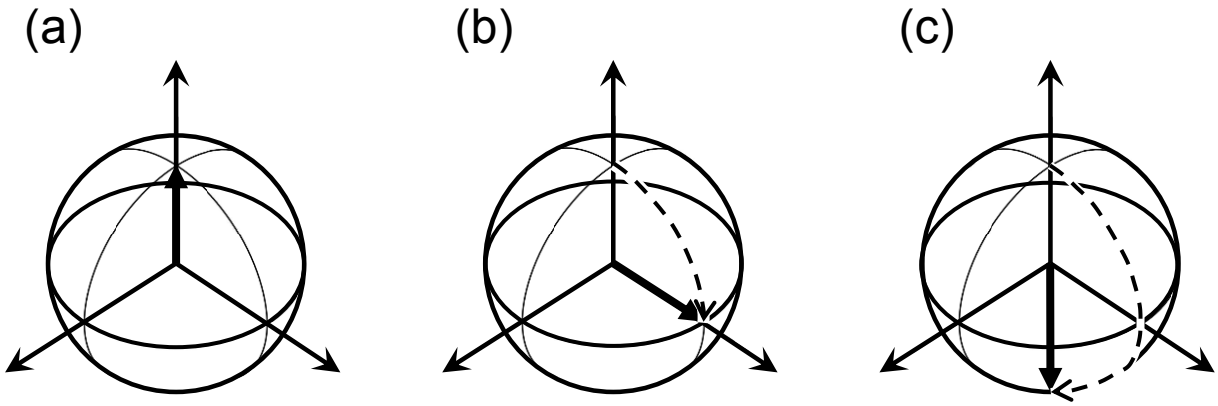

Figure 2.3: The net magnetisation vector at static equilibrium in (a) and having acquired energy from a 90° r.f. pulse in (b), and a 180° pulse in (c). The rotation around the B_1 field is illustrated by the dashed line trajectory.

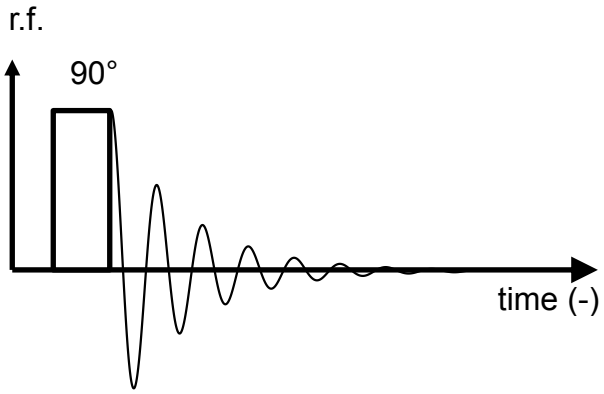

Figure 2.4: A simple pulse-acquire pulse sequence

The acquired signal is mixed with reference signals which are 90° out of phase and with one another thus it is acquired as a 'real' and 'imaginary' component. A reference frequency is also used to offset the signal, which is the equivalent of viewing the magnetisation in the rotating frame of reference. This process is known as heterodyning, and the NMR signal is therefore:

$$S(t) \propto M_0 \mathrm{e}^{i\phi_R} \mathrm{e}^{i\omega_0 t}\,, \tag{2.11}$$

where ϕ_R is the arbitrary receiver phase. The signal can be transformed into the frequency domain using the Fourier transform as follows:

$$S(\omega) = \int_{-\infty}^{\infty} S(t)\, \mathrm{e}^{i2\pi\omega t} dt\,, \tag{2.12}$$

which is useful in many NMR-based experiments for frequency identification. A simple pulse-acquire pulse sequence, in which the magnetisation vector is tipped 90° and allowed to relax is shown in Figure 2.3. The pulse sequence is shown in Figure 2.4. The signal resulting from this

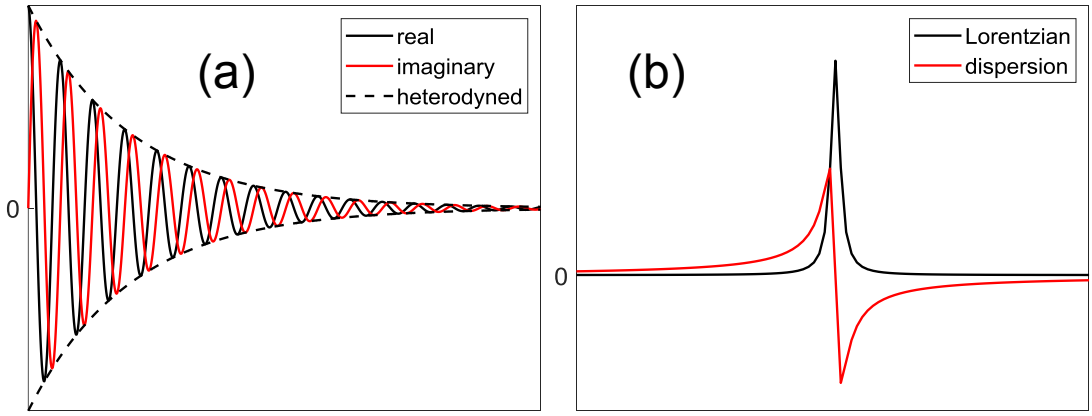

Figure 2.5: The acquisition of NMR signal in the time domain (a) and the Fourier-transformed signal in the frequency domain (b).

experiment including the FID signal, the heterodyned signal, and the Fourier-transformed frequency domain signal is shown in Figure 2.5. In practice the NMR signal is digitally sampled in time by a digitiser unit. The reproduction of signal is therefore dependent on the Nyquist-Shannon sampling theory. The interval between sampled points is termed the dwell-time t_d, and due to the Fourier relationship, it determines the window of the spectrum acquired in the frequency domain which is known as the spectral width (SW) according to $1/t_d$. This is required by the Nyquist theory to be twice the highest frequency present in the signal.

2.4. RELAXATION PROCESSES

The processes governing the emission of energy by nuclei back to the environment causing them to transition from the high energy state back down to the low energy state are discussed in this section. The processes are collectively called relaxation processes and will be discussed in terms of the Bloch vector model.

2.4.1. SPIN-LATTICE RELAXATION

At equilibrium, the position of the magnetisation vector is aligned vertically along the direction of B_0 or z-direction. In the rotating frame, when the vector is excited by r.f. pulses, it rotates only around the direction of B_1. Once B_1 has been turned off, several relaxation processes govern the return of the excited magnetisation vector back to its equilibrium position. Spin-lattice or T_1 relaxation results from exchange of energy from the excited spins and the surrounding molecules. The nomenclature T_1 arises from the time constant of the vector equation, which is written in the rotating frame of reference as:

$$\frac{dM_z}{dt} = -\frac{M_z - M_0}{T_1}. \tag{2.13}$$

The solution to this equation applying the initial condition $M_z(t = 0) = M_z(0)$ gives the solution:

$$M_z(t) = M_z(0)\exp\left(-\frac{t}{T_1}\right) + M_0\left[1 - \exp\left(-\frac{t}{T_1}\right)\right]. \tag{2.14}$$

T_1 for a given sample is the time it takes for the magnetisation vector to attain a value of 63% of its equilibrium magnitude. The value of T_1 is related to the rate of molecular tumbling in a system as each spin tumbles and generates a local magnetic field which influences the surrounding spins. Spins with higher tumbling rates which are closer to the Larmor frequency

interact with surrounding spins more. Therefore, T_1 decreases with increasing temperature and is smaller in gases than in liquids, which are in turn lower than solids. Measurement of T_1 can therefore be used for diagnostic purposes when studying materials. In addition to being a valuable characteristic of the nuclear spin system under study, the value of T_1 also determines the amount of time one has to wait between applying successive excitations of the magnetisation vector, and it is thus desirable to have shorter T_1 times. The time between successive pulses of r.f. energy is called the recycle time T_R. For gases T_1 is usually in the range of milliseconds, whilst for liquids it can be several seconds, as in the case of bulk water where $T_1 \sim 3$ seconds. To decrease the recycle time of experiments with materials with large values of T_1, systems are often 'doped' using paramagnetic ions which have valence electron bands which have a permanent magnetic dipole. This causes more rapid relaxation due to the strong interaction of the ions with the tumbling spins.

T_1 is usually measured using the inversion recovery pulse sequence, which applies a 180° r.f. pulse to the sample, resulting in **M** flipping onto the negative *z*-axis – the inversion step. After a time τ which is variable in the experiment, the signal has relaxed a certain amount longitudinally, a 90° is then applied which rotates the remaining magnetisation into the transverse plain in which it is detected. A diagram of this sequence is provided in Figure 2.6. The recorded signal strengths are then plotted as a function of τ and fitted to Equation 2.15 to determine T_1.

$$M_z(\tau) = M_0\left[1 - 2\exp\left(-\frac{\tau}{T_1}\right)\right]. \tag{2.15}$$

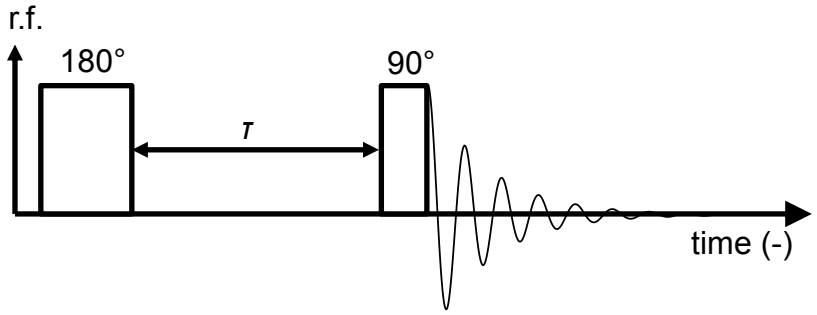

Figure 2.6: The inversion-recovery pulse sequence for the determination of the T_1 relaxation time constant.

Other methods used to determine T_1 are reviewed by Fukushima [8]. Usually, a value of a least $5T_1$ is used for the recycle time T_R to ensure the recovery of magnetisation is greater than 99% between successive excitation pulses.

2.4.2. SPIN-SPIN RELAXATION

Spin-spin or T_2 relaxation occurs when the spins themselves thermally equilibrate, which in turn causes a diminishing of the magnetisation vector due to dephasing. In the vector framework, M_z relaxation is governed by T_1 whilst the transverse plane component $M_{x,y}$ relaxes according to T_2. As each spin in the sample experiences a slightly different local magnetic field, the ensemble will dephase which leads to a decay in the transverse component. This behaviour is modelled according to the following expression:

$$\frac{dM_{x,y}}{dt} = -\frac{M_{x,y}}{T_2}. \tag{2.16}$$

The solution of Equation 2.16 is an exponential decay:

$$M_{x,y}(t) = M_{x,y}(0)\exp\left(-\frac{t}{T_2}\right). \tag{2.17}$$

T_2 relaxation is sometimes termed transverse relaxation. It is irreversible and is strictly smaller than T_1 as it is influenced by both transverse components. It is also apparent therefore that it governs the lifetime of the detectable signal, following Faraday's laws. The value of T_2 is typically determined using the Carr-Purcell-Meiboom-Gill or CPMG pulse sequence [9,10]. This is illustrated in Figure 2.7. A train of 180° pulses are applied after an initial 90° excitation which successively refocus the magnetisation in the transverse plane, allowing the signal to decay purely in the transverse plane according to T_2.

It is usually desirable to maximise the lifetime of the NMR signal, and thus have long T_2 times. However, other influences such as local inhomogeneities in the external field B_0 cause different nuclei to have locally varied Larmor frequencies and thus cause an apparent spin-spin relaxation effect and dephasing. This combined relaxation is termed T_2^*, and causes more rapid signal decay than T_2. This combined relaxation is expressed as follows:

$$\frac{1}{T_2^*} = \frac{1}{T_2'} + \frac{1}{T_2}. \tag{2.18}$$

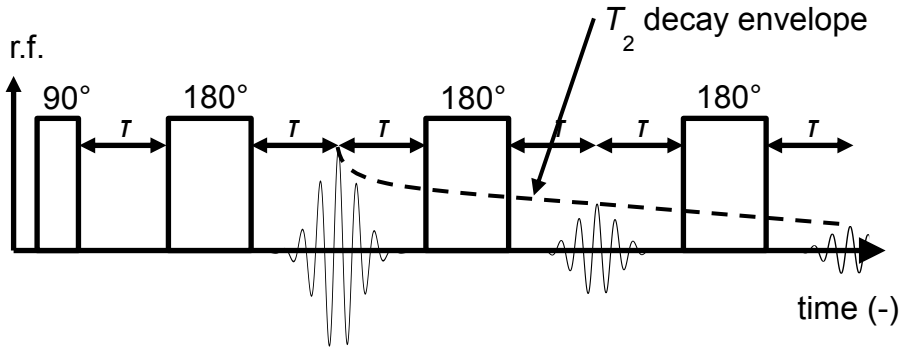

Figure 2.7: The CPMG pulse sequence for the measurement of T_2 relaxation time constant.

In Equation 2.18 T_2' represents the transverse relaxation component due to local magnetic field variations. For increasingly homogeneous B_0 fields, T_2^* approaches T_2. In practise, signal lifetime is always governed by T_2^*, and it is determined by measuring the full width half maximum (FWHM) of the spectrum produced from the FID according to:

$$T_2^* = \frac{1}{\pi(\Delta\nu_{FWHM})}. \tag{2.19}$$

In this expression, $\Delta\nu_{FWHM}$ is the frequency difference of the spectrum at FWHM.

The signal decay due to background gradients can be reversed by a magnetic pulse-acquire experiment known as the spin echo. Chemical shift also causes variations in the Larmor frequency of extended molecules in which individual atoms occur in different electronic environments from one another. This enables detailed chemical investigations to take place as in NMR spectroscopy. It also allows NMR and indeed MRI to be chemically-specific analysis tools.

2.5. ECHOES

2.5.1. SPIN-ECHO

The spin-echo experiment was developed by Hahn [11] in order to mitigate the effects of an inhomogeneous magnetic field. It refocuses the transverse component of the net magnetisation vector, effectively reversing the effects due to T_2^* dephasing. The pulse sequence and its effects on the magnetisation vector are given in Figure 2.8. After an initial 90° r.f. pulse, at a time τ a 180° pulse is applied to the sample. Local variations in the magnetic field causes the transverse plane components of the magnetisation to spread out relative to one another after the 90° pulse. The 180° pulse inverts the in-phase components and reflects the dephased components through

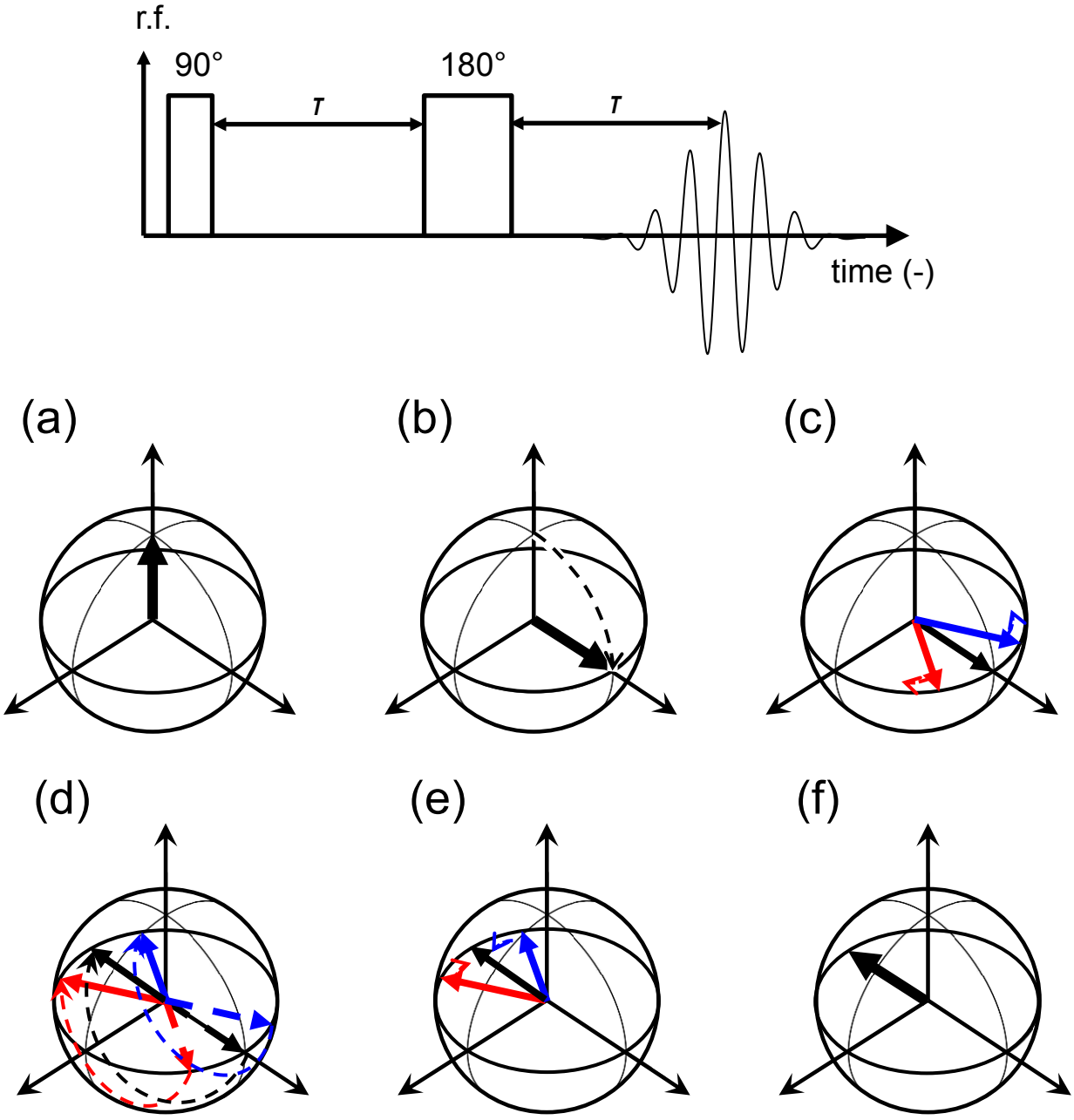

Figure 2.8: The spin echo pulse sequence and its effects on the Bloch vector. (a) the spins are at thermal equilibrium which is disturbed by a 90° r.f. pulse which tips the net magnetisation into the transverse plane as in (b). After the 90° pulse the spins in the presence of local magnetic fields which are either stronger or weaker than $\boldsymbol{B_0}$, the spin ensemble begins to diphase as shown in (c) using the red and blue vectors which are representative of the 'fastest' and 'slowest' spins in the ensemble respectively. This causes the transverse component to decay with time. In (d), a 180° r.f. has been applied at a time $\boldsymbol{\tau}$ after the initial 90° pulse such that the spins are reflected through the transverse plane. Consequently, the dephased spins now move towards each other and begin to coherently rephase as shown in (e). This causes an 'echo' to form as in (f). The peak of the echo occurs at the echo time $\boldsymbol{\tau}$ after the application of the 180° refocussing pulse.

the plane but maintains their relative positions. Since the field inhomogeneities are not reflected, they act in the same way to rephrase the magnetisation, which forms a coherent 'echo' when the coherence of the spin ensemble peaks.

The total time between the initial excitation r.f. 90° pulse and the echo formation is 2τ which is called the echo time T_E. The echo procedure is used cyclically to measure T_2 using a train of 180° pulses as described previously in the CPMG sequence.

2.5.2. STIMULATED ECHO

A stimulated echo is formed by the application of three 90° pulses. The attenuation of the final signal in a stimulated echo is based primarily on T_1 relaxation effects, and it is therefore used in cases where $T_1 >> T_2$. The pulse sequence is illustrated in Figure 2.9. Following excitation, the magnetisation vector is tipped back into the vertical direction by a 90° pulse for a storage time T_{store} in which the relaxation is due solely to T_1. A vertical direction magnetic field gradient is applied during this storage period to purposefully dephase residual transverse plane magnetisation. Gradients are discussed in greater detail in Section 2.10. The magnetisation vector is then tipped back into the transverse plane by a final 90° pulse. When it is in the transverse plane it refocuses to form an echo which was 'stimulated' by the final 90° pulse. The echo forms at a time $T_{\text{E}} = 2\tau + T_{\text{store}}$ after the initial 90° pulse. The sequence is often used in cases where T_2 are sufficiently small to negate the use of the spin-echo.

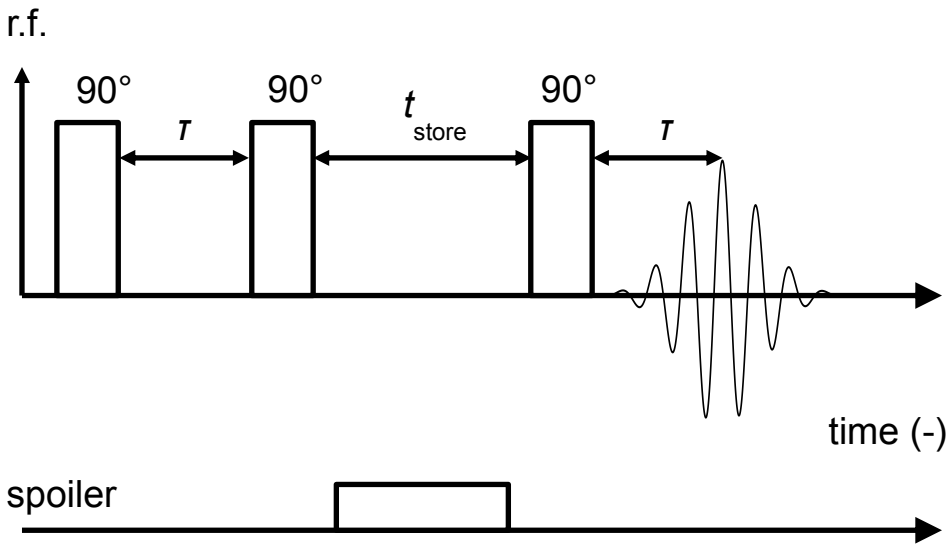

Figure 2.9: The stimulated-echo pulse sequence in which the sample is excited by a 90° pulse followed by a single 90° which flips the magnetisation into the vertical plane for a storage period denoted t_{store}. In this period, the relaxation is purely due to $\boldsymbol{T_2}$ as there is no magnetisation present in the transverse plane. During this time a homospoil or spoiler gradient is applied in the vertical direction which dephases all remaining magnetisation in the transverse plane. A final 90° pulse flips the inverted vertical magnetisation back into the transverse plane, where it is allowed to regain coherence and form an echo which has been 'stimulated' by the 90° pulse after the storage time.

2.5.3. DOUBLE SPIN ECHO AND BACKGROUND GRADIENTS

The double spin echo is a standard spin echo experiment which has an additional 180° refocussing pulse. A schematic depicting the pulse sequence is shown in Figure 2.10. An initial refocussing 180° pulse is used at a time τ after the 90° pulse as in the spin echo. The second 180° pulse is applied at a time 2τ after this which means the echo forms 4τ after the 90° pulse. The mechanism by which the coherence forms is identical to the spin echo sequence discussed previously. Despite requiring double the time for signal acquisition as the single spin echo, this sequence offers a unique benefit with respect to background gradients.

Background gradients refer to permanent inhomogeneities which are present in addition to the B_0 magnetic field. The effect of these gradients on certain types of measurements, particularly velocity measurements, will be discussed in Section 2.9. Figure 2.11 gives the net effect of a permanent background gradient from the perspective of the spin ensemble for a standard spin echo and double spin echo experiment. In Figure 2.11 (a) a standard spin echo is seen to reverse the direction of the acting background gradients from the perspective of the spins as seen in (b). In the double spin echo sequence in Figure 2.11 (c), the direction of the background gradient experienced by the ensemble is reversed twice. The significance of this is that, if moments of the background gradient are taken the first moment of the background gradient in the spin echo sequence is non-zero, whilst it is zero in the case of the double spin echo sequence. The first moment of the gradient encodes the signal for velocity, thus a non-zero first moment with respect to the background gradient will cause a spurious velocity to be attributed to the signal due to the background gradient. This effect is negated in the case of the double spin echo. Therefore, the double spin echo is an important sequence in systems where there are

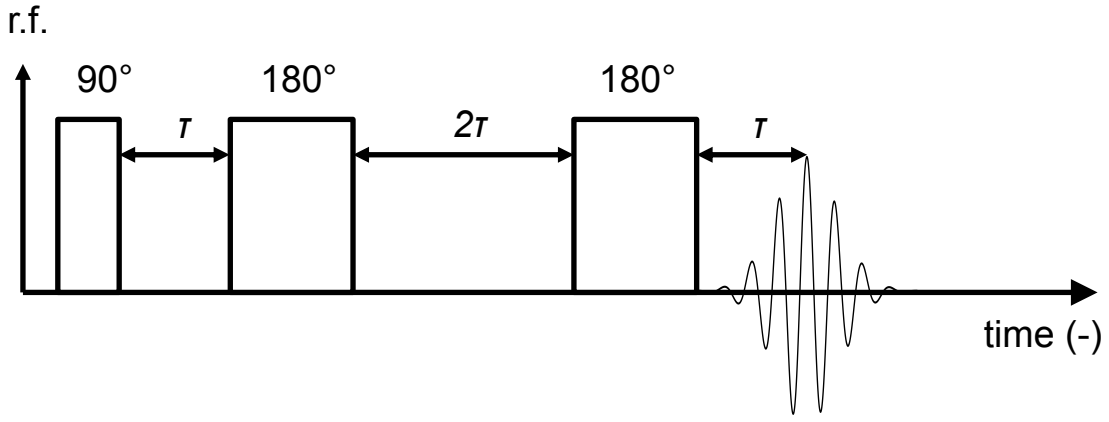

Figure 2.10: The double spin-echo pulse sequence showing the formation of a coherence echo after the application of two successive 180° r.f. pulses.

significant differences in the magnetic susceptibility between materials. These susceptibility differences will lead to local background gradients. In this thesis the double spin echo is used for velocity encoding in the gas phase, where susceptibility differences and very short T_2^* times make standard spin echo sequences impossible to use for velocity measurement.

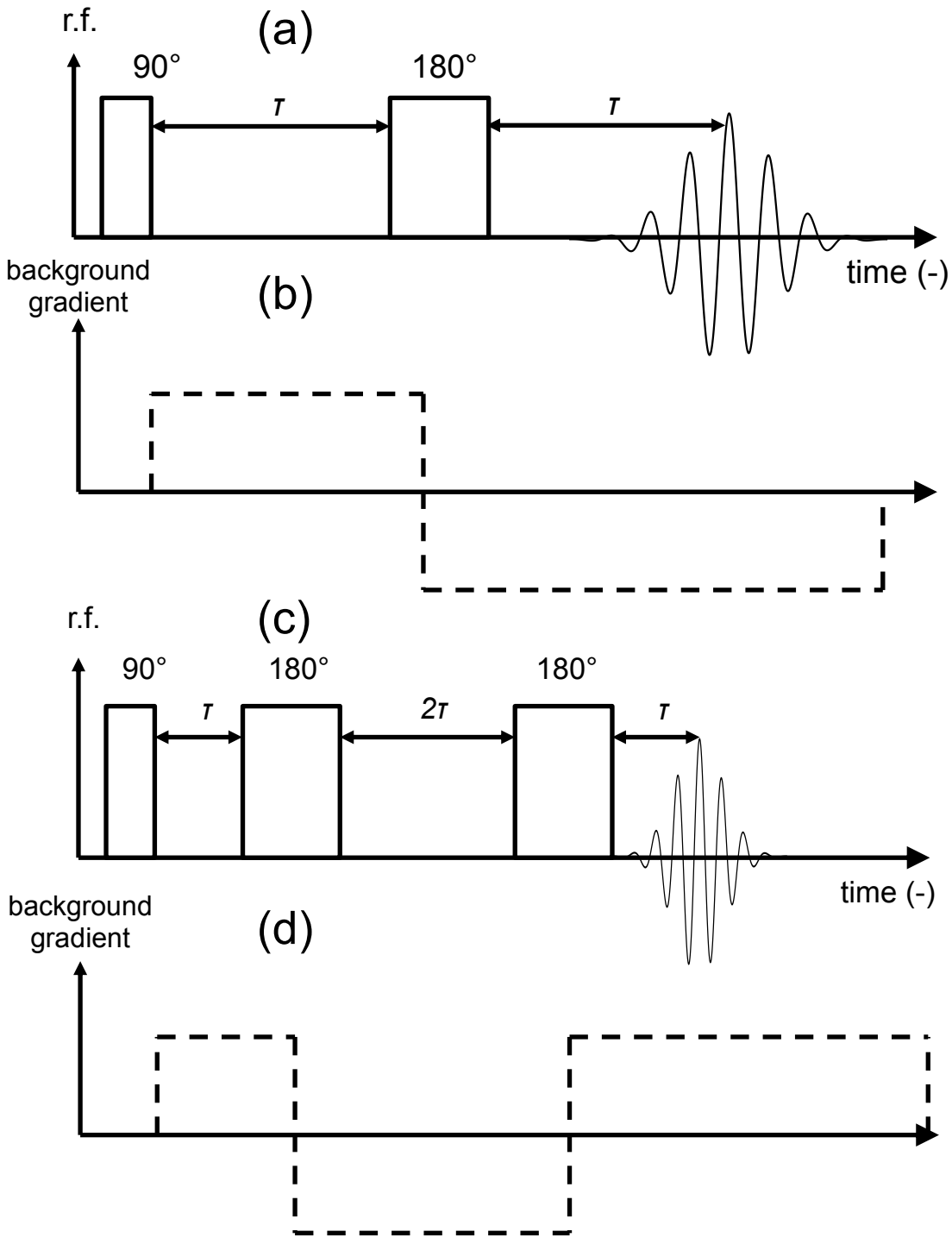

Figure 2.11: The effect of spin echoes on the presence of background gradients. (a) is a standard spin echo and (b) is the result on the background gradients and (c) shows a double spin echo with the resulting background gradient effect in (d).

2.6. CHEMICAL SHIFT

The local magnetic environment of different nuclei within a molecule is influenced by the surrounding electron distribution. Subtle variations in the local electron density in the molecular orbital will cause variations in the magnetic environment experienced by different nuclei across a molecule. Thus, the Larmor frequency of different nuclei within a molecule may conceivably vary according to their position within the molecule due to the relative amount of magnetic "shielding" on behalf of orbiting electrons. This gives rise to the chemical shift phenomenon; whereby different atoms of the same type may have different resonant frequencies based on their chemical properties. These subtle differences are detectable in NMR, especially for instruments of high field strength. The analysis of chemical shift spectra, chemical spectroscopy, is an extremely powerful field for the analysis and identification of chemical structures. This thesis does not contain any chemical shift analysis, but the interested reader is referred to any standard text on NMR spectroscopy such as that by Keeler [6].

2.7. SIGNAL-TO-NOISE RATIO

The inherent sensitivity of NMR experiments is low owing to the very low levels of signal emitted by nuclei. The signal is also subject to noise from several sources: thermal motion of molecules (Johnson noise), interference from the environment and electrical components and imperfections in the equipment. The noise is Gaussian distributed, implying that the signal-to-noise (SNR) ratio is defined as:

$$\text{SNR} \equiv \frac{\mu_S}{\sigma_N}. \tag{2.20}$$

Here, μ_S is the true signal mean and σ_N is the standard deviation of the noise distribution. In the absence of improving the quality of the electrical components and shielding for the cables, the SNR can be improved by using higher field strengths according to $\text{SNR} \propto B_0^{7/4}$. However, for a set magnetic field strength and sample size, the SNR is improved only by averaging the signal acquired from several experiments. Coherent signal adds and the noise will add incoherently. The signal is directly proportional to the number of averages therefore, and the noise is proportional to the root of the averages and therefore:

$$\text{SNR} \propto \sqrt{n_a}, \tag{2.21}$$

where n_a is the number of experimental averages.

2.8. PHASE CYCLING

Phase cycling in NMR experiments is a technique which allows only the desired signals to be selected by selectively varying the pulse and receiver phases. The acquired signal is averaged and thus some artefacts cancel themselves out. For a full description the reader is referred to the text by Levitt [7]. Phase cycling can also suppress spurious signals which originate from irregularities in the NMR hardware.

The NMR signal is a coherence between spin states, and the coherence order designated *p* can be used to quantify the level of coherence. This is an alternative to the Bloch vector model which is used to describe the effect of r.f. pulses on the ensemble of nuclear spins recognising their inherently quantum nature. It is more convenient to recognise the nature of quantum coherences and the superposition of states for the understanding of phase cycling. Vertical coherence corresponds to $p = 0$ and transverse magnetisation corresponds to $p = \pm 1$. The phase of the transverse polarisation is indicative of the angle in the transverse plane, but conventionally $p = -1$ is the detectable signal pathway in the transverse pane. For other nuclei with spin numbers higher than ½, or for systems which experience nuclear coupling higher order quantum coherences may exist. By these definitions, for spin-1/2 nuclei such as those used in the present study, a 90° pulse causes *p* to increment by ±1 whilst a 180° reverses the sign of *p*. Therefore, the acquired NMR signal consists of several pathways to the final coherence recorded. This is known as the coherence transfer pathway (CTP) and can be represented in a CTP diagram such as that shown for a spin-echo sequence in Figure 2.12.

In this experiment it is seen that nine possible coherence pathways are possible, but only one desired path for the experiment to work as designed. The other CTPs will behave as unwanted artefacts which lead to spikes in the spectrum (direct current offset) or to reflected peaks with a loss of quadrature. A phase cycle consists of n_P experiments in which the phase of each pulse (ϕ_A and ϕ_B in the basic example) as well as the receiver phase ϕ_R are stepped and varied and the final signal averaged to select the desired coherence pathway. The desired CTP adds constructively, and all other CTPs add destructively in the final signal. For a pulse-acquire experiment, a typical phase cycle called the CYCLOPS [12] cycle is used to remove baseline offset and quadrature artefacts. More complex sequences with more pulses require the cycle to be stepped for every pulse, which can sometimes lead to very long experiment times. Both using homospoil gradients and using cogwheel sequences, which were developed by

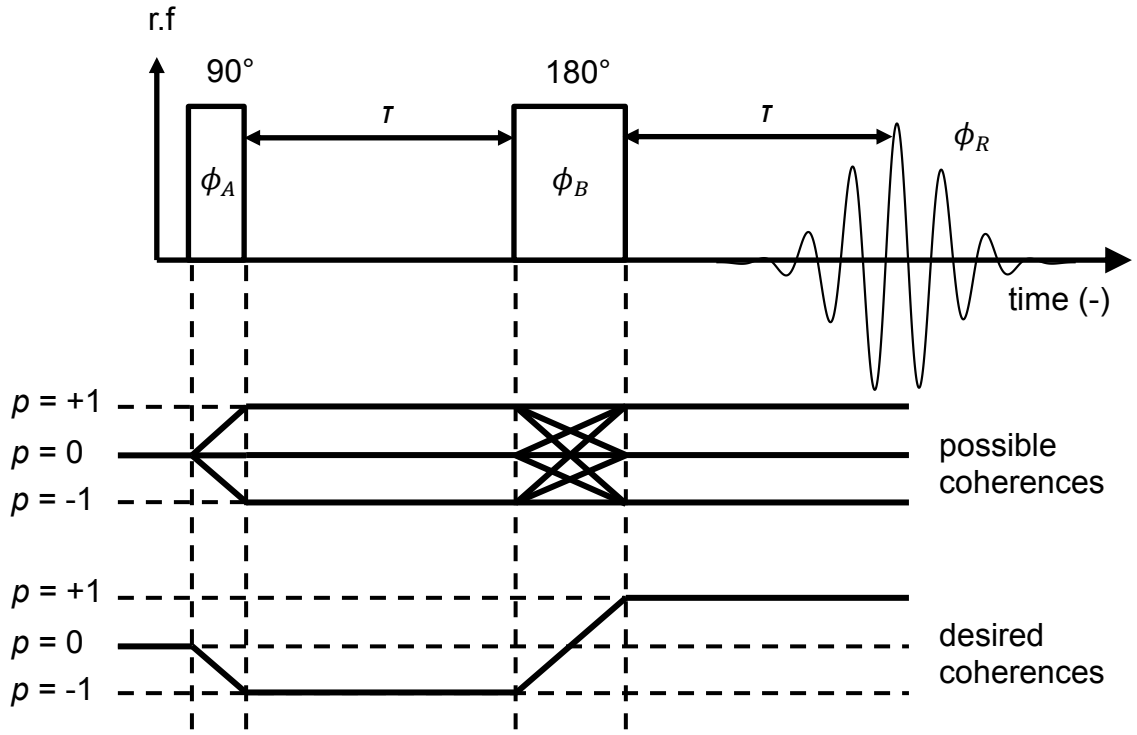

Figure 2.12: Possible coherence pathways for the spin-echo pulse sequence shown together with the desired coherence pathway.

Levitt *et al.* [13], circumvent this. The cogwheel approach independently cycles each pulse phase, which leads to much improved times over traditional nested cycles.

In this thesis a traditional four-step phase cycle is used for the spin-echo pulse sequences. A more complex 12-step cogwheel phase cycle was used for the double spin echo SF_6 imaging sequences developed by Boyce *et al.* [14] using the CCCP++ software.

2.9. MAGNETIC RESONANCE IMAGING

In this section the basics of imaging and imaging strategies including spin-warp and single point imaging are discussed. Fast imaging techniques, such as RARE [15], FLASH [16] and EPI [17] are not discussed here as there were not used in this thesis. The interested reader is referred to the standard texts on MRI for detailed descriptions of these methods [5].

2.9.1. MAGNETIC FIELD GRADIENTS

Imaging using the principles of magnetic resonance is accomplished by encoding the acquired signal for position by the application of magnetic field gradients. Using the Fourier transform, the distribution of frequencies is thus relatable to the spatial distribution of spins. If a gradient vector is applied to a sample the Larmor frequency is dependent on the gradient according to

$$\omega(\mathbf{r}) = \gamma(B_0 + \mathbf{G} \cdot \mathbf{r}). \tag{2.22}$$

Here **r** is the position vector and **G** is the gradient field $\nabla\mathbf{B}$. Thus we obtain a signal which has a frequency distribution which is a direct map of the physical spin density distribution.

This principle is illustrated simplistically in Figure 2.13, which shows a single dimension imaging experiment on a tube filled with a pure substance. The linear spatial gradient results in a signal which when Fourier transformed gives a frequency spectrum which is a projection of the physical object. This can be extended to three dimensions, in which spin density is then encoded in 3D by the application of three spatial gradients.

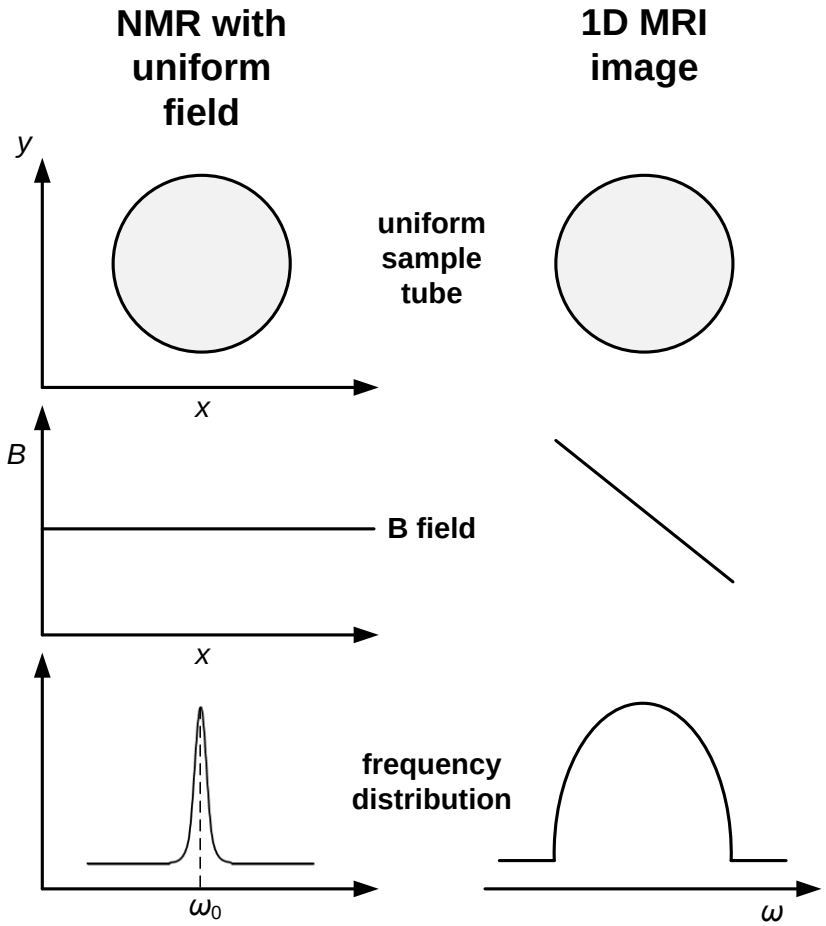

Figure 2.13: Schematic representation of spatial encoding using magnetic field gradients. Left we see a standard field with no gradient resulting in the single-peak frequency spectrum at the Larmor frequency. Right we see the application of a gradient which gives a frequency distribution which is the 1D projection of the tube.

2.9.2. K-SPACE

It is useful to make the transformation into so-called "**k**-space". The signal *S* arising from a differential volume element of sample is:

$$dS(\mathbf{G},t) \propto \rho(\mathbf{r})\mathrm{e}^{i\omega(r)t}dV. \tag{2.23}$$

In Equation 2.23 $\rho(\mathbf{r})$ is known as the spin density spatial distribution. The total signal acquired in the three dimensions by a sample when integrated is given by:

$$S(\mathbf{G},t) = \iiint \rho(\mathbf{r}) \exp(i\gamma \mathbf{G}\cdot\mathbf{r}t)\, d\mathbf{r}. \tag{2.24}$$

In this expression $\mathbf{G}$ is the applied gradient of the magnetic field. Exploiting the form of the Fourier transform and making the vector transformation into **k**-space, we define the **k**-vector as:

$$\mathbf{k} = \frac{\gamma \mathbf{G} t}{2\pi}. \tag{2.25}$$

For time-varying gradient fields the definition is:

$$\mathbf{k} = \frac{\gamma t}{2\pi}\int \mathbf{G} dt. \tag{2.26}$$

Making these definitions Equation 2.24 becomes:

$$S(\mathbf{k}) = \iiint \rho(\mathbf{r}) \exp(i2\pi\mathbf{k}\cdot\mathbf{r})\, d\mathbf{r}. \tag{2.27}$$

It can thus be seen that $S(\mathbf{k})$ and $\rho(\mathbf{r})$ are a Fourier pair, and a signal acquired by traversing **k**-space by altering $\mathbf{G}$ and time can be converted to an image of the spin density by a simple Fourier transform, which gives the real image $\rho(\mathbf{r})$ according to:

$$\rho(\mathbf{r}) = \iiint S(\mathbf{k})\exp(-i2\pi\mathbf{k}\cdot\mathbf{r})\, d\mathbf{k}. \tag{2.28}$$

Digitally, it is required that the same number of discrete points (or pixels in 2D, voxels in 3D) in **k**-space are sampled as are required in real space. Points in **k**-space are sampled using magnetic field gradients which encode spins for position using either their frequency or phase distribution. The inverse Fourier relationship between $S(\mathbf{k})$ and $\rho(\mathbf{r})$ is then exploited to yield real-space images from the NMR signals acquired in **k**-space. The field-of-view of the real-space image is inversely proportional to the spacing of points in **k**-space, and the spatial resolution of the real-space image is related to the extent of **k**-space sampled. The intensity of

points toward the centre of **k**-space are responsible for most of the image contrast information, whilst points toward the edges encode the image finer detail.

2.9.3. FREQUENCY ENCODING

Frequency encoding is a technique in which several k-space points are sampled from a single FID. It is accomplished using a constant gradient G_{read} in the "read" direction which traverses a straight line in **k**-space. The gradient is applied during the signal acquisition phase of a pulse sequence. This gives position-dependent frequency information about the sample. The line in **k**-space is sampled in the direction of the applied read gradient, and each point sampled is separated by a typically constant dwell-time t_d. The field-of-view (FOV) of a frequency encoded line in **k**-space is given by:

$$\text{FOV} = \frac{2\pi}{\gamma G_{\text{read}} t_d} \tag{2.29}$$

2.9.4. PHASE ENCODING

To acquire information about a second spatial dimension, a strategy other than frequency encoding is required. This is because the application of two frequency encoding gradients applied orthogonally will result in a net gradient oblique projection through **k**-space, which would negate the use of Fourier reconstruction. Instead, another 'phase encoding' gradient G_{phase} is applied in the second dimension which winds up the phases of spins according to their position. A series of different incremental strengths of G_{phase} are applied for a single G_{read}, which allows the relative magnitude of phase change for different positions in real space to be resolved also using a Fourier transform, and thus **k**-space can be raster-scanned using two gradients, G_{read} and G_{phase}, with increments of the latter giving spatial information in other higher dimensions. In practice the echo time of the experiment is constant, and thus a constant phase encoding time t_p is used and the gradient is incremented. The FOV in the phase-encoding direction is given by:

$$\text{FOV} = \frac{2\pi}{\gamma(\Delta G_{\text{phase}}) t_p} \tag{2.30}$$

2.9.5. SOFT PULSE SLICE SELECTION

Magnetic field gradients are also used to selectively excite tomographic slices in samples. A linear gradient G_{slice} is applied in the direction of the desired slice at the same time as a shaped r.f. pulse. Because of the inverse Fourier-relationship between the real and **k**-space, the shape of the pulse in real space will be inverted in the excited slice. Therefore, for convenience, a 'soft' Gaussian is conventionally used as its Fourier transform is a Gaussian. The pulse is therefore only in resonance with the spins which are selected in a frequency bandwidth dictated by the width of the r.f. pulse and magnitude of the applied slice gradient. The slice thickness is given by:

$$\Delta z = \frac{\Delta\omega}{\gamma G_{\text{slice}}}, \tag{2.31}$$

where $\Delta\omega$ is the frequency bandwidth of the selected slice and Δz is the slice thickness. This process is illustrated in Figure 2.14. Due to the non-rectangular nature of the selected slice, the thickness is defined as the width of the selected slice at the half-maximum of the Gaussian peak. Using a sinc-shaped soft pulse would require truncation which would lead to artefacts greater than using a Gaussian soft pulse. The slice gradient is often applied simultaneously with a 180° refocussing pulse in a spin-echo pulse sequence.

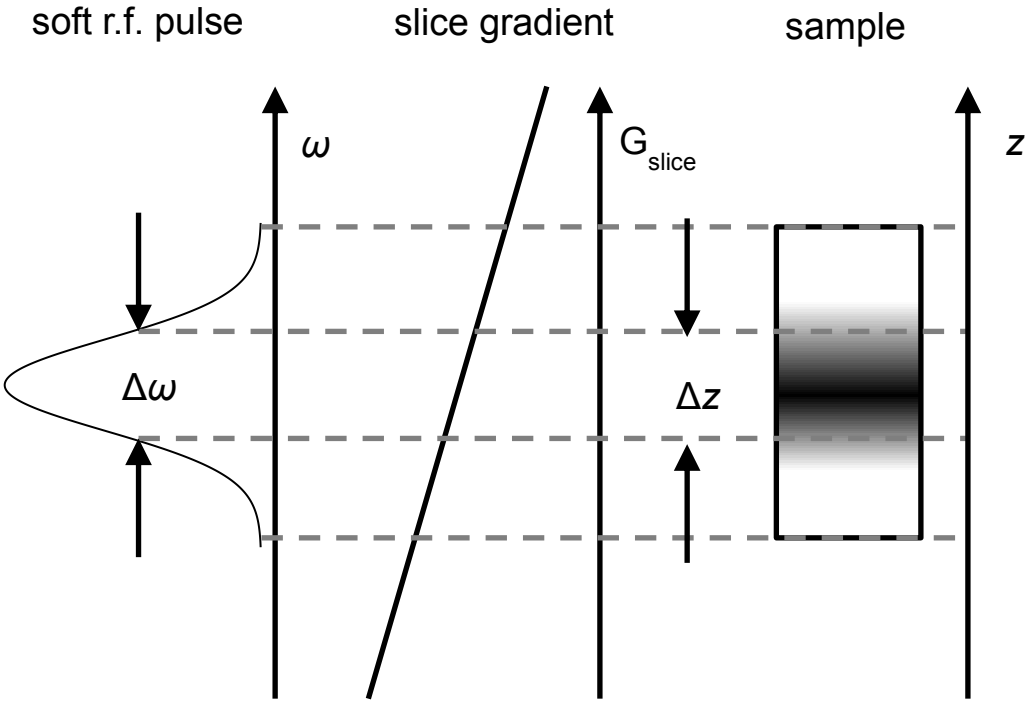

Figure 2.14: The soft-slice selection process shown using a linear spatial gradient and Gaussian shaped r.f. pulse. A Gaussian shaped pulse results in a Gaussian selection of excited spins.

2.9.6. SPIN-WARP IMAGING

Spin-warp imaging is a popular method of sampling points in **k**-space first reported by Edelstein *et al.* [18]. The pulse sequence employs a spin-echo together with frequency encoding and phase encoding gradients to produce a raster-scanned matrix of sampled **k**-space points. For two dimensions, the spin-warp sequence is shown in Figure 2.15. At equilibrium the magnetisation is at the origin of **k**-space. After the 90° pulse tips the spins into the transverse plane, the read and phase gradient increment are applied simultaneously which have the effect of moving the magnetisation in the first case to the edge of both the read and phase directions in **k**-space. A soft slice-selection 180° pulse is then applied, which both refocuses the spins in the transverse plane and selects a tomographic slice. This pulse reflects the magnetisation through the origin. After this during the readout of the echo FID, the read gradient is applied which moves the magnetisation through a line of **k**-space which is then sampled. This readout gradient is applied for twice the duration of the first read gradient to traverse a whole line in **k**-space.

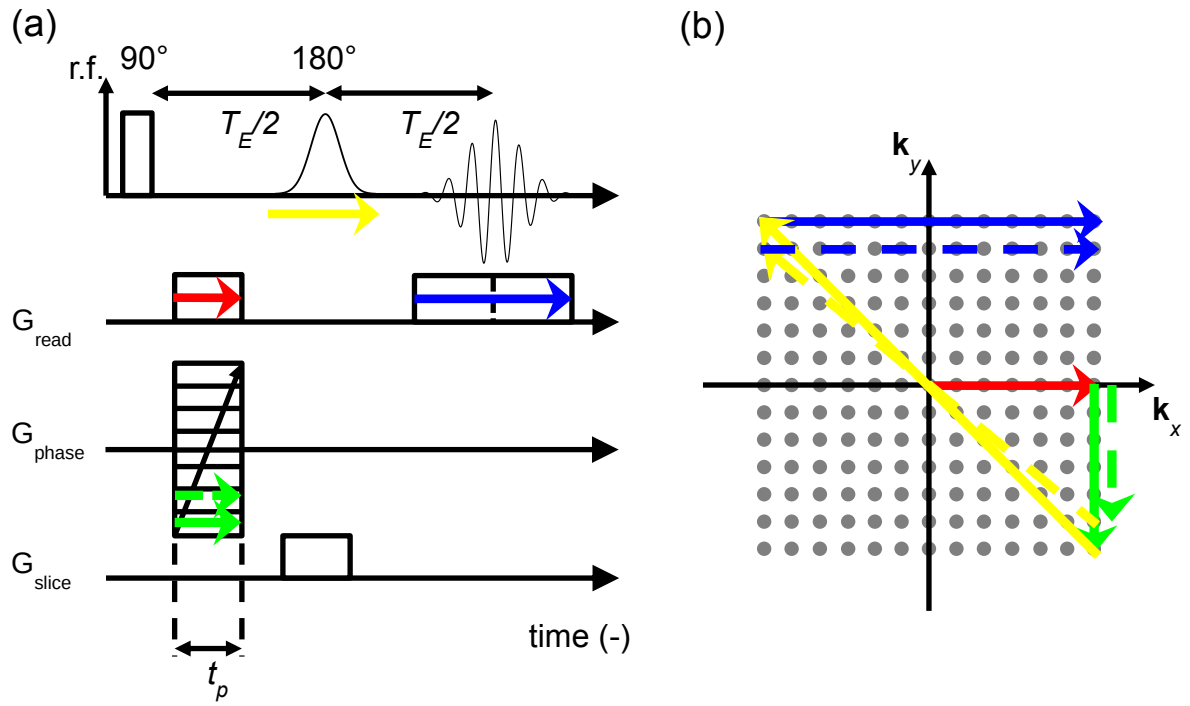

Figure 2.15: The spin-warp imaging pulse sequence in 2D. (a) shows the pulse sequence while (b) shows how **k**-space is traversed. The 90° pulse excites the spin population into the transverse plane. After this, a single increment of the phase encoding gradient is applied (the green line) which moves the magnetisation to the edge of the phase direction $\mathbf{k}_x$, whilst the read gradient (in red) moves the magnetisation to the edge of the read direction $\mathbf{k}_y$. The soft 180° pulse both refocuses the spins and together with the slice gradient performs slice-selection. The 180° inverts the magnetisation through the origin (shown by the yellow line). During readout of the echo, the read gradient is applied to read out a line of **k**-space, shown in blue. This process is repeated for different increments of the phase encoding gradient to obtain a full raster scan of **k**-space (shown by the dashed green, yellow and blue lines).

Allowing the signal to relax for T_R ensures there is sufficient recovery of magnetisation between scans. For the next scan, the phase encoding gradient is incremented by ΔG_{phase}. This process is illustrated using dashed lines for the read, phase and readout gradients. If 3D imaging is required, a second phase-encoding gradient is applied to acquire more rows of a 3D matrix. The total experimental time for spin-warp imaging is given by the expression:

$$T_{exp} = N_{\text{scans}} \times N_{\text{phase}} \times T_R, \tag{2.32}$$

where N_{scans} is the number of signal averaging scans and N_{phase} is the number of phase encoding increments.

2.9.7. SINGLE POINT IMAGING (SPI)

Single point imaging [19] is an alternative strategy for sampling **k**-space which involves acquiring an individual FID for each point in the **k**-space matrix. Two phase-encoding gradients are therefore used to traverse **k**-space, instead of using a read gradient to acquire a whole line as in spin-warp imaging. A typical 2D single-point imaging sequence is depicted in Figure 2.16. Two phase encoding gradients are incremented ($\Delta G_{\text{phase},x}$ and $\Delta G_{\text{phase},y}$) after the initial 90° excitation for each phase-encoding direction, $\mathbf{k}_x$ and $\mathbf{k}_y$. In Figure 2.16 the gradients are shown taking the magnetisation to two points in the upper left-hand quadrant for two successive increments of $G_{\text{phase},y}$ however this is arbitrary. In principle, the gradients can be applied to sample single points in any random order. This makes SPI easy to adapt for compressed sensing imaging, which allows **k**-space to be undersampled (discussed in Section 2.11). The full FID or representative points through time for each point in the **k**-space matrix can be sampled according to the needs of the experiment. The experiment time can be determined according to:

$$T_{exp} = N_{\text{scans}} \times N_{\text{phase,x}} \times N_{\text{phase,y}} \times T_R, \tag{2.33}$$

where $N_{\text{phase},x}$ and $N_{\text{phase},y}$ are the number of phase encoding increments used in the *x* and *y* directions respectively. Owing to the use of two phase encoding directions, the experimental time is considerably more than for frequency encoding techniques typically. SPI is therefore

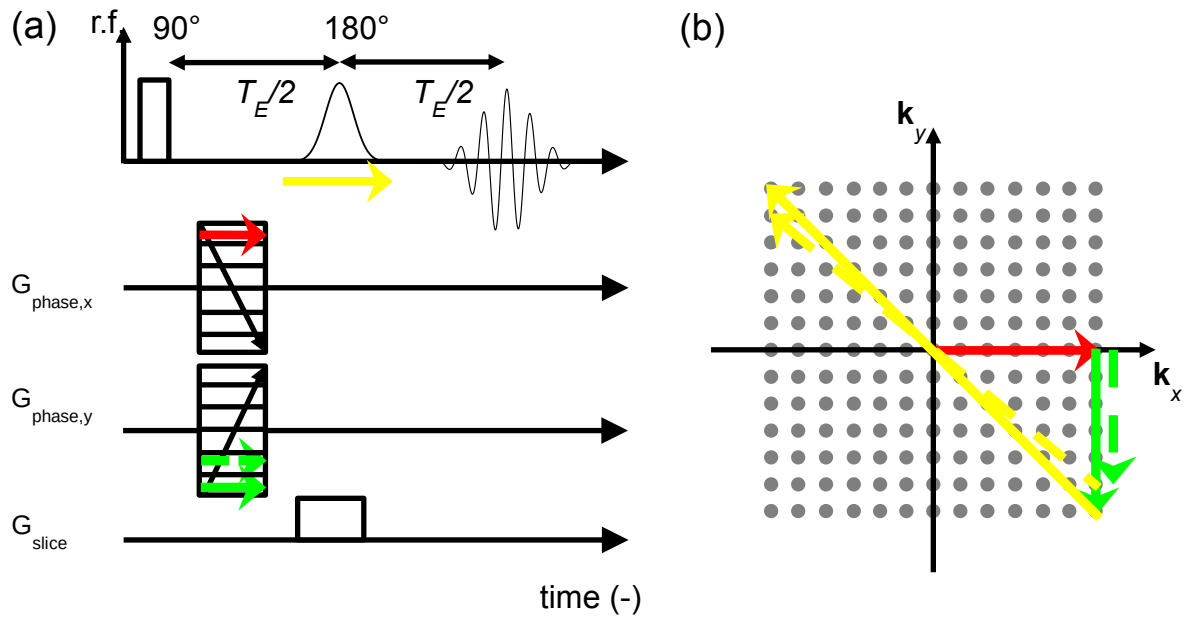

Figure 2.16: A single point imaging pulse sequence (a) shown alongside the corresponding trajectory through **k**-space (b) which employs two phase encoding gradients to sample each point individually in **k**-space.

only used for cases where T_2^* is prohibitively short to use frequency-encoding methods, which is the case in this thesis for SF_6 velocity imaging.

2.10. MEASURING MOTION USING MRI

The signal from MRI experiments can be used to encode information regarding the displacement of spins. Velocity encoding makes use of the pulsed field gradients (PFG) technique. If a bipolar pair of gradients is applied to a sample moving within the magnetic field, an offset in the phase of the magnetisation vector will have occurred. This phase offset is extracted from the complex part of the FID and is proportional to the velocity. This is illustrated in Figure 2.17 which shows a pair of spatial magnetic field gradients applied in a pulse sequence. In Figure 2.17 (a) the gradients are bipolar i.e. equal in magnitude and opposite in direction. Alternatively, in (b), a 180° refocussing pulse is used which allows a gradient of the same magnitude and sign to have the same effect from the perspective of the spins which have been reflected through the origin of **k**-space. This is known as phase contrast imaging and is a popular method for velocity encoding.

More formally, the NMR signal can be expressed as:

$$S(\phi, t) = \iiint \rho(\mathbf{r}) \exp(-i\phi)\, d\mathbf{r}. \tag{2.34}$$

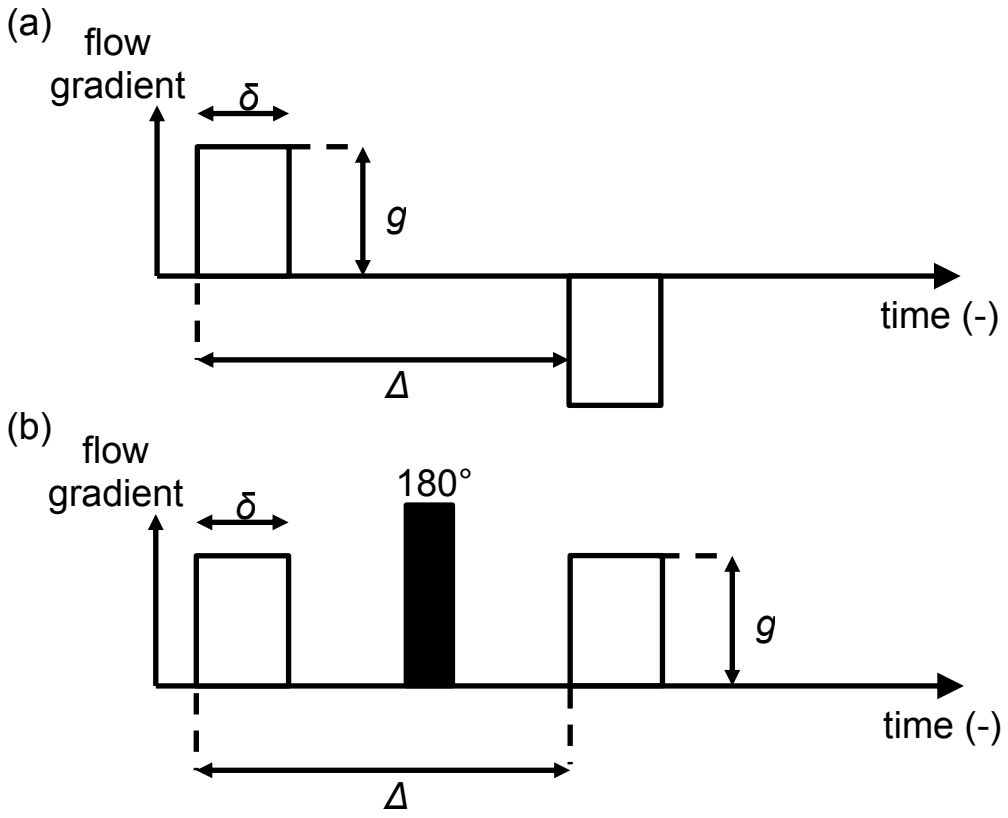

Figure 2.17: The application of a pair of bipolar gradients in (a), and two gradients either side of a 180° pulse in (b) which accomplishes the same effect on the phase of the magnetisation vector.

The phase is therefore accumulated over time as a function of the gradient waveform which is applied to the spin ensemble as follows:

$$\phi(t) = \gamma \int \mathbf{G}(t) \cdot \mathbf{r}(t) dt. \tag{2.35}$$

This can be expanded using the Taylor series to the following:

$$\phi(t) = \gamma \mathbf{r} \int \mathbf{G}(t) dt + \gamma \frac{d\mathbf{r}}{\mathrm{d}t} \int t\mathbf{G}(t) dt + \gamma \frac{1}{2} \frac{d^2\mathbf{r}}{\mathrm{d}t^2} \int t^2 \mathbf{G}(t) dt + \cdots. \tag{2.36}$$

In Equation 2.35, the first order term is the zeroth moment of the gradient waveform and it encodes for position. The second term clearly encodes for velocity from the presence of the term $d\mathbf{r}/dt$ which is known as the first moment. The second moment consequently encodes for acceleration from the presence of the weighting $d^2\mathbf{r}/dt^2$. Higher order terms will be sensitive to the jerk and the jounce accordingly.

Therefore, one can carefully design the transient gradient waveform $\int \mathbf{G}(t) dt$ to encode for these terms or cancel them as required. It was seen that the presence of a permanent background

gradient can be cancelled in terms of the second moment by using the double spin echo. The simplest gradient waveform which imparts a non-zero weighting on the second moment of Equation 2.36 is by using a bipolar gradient pair as per Figure 2.17. Applying Equation 2.36 to a bipolar square gradient pair, simplifying and solving for the velocity yields:

$$v = \frac{\phi}{\gamma g \delta \Delta'} \tag{2.37}$$

where δ is the duration each gradient is on, g is the magnitude of the gradient applied and Δ is the interval between gradient applications. This can be explained simply in terms of the vector model. If a collection of spins receives a pulse of a dephasing gradient g their phases will be 'wound up' in a helical fashion based on their initial position. If at some time Δ after this initial pulse, an equal but opposite pulse is applied, their phases will be unwound. However, if within the time Δ there has been a net coherent displacement of the spins, there will be a residual phase shift present which is proportional to the residual phase in the signal according to Equation 2.37. Velocity can be spatially resolved into voxels by overlapping the flow gradients with spatial gradients, and thus velocity maps in up to three dimensions can be obtained. The field-of-flow (FOF) is defined as the range of velocity which can be measured for a certain gradient waveform and is given by:

$$\mathrm{FOF} = \frac{2\pi}{\gamma g \delta \Delta}. \tag{2.38}$$

This is limited by the fact that the maximum phase is 2π. Thus experiments are designed where g, δ and Δ are chosen based on the predicted maximum velocity present in the system such that no fold-over will be present in the recorded phase. An alternative method for recording velocity information from NMR signals is the use of so-called propagators. These were not used in this thesis, but the reader is referred to the text by Kager and Heink [20] or Levitt [7] for a thorough explanation on propagator theory.

2.11. MRI VELOCITY MEASUREMENT ERRORS

The errors which MRI velocity measurements are subject to are briefly reviewed here. The intensity of a voxel may be incorrectly assigned based on relaxation weighting differences at phase interfaces [21]. Alternatively, the presence of the birdcage r.f. coil may cause localised inhomogeneities in the intensity image. Other image artefacts such as Gibbs ringing, DC spikes and image aliasing may also cause voxels to have incorrectly assigned intensities which may

lead to them being erroneously included or excluded from velocity measurements. Partial volume effects, whereby square voxels are assigned a single velocity which is only due to fraction of the voxel area can be compensated by weighting the velocity by the normalised signal intensity.

Washout or inflow, whereby the sample in the coil which has been encoded for velocity is either out of the coil by the time the signal is read out, or is replaced by nuclei which have not had time to polarise or attain velocity encoding, will also lead to errors. This is minimised by choosing the appropriate values of δ and Δ based on the estimated velocities in the system and length of the r.f. coil. The NMR signal additionally undergoes velocity attenuation due to motion blurring primarily in the phase direction [22,23].

Time averaging over both the observation time Δ and the experiment time leads to subtle differences in interpreting the velocity field. Firstly, it is a Lagrangian field (due to the tagging of spin ensembles) and not Eulerian. The voxels therefore do not necessarily represent the instantaneous velocity of the field in space. Additionally, the average velocity of the experimental duration does not give information on the variation of velocity. This can however be accomplished using propagator measurements. Furthermore, each voxel is an average of the displacement of all the spins within the voxel and cannot distinguish between different velocities within the voxel.

Lastly, the velocity measurement is inherently limited by the presence of background noise [22]. If the signal-to-noise ratio is >> 1, the error in the phase is approximately:

$$\sigma_{\phi} \approx \frac{1}{\mathrm{SNR}} \tag{2.39}$$

Since both the signal and the phase are Gaussian distributed, the inherent velocity resolution is therefore $\sigma_v = \sigma_{\phi}/\gamma g \delta \Delta$.

2.12. COMPRESSED SENSING MRI

Due to the time-consuming nature of phase encoding, the need for spin relaxation and the finite bandwidth of the analogue-to-digital converter MRI is a technique which suffers from typically poor temporal resolution. In some cases imaging experiments can become prohibitively long, such as for 3D images with velocity encoding in multiple dimensions. Therefore, the reduction of image acquisition times has been an area of persistent research. Fast imaging sequences can

only circumvent some of these concerns, and some physical phenomena are presently too fast to be studied using MRI at all. Simply acquiring less data in the FID or in **k**-space will lead to coherent artefacts. Several approaches which seek to undersample NMR signal without producing egregious artefacts have been studied. The SNR of images can be sacrificed in favour of electing points which produce only incoherent artefacts [24,25]. The Hermitian symmetry property of **k**-space can be used to selectively sample half of the space in partial-Fourier imaging [26]. Any redundancies and prior knowledge about image spatiotemporal content can be used to undersample and still produce faithful reconstructions [27,28]. In compressed sensing however, artefacts are made to add incoherently as noise. The theory also gives information as to how precisely to undersample to achieve this effect.

Compressed sensing (CS) is a powerful and rapidly developing tool used in signal and data processing, particularly in MRI [29]. The theory developed from compression theory, which seeks to use the underlying structure of the information to represent it faithfully using fewer elements than in a fully-sampled representation. This idea takes advantage of the fact that most signals of interest contain a great deal of structure, and can thus be *sparsely* represented. This means that the information can be reasonably faithfully represented by just a few non-zero elements. Compression algorithms work by transforming a fully sampled signal into some new basis which is sparse, then performing some selection of elements in this basis which when transformed will give a reasonable representation of the original signal with significantly fewer elements. This concept thus prompts the question as to whether the original signal may have been reasonably represented by taking fewer measured elements in the first instance. This is precisely what compressed sensing aims to do. It gives a rigorous mathematical framework in which to reconstruct signals from fewer originally measured points, and gives guidance as to how these should be acquired. Thus the *sensing* process has in effect become *compressed* [30].

Simply acquiring measurements of a signal at lower than the Nyquist frequency will lead to artefacts and aliasing. Compressed sensing circumvents the production of excessive artefacts by acquiring measurements which allow artefacts to add incoherently and thus produce a much more faithful reproduction than simply acquiring fewer points. The artefacts produced by undersampling and CS reconstruction resemble noise rather than coherent aliasing-type artefacts. In MRI, CS allows the acquisition time of measurements to be significantly reduced. This allows higher spatial resolution, improved temporal resolution or significantly higher signal-to-noise ratio to be achieved in the same amount of time as a standard acquisition. MRI lends itself naturally to a compressed sensing approach, as the space in which signal is acquired,

k-space, is naturally sparse, with most of the information about the image occurring towards the centre of **k**-space. Mathematically, CS is accomplished by following a minimisation of an inverse problem. The number of non-zero elements of the signal can be represented by the l_0-psuedo norm. We want to minimise this norm subject to some prior information – our measured data. The problem of finding the l_0 norm is very complex, but this norm can be approximated by using the l_1 norm. This is geometrically interpreted in terms of the norms' unit spheres. The standard Euclidean norm used for least-squares minimisation does not produce spare solutions for linear systems, while both the l_0 and l_1 do. The problem can thus be presented as the minimisation of

$$\|\psi \mathbf{x}\|_1 \tag{2.40}$$

subject to

$$\|F\mathbf{x} - \mathbf{y}\|_2 \leq \varepsilon. \tag{2.41}$$

In these equations, ψ is some linear operator which transforms the signal **x** into a sparse domain, F is the discrete Fourier transform matrix and **y** are our measured data. A popular choice for ψ is the total variation based transform, which computes the spatial finite differences of the image. This has demonstrated good applicability for images of porous media. It has been shown that introducing a binary mask $\mathbf{M_b}$ of the interstitial void space as additional prior information greatly improves the accuracy of the velocity measurements [31]. The final problem is thus written as

$$\arg\min(\|F\mathbf{x} - \mathbf{y}\|_2 + \alpha\|\psi\mathbf{x}\|_1 + \mathrm{B}\|(1 - \mathbf{M_b}).*\mathbf{x}\|_1). \tag{2.42}$$

In Equation 2.42 α and B are adjustable parameters which adjust the weighting of the regularisation terms. The notation $.*$ denotes an element-by-element multiplication. Higher values of α will generally produce a smoother reconstruction which is further from a simple Fourier reconstruction of the under sampled data. In this work, the compressed sensing code and algorithm developed by Benning [32] will be utilised.

NOMENCLATURE

ABBREVIATIONS

1D, 2D, 3D	one, two or three dimensional
CTP	coherence transfer pathway
CPMG	Carr Purcell Meiboom Gill
CS	compressed sensing
DC	direct current
FID	free induction decay
FOF	field-of-flow
FOV	field-of-view
FWHM	full width at half maximum
PFG	pulsed field gradients
r.f.	radiofrequency
MRI	magnetic resonance imaging
NMR	nuclear magnetic resonance
SNR	signal-to-noise ratio
SPI	single point imaging
SW	sweep width

SYMBOLS

B_0	polarisation magnetic field	T
B_1	secondary magnetic field	T
E	energy	J
F	discrete Fourier transform matrix	-
G	magnetic field gradient field	T m^{-1}
G_{read}	read direction magnetic field gradient	T m^{-1}
G_{phase}	phase direction magnetic field gradient	T m^{-1}
G_{slice}	flow encoding magnetic field gradient	T m^{-1}
g	magnetic field gradient strength	T m^{-1}
h	Planck constant	J s
$\hbar$	reduced Planck constant	J s
I	spin quantum number	-

k	reciprocal space vector	m^{-1}
k_B	Boltzmann constant	$J\ K^{-1}$
M	overall magnetisation vector	T
$\mathbf{M_b}$	binary mask prior	-
m_s	magnetic quantum number	-
n_a	number of averages	-
N	number of items	-
N_α	Boltzmann low energy population	-
N_β	Boltzmann high energy population	-
P	spin angular momentum	J s
p	coherence order	-
r	position	m
S	NMR signal	a.u.
T	temperature	K
T_1	spin-lattice relaxation time	s
T_2	spin-spin relaxation time	s
T_2^*	apparent transverse relation time	s
T_2'	transverse relaxation due to background gradients	s
T_{store}	storage time	s
T_R	repetition time	s
T_{exp}	experimental time	s
t	time	s
t_d	dwell time	s
v	velocity	$m\ s^{-1}$
V	volume	m^3
x	reconstructed signal	-
y	measured CS data	-
x, y, z	Cartesian spatial co-ordinates	m

GREEK LETTERS

α	first regularisation parameter	-
B	second regularisation parameter	-
γ	gyromagnetic ratio	$T^{-1}\ s^{-1}$

Δ	time between flow gradients	s
δ	flow gradient duration	s
ε	error	-
$\boldsymbol{\mu}$	magnetic dipole moment	J T^{-1}
μ_S	signal mean	-
ρ	density	$kg.m^{-3}$
σ	standard deviation	-
τ	variable time delay/0.5×echo time	s
ν	frequency in spectrum	s^{-1}
ν_{FWHM}	frequency at half the maximum width of spectrum	s^{-1}
ϕ	phase	rad
ψ	sparsifying transform	-
ω_0	Larmor frequency	Hz

REFERENCES

[1] Bloch, F. Nuclear induction. *Phys. Rev.* 1946;70: pp. 460.

[2] Purcell, E.M., Torrey, H.C., Pound, R. V. Resonance absorption by nuclear magnetic moments in a solid. *Phys. Rev.* 1946;69: pp. 37.

[3] Lauterbur, P.C. Image formation by induced local interactions: examples employing nuclear magnetic resonance 1973.

[4] Mansfield, P., Grannell, P.K. NMR "diffraction" in solids? *J. Phys. C Solid State Phys.* 1973;6: pp. L422.

[5] Callaghan, P.T. Principles of nuclear magnetic resonance microscopy. Oxford University Press on Demand; 1993.

[6] Keeler, J. Understanding NMR spectroscopy. John Wiley & Sons; 2011.

[7] Levitt, M.H. Spin dynamics: basics of nuclear magnetic resonance. John Wiley & Sons; 2008.

[8] Fukushima, E. Experimental pulse NMR: a nuts and bolts approach. CRC Press; 2018.

[9] Carr, H.Y., Purcell, E.M. Effects of diffusion on free precession in nuclear magnetic resonance experiments. *Phys. Rev.* 1954;94: pp. 630.

[10] Meiboom, S., Gill, D. Modified spin-echo method for measuring nuclear relaxation times. *Rev. Sci. Instrum.* 1958;29: pp. 688–91.

[11] Hahn, E.L. Spin echoes. *Phys. Rev.* 1950;80: pp. 580.

[12] Hoult, D.I. Critical factors in the design of sensitive high resolution nuclear magnetic resonance spectrometers. *Proc. R. Soc. Lond. A* 1975;344: pp. 311–40.

[13] Levitt, M.H., Madhu, P.K., Hughes, C.E. Cogwheel phase cycling 2002.

[14] Boyce, C.M., Rice, N.P., Sederman, A.J., Dennis, J.S., Holland, D.J. 11-interval PFG pulse sequence for improved measurement of fast velocities of fluids with high diffusivity in systems with short T $2*$. *J. Magn. Reson.* 2016;265: pp. 67–76.

[15] Hennig, J., Nauerth, A., Friedburg, H. RARE imaging: a fast imaging method for clinical MR. *Magn. Reson. Med.* 1986;3: pp. 823–33.

[16] Haase, A., Frahm, J., Matthaei, D., Hanicke, W., Merboldt, K.-D. FLASH imaging. Rapid NMR imaging using low flip-angle pulses. *J. Magn. Reson.* 1986;67: pp. 258–66.

[17] Mansfield, P. Multi-planar image formation using NMR spin echoes. *J. Phys. C Solid State Phys.* 1977;10: pp. 55.

[18] Edelstein, W.A., Hutchison, J.M.S., Johnson, G., Redpath, T. Spin warp NMR imaging and applications to human whole-body imaging. *Phys. Med. Biol.* 1980;25: pp. 751.

[19] Emid, S., Creyghton, J.H.N. High resolution NMR imaging in solids. *Phys. B+ C* 1985;128: pp. 81–3.

[20] Karger, J., Heink, W. The Propagator Representation of Molecular Transport in Microporous Crystallites. *J. Magn. Reson.* 1983;51: pp. 1–7.

[21] Gladden, L.F., Alexander, P. Applications of nuclear magnetic resonance imaging in process engineering. *Meas. Sci. Technol.* 1996;7: pp. 423–35.

[22] Haacke, E.M., Brown, R.W., Thompson, M.R., Venkatesan, R. Magnetic resonance imaging: physical principles and sequence design. vol. 82. Wiley-liss New York:; 1999.

[23] Johns, M.L., Sederman, A.J., Bramley, A.S., Gladden, L.F., Alexander, P. Local transitions in flow phenomena through packed beds identified by MRI. *AIChE J.* 2000;46: pp. 2151–61.

[24] Tsai, C., Nishimura, D.G. Reduced aliasing artifacts using variable-density k-space sampling trajectories. *Magn. Reson. Med.* 2000;43: pp. 452–8.

[25] Peters, D.C., Korosec, F.R., Grist, T.M., Block, W.F., Holden, J.E., Vigen, K.K., *et al.* Undersampled projection reconstruction applied to MR angiography. *Magn. Reson. Med.* 2000;43: pp. 91–101.

[26] McRobbie, D.W., Moore, E.A., Graves, M.J. MRI from Picture to Proton. Cambridge University Press Cambridge, UK; 2017.

[27] Korosec, F.R., Frayne, R., Grist, T.M., Mistretta, C.A. Time-resolved contrast-enhanced 3D MR angiography. *Magn. Reson. Med.* 1996;36: pp. 345–51.

[28] Parasoglou, P., Malioutov, D., Sederman, A.J., Rasburn, J., Powell, H., Gladden, L.F., *et al.* Quantitative single point imaging with compressed sensing. *J. Magn. Reson.* 2009;201: pp. 72–80.

[29] Lustig, M., Donoho, D.L., Santos, J.M., Pauly, J.M. Compressed sensing MRI. *IEEE Signal Process. Mag.* 2008;25: pp. 72–82.

[30] Holland, D.J., Gladden, L.F. Less is More: How Compressed Sensing is Transforming Metrology in Chemistry. *Angew. Chemie Int. Ed.* 2014;53: pp. 13330–40.

[31] Holland, D.J., Malioutov, D.M., Blake, A., Sederman, A.J., Gladden, L.F. Reducing data acquisition times in phase-encoded velocity imaging using compressed sensing. *J. Magn. Reson.* 2010;203: pp. 236–46.

[32] Benning, M., Gladden, L., Holland, D., Schönlieb, C.-B., Valkonen, T. Phase reconstruction from velocity-encoded MRI measurements–a survey of sparsity-promoting variational approaches. *J. Magn. Reson.* 2014;238: pp. 26–43.

CHAPTER 3 – GAS-LIQUID FLOW IN A CO-CURRENT UPFLOWING PACKED BED

3.1. INTRODUCTION AND THEORY

The hydrodynamic behaviour of co-current upflow beds has, with reasonable success, been modelled using empirical correlations and numerical models which assume homogeneous phase behaviour. Despite this, an understanding of the fundamental hydrodynamic behaviour eludes design engineers. Having a greater understanding of the fundamental interplay between gas-liquid material and heat transfer will enable improved design and operation of multiphase reactors including upflow vessels. This is due largely to the difficulty of experimentally studying these systems, in which transient gas and liquid behaviour occurs within opaque containers. The aim of this study is therefore to employ MRI for the first time to measure the spatial distributions of the gas and liquid velocity fields in an upflow bed. These are performed with the aim of advancing methodologies to study the interfacial characteristics of the bed, as it is the hydrodynamics of the gas-liquid interface which generally govern the rate of heat and mass transfer, and thus overall performance of reactor vessels.

3.2. FLOW REGIMES

The macroscopic fluid behaviour within the bed, or regime, is a function of both the liquid and gas flow rates. The existence of different regimes of flow behaviour was first observed by Eisenklam and Ford [1]. These authors categorised the flow behaviour based on observations into 1) single-phase pore flow and 2) two-phase pore flow. These were formed of 1) pores filled either with almost pure continuous liquid or gas, and 2) a discontinuous two-phase mixture within the pore space at elevated gas feed rates. In this early work it was seen that a definite transition occurred at some critical gas velocity for a given liquid feed rate. Turpin and Huntington [2] suggested further that three regimes are possible with distinct characteristics. These were 1) spray flow, 2) bubble flow and 3) slug flow (or pulsing flow). The slug flow regime, which consists of rising regions of alternately liquid-rich and gas-rich “slugs” is particularly distinct from the early observations. This regime was identified at mutually high gas and liquid flow rates. Spray flow and bubble flow is an extension of the two-phase flow regime. Spray flow consists of dispersed liquid droplets being conveyed by the gas phase in the interparticle void space. In bubble flow, small gas bubbles travel upwards unbroken in the

particle void space. As the microscopic material and heat transfer characteristics differ substantially based on flow regime behaviour, it is important for industrial design to have a precise knowledge of different regime locations and transitions. These are often plotted on a flow regime "map", which gives the locations of observed regimes as a function of liquid and gas feed rate. Flow regime also has a strong influence on the material characteristics and requirements of the reactor vessel, and strongly affects the operating costs via the pressure drop.

Fukushima and Kusaka [3] have suggested the existence of several different flow regimes, based on refined observations of the flow behaviour in upflow systems. They propose the following set of experimentally-determined correlations for the regime boundaries (Table 3.1).

Table 3.1: Correlations for hydrodynamic flow regimes identified by Fukushima and Fuksaka [3]

Phase boundary	**Correlation**
Bubble (I) – churn	$\mathrm{Re}_G\left(d_p/d_t\right)^{-2.5} = 1.9 \times 10^{-4}$
Bubble (I) – pseudo-spray	$\mathrm{Re}_L\mathrm{Re}_G^{1.8}\left(d_p/d_t\right)^{-3.1} = 2 \times 10^{8}$
Churn – pseudo-spray	$\mathrm{Re}_L\mathrm{Re}_G^{10.9}\left(d_p/d_t\right)^{-0.9} = 2.3 \times 10^{4}$
Bubble (I) – bubble (II)	$\mathrm{Re}_L\mathrm{Re}_G^{0.24}\left(d_p/d_t\right)^{-0.64} = 7.6 \times 10^{2}$
Bubble (II) – pseudo-pulse	$\mathrm{Re}_G\left(d_p/d_t\right)^{-4.0} = 4.5 \times 10^{5}$
Pseudo-spray – pseudo-pulse	$\mathrm{Re}_L\left(d_p/d_t\right)^{-1.7} = 2.8 \times 10^{3}$
Pseudo-pulse – pulse	$\mathrm{Re}_G\left(d_p/d_t\right)^{-5.5} = 4.8 \times 10^{7}$
Pseudo-spray – pulse	$\mathrm{Re}_L\mathrm{Re}_G^{0.5}\left(d_p/d_t\right)^{-4.5} = 2 \times 10^{7}$

In these equations, Re is the Reynolds number, d_p is the particle diameter and d_t is the column diameter. This set of correlated phase transition boundaries is plotted in Figure 3.1 for the packed bed used in this study, which has a d_p/d_t ratio of 5/52. The key additions to the flow regime map introduced by this set of relations is the identification of transition, or 'pseudo' flow regimes which occur between those identified by Turpin and Huntington [2]. Additionally, the variation of the flow regime boundaries is elegantly captured by the inclusion of Re_L, Re_G and d_p/d_t. Furthermore, the authors split the bubbling regime into two distinct regions, bubble (I) and (II). Bubble (I) contains smaller bubbles at lower gas rates, and the bubble behaviour was found to change at slightly elevated gas rates to form larger bubbles

which have higher rise velocities in bubble (II). The churn flow regime contains larger droplets of liquid which are not yet entirely entrained in the gas stream, which occurs only in the distinct pseudo spray regime C.

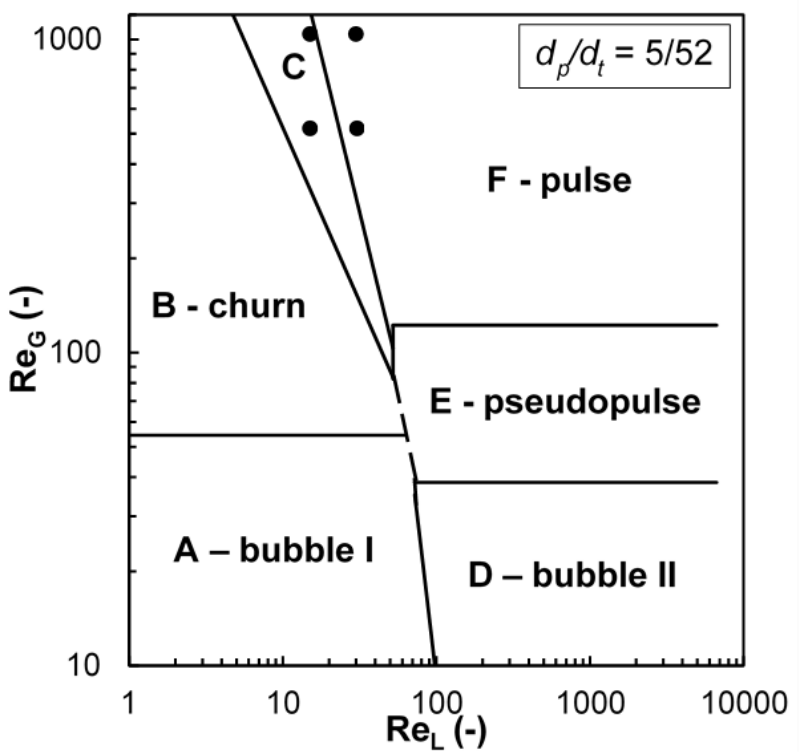

Figure 3.1: Flow regime map for the co-current upflow reactor used in the present study. The regimes are drawn using the correlations of Fukushima and Kusaka [11] for a particle-to-column diameter ratio of 5/52. Region C- denotes the pseudo-spray flow regime. The ● points indicate the location of the experimentally-chosen velocities of each phase (as demonstrated in Section 3.8 later). These traverse the pulsing and pseudo-spray regimes.

3.3. PRESSURE DROP

The reactor pressure drop is an important characteristic for design as it not only greatly influences operating costs through fluid conveying energy requirements but is also used as a correlating variable for mass and heat transfer coefficients and catalytic variables. Early approaches took a purely semi-empirical view and aimed to correlate the two-phase friction factor of the bed with the pressure drop through various experimental correlations [2,4–6]. The total two-phase pressure drop is a combination of both fluids' frictional energy losses, the hydrostatic pressure drop and a contribution from the momentum transfer. Several authors have studied the total pressure drop as a function of the gas and liquid flow rates for different packing geometries [7,8]. In general, the total pressure drop decreases for increasing gas flow, and increases with increasing liquid flow. The friction factor approach uses a phenomenological concept of the friction factor, like single-phase flow in ducts and pipes, to correlate energy dissipation along a bed of known packing structure. This approach simplifies the physics of multiphase flow and shear stress interactions but is nevertheless successful for industrial

design. This approach has been followed by many workers [2,6,9,10] and leads to equations of the form:

$$\frac{\Delta P}{\Delta z} = \frac{U_G^2 \rho_G}{d_p g} \phi(\mathrm{Re}_L, \mathrm{Re}_G), \tag{3.1}$$

in which ϕ is a correlation for the friction factor. These expressions include the effects of fluid physical properties, feed rates and the packing geometry, but fail to account for the subtle differences in the fluid behaviour between flow regimes. They are typically only valid for particular flow regimes and a limited range of operating conditions.

From a more fundamental perspective, Rao, Ananth and Varna [11] proposed a model developed from the energy balance of both phases which accounts for bubble formation. Numerous authors [12–16] have used the drift flux approach developed by Wallis [17]. The gas phase drift flux is insensitive to the liquid superficial velocity but is proportional to the gas superficial velocity. Few authors have followed a fundamental development such as that for the Carman-Kozeny [18] or Ergun [19] equations, owing to the complexity of accounting for the presence and rise behaviour of bubbles in the bed. Colquhoun-Lee and Stepanek [8] suggest the use of the single-phase energy loss in the liquid phase as a correlating parameter for their model, which additionally uses the Ergun relation to estimate this quantity. Benkrid, Rode and Midoux [15] have combined the development of the Ergun equation with the drift flux approach to develop a model for the estimation of both pressure drop and liquid holdup which requires only a single fitting parameter. Attou and Ferschneider [20] develop a phenomenological model based on the fundamental balance equations of mass, momentum and energy. They introduce interphase interaction force equations between the solid and liquid, and gas and liquid. Additionally, their model accounts for the forces of drag on an isolated bubble rising in a liquid. Their model compares favourably with pressure drop experimental data from numerous studies. This work is analogous to their slit models for concurrent downward flow in trickle beds. Boyer and Ferschneider [21] have modified the model to solve the mass and momentum balances for a two-phase mixture and introducing different closure laws. These latter two models additionally predict the liquid holdup in the bed.

3.4. FLUID HOLDUP

Holdup is defined as the quantity of liquid and gas inside the reactor vessel. It is sometimes expressed as the saturation, which is the fraction of available pore space occupied by either gas or liquid. Liquid holdup is usually much higher in upflow beds compared to trickle beds, as they are often operated with small gas flows which are introduced into a totally liquid-saturated bed to form a bubbling bed [9]. In upflow beds, design equations are usually given in terms of the gas holdup although in practise the liquid holdup is easier to determine [22]. It is measured using either a shutoff drainage technique, in which the reactor inlets and outlets are suddenly closed, and the liquid volume is found gravimetrically, or via tracer studies which estimate the holdup based on residence time distribution models [23]. It can also be measured directly using local tomographic techniques [24], including electrical capacitance tomography [25]. If the liquid holdup is measured, the gas holdup can be determined from the overall porosity of the bed through the relationship:

$$\varepsilon_G + \varepsilon_L = \varepsilon_B, \tag{3.2}$$

where ε_G is the gaseous fractional holdup, ε_L is the liquid fractional holdup and ε_B is the average porosity of the bed. Alternatively, if the saturation is required the following relationship is used:

$$\beta_G + \beta_L = 1, \tag{3.3}$$

in which β_G is the gas saturation, defined as the fraction of available pore space occupied by the gas and β_L is the liquid saturation. Early studies by Weber [26] found that gas holdup was insensitive to liquid flow rate, however modern work has disputed this observation [23]. He proposed several correlations found by conducting air-water experiments in various packing times which give the gas holdup as a function of the gas superficial velocity only. von Heilman [27] proposed an early correlation for the gas phase holdup based on the properties of the packing, fluids and column. In this study it was reported that despite shutting off the gas supply completely, some gas remained ‘trapped’ in the bed matrix which the author termed ‘static’ gas holdup. Other authors have since confirmed the existence of static gas holdup and stationary bubbles [28,29]. The static gas holdup is not a function of the gas feed rate and diminishes with increasing liquid flow to zero at the minimum fluidisation velocity of the

liquid [30]. Table 3.2 provides a summary of some important design correlations for fluid holdup in upflow beds.

Table 3.2: Experimental correlations for the determination of gas and liquid holdup in various studies

Authors	**Correlation**
Fukushima and Kusaka [3]	$\frac{\varepsilon_L}{\varepsilon_B} = \begin{matrix} 1.8\mathrm{Re}_L^{0.03}\mathrm{Re}_G^{-0.28} & (\mathrm{Re}_L\mathrm{Re}_G^{0.5} < 695) \\ 0.72\mathrm{Re}_L^{0.17}\mathrm{Re}_G^{-0.21} & (\mathrm{Re}_L\mathrm{Re}_G^{0.5} > 695) \end{matrix}$
Stiegel and Shah [23]	$\frac{\varepsilon_L}{\varepsilon_B} = 1.47\ \mathrm{Re}_L^{0.11}\mathrm{Re}_G^{-0.19}\left(a_p d_p\right)^{-0.41}$
Achwal and Stepanek [28]	$\frac{\varepsilon_L}{\varepsilon_B} = 2\left\{1 + \left[1 + 72.3U_L^{-0.229\left(\frac{U_L}{U_G^2}\right)^{0.423}}\right]^{0.5}\right\}^{-1}$
Hutton and Leung [31]	$U_L = \frac{\varepsilon_L}{F_c} l_P^{0.5}\left(\frac{1}{\rho_L}\delta_{GL} - g\right)^{0.5}$ δ_{GL} - two-phase pressure gradient
Saada [32]	$\frac{\varepsilon_L}{\varepsilon_B} = 0.48\left(\frac{\mathrm{Re}_L}{\mathrm{Re}_G}\right)^{0.25}$ (single−phase pore flow) $\frac{\varepsilon_L}{\varepsilon_B} = 0.32\left(\frac{\mathrm{Re}_L}{\mathrm{Re}_G}\right)^{0.07}$ (two-phase pore flow)
Turpin and Huntington [2]	$\frac{\varepsilon_L}{\varepsilon_B} = -0.035 + 0.182\left(\frac{U_L\rho_L}{U_G\rho_G}\right)^{0.24} \quad 1 \leq \left(\frac{U_L\rho_L}{U_G\rho_G}\right)^{0.24}$

Due to their simplicity, the correlations by Saada [7,32] are often employed for first-pass design calculations. In all these relations and studies, it is observed that liquid holdup is increased with increasing liquid feed rate, and similarly that gas holdup is increased by increasing the gas feed rate. Consequently, the gas holdup is inversely related to the liquid feed rate and vice versa although the extent of the effect is determined by the relative gas and liquid flow (i.e. the operating flow regime). The model of Attou and Ferschneider [20] is more sophisticated than the above empirical correlations and compares well with available data. An early attempt to record local holdup data was undertaken at the Pittsburgh Energy Research Centre [33], which made use of a conductivity probe which gave a radial holdup distribution. The probe measurement showed an increase in the local liquid holdup towards the walls of the vessel.

3.5. MASS AND HEAT TRANSFER

In heterogeneously catalysed chemical reactions, it is very often the transfer of material across the gas-liquid interface which is the rate-determining process [9]. The calculation of mass transfer driving forces and mass transfer coefficients across the gas-liquid interface has therefore been studied well in the open literature [9,22,34]. As for other types of multiphase reaction vessels, modelling of gas-liquid transfer has typically been done using the two-film theory which assumes a laminar boundary layer at the interface. The mass transfer driving forces in both phases may be equated and simplified therefore in terms of the lumped parameter $k_L a$ which negates the need to have knowledge of the exact surface area available for transfer. This quantity is estimated using concentration measurements of a known gas within the liquid phase assessed at the reactor outlet for various gas phase concentrations [35]. Packed upflow columns are known to exhibit high values of mass transfer coefficients, particularly at low gas residence times [22]. Improvements in $k_L a$ of between 100% and 150% have been observed when compared to downward trickle flow. In a notable study, Specchia *et al.* [5] derived the following correlations for both the interfacial area and mass transfer coefficient:

$$\frac{a_L}{a_s} = 0.29\left[\left(-\frac{\Delta P}{\Delta z}\right)_{LG}\frac{\varepsilon}{a_s}\right]^{1.17} + 0.61 \tag{3.4}$$

$$\frac{10^3 k_L \varepsilon}{U_L} = 7.96\left[\left(-\frac{\Delta P}{\Delta z}\right)_{LG}\frac{g\varepsilon}{a_s \rho_L U_L^2}\right]^{0.275} - 9.41. \tag{3.5}$$

where a_L is the gas-liquid interfacial surface area and a_s is the specific surface area of the packing material.

Work using specifically catalytic particles has been undertaken by Goto *et al.* [36] and Alexander and Shah [37]. Most other studies on the subject are concerned with structured packings of the type found in non-reactive absorption columns [9]. Saada [32] proposed the following correlations which account for the differences in flow regime:

$$\frac{k_L a\, d_p^2}{D} = 10.71\mathrm{Re}_G^{0.22}\mathrm{Re}_L^{0.32}\left(\frac{d_p}{d_t}\right)^{0.33} \quad \text{single-phase pore flow} \tag{3.6}$$

$$\frac{k_L a\, d_p^2}{D} = 10.34\mathrm{Re}_G^{0.09}\mathrm{Re}_L^{0.58}\left(\frac{d_p}{d_t}\right)^{0.34} \quad \text{two-phase pore flow} \tag{3.7}$$

For their wider range of identified flow regimes, Fukushima and Kusaka [3] propose the correlations in Table 3.3.

Table 3.3: Correlations for the gas-liquid mass transfer constants in upflow beds by Fukushima and Kusaka [3]

Flow regime	**Correlation for $a_p d_p/\left(1-\frac{\varepsilon_L}{\varepsilon_B}\right)$**
Bubble (I)	$16\mathrm{Re}_L^{0.05}\mathrm{Re}_G^{-0.4}$
Churn	$2.2\mathrm{Re}_L^{0.05}\mathrm{Re}_G^{-0.2}\left(d_p/d_t\right)^{-0.5}$
Pseudo-spray	$0.24\mathrm{Re}_L^{0.27}\left(d_p/d_t\right)^{-0.7}$
Bubble (II)	$0.26\mathrm{Re}_L^{0.67}\mathrm{Re}_G^{-0.25}\left(d_p/d_t\right)^{-0.4}$
Pseudo-pulse	$1\times10^{-2}\mathrm{Re}_L^{0.67}\left(d_p/d_t\right)^{-1.4}$
Pulse	$2.9\times10^{-4}\mathrm{Re}_L^{0.67}\mathrm{Re}_G^{0.2}\left(d_p/d_t\right)^{-2.5}$

Design equations additionally employ the liquid-solid mass transfer coefficient. This quantity has similarly been correlated as a function of the fluid physical properties and operating conditions, and a few noteworthy examples are detailed in Table 3.4.

For a more complete review of additional studies, the reader is referred to the classical review papers [9] and textbooks on the subject [22,34].

Axial mixing of both phases has been identified as significant in upflow reactors, especially when compared to downward trickle flow [23,38]. Most authors have found that the magnitude of the Peclet number, indicative of the extent of back mixing, is diminished for increasing gas

Table 3.4: Various experimental correlations for the liquid-solid mass transfer coefficient found in the open literature

Authors	**Correlation**
Mochizuki and Matsui [39]	$\frac{k_s d_p}{D}=48\mathrm{Re}_G^{0.25}\quad \mathrm{Re}_L>5$
	$\frac{k_s d_p}{D}=0.75\mathrm{Re}_L^{0.5}\left(\frac{\mu_L}{\rho_L D}\right)^{0.33}\left(1+\frac{4\mathrm{Re}_G^{0.55}}{\mathrm{Re}_L^{0.7}}\right)\quad \mathrm{Re}_L>5$
Specchia *et al.* [40]	$\frac{k_s a_w d_p}{a_p D\mathrm{Sh}_0}=0.48\ln\left(\frac{Re_G}{Re_L}\times10^2\right)-0.03\left[\ln\left(\frac{Re_G}{Re_L}\times10^2\right)\right]^2-0.3$
	$\mathrm{Sh}_0=(2.14\mathrm{Re}_L^{0.5}+0.99)\left(\frac{\mu_L}{\rho_L D}\right)^{\frac{1}{3}}$
Colquhoun-Lee and Stepanek [8]	$\frac{k_s d_p}{D}=0.155\left(\frac{\mu_L}{\rho_L D}\right)^{\frac{1}{3}}\left[\frac{e_L d_p^4\rho_L^2}{\mu_L^3\left\{\frac{\varepsilon_G}{\varepsilon_B}\left[\frac{\rho_G}{\rho_L}\left(\frac{U_G}{U_L}\right)^3-1\right]+1\right\}}\right]^{0.28}$

velocity and decreasing liquid velocity. Several authors [23,27,41,42] have correlated the Peclet number as a function of flow velocities and fluid properties. An exemplary correlation is that by Stiegel and Shah [23], which is given as:

$$\frac{\mathrm{Pe}_L}{\varepsilon_L} = 0.128\mathrm{Re}_L^{0.245}\mathrm{Re}_G^{-0.16}. \tag{3.8}$$

Studies on heat transfer in catalytic upflow systems are relatively scarce. Kirillov and Ogarkov [43] measured the temperature gradient and particle-to-fluid heat transfer coefficient from hollow model spheres heated by an electric heater to an upflow bed, and found that it obeyed the following relation:

$$h = \frac{i^2 R_w}{4\pi R^2 \Delta T}, \tag{3.9}$$

where i is the current applied, R is the particle radius, R_w is the wire resistance and ΔT is the temperature gradient from the fluid to the sphere surface. Furthermore, the authors noted that a maximum value of the heat transfer coefficient h as a function of Re_G is achieved which they attributed to the onset of different flow regimes.

3.6. RECENT WORK AND EXPERIMENTAL METHODS

Recent interest has been generated regarding co-current upflow beds for use in reactive absorption systems for climate change abatement strategies, and for offshore marine processing activities. For the latter application, interest is mainly in studying the effects of using these systems on an incline [44] and under pulsed conditions or both [45]. These modern studies typically use a either optical [46–51] or electrical probes [52] or a combination of probes and CFD [53] or other computer modelling techniques [54] to extract many of the hydrodynamic variables already presented in this discussion. The CFD models usually use the Eulerian-Eulerian form [55], which require closure models to estimate the degree of interphase interaction. The so-called two fluid models assume each phase is continuous and behaves as a Newtonian fluid, and they employ additional models which depend on flow regime to give mathematical closure [56,57]. The fundamental balance equations of mass, momentum and energy are therefore solved for each phase computationally. Often the phases are assumed to be interpenetrating continua, which removes the complexity of having to calculate a gas-liquid interfacial boundary. More advanced nonequilibrium thermochemical models can be developed, in which the assumptions of static equilibrium are relaxed. These are

computationally very intensive however as the partial differential equations are thus all functions of time. The rigorous framework of Iliuta *et al.* [58] importantly regards the contribution of the presence of phase interfaces on the balance equations, and includes explicit interfacial thermodynamic relations which treat the phases as independent continua. A more thorough description of these models is given in the book by Onsan [59].

An increased fundamental understanding will come from studying the detailed phase dynamics and bubbling characteristics inside the pore space, therefore many recent works have sought to elucidate the behaviour of bubbles and their rise characteristics in upflow beds [46,49,50]. Other authors [5,60] have focused on using dissolution rates to infer the mass transfer area, thus allowing determinations regarding the available gas-liquid mass transfer area. One of the more important outcomes regarding bubble behaviour came from Pokusaev *et al.* [47,48], in which the authors found that bubbles could move either as a 'train' within single liquid-filled pores and not change shape, or as an 'amoeboid' that as it rises, envelopes packing elements which occasionally leads to bubble breakup or coalescence.

MRI has also been used before in upflow beds by Collins *et al.* [61]. This study complements the widespread use of MRI to study co-current downward trickle flow. In this study, the authors made use of rapid imaging techniques and 1D profiles to calculate bubble rise velocities and gas holdup. Rise velocities were successfully determined for several packing sizes, and the gas holdup showed trends which also agree with previous observations. The data were also analysed to give information regarding bubble shape, and elongation of the bubbles within liquid channels was observed. The data also confirmed the existence of static gas holdup within regions of the bed.

The purpose of this study is to use MRI for the first time to acquire spatially-resolved time-averaged maps of the gas and liquid velocity fields within an upflow bed. The intensity images will also reveal information regarding the spatial distribution of both phases within a slice. These will be determined at a few different operating conditions and compared with the conventional measurements of two-phase pressure drop and gravimetrically determined liquid holdup to assess the extent to which MRI can in the future be used to give more fundamental information about two-phase reactor hydrodynamics.

3.7. EXPERIMENTAL

3.7.1. APPARATUS

The fixed bed upflow system used in this chapter is schematically represented in the process flow diagram in Figure 3.2.

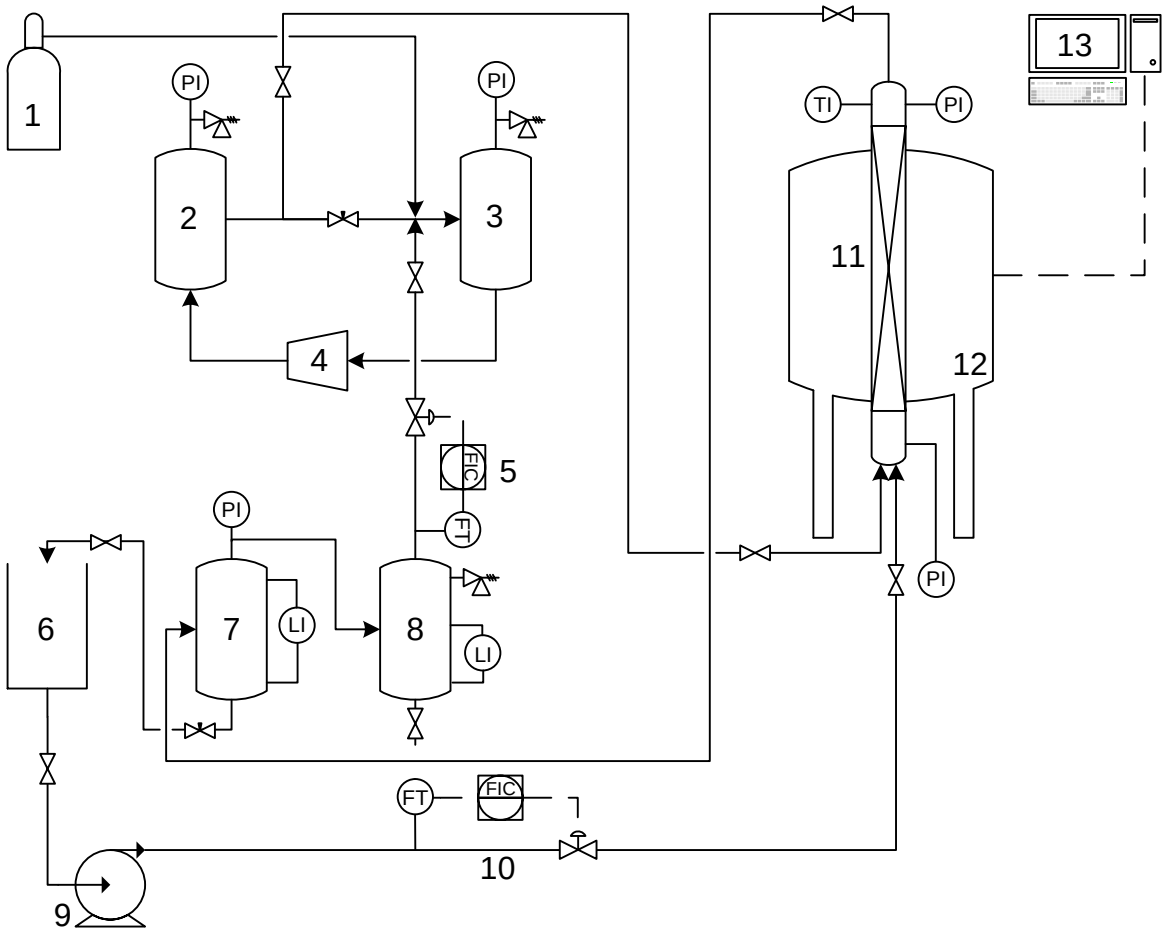

Figure 3.2: Process flow diagram of the pilot-scale experimental co-current upflow bed. Key equipment is labelled as follows 1: SF_6 cylinder, 2: high pressure gas receiver vessel, 3: low pressure gas receiver vessel, 4: SF_6 compressor, 5: gas mass flow controller, 6: water feed tank, 7: stage 1 gas-liquid separator vessel, 8: stage 2 gas-liquid separator vessel, 9: liquid water centrifugal pump, 10: liquid mass flow controller, 11: PVC upflow packed bed vessel, 12: superconducting MRI magnet, 13: controller computer for NMR setup and software.

The system used was an inert pilot-scale fixed bed setup, which consisted of three sections: the gas delivery feed, liquid feed and separation, and MRI and fixed bed sections. Sulphur hexafluoride gas is chosen as the test gas because of the NMR sensitivity of the ^{19}F nucleus. The ^{19}F nucleus is 100% naturally abundant, and the high density and relatively low self-diffusion coefficient of SF_6 makes it an ideal choice for thermally-polarised gas phase NMR [62]. SF_6 gas was supplied by a 20 barg cylinder from Air Liquide® at a purity of 99.999%. Owing it its high global warming potential, recirculation of the gas was required. This meant using a gas recirculation system together with a gas-liquid separation unit. The recirculation

system consists of two pressure vessels, (2) and (3) in the chart above. These are connected to the discharge and suction lines respectively of a specialised Dilo® SF_6 gas compressor, labelled (4), which handles suction pressures of ~0.5 bara and delivers a compression ratio of 24 typically to give gas pressures of 10-12 bara. Both the low and high-pressure receiver tanks (2) and (3) are 6L, 316 stainless steel rated to a working pressure of 20 bara. The high-pressure tank outlet is connected via a system of non-return valves directly to the bottom of the packed bed (11). The low-pressure tank (3) received both gas delivered at a regulated pressure from the cylinder (used only to pressurise the system), as well as the low pressure return from the gas-liquid separation train. The compressor provided a pressure gradient between tanks (2) and (3). The needle valve pictured between the tanks was used to control the pressure gradient by allowing an amount of gas to bypass the fixed bed system.

Liquid water was supplied to the system by a 5L glass feed vessel (6) and pumped to pressure by a Verder ® VG330-10 gear pump (9). The water was deionised water which had been doped with gadolinium chloride hexahydrate ($GdCl_3 \cdot 6H_2O$), used because of the paramagnetic gadolinium ions (Gd^{3+}) to a concentration of 0.022 g/100 mL to reduce the T_1 time to 120 ms (as measured using a standard inversion recovery sequence) which reduces the time between successive MR excitations. The liquid feed to the packed bed is controlled by a Bronkhorst Cori-Flow M55C4-AAD-22-K-C mass flow controller (10). The fluids are returned from the packed bed as two-phase flow which undergoes separation before both being recycled. The two-phase outlet was fed into the first stage separator vessel (7). The vessel capacity was 6L and made from 316 stainless steel rated to a working pressure of 20 barg. A liquid recycle feed was taken from the bottom of this vessel, the flow rate of which was controlled by a needle valve. The liquid level in vessel (7) was monitored manually by a liquid level indicator, and by a pressure indicator attached to the vessel. It was maintained at approximately 50% to ensure mostly pure liquid and gas feeds exiting from the bottom and top of the vessel respectively. The needle valve on the liquid outlet line of vessel (7) was adjusted manually to maintain the desired pressure and liquid level. Gas was withdrawn from the top of the vessel and fed into the second stage separation vessel (8). This vessel was run as an accumulator for any residual water entrained in the gas stream. The vessel capacity was 2L and was of 316 stainless steel rated to a working pressure of 5 barg. To monitor the amount of accumulation, a level indicator was fitted to the vessel. However, as low gas flow rates were used in the experiments, in practice very little liquid was retained from vessel (7) and no accumulation of liquid was found in (8) over the course of the experiments. Vessel (8) was also fitted with a pressure relief valve

set to 4.5 barg for safety purposes. Gas from the top of this vessel was fed back into the gas recirculation system via a gas mass flow controller. The location of this controller as a back-pressure controller was deliberate, as it allowed the throttling of flow rate to be synergistic with lowering the flow rate and not vice versa as high bed pressures and low flow rates were desirable. The type of mass flow controller used was a Bronkhorst EL-FLOW® Select thermal mass flow controller.

The fixed bed was a 2 m long section of PVC tubing which had an internal diameter of 52 mm. It was sealed either end with threaded end-caps and was rated to a working pressure of 8 barg. The gas-liquid distributor consisted of a 60 cm long fluid mixing chamber with an inner diameter of 43 mm, outer diameter 51 mm, which was inserted into the bottom of the PVC tube. This tube was filled entirely with a polydisperse mixture of 1 mm and 3 mm glass beads, which were held in place by a sintered bronze distributor plate attached to the top of the tube. The gas was fed into the distributor via a sparger tube, which was 300 mm long and drilled with 120 equally-spaced, 2 mm holes for gas distribution. The gas was then able to enter the mixing chamber and contact the liquid water. Water was fed into the fluid mixing chamber to the same spatial location as the gas sparger via a ¼″ Swagelok® tube. The gas and liquid were mixed inside the chamber and allowed to pass upwards through the sintered bronze distributor disc, ensuring an even two-phase flow entered the bottom of the bed. The reactor temperature was monitored on the outlet with a k-type digital thermocouple, and the pressure drop across the bed was recorded using two digital pressure gauges located above and below the packed bed. Pressure drop measurements were made three times in 10-minute intervals and averaged for reporting. Block valves were located on the reactor inlets and outlet to allow a rapid switching-off of the flow to and from the bed.

The bed was filled to a packed height of 132 cm from the fluid distributor with randomly-packed 5 mm soda lime glass ballotini. Upon each addition of 100 mm of packing, the bed was tapped to consolidate the random packing of particles to ensure close random packing. This gave a bed with average porosity measured at $\varepsilon_B = 0.38$.

3.7.2. MAGNETIC RESONANCE SETUP

Magnetic resonance experiments were conducted using a vertical bore Bruker Spectrospin DMX 200 superconducting magnet with field strength of 4.7 T (200 MHz Larmor frequency for ^{1}H) and bore diameter of 149 mm. A dual-tune birdcage-type radio frequency coil 64 mm in diameter was used. The magnet was tuned to a frequency of 200.11 MHz in order to image

the ^{1}H signal from the water, and a frequency of 187.64 MHz to image the ^{19}F nucleus in the SF_6 gas. The gradient set used was a Bruker Mini 0.36 shielded gradient with a maximum gradient strength of 13.88 G cm^{-1} in all three orthogonal spatial directions. All experiments were performed using the Bruker TopSpin™ software on a standard desktop computer.

3.7.3. COMPRESSED SENSING

A compressed sensing scheme was used to significantly reduce the acquisition times of the gas phase. The theory of compressed sensing MRI and velocimetry has been discussed previously in greater detail [63–66]. Gas phase images are acquired using a single-point-imaging (SPI) approach, which samples a single point in **k**-space for every free induction decay. This approach is favourable for gas phase imaging as T_2 times are typically too short to employ frequency encoding methods. It thus allows a greater signal-to-noise ratio to be achieved. It is ideally suited to a compressed sensing scheme as these aim to under sample **k**-space, and therefore by careful choice of which points to sample **k**-space can be directly under sampled.

The chief drawback of SPI experiments is they are typically much slower for similar spatial resolutions, owing to the use of two phase encoding gradients and the lack of time-based frequency encoding which raster scans lines from **k**-space. In these experiments, the 32 × 32 **k**-space matrix was under sampled by 50%, resulting in a reduction in acquisition times by a factor of 2. The high resolution single-phase gas flow experiments also used compressed sensing, with a 12.5% under sampling rate to achieve an experimental time improvement of 8. Even at this low under sampling rate the images are shown to be quantitative. A pseudo-random under sampling pattern was obtained using the algorithms developed by Lustig [63,64]. Regularisation parameters were chosen by inspection of the resulting intensity and phase images, and were found to be approximately $\alpha = 1.4\times10^4$ and $B = 4.0\times10^4$. The definition of these parameters is given in Equation 2.42.

3.7.4. SINGLE-PHASE IMAGES

The principles of MRI velocimetry have been described previously. Single-phase fluid velocity maps of both the gas and liquid phases were acquired in the unpacked 52 mm tube. These were done to demonstrate the quantitative nature of both pulse sequences. The pulse sequences used were the same as those to be used on the packed bed system, and pulse sequence diagram schematics are provided in Figure 3.3. The sequences used were modifications of the classical pulse sequences given in Section 2.9 but using compressed sensing sampling patterns and

gradient parameters. This was done to achieve time savings of up to 8× for the same spatial resolution. Key parameters for each velocity-encoded pulse sequence and image is tabulated in Table 3.5. The high inherent signal-to-noise in the single-phase system allowed the use of a much higher spatial resolution when compared with the two-phase images. This was chosen to properly resolve the spatial gradient of the velocity profiles in the empty tube. The gas phase images are at a slightly larger field-of-view, as the maximum imaging gradient strengths at this high resolution for the pulse sequence used meant that this was the smallest FOV achievable. The FOV for the two-phase experiments is identical.

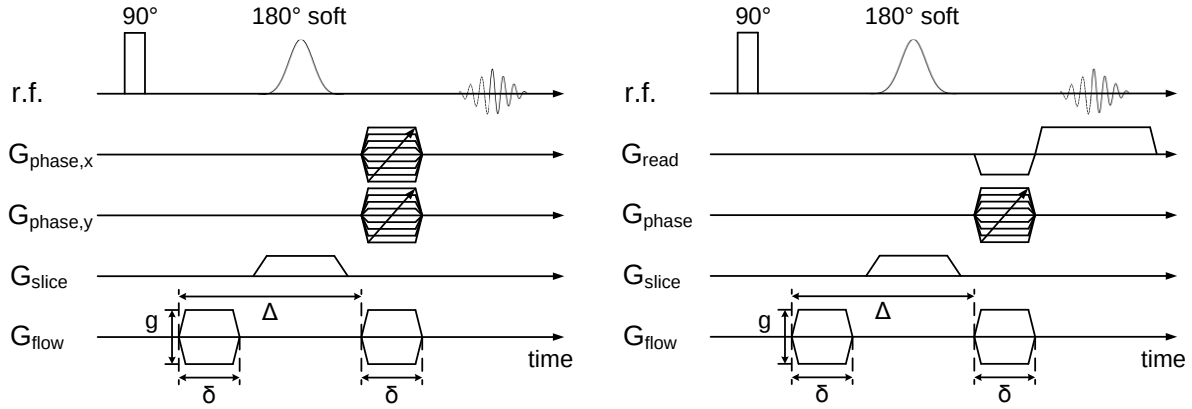

Figure 3.3: Pulse sequences used for velocity imaging of (a) the gas phase and (b) the liquid phase. In (a) a single-point imaging pure phase encoding approach is used to enable compressed sensing. In (b) a standard spin-echo frequency encoding sequence is used.

Table 3.5: NMR constants for the single-phase imaging experiments in the 52 mm open tube for gas and liquid

Parameter	**Gas**	**Liquid**
Field-of-view	62 mm × 62 mm	60 mm × 60 mm
Resolution	969 μm	469 μm
Slice thickness	3 mm	3 mm
Pulse sequence	11-interval SPI	Frequency encoded spin echo
Observation time (Δ)	6 ms	3.10 ms
Flow encoding gradient time (δ)	100 μs	995 μs
Echo time (τ)	360 μs	600 μs
Field of flow	3 m s^{-1}	0.5 m s^{-1}
Experiment time	36 minutes	32 minutes
Number of averages	4	2

3.7.5. LIQUID 1D PROFILES

One dimensional profiles of the liquid phase were acquired using a spin-echo pulse sequence with a single spatial-encoding gradient applied during signal acquisition. This allows the signal from the liquid phase to be acquired in a direction. For example, if applied in the vertical *z*-direction, the profile yields the amount of liquid present integrated along the radial direction within every recorded voxel of the profile. These were recorded to assess the temporal stability of the liquid phase, and to measure the degree of bubbling present. Bubbles of SF_6 gas would show up as regions of reduced liquid signal intensity. A series of profiles showing intensity fluctuations with time indicate the presence of temporal instabilities caused by the presence of passing bubbles. The extent of the intensity fluctuation in time is representative of the amount of bubbling. Profiles were recorded in all three orthogonal directions, and reference profiles were recorded during stable single-phase liquid flow at the same flow rates as the two-phase experiments. Key experimental constants are provided in the Table 3.6.

Table 3.6: Experimental constants for the liquid-phase 1D profile experiments in the packed bed

Parameter	Value
Field-of-view (*z*, *x*, *y*)	100 mm, 60 mm, 60 mm
Resolution (*z*, *x*, *y*)	1.25 mm, 0.470 mm, 0.470 mm
Pulse sequence	Spin echo
Recycle time	2 ms
Experiment time	128 ms
Number of profiles	64

3.7.6. TWO-PHASE IMAGES

The same pulse sequences used to image the single-phase flow in the tube discussed previously were used to image the gas and liquid under conditions of two-phase flow in the upflow bed. The gas phase imaging pulse sequence was chosen as it was designed to minimise the contribution of background gradients to the phase shift. It is based on the work of Cotts *et al.* [67] and the development and use of the sequence on other gas imaging applications is described by Boyce [68]. The liquid phase is more robust to these effects and has significantly longer T_2 values, and thus a spin-echo based sequence can be used with standard phase contrast gradients for the encoding of velocity. Key parameters for the imaging sequences used in the two-phase flow experiments are quote in Table 3.7.

Table 3.7: NMR constants used in the two-phase upflow experiments in the packed bed for both the gas and liquid imaging

Parameter	Gas	Liquid
Field-of-view	60 mm × 60 mm	60 mm × 60 mm
Resolution	1.875 mm	1.875 mm
Slice thickness	3 mm	3 mm
Pulse sequence	11-interval SPI	Frequency encoded spin echo
Observation time (Δ)	6 ms	3.10 ms
Flow encoding gradient time (δ)	100 μs	995 μs
Echo time (τ)	360 μs	600 μs
Field of flow	3 m s^{-1}	0.5 m s^{-1}
Experiment time	148 minutes	148 minutes
Number of averages	6	128

As the flow in two-phase upflow beds is temporally unstable, standard imaging sequences which have long running times must be modified to acquire signal from the moving materials. An alternative to modification of longer sequences would be to use rapid imaging sequences such as RARE [69], FLASH [70] or UTE [71,72], however velocity encoding with these sequences for both gas and liquid flow becomes exceptionally complex if not impossible. Therefore, the sequences presented here were time-averaged for the same amount of time, 2.5 hours, to capture a time-averaged view of the reactor behaviour under two-phase flow conditions. The images represent an averaged picture of the flow and phase behaviour over the same extended period for both phases. Passing individual slugs and bubbles will contribute over a time-averaged basis to both the spin density intensity maps and velocity maps, which will enable the average flow and phase behaviour to be analysed.

This is contrasted with trickle flow, which is examined in Chapters 4 and 5. In trickle flow, stable contiguous channels of each phase can form. In Chapters 6 and 7 an alternative approach to imaging rapid phenomena is taken, in which the bubbling behaviour of fluidised beds is controlled to use conventional imaging approaches.

3.8. OPERATING PROCEDURE

For all two-phase flow experiments, the bed was initially run in single-phase liquid mode with the gas flow introduced after establishing stable liquid-only flow. This procedure is known as complete or total prewetting, as the solid phase will completely cover with liquid before gas

was introduced. Gas flow was then introduced at the desired flow rate, and the operating pressure was established by adjusting the pressures in vessels (2) and (7). Before each experiment, the flow rates and pressure were allowed to stabilise over a running period of 30 minutes, which was found to be sufficient time to enable transient behaviour to die out and steady state flow to be established. During an experiment, the liquid level in vessel (7) was maintained which was found to give stable pressures. Together with the tuned gas and liquid mass flow controllers, this gave temporally stable operating conditions. The experiments were all run at the elevated pressure of 7.0 ± 0.12 barg.

NMR experiments were conducted on a slice located 60 cm above the inlet of the bed. The slice is located approximately 1200 particle diameters from the inlet, at which point is it expected that all bubbles and flow characteristics should stabilise, well within the limit suggested by Bordas [49]. During stable flow, the total two-phase pressure drop across the bed was recorded by noting the pressure readings on the gauges located above and below the bed. The temperature was recorded as displayed on the thermocouple. The average laboratory temperature was 22.3 ± 0.7 °C. Owing to the lengthy experimental times (2.5 hours), a 2 × 2 experimental matrix for two-phase flow was undertaken. The values of the fluid Reynolds numbers (hence the coordinates on the flow regime map) are tabulated in Table 3.8. The liquid holdup was determined by rapidly shutting the inlet and outlet valves simultaneously. The bed was subsequently drained, and together with the static bed average void fraction, the liquid saturation was determined by measuring the amount of liquid present in the bed at each flow rate.

Table 3.8: Experimental matrix and range of gas and liquid velocities with tabulated values of the Reynolds numbers of both phases

	U_G = 2.50 cm s^{-1}	U_G = 5.0 cm s^{-1}
U_L = 0.26 cm s^{-1}	Re_G, Re_L = (520, 15)	Re_G, Re_L = (1040, 15)
U_L = 0.52 cm s^{-1}	Re_G, Re_L = (520, 30)	Re_G, Re_L = (1040, 30)

The range of velocities examined for both gas and liquid flows means that experiments are conducted between the churning and the pulsing flow regimes according to Figure 3.1. This was primarily limited by the gas mass flow controller, which was specified and designed to run at much higher gas Reynolds numbers than are typically encountered in upflow beds. It was specified for use on an SF_6 fluidised bed (see Chapters 6 and 7). However, no other reliable method of measuring and controlling the gas flow rate was available, and thus the lowest achievable gas mass flow rate of 12 g/min SF_6 was used for the minimum flow experiments.

The range still enables the investigation of how the spatial distributions and velocity fields respond to changes in flow rates and allows the investigation of holdup and pressure drop. For future studies, a mass flow controller able to control gas rates which enable study in the bubbling regimes and the transitions between these regimes is suggested.

3.9. RESULTS

3.9.1. SINGLE-PHASE FLOW IN TUBE

Figure 3.4 shows the single-phase intensity images of the liquid phase (a) and the gas phase (b) under static conditions. Owing to the use of different pulse sequences, the field-of-view of the liquid images is 60 mm × 60 mm and the gas images is 62 mm × 62 mm. Both images show a circle of nearly constant intensity. Regular reductions of intensity are observed around the edges of the tube for both the liquid and the gas phase. These are seen to occur on the vertices of a decagonal shape. Additionally, the gas phase image shows a slightly higher variation in intensity in the centre of the tube than does the liquid phase.

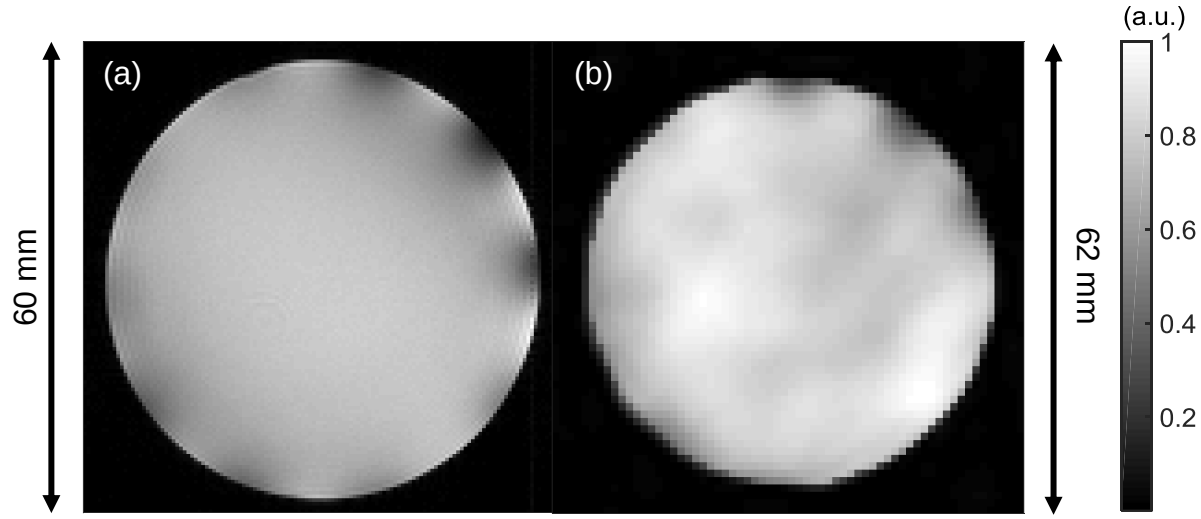

Figure 3.4: Signal intensity images for the tube filled with (a) liquid and (b) gas. The field-of-view for the liquid is 60 mm × 60 mm and the resolution is 469 µm × 469 µm, and for the gas (b) the field-of-view is 62 mm × 62 mm and the resolution is 969 µm × 969 µm. The presence of signal, indicated by white, is representative of the presence of ^{1}H nuclei (a) and ^{19}F nuclei (b). The colour bar indicates relative signal strength in arbitrary units (a.u.).

The phase of the NMR signal for flowing conditions can be related to the velocity of each voxel (see section 2.10), and thus the velocity images can be plotted for both the liquid and gas phases in the tube. These images are given for the liquid phase in Figure 3.5 and for the gas phase in Figure 3.6. These are shown for 10 velocity increments in each case ranging from static to a chosen maximum flow. For each phase, the images are shown on the same colour axis across the range of velocities to illustrate how the flow profile develops with increasing flow.

In Figure 3.5 for the liquid under static conditions, an annular region of near-static flow exists around the perimeter of the tube. However, a region of low negative (downward) flow exists towards the centre of the bed. This flow is purely induced under convective conditions due to the presence of density gradients along the tube. As the flow is increased, this region of downward-flow is reduced. The up-flow provided by the pump manifests primarily in (b) and (c) as positive (upward) flow in the annular perimeter. This shape continues to develop until image (g) in which an inversion is seen, where the maximum flow occurs towards the centre of the bed rather than in an annular ring. As the flow is increased further, the profile takes on a more familiar shape approaching Poiseuille flow, in which the maximum is found towards the centre of the bed and the shape of the profile is approximately parabolic with static flow found around the perimeter of the tube.

For the gas in Figure 3.6, analogous behaviour is recorded to that of the liquid. A central region of downward flow is initially observed under conditions of no-flow due to natural convection. The annular region around the edge demonstrates slight positive flow in this case as the net flow within the slice is necessarily zero. In the gas, the profile inversion, whereby the downward flow is ceased, and the maximum flow occurs towards the tube centre, is observed in image (c). It is noted that for all images the Reynolds number is much higher for the gas phase, due to the viscosity being an order of magnitude lower. From image (c) onwards, the profile develops as expected, with the axial flow maximum approximately at the tube centre and the shape of the field approximately parabolic with an annular region of minimum flow around the edges of the tube. In images (g), (h) and (j) it is observed that the centroid of the region of high flow seems to drift from the tube centre, and thus regions around the tube walls which were approximately quiescent achieve nonzero velocity in subsequent images. The high flow region begins to flatten as the velocity is increased, with more of the central tube area achieving higher velocities as the flow rate is increased.

For both phases and in each slice, the average axial velocity was calculated by taking the numerical average of the velocity in each voxel. These average velocities were then compared to the expected superficial velocity determined by the readings on the mass flow controllers of each phase. The results of this comparison are shown in Figure 3.7. Ideally the quantities would be identical. For the liquid phase in (a), good agreement is shown between the velocity

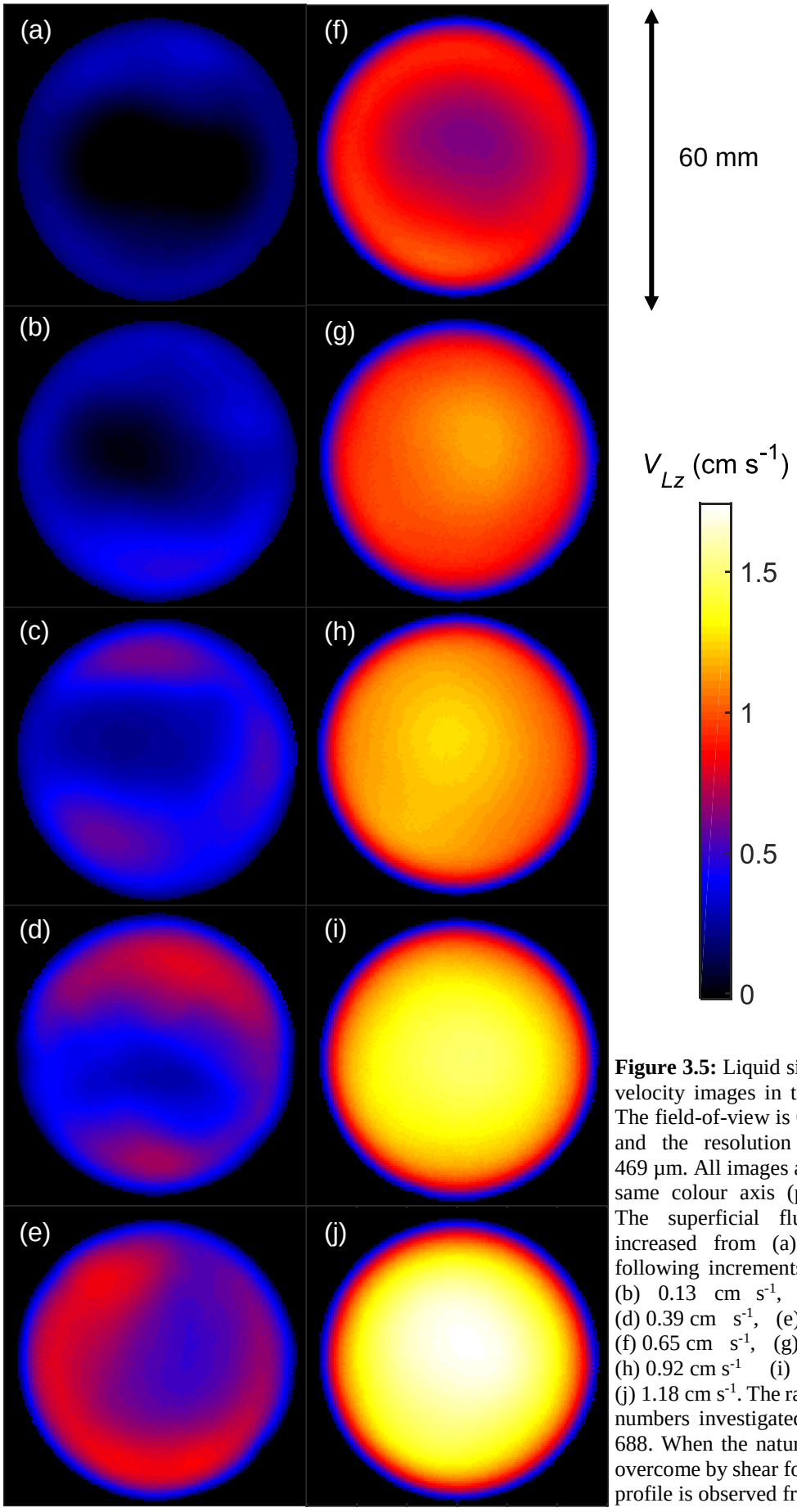

Figure 3.5: Liquid single-phase axial velocity images in the 52 mm tube. The field-of-view is 60 mm × 60 mm and the resolution is 469 µm × 469 µm. All images are shown on the same colour axis (pictured above). The superficial fluid velocity is increased from (a) to (j) in the following increments: (a) 0.0 cm s^{-1}, (b) 0.13 cm s^{-1}, (c) 0.26 cm s^{-1}, (d) 0.39 cm s^{-1}, (e) 0.52 cm s^{-1}, (f) 0.65 cm s^{-1}, (g) 0.79 cm s^{-1}, (h) 0.92 cm s^{-1} (i) 1.03 cm s^{-1}, (j) 1.18 cm s^{-1}. The range of Reynolds numbers investigated is therefore 0-688. When the natural convection is overcome by shear forces, a parabolic profile is observed from (g) to (j).

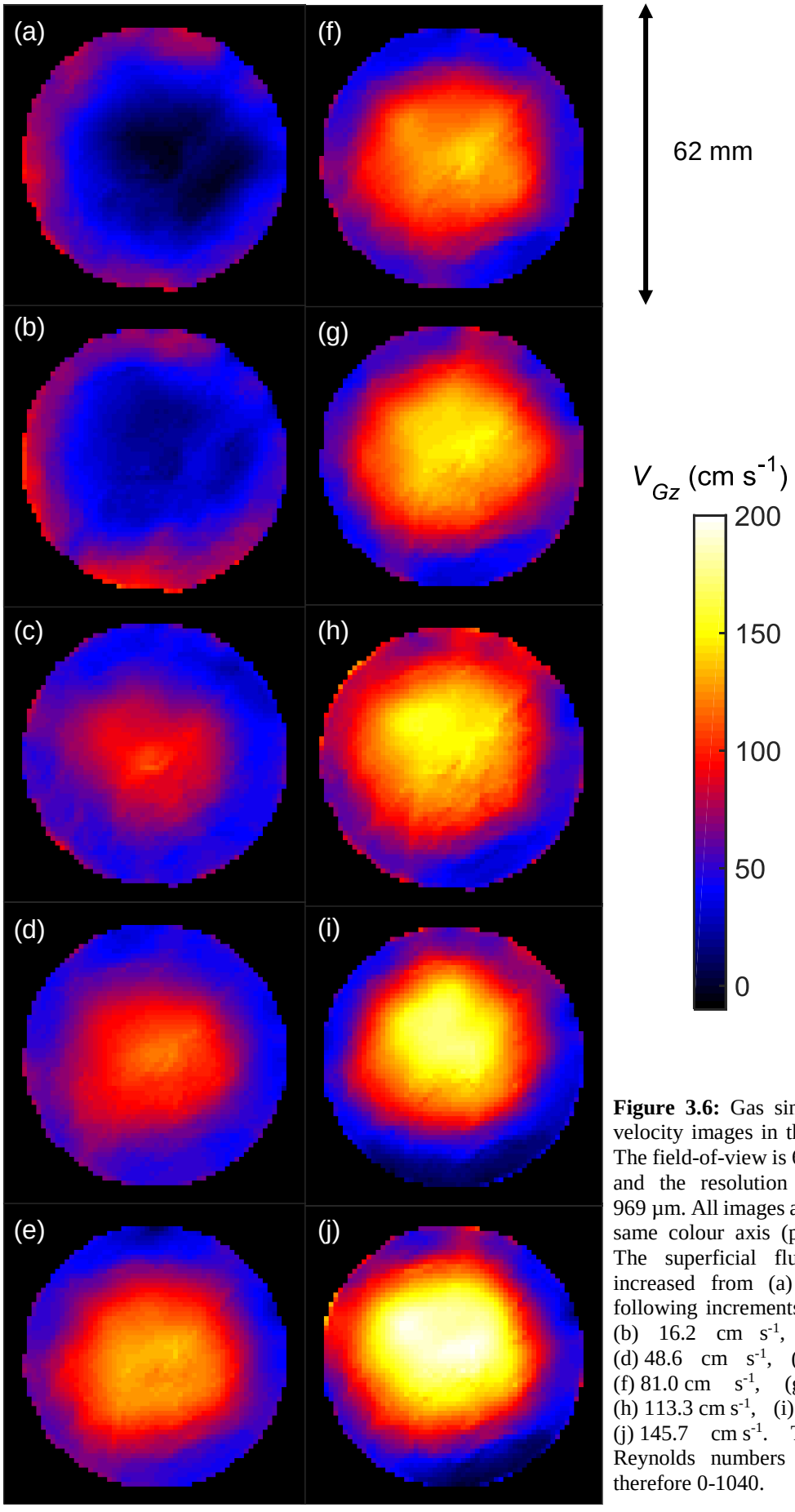

Figure 3.6: Gas single-phase axial velocity images in the 52 mm tube. The field-of-view is 62 mm × 62 mm and the resolution is 969 µm × 969 µm. All images are shown on the same colour axis (pictured above). The superficial fluid velocity is increased from (a) to (j) in the following increments: (a) 0.0 cm s^{-1}, (b) 16.2 cm s^{-1}, (c) 32.4 cm s^{-1}, (d) 48.6 cm s^{-1}, (e) 64.8 cm s^{-1}, (f) 81.0 cm s^{-1}, (g) 97.1 cm s^{-1}, (h) 113.3 cm s^{-1}, (i) 129.5 cm s^{-1}, (j) 145.7 cm s^{-1}. The range of Reynolds numbers investigated is therefore 0-1040.

measured by MRI and by the mass flow controller. This is similar for the gas (b) however slightly more variation is observed. The correlation coefficients and fitted linear calibration curves are shown on both figures. Both gradients are close to unity and correlation coefficient values are 0.99, indicating strong goodness of fit and agreement between measurements.

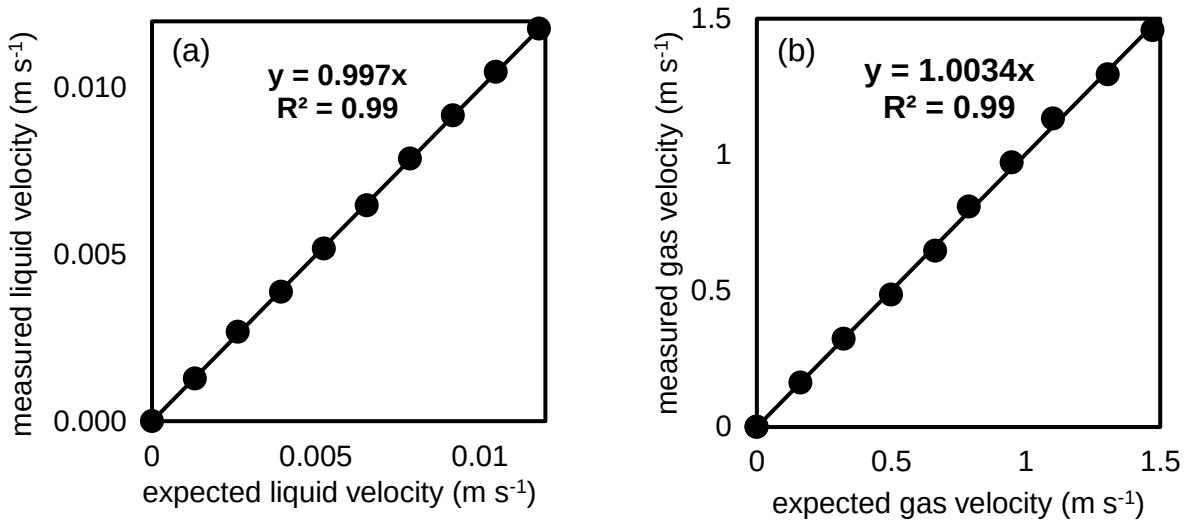

Figure 3.7: Calibration curves for the measurement of (a) liquid and (b) gas developed from averaged velocities determined from the images in Figures 1 and 2. The ordinate (measured) value is determined from the average velocity across the images and the abscissa (expected) value is determined from the mass flow controller measurements all in m s^{-1}. The line denotes the ideal $y = x$ relationship. The equations of fitted lines, together with the correlation coefficients are provided on the charts. Error bars denote the standard error at the 95% confidence level but are too small to be visible on this chart.

3.9.2. SINGLE-PHASE FLOW IN PACKED BED

For comparison with the images acquired under conditions of two-phase flow, the bed was packed with spherical non-porous particles and single-phase flow images were acquired at the same gas and liquid flow rates as used in the two-phase experiments. Figure 3.8 shows the intensity images for the gas and liquid phases in the packed bed under static conditions. The liquid data were acquired at a higher resolution in the frequency-encoding direction, as this had no additional time-cost associated with it. However, it was subsequently averaged in **k**-space to allow comparisons at the same spatial resolution as the gas images. This process is shown in Figure 3.8 (a) and (b) which shows the reduction in spatial resolution. The gas phase image is shown in Figure 3.8 (c). The images show a classical packed bed form, with regions of no signal intensity representing the packing particles randomly allocated within the bed area. The interstitial pore space is shown by the regions of increasing intensity. Both the gas and liquid display noteworthy depressions in signal intensity around one particle radius from the edge of the packed bed, which is associated with the wall effect in packed beds [30]. The gas image shows a slightly greater degree of spatial blurring than the liquid image, with areas associated

with particles not as clearly resolved as in the liquid image. Both images are shown here have the same fields-of-view of 60 mm × 60 mm.

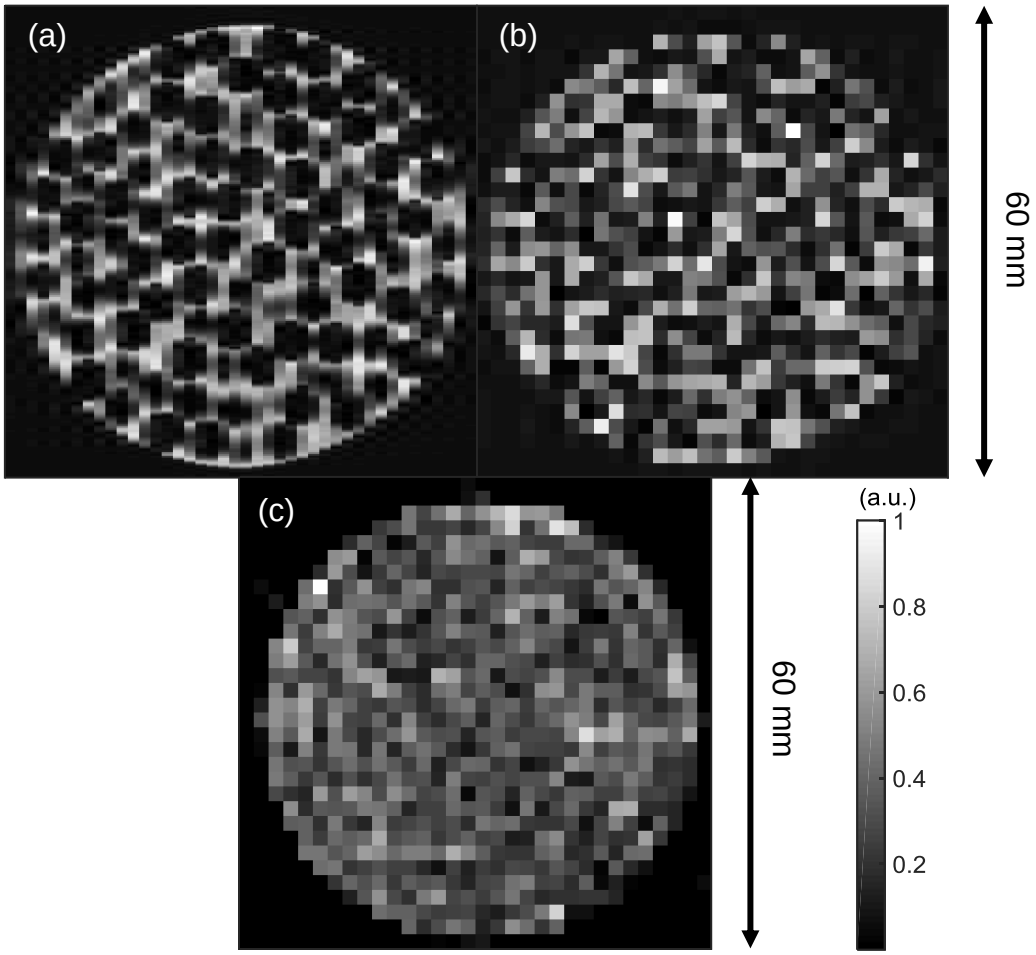

Figure 3.8: Single-phase static flow signal intensity images in the 52 mm packed bed filled with 5 mm glass spheres shown for liquid (a) and (b), and gas (c). (a) shows the liquid phase image at the acquired resolution, and (b) shows the same data at a lower sampled resolution shown for comparison with the gas-phase image in (c). All images are acquired with the same field-of-view of 60 mm × 60 mm. The colour bar indicates relative signal in (a.u.), with white showing the presence of signal.

The resulting single-phase velocity images for both phases are given in Figure 3.9. The liquid images are shown in Figure 3.9 (a) and (b) and the gas are shown in Figure 3.9 (c) and (d). The liquid and gas images are respectively shown on the same colour axis for the two flow rates studied. The liquid data exhibit a typical axial velocity flow field in a packed bed, with most flow in the bed near static for both flow rates. Isolated pores can be seen to have high flow in both cases, and both flow rates show a degree of backflow (in the downward direction). When the flow rate is doubled from (a) to (b) the additional volume is seen to increase the flow of pores which are responsible for above-average flow in (a). Some new high-flow pores are also seen to be created upon the addition of higher flow.

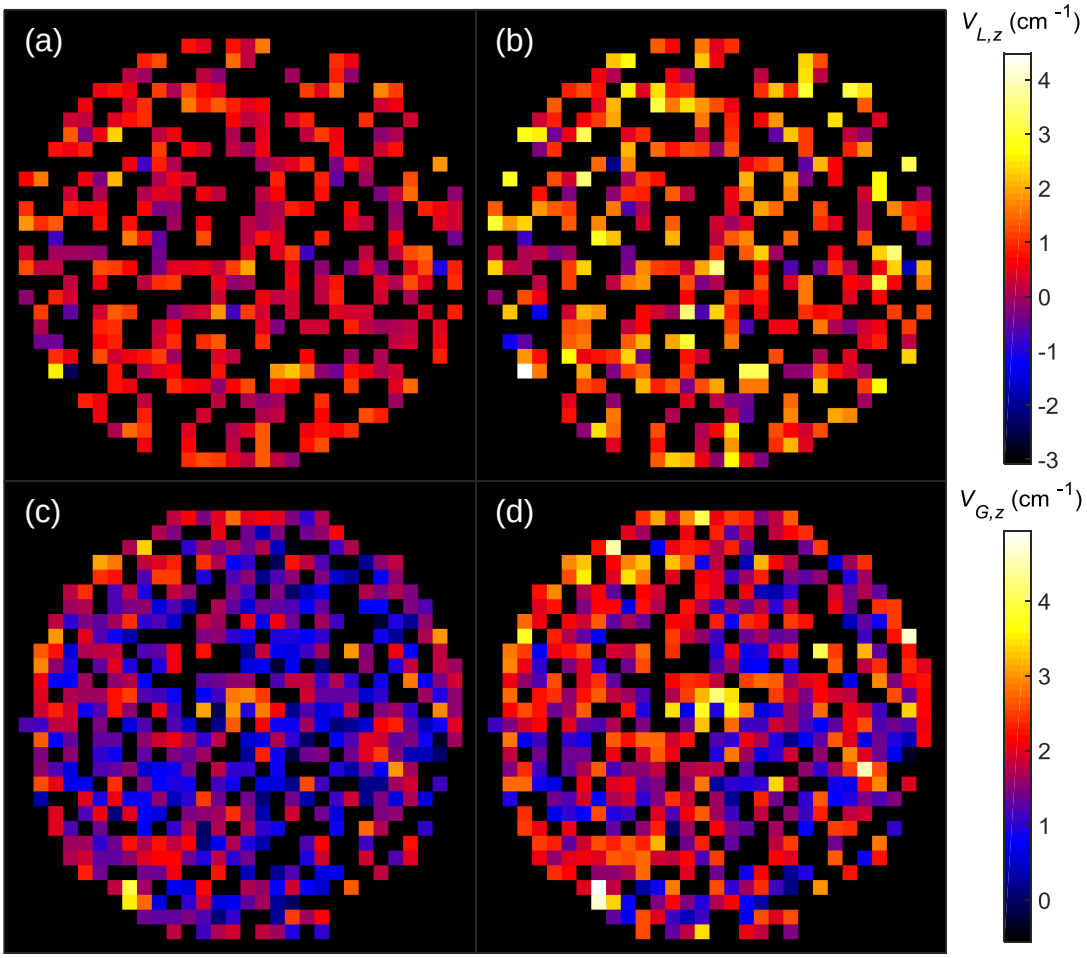

Figure 3.9: Single-phase axial velocity images in the 52 mm packed bed of the liquid phase (a) and (b), and gas phase (c) and (d). The field-of-view is 60 mm × 60 mm and the resolution is 1.875 mm × 1.875 mm. These images are used for comparison with the time averaged two-phase images and were acquired over the same time-averaged period of 2.5 hours each at superficial velocities of (a) 0.26 cm s^{-1}, (b) 0.52 cm s^{-1}, (c) 2.5 cm s^{-1} and (d) 5.0 cm s^{-1}. 5 mm spherical particles are identified as regions which lack signal in both sets of images.

For the gas images, the axial flow is seen to be more poorly spatially distributed than the liquid flow. Regions of high flow in (c) are seen to typically occur towards the outer edge of the bed, and most of the flow within the bed centre is near stationary. Some isolated pores which carry high flow rates are seen throughout the bed. Upon doubling the flow rate from (c) to (d), the additional flow is mostly carried by pores which are already carrying high flow rates. This is analogous to observations in the liquid phase, but to a higher degree. Most of the high flowing pores are seen towards the bed walls. In both images regions of back-flow are observed as in the liquid images. It is seen that at both flow rates tested, the gas field shows more spatial inhomogeneity in flow distribution than the liquid field.

3.9.3. INTENSITY PROFILES

1D intensity profiles acquired at regular time intervals were obtained to assess the stability of the flow fields and the extent of bubbling. These were acquired in all three orthogonal spatial directions. Figure 3.10 gives the series of 64 profiles in the (a) *z*-, (b) *x*- and (c) *y*-directions under conditions of stable single-phase liquid flow at U_L = 0.26 cm $^{-1}$. These are acquired as a control for the purposes of comparison with the two-phase cases. In each image the direction of time is from left to right, and thus fluctuations in this direction indicate temporal instabilities in the liquid flow field. In the vertical direction, the intensity of the signal is resolved in the direction of the profile as integrated in the corresponding directions, i.e. in the radial direction for (a) and the axial direction for (b) and (c). Fluctuations in intensity up and down in the image is therefore indicative of the presence of solid particles. All three images in the single-phase case display near total temporal stability with no fluctuations observed in the time direction.

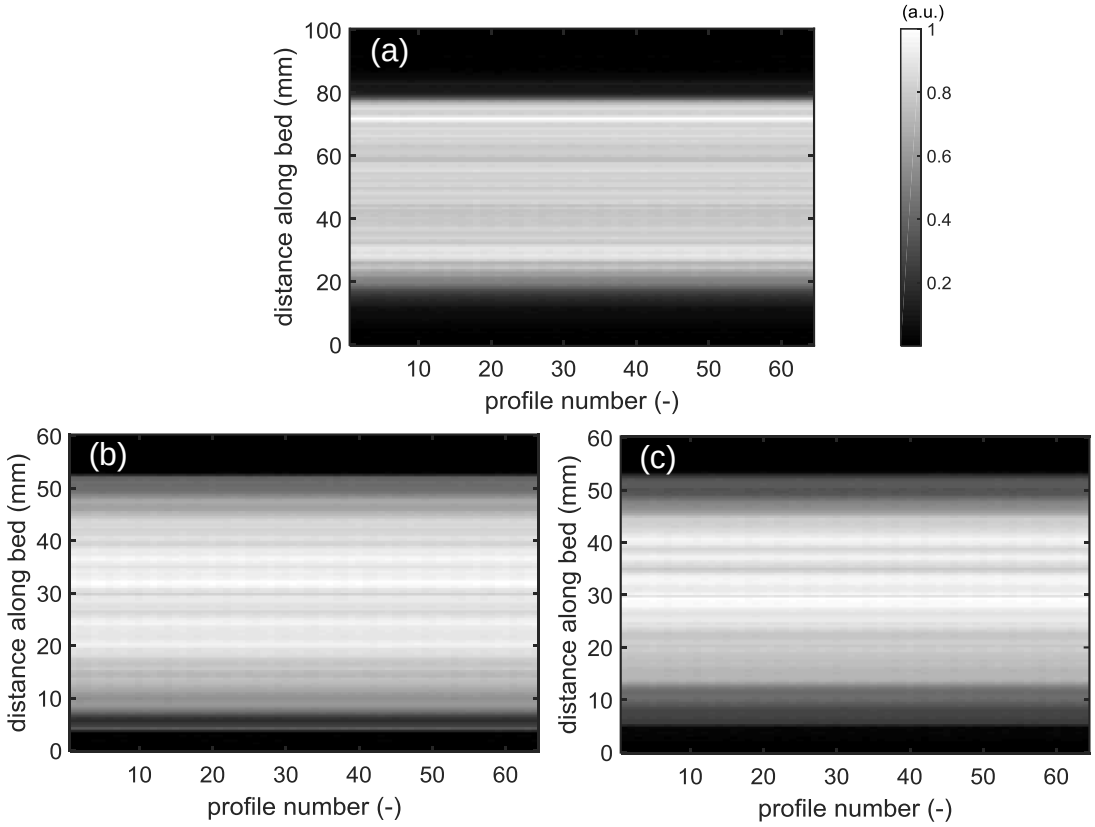

Figure 3.10: Series of 64 1D intensity profiles shown for each orthogonal direction (a) *z*, (b) *x* and (c) *y*. Profiles were acquired under conditions of constant stable liquid single-phase flow at a constant liquid superficial velocity of U_L = 0.26 cm s^{-1}. This is done for comparison with the two-phase flow cases. Each profile is acquired with a 5 ms delay. The presence of liquid is indicated by white, and the profiles display a "rippled" appearance due to the presence of particles. The colour bar indicates relative signal in (a.u.), with white showing the presence of signal.

The same experiments were run at conditions of two-phase flow for the experimental conditions given in Table 3.8. Only the full axial profile results are given in Figure 3.11, with a single set of radial *x*- and *y*-profiles shown in Figure 3.12. The profiles in Figure 3.11 and 3.12 show noteworthy differences from those in Figure 3.10, with clear fluctuations in the time directions (i.e. increasing profile number) visible for each experiment. For changing flow conditions however, the amount of fluctuation is different. For increases in gas flow at lower and constant liquid flow, the change from (a) to (b) shows an increase in the amount of gas present and amount of fluctuation. Diagonal streaks which may indicate regular bubble rise are faintly identified but are not sufficiently quantitative to calculate bubble rise velocities. As the liquid flow is increased from 0.26 cm s^{-1} to 0.52 cm s^{-1} as in the second row of images (c) and (d), it is observed that in general less fluctuation is present in the liquid field. In (c) particularly, which has the highest ratio of liquid-to-gas flow rate, less gas bubbling is observed when compared to (a) and (b). When the gas rate is again increased as in (d), a depression of the signal intensity associated with increased gas presence is observed. Less definitive evidence of bubbling (diagonal darkened streaks) is however observed. New channels of gas are seen to

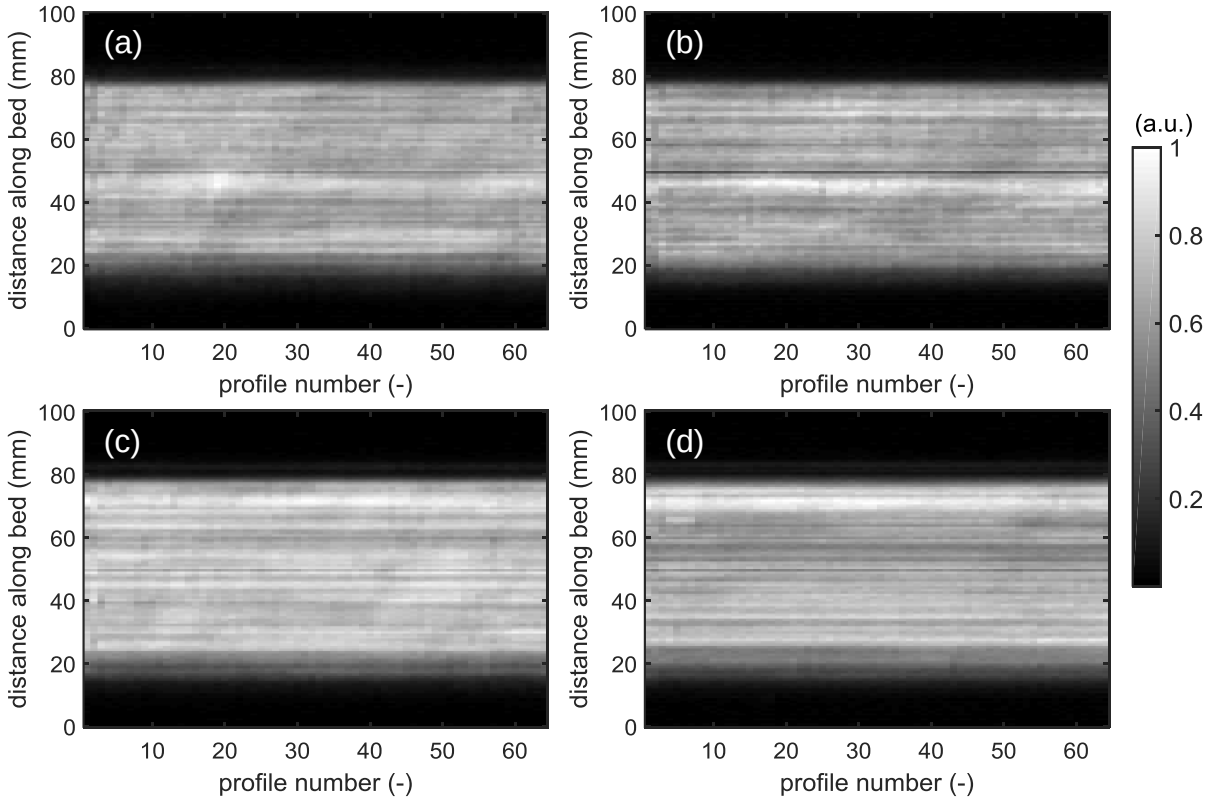

Figure 3.11: Series of vertical 1D intensity profiles for the liquid phase under changing conditions of two-phase flow in the 52 mm bed packed with 5 mm glass spheres. The liquid and gas superficial velocity values in each image are $[U_L, U_G]$ = (a) [0.26, 2.5] cm s^{-1} (b) [0.26, 5.0] cm s^{-1}, (c) [0.52, 2.5] cm s^{-1} (d) [0.52, 5.0] cm s^{-1}. Increasing amount of white indicates stronger signal, and thus a higher spatial concentration of the liquid phase. The colour bar indicates relative signal in (a.u.), with white showing the presence of signal.

emerge particularly in the top third of the imaging region. The two radial profile images in Figure 3.12 show similarly clear evidence of bubbling in the form of temporal instabilities at liquid and gas flows of U_L = 0.26 cm s^{-1} and U_G = 2.5 cm s^{-1}.

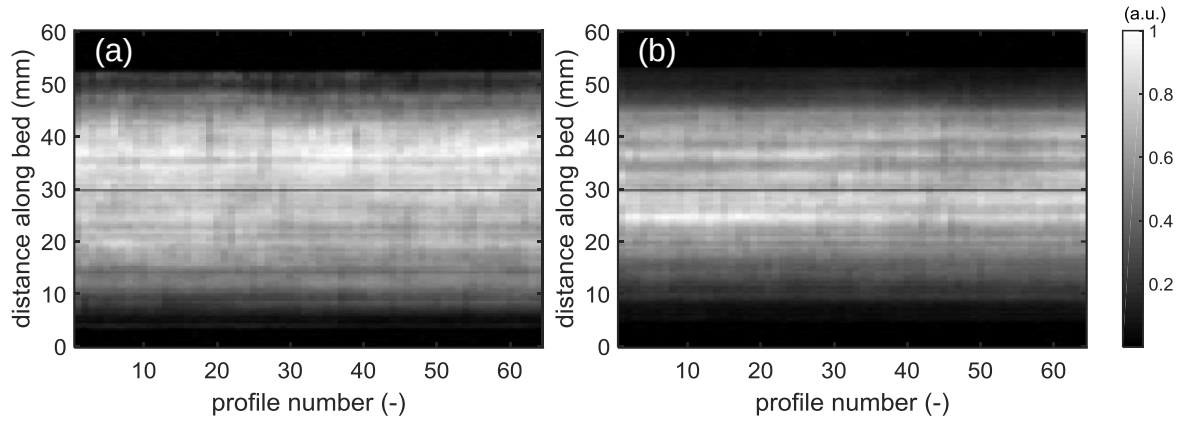

Figure 3.12: Series of horizontal (a) *x*- and (b) *y*-component 1D intensity profiles for the liquid phase under conditions of two-phase flow in the 52 mm bed packed with 5 mm glass spheres. The liquid and gas superficial velocity values in both images are [U_L, U_G] = [0.26, 2.5] cm s^{-1}. Increasing amount of white indicates stronger signal, and thus a higher spatial concentration of the liquid phase. Fluctuations in signal intensity are representative of bubbles passing through the imaging plane between the particles. The colour bar indicates relative signal in (a.u.), with white showing the presence of signal.

The standard deviation across time of each voxel can be summed to give a measure of the amount of fluctuation present because of bubbling. This metric is plotted for each orthogonal direction and flow rate, as a function of liquid flow rate in Figure 3.13. It has been normalised to the no-flow liquid phase data. For each direction, the standard deviation is greater during two-phase flow than single-phase flow, which manifests as a rise in all values from U_L = 0.0 cm s^{-1} to higher flows. It is also seen that for increases in liquid flow beyond zero, a reduction in the amount of fluctuation is observed. The only exception to this is in the *y*-direction, which remains roughly constant. Furthermore, it is seen that increasing the gas flow at a given liquid flow rate causes a reduction in the amount of measured temporal fluctuation.

3.9.4. LIQUID SATURATION AND PRESSURE DROP

The gravimetrically determined measurements of liquid saturation are given in Figure 3.14 and the total pressure drop is plotted for each two-phase flow value in Figure 3.15. For both measurements, an additional liquid velocity point at U_L = 0.13 cm s^{-1} was introduced for comparison with literature. The liquid saturation is given as a function of liquid flow rate for both gas flow rates studied. It is seen that liquid saturation increases for increasing liquid flow, but that the increase is non-linear and slows for higher liquid flows. This is especially true for the lower gas flow rate of U_G = 2.5 cm s^{-1}, where the liquid saturation increases minimally from U_L = 0.26 cm s^{-1} to U_L = 0.52 cm s^{-1} compared with the values at a gas flow of U_G =5.0 cm s^{-1}.

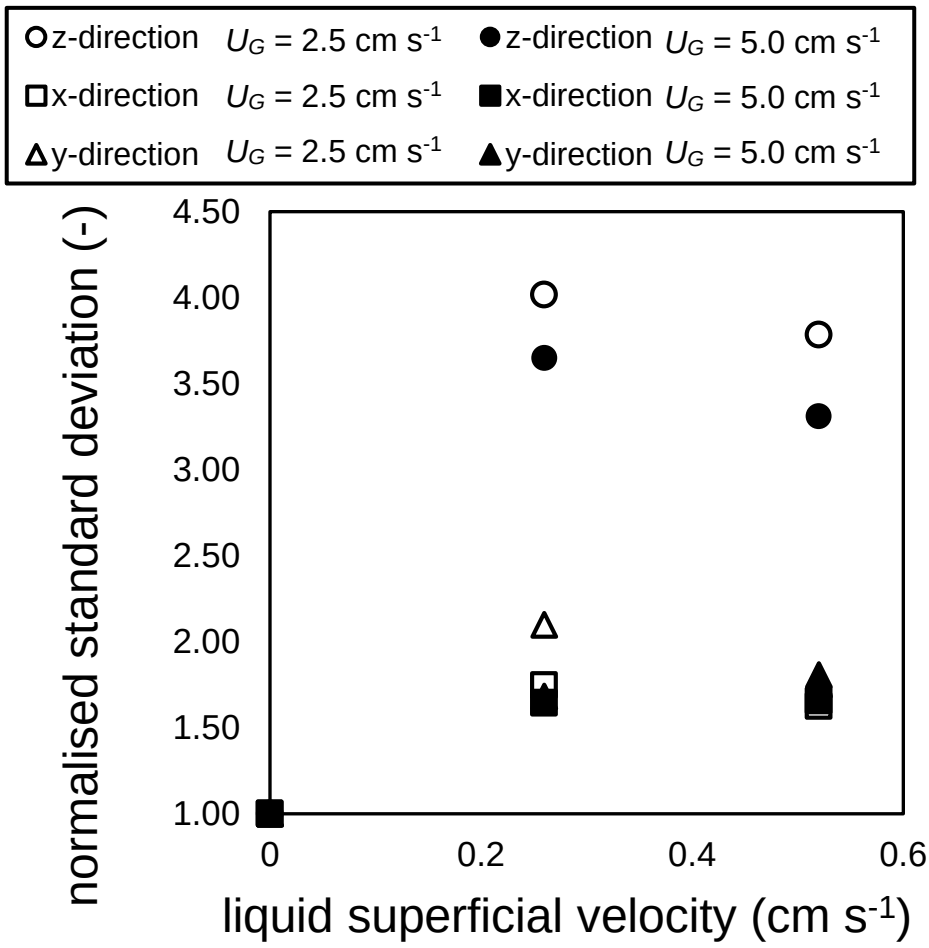

Figure 3.13: Normalised standard deviation of intensity profiles across time shown for each orthogonal direction [● *z*, ■ *x*, ▲ *y*] and for two constant gas superficial velocities of 2.5 cm s^{-1} (hollow shapes) and 5.0 cm s^{-1} (solid shapes) here shown as function of increasing liquid superficial velocity. The average standard deviation of each direction across time indicates the amount of fluctuation in time, which relates to how much the concentration of liquid in a spatial location is changing.

The two-phase total pressure drop is seen to increase with increasing liquid flow rate. It is also seen to increase with increasing gas flow rate at fixed values of the liquid flow. The increase in pressure drop is seen not to increase linearly with liquid flow rate and shows diminishing increases for higher values of the liquid flow. The amount of increase for increases in gas flow rate is seen to be approximately constant across the range of values studied.

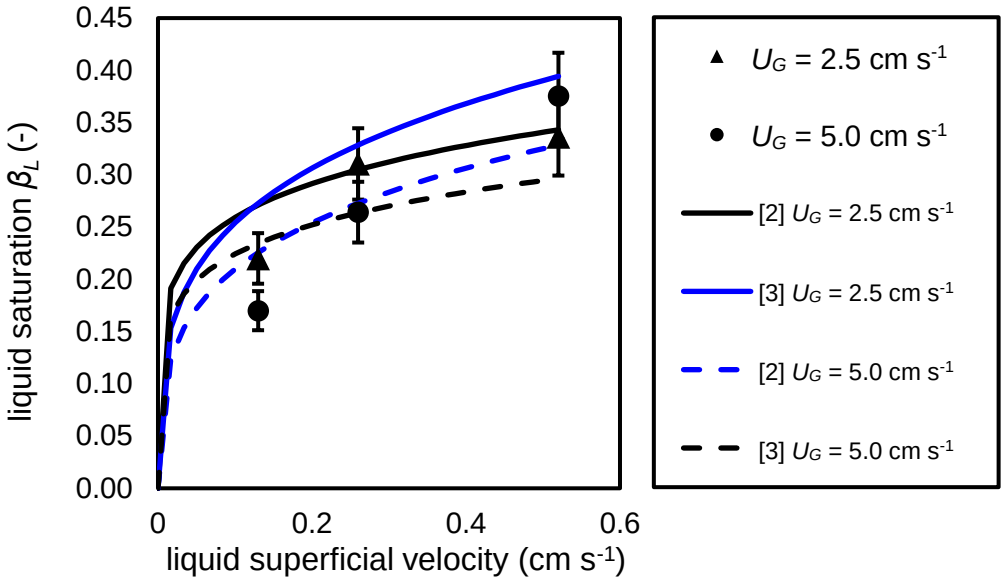

Figure 3.14: Fractional liquid saturation in the packed bed as measured by the drainage gravimetric technique. Saturation is shown as a function of the liquid superficial velocity for two constant gas superficial velocities, indicated using different shapes as per the legend on the axis. Error bars denote the standard error calculated at the 95% confidence limit. The lines show the saturation correlations by Fukushima and Kusaka [3] and by Turpin and Huntington [2].

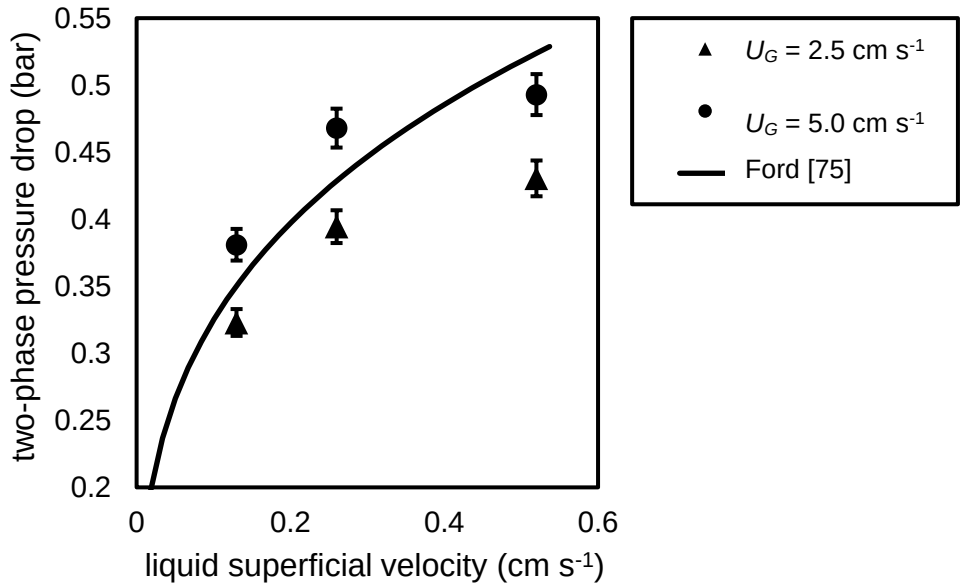

Figure 3.15: Two-phase pressure drop measured across the bed as a function of liquid superficial velocity for two constant gas superficial velocities, indicated using different shapes as per the legend on the axis. Error bars denote the standard error calculated at the 95% confidence limit. The solid black line shows the pressure drop correlation by Ford [75].

3.9.5. TWO-PHASE FLOW IMAGES

The two-phase flow signal intensity images are shown together with their single-phase flow images in Figure 3.16 for the liquid phase and Figure 3.17 for the gas phase. In Figure 3.16 the left-hand column is a constant liquid phase velocity of U_L = 0.26 cm s^{-1} and the righthand column is a constant liquid phase velocity of U_L = 0.52 cm s^{-1}. In Figure 3.17 the left-hand column is a constant gas phase velocity of U_G = 2.5 cm s^{-1} and the righthand column is a constant U_G = 5.0 cm s^{-1}. All images are shown on the same colour axis with limits set by the single-phase images. This layout enables easy visual comparisons to be made.

For the liquid phase during single-phase flow, increasing the flow rate has no effect on the intensity distribution. Introducing the gas dramatically reduces the overall intensity of the liquid phase. The liquid remains relatively evenly spatially distributed at a gas flow of U_G = 2.5 cm s^{-1} across the column, with a few pores showing higher liquid concentrations than others. These pores are seen to occur mostly just off the bed centroid, with one occurring near the bed walls. At a fixed gas flow rate, increasing the liquid flow to U_L = 0.52 cm s^{-1} does not drastically change the fluid distribution. Most of the liquid-rich pores from the lower gas rate are seen to remain liquid rich, except for those near the bed wall which are seen to have become leaner in liquid phase at the elevated gas rate. Signal is however recovered from most of the slice area, indicating that within the time averaging duration liquid was present in most of the interstitial pore space. At even higher gas rates, we see further reductions in the over intensity of the liquid phase maps.

At the gas rate of U_G = 5.0 cm s^{-1}, the lowest overall liquid intensity is recorded at the lower of the two liquid velocities U_L = 0.26 cm s^{-1}. This represents the largest ratio between gas and liquid flow rates, and consequently the liquid intensity across the bed is much lower than other flow rates imaged. A few pores of liquid-rich regions are still found, located mostly at the bed edges and their number and size greatly diminished. An increase to the higher liquid flow U_L = 5.0 cm s^{-1} sees some of the liquid in-slice holdup recover, and more liquid-rich pores appearing on the bed walls and towards the centre. Two pores in the bottom right quadrant grow to contain most of the signal. When (e) and (f) are compared, it is seen that increasing the gas flow at elevated liquid rates has less of an effect than at the lower liquid flow rate c.f. (b) and (c). The increase in gas velocity between (e) and (f) serves mainly to push the liquid rich pores towards the bed walls and reduce the number of liquid rich pores towards the bed centre.

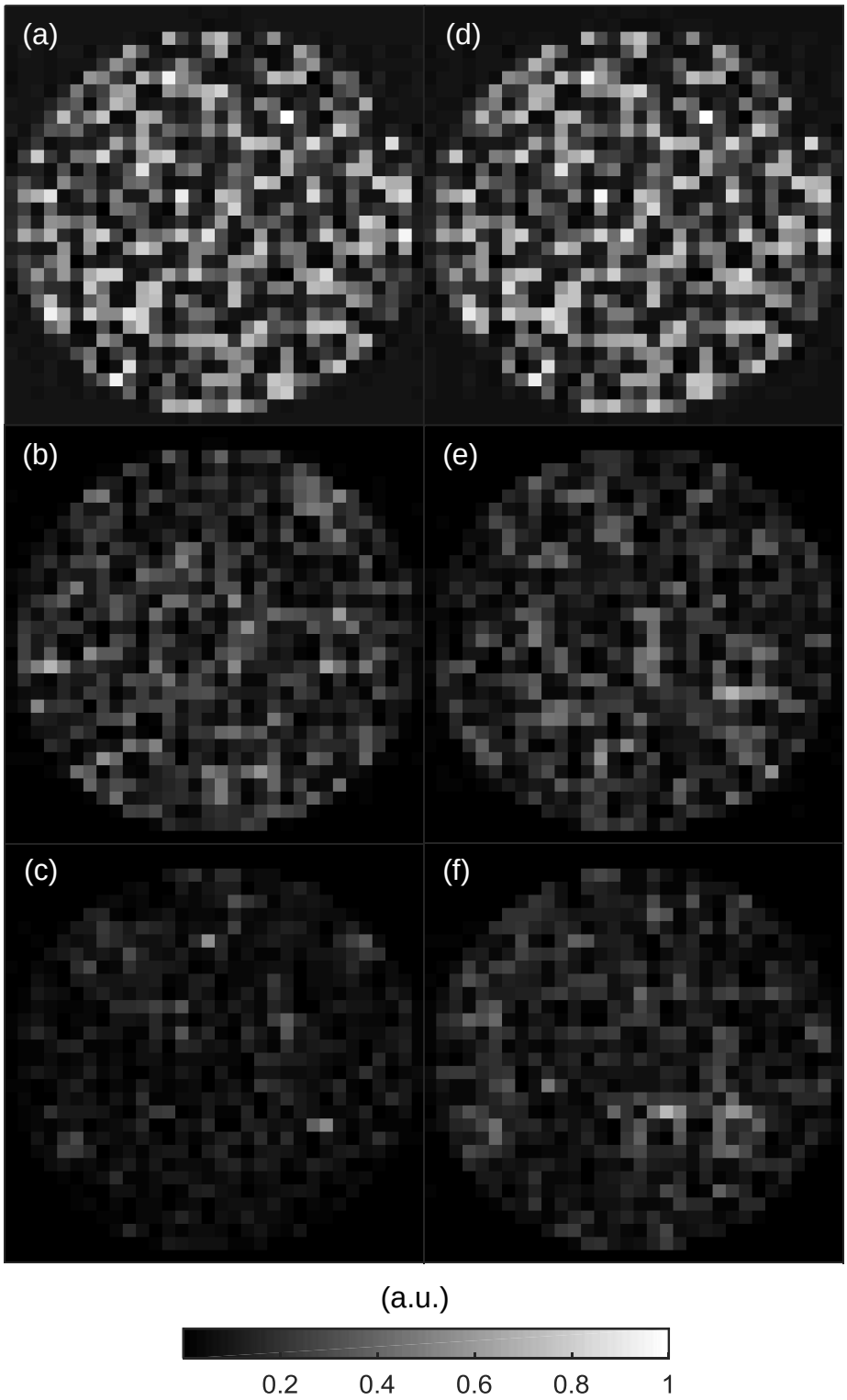

Figure 3.16: Liquid phase signal intensity images in the 52 mm packed bed filled with 5 mm glass spheres. The field-of-view is 60 mm × 60 mm and the resolution is 1.875 mm × 1.875 mm. The images are shown on the same grayscale colour scale, with increasing signal shown as increasing degree of white. The superficial fluid velocities in each image are as follows, $[U_L, U_G]$ = (a) [0.26, 0.0] cm s^{-1} (b) [0.26, 2.5] cm s^{-1}, (c) [0.26, 5.0] cm s^{-1} (d) [0.52, 0.0] cm s^{-1}, (e) [0.52, 2.5] cm s^{-1} (f) [0.52, 5.0] cm s^{-1}.

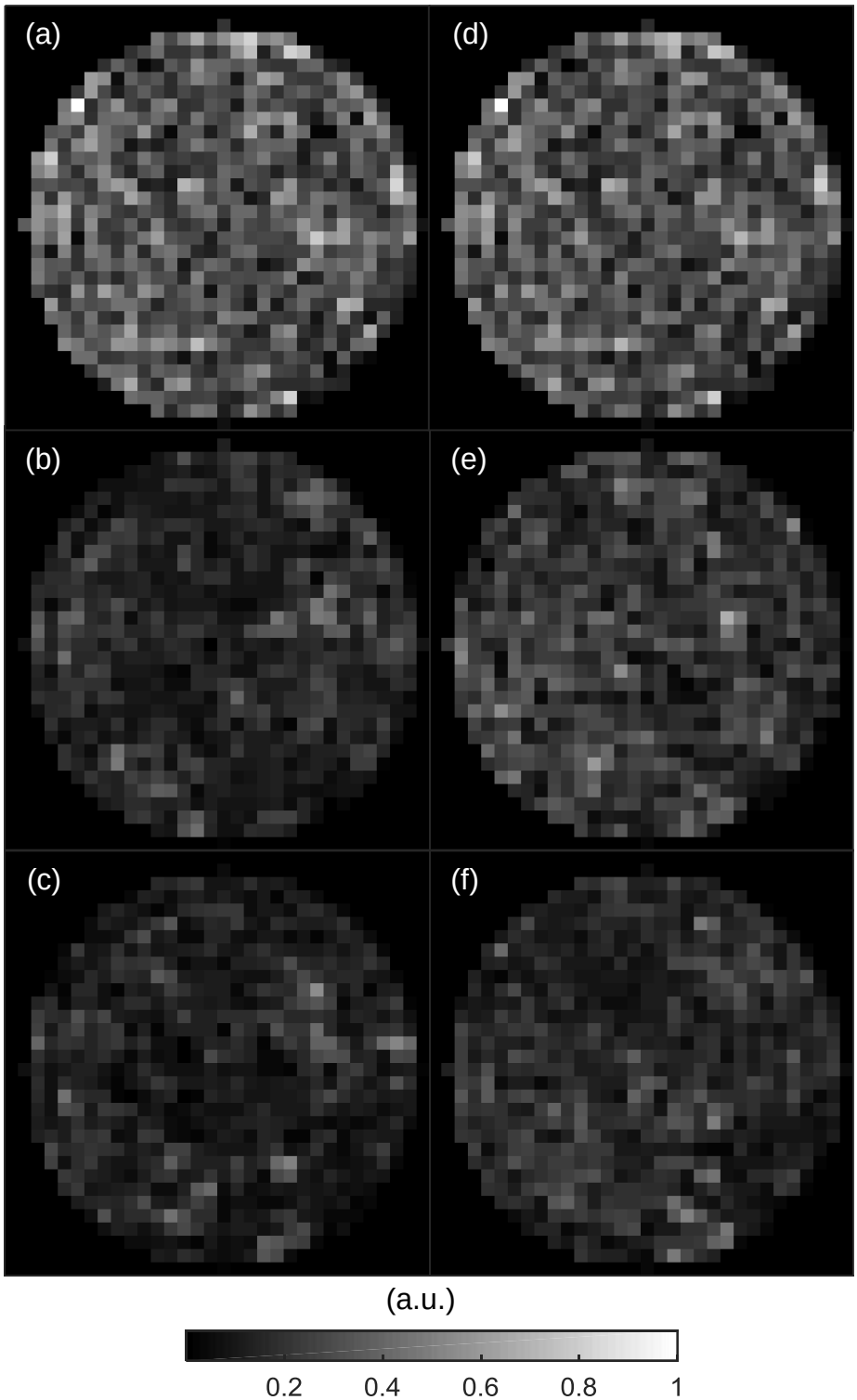

Figure 3.17: Gas phase signal intensity images in the 52 mm packed bed filled with 5 mm glass spheres. The field-of-view is 60 mm × 60 mm and the resolution is 1.875 mm × 1.875 mm. The images are shown on the same grayscale colour scale, with increasing signal shown as increasing degree of white. The superficial fluid velocities in each image are as follows, [U_L, U_G] = (a) [0.0, 2.5] cm s^{-1} (b) [0.26, 2.5] cm s^{-1}, (c) [0.52, 2.5] cm s^{-1} (d) [0.0, 5.0] cm s^{-1}, (e) [0.26, 5.0] cm s^{-1} (f) [0.52, 5.0] cm s^{-1}.

The gas intensities are plotted in the same way in Figure 3.17. No discernible difference is seen between the two single-phase flow images. Introducing the liquid phase causes a large depression in the overall signal intensity across the bed in (b) and (c). At the lower liquid flow rate of U_L = 0.26 cm s^{-1}, the gas is seen to exist relatively evenly distributed across the slice area, with a few isolated pores being gas-rich. Increasing the gas flow rate from (b) to (e) shows the concentration of gas in the bed increasing with increased flow. The intensity of gas within the bed area becomes slightly flatter with fewer clearly gas-rich pores shown. Increasing the liquid flow rate between (b) and (c) and between (e) and (f) shows relatively slight changes in the gas flow field. The lowest overall gas intensity is recorded for (c) which has the lowest gas flow to liquid flow ratio of the images. In this image, approximately seven isolated pores are seen to be gas-rich. Increasing the gas flow from (c) to (f) has the effect of evening out the flow field, which seems to diminish the number of clearly isolated gas-rich pores. Approximately four gas-rich pores in the lower right quadrant of the bed remain gas-rich under the elevated gas flow conditions in (f). Comparing increases in liquid flow between (e) and (f) at the elevated gas flow rate shows that liquid flow changes have less of an effect at elevated gas flow rates. The gas flow field remains very similar between (e) and (f), except for a region which becomes lean in gas towards the bed centre. Across all images it is however noted that gas signal is recorded within the total interstitial pore space available in the slice.

The intensities in the two-phase upflow images can be summed and compared between flow rates relative to the single-phase flow images. These data are plotted in Figure 3.18. Figure 3.18 (a) shows the liquid phase intensity as a function of the liquid flow rate and Figure 3.18 (b) shows the gas phase intensity as a function of the gas flow rate. These have been normalised to the single-phase flow images total intensity. For both the gas and the liquid, it is seen that upon the introduction of two-phase flow the total intensity is diminished. For the liquid phase at the lower gas rate of U_G = 2.5 cm s^{-1}, it is seen the total liquid intensity decreases slightly for increased liquid flow. This is however the exception, as for all other cases of liquid and gas, the total intensity shows an increase with increasing flow rate of the phase in question. This is seen for the elevated gas rate of U_G = 5.0 cm s^{-1} in which the total liquid intensity is seen to increase with increasing liquid rate. For fixed liquid flow, increasing the gas flow is associated with a reduction in the total liquid intensity in the slice. This effect is smaller at the higher liquid flow rate. In terms of the gas, for both liquid velocities studied the gas intensity shows an increase with increasing gas flow rate. For a fixed gas flow rate, the effect of increasing the

liquid flow is to decrease the total gas phase intensity. This effect is seen to be greater at the higher gas flow rate.

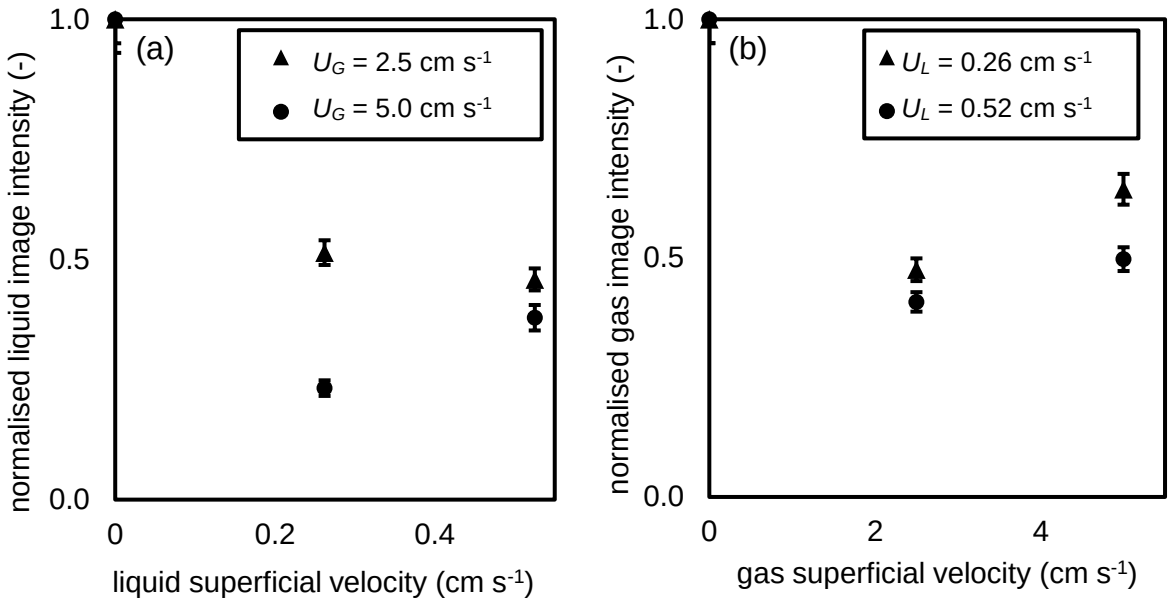

Figure 3.18: Comparison of the summed normalised signal intensity of (a) gas and (b) liquid images relative to the stationary intensity images. The data are shown as a function of increasing (a) liquid superficial velocity for the gas and (b) gas superficial velocity for the liquid. In (a) the two constant gas superficial velocities are [▲ U_G = 2.5 cm s^{-1}, ● U_G = 5.0 cm s^{-1}] and in (b) the two constant liquid superficial velocities are [▲ U_L = 0.26 cm s^{-1}, ● U_G = 0.52 cm s^{-1}]. Error bars show the standard error for each measurement expressed at the 95% confidence level.

The axial velocity maps for the gas and liquid phases under conditions of two-phase upflow in the packed bed are provided in Figure 3.19. The liquid and gas images are shown in adjacent columns, for each two-phase experiment. For both the gas and liquid phase maps, a similar form is seen whereby most of the area available for flow is found to be near static in the axial direction. This is interspersed with isolated pores which have much higher than average flow rates. This can be seen for the liquid image in (a) in which three notable pores show high flow. It is also noted that the velocity maps contain coherent signal from a large portion of the available area flow, indicating that no region in the bed is exclusively filled with either phase. The corresponding gas image in (b) is relatively flat. From (a) to (c) and from (b) to (d) the gas flow rate is increased from U_G = 2.5 cm s^{-1} to U_G = 5.0 cm s^{-1}. This change causes a reduction in the visible liquid signal in (c) and causes an increase in the signal from the gas phase in (d). The gas flow field undergoes a shift to show higher flow around the bed walls, with the central regions showing flow closer to zero. The liquid flow field in (c) shows fewer regions of reverse flow and of higher flow as the profile across the pores undergoes a slight flattening. Signal is particularly lost from the bed walls.

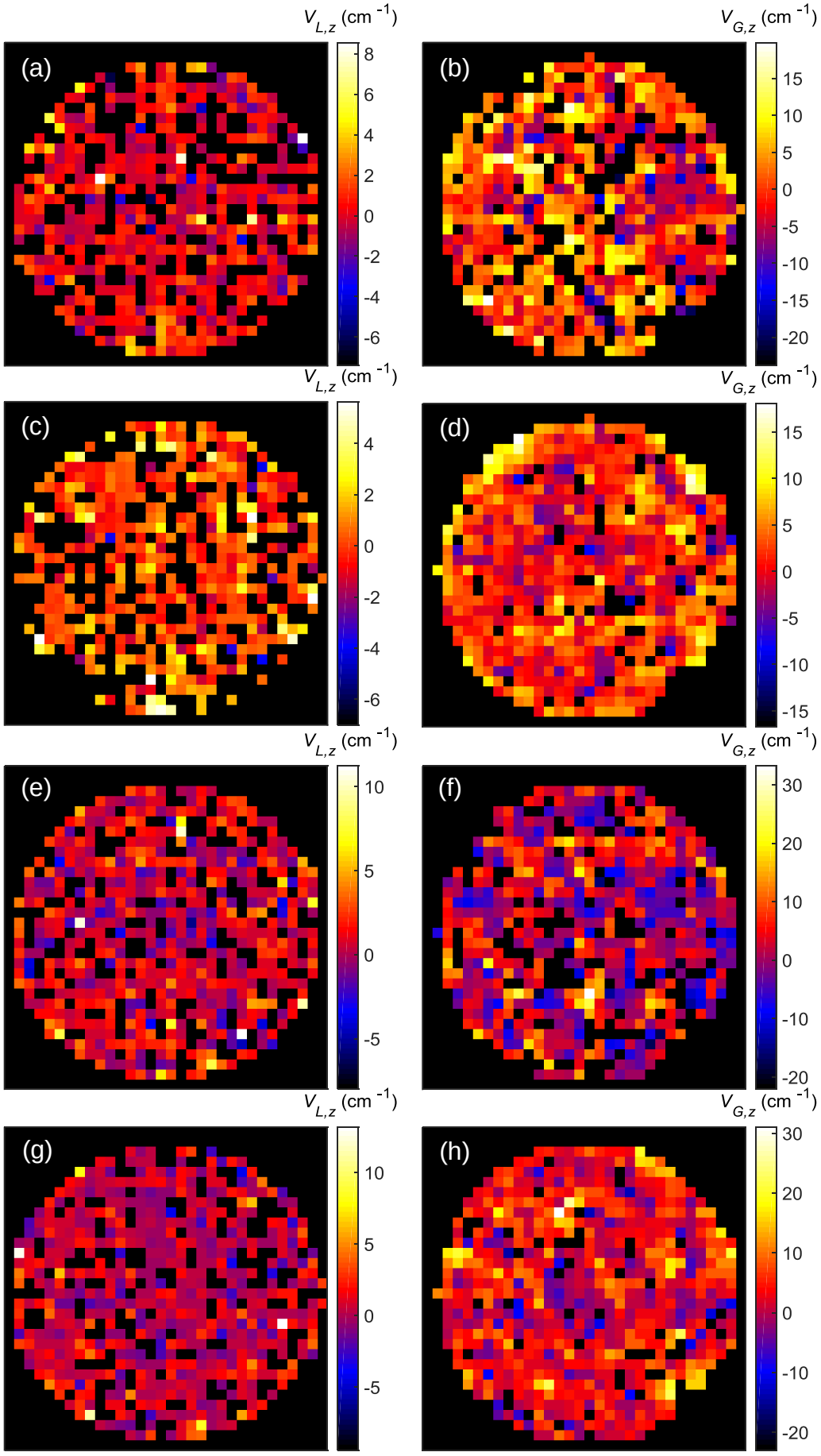

Figure 3.19: Time-averaged axial (vertical component) velocity images acquired under conditions of two-phase flow at various flow conditions for the liquid and gas phases in the packed bed. The liquid phase images are shown in the left-hand column (a), (c), (e) and (g) while the gas phase images are shown in the righthand column (b), (d), (f) and (h). Each image was acquired over a 2.5 hour period. The field-of-view is 60 mm × 60 mm and the resolution is 1.875 mm × 1.875 mm. The colour bar denotes the magnitude of the voxel velocity in cm s^{-1}. The superficial fluid velocities in each image are as follows, [U_L, U_G] = (a) and (b) [0.26, 2.5] cm s^{-1}, (c) and (d) [0.26, 5.0] cm s^{-1}, (e) and (f) [0.52, 2.5] cm s^{-1} and (g) and (h) [0.52, 5.0] cm s^{-1}.

Moving from (a) to (e) and from (b) to (f) sees an increase in the liquid velocity at fixed gas velocity from U_L = 0.26 cm s^{-1} to U_L = 0.52 cm s^{-1}. The overall area for liquid flow increases slightly, and the number of static voxels increases. A few isolated pores are seen to carry high flow rates. The gas field exhibits an increase in the amount of backflow and general spatial inhomogeneity with an increase in the number of isolated high-flow pores. The amount of static flow is also seen to increase in the gas field from (b) to (f). There is a corresponding reduction in gas signal for the increase in liquid flow observed between (b) and (f). The gas flow rate is increased at the elevated liquid flow rate between (e) and (g) and between (f) and (h). The liquid phase flow map is flattened out by this increase, with fewer regions in (g) of notably high flow or backflow compared to (e). The area available for liquid flow is not substantially changed by the gas flow rate increase. The gas phase area undergoes an increase between (f) and (h). The field becomes flatter, with fewer regions of near-static flow and fewer high-flow pores. Pores exhibiting definite back-flow are also reduced in number in (h) compared to (f). Regions of high flow drift closer to the bed walls, as was observed between (b) and (d).

Comparing (c) with (g), and (d) with (h) allows a comparison to be made at the elevated constant gas flow rate of U_G = 5.0 cm s^{-1} and an increase in the liquid flow rate from U_L = 0.26 cm s^{-1} and U_L = 0.52 cm s^{-1}. The liquid flow area is seen to substantially increase between (c) and (g), however more static regions are observed. The number of high flowing pores also increases slightly. The gas flow area does not undergo substantial change. The regions of high gas flow nearer the bed walls in (d) are seen to diminish slightly, leaving only a few isolated pores near the bed walls carrying high flow in (h). More regions of backflow in the gas field are observed in (h) when compared to (d). It is noted that more dramatic changes in the gas flow field are observed for changes in either macroscopic flow rate. The liquid phase remains comparatively stable, with the main changes involving the number of high-flowing pores and backflow regions.

3.9.6. TIME AVERAGED VELOCITY DISTRIBUTIONS

The data from the two-phase velocity images can be plotted as a probability distribution which helps gain insight into the overall statistical nature of the flow field and its response to flow rate changes. In Figure 3.20 the probability distributions of the axial flow fields are given for the (a) liquid phase and (b) gas phase. The distributions are also compared to those for single-phase flow at the same experimental flow rates for each phase. The liquid phase distributions in (a) show the classic form for liquid flow in a packed bed, with a large peak near to zero, a

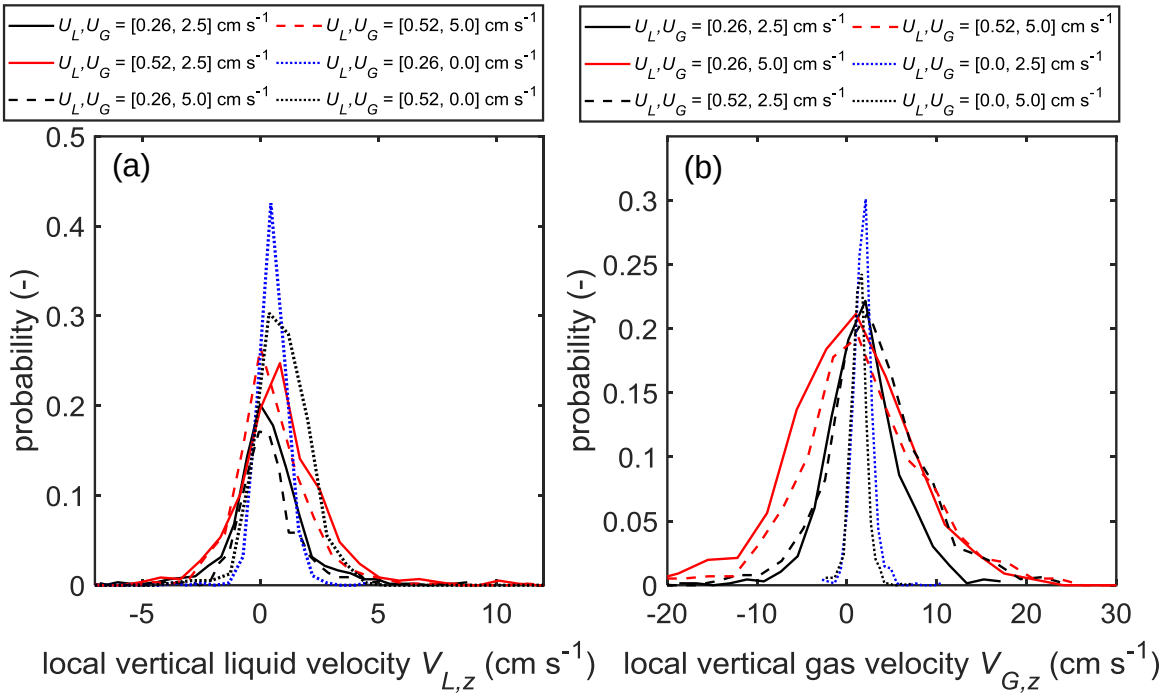

Figure 3.20: Distribution of axial (a) liquid and (b) gas local velocity as a function of changing two-phase flow conditions in the packed bed. The data are shown in both axes as a function of changing liquid and gas superficial velocity, with the solid lines denoting the lowest flow conditions of the corresponding phase, the dashed lines indicating elevated flow of the corresponding phase and the dotted lines indicate the single-phase flow velocity distributions for each phase. Changes in the flow conditions of the phase which is plotted are shown by changing line colour, which are indicated on the axis legend above the axes.

small negative tail indicative of backflow and a long positive tail. The largest static peaks are found for the single-phase distributions. In general, the liquid distribution becomes broader for increased liquid flow rates. This is seen for both the single and two-phase cases. They are relatively insensitive to increases in gas flow rate however. For increasing gas flow rate at both liquid rates, the distributions narrow slightly and the amount of zero flow is reduced. The shape of the tails in all two-flow cases does not differ substantially from the single-phase distributions. The most noteworthy change seen when introducing the gas flow is to substantially reduce the probability of zero flow within the slice.

For the gas distributions, a substantial change is seen when going from single-phase flow to two-phase flow. The distributions become much broader, indicating a much greater degree of both backflow and high upward velocities. The shape of the distributions is also markedly different, with those recorded during two-phase flow being much more symmetric around zero indicating substantial backflow in the gas field. The single-phase examples have much smaller negative tails. Changing gas flow rate has a much larger effect on the gas distributions than changes in the liquid flow rate. Doubling the gas flow rate causes the distribution to broaden substantially for both liquid flow rates investigated. Increasing the liquid flow causes the gas

distributions to broaden slightly and for negative and static flow in the gas phase to diminish slightly. The shape of the positive tails remains relatively consistent within the two-phase flow experiments and is insensitive to changes in both gas and liquid flow.

3.10. DISCUSSION

3.10.1. SINGLE-PHASE FLOW IN TUBE

The intensity images of the single-phase flow in the empty 52 mm tube are as expected. In terms of typical equipment sizing for MRI experiments, a tube of 52 mm inner diameter is relatively large and occupies approximately 85% of the diameter of the imaging r.f. coil. Most MRI experiments on tube flow are conducted in tubes around half the diameter, which allows the active imaging region to be shimmed a lot more precisely. Despite this, the imaging region in Figure 3.4 shows a good shim, with more of the 3 mm slice showing a very flat profile. The most noteworthy deviations in the flat profile occur as periodic oscillations in intensity when approaching the tube walls in both the liquid and gas image. The geometric regularity of these is indicative of B_1 magnetic effects, as the birdcage-type coil has capacitor pylons spaced at intervals exactly mirroring the artefacts seen in the image. These cause localised variations in the excitation and polarisation of nuclei in their mediate vicinity, causing some regions to appear higher in intensity and others to show diminished intensity. Attempts were made to wedge the tube centrally to minimise these distortions, although even in the low signal regions the signal-to-noise ratio is sufficient that binary gating still allows a mask to be confidently constructed at the minimum gating level.

The flow images were acquired 80 cm from the tube inlet at the bottom. In Figure 3.5 it is seen that significant free convection exists within the tube under conditions of static flow. This is also a function of the size of the tube, as the total volume of the 2 m long tube is sufficient that density gradients owing to the different temperatures across the tube length cause flow to occur. The bore of the magnet is much cooler than the tube ends due to cryogenic cooling, and it is therefore unsurprising that natural convection behaviour is observed. The net flow in Figure 3.5 (a) is still however zero. When the flow is started, it adds initially to the region around the bed centre in an annulus shape and the convection is only fully overcome by the shear forces at image (g) with images before this showing a lowered velocity towards the centre of the bed. Flow begins to take on a developed profile from image (g) onwards, approaching the classical parabolic form of Poiseuille flow. The region of near-static flow at the tube walls remains relatively consistent in size of around 1.8 mm in thickness. The flow field is radially symmetric,

with only slight variations in the location of the maximum flow observed. The profile is also not purely parabolic, deviating in being slightly flatter towards the centre. This is probably due to irregularities in the tube and inlet/outlet structure, and the finite entry-length for the tube.

The gas images in Figure 3.6 behave very similarly, albeit they cover a range of much higher Reynolds numbers. Free convection is seen in the same direction as the liquid, which is also overcome by the shear forces of the fluid as the flow rate is gradually increased. The profile appears approximately parabolic, which is surprising as the Reynolds number ranges between 0 and 320,000 in (j). At such high Reynolds numbers high turbulent flow would be expected, with a much flatter velocity profile. The velocity could not unfortunately be tested beyond this Reynolds number due to equipment limitations.

Despite large variations in the shape of the flow profiles for both liquid and gas, and in the local velocities, the average velocity in the slice agrees very well with values for the superficial velocity expected from mass flow controller measurements. These are shown for each image in Figure 3.7. Both the liquid and the gas calibration lines have correlation coefficients of 0.99, indicating strong linear correlation as described by the fitted lines. The liquid velocities are slightly overpredicted by the mass flow controller, and the gas velocities are slightly underpredicted. Nevertheless, this is very good quantitative agreement, and confidence can be placed in the MR velocimetry techniques used in this thesis.

3.10.2. SINGLE-PHASE FLOW IN PACKED BED

The packed bed static intensity images show the signal from the interpore space is as expected. Although the same outer tube was used as in the tube flow experiments, the peripheral fluctuations due to the B_1 r.f. coil are no longer visible in the packed bed, due both to a reduction in the amount of signal present and a reduction in the image resolution. The spatial resolution of the liquid image is reduced from the acquired image in the frequency encoding direction to allow a more direct comparison with the liquid phase results. In Figure 3.8 (b) the particle phase is discernible by the dark regions within the tube area. The same can be seen in the gas phase in (c) however the borders of the particle phase are not as well resolved as in the liquid. This is due to a combination of lower signal-to-noise in the gas images, and the use of under-sampled compressed sensing MRI at the current spatial resolution. If however the binary gating level is consistently chosen, it will ensure that only regions containing gas signal are included in the velocity images. The gas image does however clearly show a ring of lowered signal

intensity occurring approximately 1 particle radius (2.5 mm) from the bed wall, consistent with models of beds randomly packed with spheres.

The axial flow images for both phases show the expected profiles in the interpore space. Local maxima in the liquid flow fields in Figure 3.9 (a) and (b) generally occur where the local hydraulic radius is at a maximum, i.e. in the centre of pores. For both flow rates in (a) and (b), most of the flow in the slice is near stationary. Some regions of backflow are observed, with a few pores carrying high axial flow. This sort of profile is well documented in liquid phase flow through packed beds [73,74]. No spatial region of the bed is necessarily preferred for higher flow when increasing the flow between (a) and (b), the additional flow is distributed by additional high flow pores which emerge evenly across the bed surface. This behaviour is also typical of packed bed single flow experiments.

The gas phase images Figure 3.9 (c) and (d) show more spatial inhomogeneity than the liquid images. It is clear in (c) that regions of higher flow for the gas prefer locations nearer the bed walls. This is an expression of the wall effect, in which higher flow is found towards the bed walls due to a reduction in the local void fraction towards the bed wall. The effect is more clearly observed in the gas phase due to its mobility properties compared to the liquid. Due to this uneven distribution of flow, most of the central area in (c) is near static in flow. Raising the flow rate from (c) to (d) has the clear effect of raising the velocity of high-flowing pores around the bed walls, as well as creating several more high-flowing pores towards the bed centre. More anisotropy in the axial flow is observed for the gas compared to the liquid, although it is seen that more of the bed has positive flow at the elevated gas rate in (d).

3.10.3. INTENSITY PROFILES

The intensity profile images give insight into the temporal fluctuation of the liquid phase and thus insights also into the mobility of the gas phase. Image (a) in Figure 3.10 should occur within the pseudo-spray flow regime by the correlations of Fukushima and Kusaka [3]. The other images are all well within the pulsing flow regime. Temporal fluctuations associated with the passage of gas are easily seen in all the two-phase flow examples as compared to the control images under single-phase flow. In all examples, faint diagonals which are associated with rising bubbles can be identified. These are not quantified here as determinations of bubble rise velocity are better using slice-selective 1D vertical profile. A slice-selective profile removes the ambiguous contributions to the signal imparted by bubbles rising at differential speeds at various radial positions in the bed. These contributions cannot be isolated in the current

experiments as the signal is radially-integrated. A more robust 1D profile technique for quantifying bubble rise has been implemented by Collins [61].

It would be difficult to claim visual difference suggesting a regime transition, but in principle this technique could be used, together with measures of the fluctuation such as the total temporal standard deviation, to determine flow regime change borders between more distinct flow regimes than the pseudospray-to-pulsing regime which is a subtle transition. (a) and (b) show a larger number of passing bubbles, indicated by more frequent signal depressions than (c) and (d). Images (c) and (d) are acquired at an elevated liquid flow rate, which causes an increase in the liquid saturation which explains the suppression of visible gas bubbles observed. The image in (d) is possibly demonstrative of the spray flow regime, in which the liquid phase exists mainly as entrained droplets as no periodic behaviour and less fluctuation is observed at the highest mutual values of liquid and gas flow rate. The *x*- and *y*-direction show bubbles as interspersed signal depressions, which are seen to occur in both radial directions with an isotropic distribution, i.e. there is no one region in the radial direction which shows a bias of bubbling behaviour – which would appear as a line of oscillating intensity. Instead the intensity is shown to randomly fluctuate across the bed diameter in time.

The total temporal standard deviation almost universally decreases for increases in both the gas and liquid flow rate, indicating that the passage of bubbles is difficult to discern, and the pore flow becomes more regular in time. This could be due to the approaching of spray flow, which would mean large bubbles did not periodically pass through liquid saturated pores as is typically assumed. One exception is the *y*-direction standard deviation which stays roughly constant with increased liquid flow. Similarly, the *x*-direction only decreases slightly compared with the axial profiles, and it is thus suggested to use the axial direction for determining flow regime changes based on temporal signal fluctuations. More dramatic changes in the 1D profiles and temporal standard deviations are expected between the true bubbling and the pulsing regimes. If slice-selective profiles are used, it eliminates the spatial integration of signal in corresponding directions and thus individual bubbles may be tracked and measured. It is however confidently reported that evidence of gas passage through the porous network is identifiable, and that both quantitative and qualitative variation in the intensity profiles can be related to bed two-phase flow behaviour.

3.10.4. LIQUID SATURATION AND PRESSURE DROP

The liquid saturation data are compared to the correlations by Fukushima and Kusaka [3] and Turpin and Huntington [2]. The data are compared for both gas flow rates. The correlation in the study by Turpin and Huntington tends to predict higher saturation values, which may be due to their use of slightly larger columns and d_p/d_t ratios closer to the present study. Their correlation shows better agreement with the data from this study than the correlation by Fukushima and Kusaka [3] which tended to under predict the liquid saturation. Both correlations show very similar qualitative behaviour with each other and the data acquired in the present study. Agreement is generally good, except for the data recorded at the lowest liquid flow of U_L = 0.13 cm s^{-1}, which has predicted values from both correlations for both gas flows higher than recorded.

The correlations are both within their stipulated range of Reynolds numbers for the gas and liquid flow, however the studies were conducted at a pressure of under 2.5 bara in the case of Turpin and Huntington, and atmospheric pressure in the case of Fukushima and Kusaka [3]. Both additionally used the air-water system as a test system, with air having significantly different fluid properties than pressurised SF_6 so the comparison is made cautiously. Despite this, and acknowledging the typical accuracy limits of correlations, agreement between the recorded data and both correlations is good. It is suggested that agreement is better in the case of Turpin and Huntington because of their use of a d_p/d_t much closer to the present study and a higher-than-atmospheric operating pressure. Other correlations were compared, which showed not to predict the observed levels of variation in saturation seen here. As they were also developed using the atmospheric air-water system, across the range of velocities they predicted nearly constant saturation values of ~ 0.31 which is adequate for first-pass design.

The two-phase total pressure drop measurements obtained from pressure taps at the top and bottom of the bed are compared to the pressure drop correlation by Ford [75]. Only a single curve for the lower gas flow of 2.5 cm s^{-1} as the curve for 5 cm s^{-1} significantly over predicted the pressure drop. This was the general trend of other correlations compared, which all over-predicted the pressure drop substantially. The agreement between the curve plotted and the data are reasonable, showing the same qualitative relationship. Comparisons are again drawn cautiously, as nearly all classical correlations for pressure drop were developed on atmospheric air-water systems using narrow column diameters, and the dynamics of the present system are significantly different from such basic systems. The lower pressure drop recorded here is

attributed to the d_p/d_t ratio of 5/52 being generally smaller than those used to determine classical correlations. Additionally, elevated operating pressure may lead to less energy dissipation in the bed by either causing lower liquid saturation values (as seen in Figure 3.14) or by causing enhanced wetting of the solid surfaces, thus reducing overall drag for the gas phase and potentially leading to enhanced passage of the gas and liquid phases through energetically favourable channels. This enhanced wetting due to increased pressure has been observed in trickle flow in this Thesis in Chapter 5.

3.10.5. TWO-PHASE FLOW IMAGES

The interpretation of the phase intensity images requires consideration of the process of time averaging in MRI. Regions of stronger intensity in Figure 3.16 indicate that liquid spent more time in those regions over the 2.5 h imaging period, as signal was acquired in that location for more of the individual scans – contributing more to the numerical average of the signal. Similarly, regions which show little-to-no signal in the interstitial space do not indicate that liquid does not reside in the regions during operation, merely that it is less likely to find liquid there. Imaging over a long time period enables us to capture a broad picture of the phase distributions, and the images are better interpreted as probability maps of the likelihood of finding liquid in voxels which show stronger signal over the time window of operation.

Unsurprisingly therefore the single-phase maps show an almost identical distribution. Liquid is found throughout the interstitial space in the slice, with regions of lower signal occurring perhaps over the top of particles which have edges just outside of the imaging slice. Introducing the gas phase naturally causes a reduction in the overall intensity as there is less geometric area available for the liquid to flow. In this flow regime, flow should predominantly exist as two-phase within each pore, either as pulsing regions of gas and liquid or as spray flow. Figure 3.16 (b) is in the pseudo-spray regime and shows pores which are identifiably liquid-rich throughout the bed area. The other images all exist within the pulse regime. Fewer liquid-rich pores are seen when increasing the liquid flow rate between (b) and (e) which is suggestive of a regime change to pores which are more representative of pulsing. The leanest liquid concentration is recorded in image (c) which is at the highest gas and lowest liquid flow conditions. Here, localised spray flow is expected in pores which carry high gas rate – which explains the overall lack of liquid signal throughout the bed. Only three liquid rich pores are confidently identified, in regions which are perhaps still locally within the churning or churn-pulse boundary. Images (e) and (f) show patterns closer to what is expected in pulsing flow,

with a relatively even distribution of intensity in the porous space, and a few liquid-rich regions. The liquid-rich pores are generally found away from the bed walls.

The gas results are interpreted in a similar probabilistic sense. The two single-phase examples are again practically identical. The gas is seen for all flow rates to occupy more of the interstitial area than the liquid. This is due to a combination of the hydrodynamic properties of the gas, and the fact that comparatively high gas flow rates were used in this study which gave high gas holdups. In the flow regimes studied, it is expected that the gas exists as bubbles or localised plugs, rising through the bed or in high flow locations, entraining the liquid as droplets. Some static gas holdup is also expected. Overall gas holdup is seen to increase with increasing gas rate going from both (b) to (e) and from (c) to (f) with few dramatic effects on the gas distribution. The number of gas-rich pores is seen to diminish as the flow spreads out across the available pore space better with increased gas rate. The gas-rich pores are seen to occur mainly towards the bed walls, which is in contrast with the liquid phase. The lowest overall holdup is observed for the image in (c) which is the lowest gas rate and highest liquid rate. Here, the greatest number of gas-rich pores are seen.

Total intensity in the slice is a rough measure of the holdup of each phase within the slice. It is seen that holdup is decreased for each phase by a factor of around 50% when introducing two-phase flow to the bed. For two-phase flow, liquid holdup is generally seen to increase with increased liquid flow and decrease for increased gas flow. Similarly, gas holdup increases with increased gas velocity and is reduced for increased liquid velocity. These results are consistent with existing theory for upflow beds.

The velocity images also reflect in an averaged sense what the phase behaviour of the bed is over the operating window. It is evident over the experimental time for both phases, most of the pores in the slice contain static fluid and that only relatively few pores contain fluid which is mobile. There are also pores for which both phases display average negative velocities, indicating significant backmixing in each phase. The average velocity across all voxels is in each case roughly equivalent to U/ε where U is the superficial fluid velocity and ε is the void fraction of each phase in the slice. This indicates that overall, each phase occupies most of the void space. For the gas phase, some pores carry flow which is considerably higher than the measured average in the slice. It is postulated that this is due to these pores being primarily associated with repeated bubble rise, and that these high flow rates are a measure of the bubble rise velocity.

For the liquid, the high-flow pores are attributed either to pure liquid-flow pores which are responsible for high liquid-flowing rivulets, or they are because of localised pulsing which causes liquid plugs to rise at higher-than-average velocities due to the motion of gas bubbles. It was found that the difference between the average flow velocity and highest local flow velocity in the liquid was consistently greater than for the gas phase. In the single flow liquid images, the highest flow velocity was 3.7 times greater than the average. This was increased in the two-phase flow experiments, to 7.2 times higher than the average at the lower gas velocity of U_G = 2.5 cm s^{-1}. At the high gas velocity of U_G = 5.0 cm s^{-1}, the highest local liquid velocity was between 7 and 10 times higher than the mean liquid flow in the slice. The higher disparity supports the theory that the high-flow pores are due to gas bubbling behaviour, as the mean flow in other pores bubbling less severely would mainly be driven by liquid shear flow closer to the value of U/ε. Higher liquid flow pores were found to occur closer to the bed centre than the bed walls.

For the single-phase gas images, the ratio of the maximum local velocity to the mean velocity in the slice was ~ 3, meaning a few regions had a local velocity three times higher than the average flow. For the liquid phase, the maximum flow was around 3.5 times higher than the average flow. These values were found to substantially increase in the two-phase flow images. For the gas phase at the lowest liquid flow rate of U_L = 0.26 cm s^{-1}, the maximum flow was found to be 5 and 7 times higher than the average flow at gas velocities of U_G = 2.5 cm s^{-1} and U_G = 5.0 cm s^{-1} respectively. This ratio was diminished slightly at the elevated liquid flow rate of U_L = 0.26 cm s^{-1}, with the maximum local gas flow being 4.6 to 4.8 times higher than the average. These maxima were found to occur in generally gas-rich pores and are attributed to pores which show predominantly bubbling behaviour. The pores were also found to occur nearer the walls of the bed, as seen in both the intensity distributions and flow images, which show regions of higher flow at the bed walls. The velocity of the high-flow pores was roughly constant at a gas flow of U_G = 2.5 cm s^{-1} which was around 20 cm s^{-1}. This was found to increase at the higher liquid flow rate of U_L = 0.52 cm s^{-1} and was roughly constant with gas flow rate again at approximately 30 cm s^{-1}. This would suggest that bubble rise velocity is insensitive for this particle size to gas flow rate and is proportional to liquid flow rate. This is consistent with previous studies on bubble rise behaviour. If the gas high flow regions were caused by channelling, they would demonstrate sensitivity to the gas flow rate which is typically not seen.

3.10.6. TIME AVERAGED VELOCITY DISTRIBUTIONS

The velocity distributions confirm some of the observations made in the previous section. The positive tails of the liquid velocity distribution extend to 12 cm s^{-1} and the negative tails extend to approximately -7 cm s^{-1}. Maximum probability occurs at or very near to zero flow, indicating that most time-averaged flow is static in the bed. In all two-phase cases, the distributions are broader than during single-phase flow and the zero-flow probability is diminished, which suggests that the flow becomes more poorly distributed and occurs predominantly in high flowing isolated pores. Adding additional liquid flow has the effect of broadening the distribution, implying poorer spatial distribution of flow at the elevated liquid rate. Increasing gas flow narrows the distributions for fixed liquid flow and reduces the probability of encountering static liquid holdup. This is probably due to increased bubbling activity, making it less likely to encounter stagnant liquid pockets at elevated gas rates. The narrowed distribution and reduced liquid holdup support this hypothesis.

The gas distributions in two-phase flow are much broader than those of the liquid when compared to single-phase flow. This suggests a substantial change in statistical flow behaviour because of the onset of two-phase flow. This comes in the form of bubbling, which is very distinct from single-phase flow behaviour. The buoyancy-driven phenomenon causes higher flow rates to be observed by the bubble rise velocity, which may be substantially different from the average flow through the bed. Much more substantial backmixing is also observed. The nature of the backmixing distribution (negative tail) is relatively insensitive to changes in the liquid flow rate, but significantly broadens for increases in the gas flow rate. Alternatively, the maximum in the distributions (i.e. the length of the positive tail) is more a function of the liquid flow rate than the gas flow. It increases with increases in the liquid flow rate. This may be suggestive of the bubble rise velocity, which has previously been shown to be a function of liquid flow and, in some cases, insensitive to changes in the gas flow. Across the range of flow rates studied, the probability of static gas holdup remains approximately constant, which is different from the liquid flow – further supporting the hypothesis regarding the influence of the gas phase on the static liquid holdup. Static gas holdup has previously been shown only to be a function of the packing type. The velocity distributions may in principle be used to fit residence time distribution (RTD) models, which seek to explain the nature of anisotropy on a global basis using networks of ideal reactors. The fitted RTD curves can be used in conjunction with kinetic and thermodynamic models to provide a realistic reactor model for non-ideal systems such as this.

3.11. CONCLUSIONS

Velocity profiles were successfully measured in the 52 mm empty tube for both phases, with the shape of both the gas and the liquid profiles approaching a paraboloid when both flows became developed. Good agreement was shown between the average flow velocity measured using MRI and the velocity obtained externally from the mass flow controllers. Similarly, in the packed bed under conditions of single-phase flow classical packed bed flow profiles were recorded, with most flow in the slice of both gas and liquid being stationary and a few pores carrying greater-than-average flow.

In two-phase flow, evidence of bubbling was identified by 1D MRI intensity profiles, which showed different fluctuation behaviour which was dependent on the gas and liquid flow rates and the flow regime. This approach could be used to measure flow regime changes and boundaries, as well as bubble rise velocities.

Liquid saturation in the slice was shown to increase with increasing liquid flow and decrease with increasing gas flow. Reasonable agreement was found for the correlations of Fukushima and Kusaka [3] and Turpin and Huntington [2], which also qualitatively predict the same type of relationship. Differences are attributed to their use of the air-water system at atmospheric operating pressures, and column-to-particle diameter ratios lower than the present study.

Pressure drop was found to be lower than predicted by most correlations, which may be a function of the operating pressure or use of different materials. The total pressure drop increased for increasing liquid and gas flow rate. Reasonable agreement was shown for the correlation by Ford [75]. Improved solids wetting efficiency at elevated pressures may lead to lower drag through the bed and hence lower total pressure drop.

The two-phase flow images showed that phase holdup increased with increasing flow of the phase in question and decreased for increasing flow of the other phase. The liquid phase was seen to exhibit liquid-rich rivulets which were more likely to appear closer to the centre of the bed than the bed walls, whilst the gas phase was also found in several gas-rich pores which were more likely found toward the bed walls. Both phases were found to occupy most of the slice area over the 2.5 h imaging time. The number of isolated pores rich in one phase was seen to diminish for increasing flow of that phase.

The average velocity across the slice for each phase was the expected average rate of U/ε. Significantly heterogeneous flow was seen, with some liquid pores having velocities 7 to 10

times higher than the average value in the slice. Similarly, some gas-filled pores were found to have velocities 5 to 7 times higher than the average in the slice. The high liquid flows recorded were attributed to regions where localised slugging or pulsing caused by gas bubbles leads to liquid plugs of much higher flow velocities than average. Similarly, the high gas velocities were attributed to pores which have bubble 'trains', where bubbles rise at velocities of between 20 cm s^{-1} and 30 cm s^{-1}. It was found that the velocity of these high flowing gas regions was insensitive to gas rate but increased with increasing liquid rate which supports the hypothesis that these are due to gas bubbling.

In the probability distributions, the static gas holdup in the slice was found to be insensitive to changes in both the liquid and gas flow rate which is consistent with previous studies. The statistical nature of the gas field was found to change from single-phase flow more than the liquid, due to the onset of bubbling behaviour. Significant backmixing was found in both phases. Gas phase back mixing was found to be more sensitive to changes in gas flow rate than liquid, and similarly liquid backmixing was more sensitive to changes in the liquid flow rate than the gas.

In addition to showing the ability of several MRI methods to characterise the flow behaviour of co-current upflow beds, the principle new insights from this study include 1) the anisotropic distribution of phases during two phase flow, and 2) the existence of high flowing pores of both gas and liquid due to the presence of bubble trains. The liquid phase showed a tendency to exist in the centre of the bed with consequently fewer pores with higher-than-average flow in the central region. The gas however preferred the bed walls, which implies an increase in the density of bubble trains (and pores with gas velocities approaching the bubble rise velocity) towards the perimeter of the bed. This is accompanied by higher liquid velocity, due to the uptake of liquid slugs in between bubbles.

NOMENCLATURE

ABBREVIATIONS

1D, 2D, 3D	one, two or three dimensional
CFD	computational fluid dynamics
FOV	field-of-view
r.f.	radiofrequency
MRI	magnetic resonance imaging
NMR	nuclear magnetic resonance

SYMBOLS

a_s	surface area for mass/heat transfer	m^2
a_L	liquid phase surface area	m^2
a_p	particle surface area	m^2
D	diffusion coefficient	m^2
d_p	diameter of particle	m
d_t	diameter of bed	m
F_C	particle shape factor	-
G	magnetic field gradient strength G cm^{-1}	T m^{-1}
G_{read}	read direction magnetic field gradient	T m^{-1}
G_{phase}	phase direction magnetic field gradient	T m^{-1}
G_{slice}	flow encoding magnetic field gradient	T m^{-1}
g	velocity gradient increment	T m^{-1}
g	acceleration due to gravity	m s^{-2}
h	heat transfer coefficient	W/(m^2K)
i	electric current	A
k_s	solid mass transfer coefficient	m/s
k_L	liquid mass transfer coefficient	m/s
l_p	characteristic length of particle	m
P	pressure	bar
Pe	Peclet number	-
Re_L	Reynolds number of liquid	-
Re_G	Reynolds number of gas	-

R_W	resistance in wire	Ohms
Sh_0	Sherwood number at reference conditions	-
T	temperature	K
T_1	spin-lattice relaxation time constant	s
T_2	spin-spin relaxation time constant	s
t	time	s
U	superficial velocity	m s^{-1}
U_L	superficial liquid velocity	cm s^{-1}
U_G	superficial gas velocity	cm s^{-1}
V_L	local liquid velocity	cm s^{-1}
V_G	local gas velocity	cm s^{-1}
y,x,z	standard cartesian coordinates	-

GREEK LETTERS

α	first CS regularisation parameter	-
B	second CS regularisation parameter	-
β_L	fractional liquid saturation	-
β_G	fractional gas saturation	-
Δ	change/observation time for velocity measurement	-/s
δ	flow encoding gradient pulse time	s
ε_L	liquid filling fraction	-
ε_G	gas filling fraction	-
ε_B	bed void fraction	-
μ_L	liquid Newtonian viscosity	-
μ_G	gas Newtonian viscosity	-
ϕ	arbitrary correlation function	-
ρ_L	liquid density	kg/m^3
ρ_G	gas density	kg/m^3
σ	sample standard deviation	-
τ	echo time	s

REFERENCES

[1] Eisenklam, P., Ford, L.H. On the interaction of fluids and solids. *Inst. Chem. Engrs. London* 1962: pp. 333–44.

[2] Turpin, J.L., Huntington, R.L. Prediction of pressure drop for two-phase, two-component concurrent flow in packed beds. *AIChE J.* 1967;13: pp. 1196–202.

[3] Fukushima, S., Kusaka, K. Gas-liquid mass transfer and hydrodynamic flow regions in packed beds with cocurrent upward flow. *J. Chem. Eng. Japan* 1979;12: pp. 296–301.

[4] Carleton, A.J., Flain, R.J., Rennie, J., Valentin, F.H.H. Some properties of a packed bubble column. *Chem. Eng. Sci.* 1967;22: pp. 1839–45.

[5] Specchia, V., Sicardi, S., Gianetto, A. Absorption in packed towers with concurrent upward flow. *AIChE J.* 1974;20: pp. 646–53.

[6] Sato, Y., Hirose, T., Ida, T. Upward co-current gas–liquid flow in packed beds. *Kagaku Kogaku* 1974;38: pp. 534.

[7] Saada, M.Y. Fluid Mechanics of Co-Current Two · Phase Flow in Packed Beds : Pressure Drop and Liquid Holdup Studies. *Period. Polytech Chem. Eng* 1975;7: pp. 231–9.

[8] Colquhoun-Lee, I., Stepanek, J.B. Solid-liquid mass transfer in two phase co-current upward flow in packed beds. *Trans. Inst. Chem. Eng* 1978;56: pp. 136.

[9] Hofmann, H.P. Multiphase Catalytic Packed-Bed Reactors. *Catal. Rev.* 1978;17: pp. 71–117.

[10] Specchia, V., Baldi, G. Pressure drop and liquid holdup for two phase concurrent flow in packed beds. *Chem. Eng. Sci.* 1977;32: pp. 515–23.

[11] Rao, V.G., Ananth, M.S., Varma, Y.B.G. Hydrodynamics of two-phase cocurrent downflow through packed beds. Part II: Experiment and correlations. *AIChE J.* 1983;29: pp. 473–83.

[12] Goda, H., Hibiki, T., Kim, S., Ishii, M., Uhle, J. Drift-flux model for downward two-phase flow. *Int. J. Heat Mass Transf.* 2003;46: pp. 4835–44.

[13] Hibiki, T., Ishii, M. One-dimensional drift–flux model for two-phase flow in a large diameter pipe. *Int. J. Heat Mass Transf.* 2003;46: pp. 1773–90.

[14] Clark, N.N., Flemmer, R.L. Predicting the holdup in two-phase bubble upflow and downflow using the Zuber and Findlay drift-flux model. *AIChE J.* 1985;31: pp. 500–3.

[15] Benkrid, K., Rode, S., Midoux, N. Prediction of pressure drop and liquid saturation in trickle-bed reactors operated in high interaction regimes. *Chem. Eng. Sci.* 1997;52: pp. 4021–32.

[16] Larachi, F., Laurent, A., Wild, G., Midoux, N. Some Experimental Liquid Saturation Results in Fixed-Bed Reactors Operated under Elevated Pressure in Cocurrent Upflow and Downflow of the Gas and the Liquid. *Ind. Eng. Chem. Res.* 1991;30: pp. 2404–10.

[17] Wallis, G.B. One-dimensional two-phase flow 1969.

[18] Carman, P.C. Fluid flow through granular beds. *Trans. Chem. Eng.* 1937;15: pp. 150–66.

[19] Ergun, S. Fluid flow through packed columns. *Chem. Eng. Prog.* 1952;48: pp. 89–94.

[20] Attou, A., Ferschneider, G. A simple model for pressure drop and liquid hold-up in packed-bed bubble reactors. *Chem. Eng. Sci.* 1999;54: pp. 5139–44.

[21] Boyer, C., Ferschneider, G. Experimental Validation of a Two-Phase Flow Model for Pressure Drop and Liquid Hold-up in Downflow Packed Bed Bubble Reactors. *Can. J. Chem. Eng.* 2003;81: pp. 808–13.

[22] Ramachandran, P.A., Chaudhari, R. Three-phase catalytic reactors. vol. 2. New York: Gordon & Breach Science Pub; 1983.

[23] Stiegel, G.J., Shah, Y.T. Backmixing and liquid holdup in a gas-liquid cocurrent upflow packed column. *Ind. Eng. Chem. Process Des. Dev.* 1977;16: pp. 37–43.

[24] Toye, D., Marchot, P., Crine, M., Pelsser, A., M., L'Homme, G. Local measurements of void fraction and liquid holdup in packed columns using X-ray computed tomography. *Chem. Eng. Process. Process Intensif.* 1998;37: pp. 511–20.

[25] Warsito, W., Fan, L.-S. ECT imaging of three-phase fluidized bed based on three-phase capacitance model. *Chem. Eng. Sci.* 2003;58: pp. 823–32.

[26] Weber, H.H. Dissertation. Techniche Hochschule Darmsteidt, 1961.

[27] von Heilmann, W., Hofman, H. Holdup data in co-current upflow beds. Proc. 4th Symp. Chem. React. Eng., London: Pergamon Press; 1971, p. 169.

[28] Achwal, S.K., Stepanek, J.B. Holdup proffies in packed beds. *Chem. Eng. J.* 1976;12: pp. 69–75.

[29] Ohshima, S., Takematsu, T., Kuriki, Y., Shimada, K., Suzuki, M., Kato, J. Liquid-phase mass transfer coefficient and gas holdup in a packed-bed cocurrent up-flow column. *J. Chem. Eng. Japan* 1976;9: pp. 29–34.

[30] Ramachandran, P.A., Chaudhari, R. Three-phase catalytic reactors. vol. 2. Gordon & Breach Science Pub; 1983.

[31] Hutton, B.E.T., Leung, L.S. Cocurrent gas—liquid flow in packed columns. *Chem. Eng. Sci.* 1974;29: pp. 1681–5.

[32] Saada, M.Y. Assessment of interfacial area in co-current 2-phase flow in packed-beds. *Chim. Ind. Genie Chim.* 1972;105: pp. 1415.

[33] Smith, D., Reznik, A., Pontello, A. Pittsburgh Energy Research Centre Quarterly Reports. Pittsburgh: 1976.

[34] Shah, Y.T. Gas-liquid-solid reactor design. McGraw-Hill; 1979.

[35] Stüber, F., Wilhelm, A.M., Delmas, H. Modelling of three phase catalytic upflow reactor: A significant chemical determination of liquid-solid and gas-liquid mass transfer coefficients. *Chem. Eng. Sci.* 1996;51: pp. 2161–7.

[36] Goto, S., Levec, J., Smith, J.M. Mass Transfer in Packed Beds with Two-Phase Flow. *Ind. Eng. Chem. Process Des. Dev.* 1975;14: pp. 473–8.

[37] Alexander, B.F., Shah, Y.T. Gas-liquid mass transfer coefficients for cocurrent upflow in packed beds—Effect of packing shape at low flow rates. *Can. J. Chem. Eng.* 1976;54: pp. 556–9.

[38] Montagna, A., Shah, Y.T. Backmixing effect in an upflow cocurrent hydrodesulfurization reactor. *Chem. Eng. J.* 1975;10: pp. 99–105.

[39] Mochizuki, S., Matsui, T. Selective hydrogenation and mass transfer in a fixed-bed catalytic reactor with gas-liquid concurrent upflow. *AIChE J.* 1976;22: pp. 904–9.

[40] Specchia, V., Baldi, G., Gianetto, A. Solid-liquid mass transfer in concurrent two-phase flow through packed beds. *Ind. Eng. Chem. Process Des. Dev.* 1978;17: pp. 362–7.

[41] Stiegel, G.J., Shah, Y.T. Axial dispersion in a rectangular bubble column. *Can. J. Chem. Eng.* 1977;55: pp. 3–8.

[42] Shah, Y.T., Stiegel, G.J., Sharma, M.M. Backmixing in gas-liquid reactors. *AIChE J.* 1978;24: pp. 369–400.

[43] Kirillov, V.A., Ogarkov, B.L. Investigation of the processes of heat and mass transfer in a three-phase bed of catalyst. *Int. Chem. Eng.* 1980;20: pp. 478–85.

[44] Bouteldja, H., Hamidipour, M., Larachi, F. Hydrodynamics of an inclined gas-liquid cocurrent upflow packed bed. *Chem. Eng. Sci.* 2013;102: pp. 397–404.

[45] Dashliborun, A.M., Larachi, F., Schubert, M. Hydrodynamics of gas-liquid cocurrent upflow in oscillating packed beds for offshore marine applications. *Chem. Eng. Sci.* 2017;170: pp. 583–96.

[46] Benkrid, K., Rode, S., Pons, M.N., Pitiot, P., Midoux, N. Bubble flow mechanisms in trickle beds — an experimental study using image processing. *Chem. Eng. Sci.* 2002;57: pp. 3347–58.

[47] Pokusaev, B.G., Karlov, S.P., Shreiber, I. Immersion Tomography of a Gas – Liquid Medium in a Granular Bed 2004;38: pp. 5795.

[48] Pokusaev, B.G., Kazenin, D.A., Karlov, S.P. Immersion Tomographic Study of the Motion of Bubbles in a Flooded Granular Bed 2004;38: pp. 561–8.

[49] Bordas, M.-L., Cartellier, A., Séchet, P., Boyer, C. Bubbly flow through fixed beds: Microscale experiments in the dilute regime and modeling. *AIChE J.* 2006;52: pp. 3722–43.

[50] Jo, D., Revankar, S.T. Effect of coalescence and breakup on bubble size distributions in a two-dimensional packed bed. *Chem. Eng. Sci.* 2010;65: pp. 4231–8.

[51] Mena, P.C., Rocha, F.A., Teixeira, J.A., Sechet, P., Cartellier, A. Measurement of gas phase characteristics using a monofibre optical probe in a three-phase flow. *Chem. Eng. Sci.* 2008;63: pp. 4100–15.

[52] Hamidipour, M., Larachi, F. Characterizing the liquid dynamics in cocurrent gas–liquid flows in porous media using twin-plane electrical capacitance tomography. *Chem. Eng. J.* 2010;165: pp. 310–23.

[53] Wang, W., Li, J. Simulation of gas–solid two-phase flow by a multi-scale CFD approach—of the EMMS model to the sub-grid level. *Chem. Eng. Sci.* 2007;62: pp. 208–31.

[54] Jiang, Y., Khadilkar, M.R., Al-Dahhan, M.H., Dudukovic, M.P. CFD of multiphase flow in packed-bed reactors: II. Results and applications. *AIChE J.* 2002;48: pp. 716–30.

[55] Sokolichin, A., Eigenberger, G., Lapin, A., Lübert, A. Dynamic numerical simulation of

gas-liquid two-phase flows Euler/Euler versus Euler/Lagrange. *Chem. Eng. Sci.* 1997;52: pp. 611–26.

[56] Attou, A., Ferschneider, G. A two-fluid model for flow regime transition in gas–liquid trickle-bed reactors. *Chem. Eng. Sci.* 1999;54: pp. 5031–7.

[57] De Bertodano, M.L., Lahey, R.T., Jones, O.C. Development of a k-ε model for bubbly two-phase flow. *J. Fluids Eng.* 1994;116: pp. 128–34.

[58] Iliuta, I., Hamidipour, M., Larachi, F. Nonequilibrium thermomechanical modeling of liquid drainage/imbibition in trickle beds. *AIChE J.* 2012;58: pp. 3123–34.

[59] Önsan, Z.I. Multiphase catalytic reactors: theory, design, manufacturing, and applications. John Wiley & Sons; 2016.

[60] Raghavendra Rao, A. V., Kishore Kumar, R., Sankarshana, T., Khan, A. Interfacial area for concurrent gas-liquid upflow through packed bed. *Can. J. Chem. Eng.* 2010;88: pp. 929–35.

[61] Collins, J.H.P., Sederman, A.J., Gladden, L.F., Afeworki, M., Kushnerick, J.D., Thomann, H. Characterising gas behaviour during gas–liquid co-current up-flow in packed beds using magnetic resonance imaging. *Chem. Eng. Sci.* 2017;157: pp. 2–14.

[62] Sankey, M.H., Holland, D.J., Sederman, A.J., Gladden, L.F. Magnetic resonance velocity imaging of liquid and gas two-phase flow in packed beds. *J. Magn. Reson.* 2009;196: pp. 142–8.

[63] Lustig, M., Donoho, D.L., Santos, J.M., Pauly, J.M. Compressed sensing MRI. *IEEE Signal Process. Mag.* 2008;25: pp. 72–82.

[64] Lustig, M., Donoho, D., Pauly, J.M. Sparse MRI: The application of compressed sensing for rapid MR imaging. *Magn. Reson. Med.* 2007;58: pp. 1182–95.

[65] Holland, D.J., Gladden, L.F. Less is More: How Compressed Sensing is Transforming Metrology in Chemistry. *Angew. Chemie Int. Ed.* 2014;53: pp. 13330–40.

[66] Holland, D.J., Malioutov, D.M., Blake, A., Sederman, A.J., Gladden, L.F. Reducing data acquisition times in phase-encoded velocity imaging using compressed sensing. *J. Magn. Reson.* 2010;203: pp. 236–46.

[67] Cotts, R.M., Hoch, M.J.R., Sun, T., Markert, J.T. Pulsed field gradient stimulated echo methods for improved NMR diffusion measurements in heterogeneous systems. *J. Magn. Reson.* 1989;83: pp. 252–66.

[68] Boyce, C.M., Rice, N.P., Sederman, A.J., Dennis, J.S., Holland, D.J. 11-interval PFG pulse sequence for improved measurement of fast velocities of fluids with high diffusivity in systems with short T 2∗. *J. Magn. Reson.* 2016;265: pp. 67–76.

[69] Sederman, A.J., Mantle, M.D., Gladden, L.F. Single excitation multiple image RARE (SEMI-RARE): ultra-fast imaging of static and flowing systems. *J. Magn. Reson.* 2003;161: pp. 15–24.

[70] Anadon, L.D., Lim, M.H.M., Sederman, A.J., Gladden, L.F. Hydrodynamics in two-phase flow within porous media. *Magn. Reson. Imaging* 2005;23: pp. 291–4.

[71] Fabich, H.T., Sederman, A.J., Holland, D.J. Study of bubble dynamics in gas-solid fluidized beds using ultrashort echo time (UTE) magnetic resonance imaging (MRI). *Chem. Eng. Sci.* 2017;172: pp. 476–86.

[72] Fabich, H.T., Sederman, A.J., Holland, D.J. Development of ultrafast UTE imaging for granular systems. *J. Magn. Reson.* 2016;273: pp. 113–23.

[73] Sederman, A.J., Johns, M.L., Alexander, P., Gladden, L.F. Visualisation of structure and flow in packed beds. *Magn. Reson. Imaging* 1998;16: pp. 497–500.

[74] Sederman, A.J., Johns, M.L., Alexander, P., Gladden, L.F. Structure-flow correlations in packed beds. *Chem. Eng. Sci.* 1998;53: pp. 2117–28.

[75] Ford, L.H. Multiphase flow through porous media, with special reference to the turbulent region. University of London, 1960.

CHAPTER 4 – FLOW MALDISTRIBUTION IN A GAS-LIQUID TRICKLE BED

4.1. INTRODUCTION AND THEORY

Trickle bed reactors (TBRs) are employed extensively in industry when intimate gas-liquid-solid contact is required. They are deployed widely in petroleum, petrochemical, chemical and biochemical processing industries in which they are popularly used for catalytic hydrotreating operations [1]. Despite having been the focus of over five decades of chemical engineering research, much remains to be understood regarding the design and operation of these vessels. This is due mainly to their inherent complexity, in that the physics of chemically reacting fluids in networks of porous solids is very difficult to describe through analytical or numerical models. Historically, TBRs are designed using a combination of phenomenological and empirical models which seek to describe the fundamental interactions of the fluids with the solids matrix. Knowledge of the hydrodynamics is therefore crucial, as the localised fluid behaviour affects heat and mass transport, which in turn affect catalyst performance and thus overall bed performance. With increased computing power, the opportunity now exists to employ more complex physics in the form of either fundamental or advanced phenomenological models which improve our understanding and predictive capabilities. The aim of this study is to present for the first time, a detailed, quantitative pore-scale assessment of the hydrodynamic behaviour of both the gas and the liquid phases in a trickle bed. This is done with the goal of improving our understanding of trickle bed behaviour, as well as validating previously observed data and modelling results. The bed liquid saturation, pore filling fraction and solids wetting efficiency are evaluated in addition to analysing the flow fields using magnetic resonance imaging (MRI).

Several extensive reviews on the subject of trickle beds have been undertaken [1–4] which include descriptions of state-of-the-art theory, experimentation and modelling. Most of the established hydrodynamic models relate macroscopic descriptions of bed operation, which include the two-phase pressure drop, liquid saturation, solids wetting efficiency to the macroscopic fluid velocities or Reynolds numbers. These models make simplifying assumptions about the complexity of hydrodynamic phenomena in trickle beds and thus simplify spatiotemporal anisotropy in the performance variables. It has been highlighted conceptually [5–8] and experimentally [9,10] that significant maldistribution exists in packed

bed reactors, and that the inhomogeneous nature of the fluid flow fields is in sharp contrast with any assumptions of uniformity within the bed. Despite introducing more sophisticated forms of packing, such as structured packing, or loading and bed pre-wetting techniques, the phase and local velocity distributions can be significantly maldistributed. Localised velocity differences can lead to dramatically different catalytic utilisation and degeneration rates, and can in many exothermic reactions contribute to hotspot formation or potential reaction runaway situations [11]. Maldistributed flow field features have been described previously in literature [1] and the contribution of features such as stagnant liquid pockets, films and rivulets of liquid flowing over particles, pendular and filament structures is in general to diminish bed performance by creating an anisotropic conversion or selectivity in reactive systems. It has also been shown that the local inception of these features and temporal instabilities is responsible for the onset, propagation and existence of the different macroscopic flow regimes of operation [12,13]. In particular, the trickle-to-pulse regime transition has received pronounced attention in research, in which localised film-level instabilities and their propagation leads to the onset of the pulsing flow regime [13–16].

The spatial characteristics of TBRs have been investigated using a range of techniques including electrical probes and conductivity meters [7,17–19], acoustic and visual investigations on transparent and 2D systems [6,20,21], electrical capacitance and resistance tomography [14,22–26], X-ray or γ-ray tomography [19,27–34] and nuclear magnetic resonance [15,35]. Of these, the tomographic methods capable of studying opaque systems non-intrusively are particularly useful as they can be used *in situ* to visualise the hydrodynamics. Further to this, magnetic resonance imaging is the tool which is most capable of acquiring quantitative velocity information on both fluid phases non-intrusively and not employing any ionising radiation sources. The state of contributions of magnetic resonance techniques to reactor engineering has recently been reviewed [36–40]. The key advantage of MR techniques over others is that by nature the MR signal is chemically selective and can be further encoded for position and velocity. This makes it a powerful tool for performing both spatial chemical mapping [41,42] and physical hydrodynamic investigations [43–46].

This study provides a detailed quantitative, pore-scale analysis of the local velocity fields of both the liquid and gas phase. Such two-phase data have previously been reported [43,47] but here focus is on the degree of anisotropy of the liquid saturation, solids wetting efficiency and local inter-pore axial velocity including that of the gas phase. Gas phase MR experiments are by nature more challenging, owing to the lower molecular density and very short T_2^* times.

This is especially true in porous systems, where relaxation times are further reduced due to differences in magnetic susceptibility at phase interfaces. Gas phase MR experiments can be performed using thermal polarisation [48,49] (as in the use of hydrocarbon or fluorinated gases) or hyperpolarisation [50,51] strategies, including the use of optical-pumping or para-hydrogen induced polarisation. Despite the challenges of gas phase NMR, recent works have demonstrated the effectiveness of using thermally polarised SF_6 gas in NMR velocimetry studies on systems such as packed beds [47], diesel particulate filters and monoliths [52–54] and fluidised beds [55–58]. In the present work, thermally polarised and pressurised SF_6 gas is used. The nucleus ^{19}F is 100% naturally abundant and SF_6 has 6 ^{19}F nuclei per molecule (meaning a high density of the NMR-active nucleus). It also has high sample mass density and a low self-diffusion coefficient which minimises diffusive attenuation and blurring. SF_6 has relatively short relaxation times, with $T_1 = T_2 = 20$ ms [59], which allow more rapid excitations and signal averaging than hydrocarbon gases. Moreover, it is non-toxic and relatively inexpensive. An additional advantage is that there is no 'contamination' of the acquired ^{19}F signal with the high ^{1}H signal associated with the liquid phase containing hydrogen nuclei.

To further reduce signal acquisition times for the gas phase images a compressed sensing approach was employed which has been implemented in several prior MR studies in which high spatiotemporal resolution is required without long (longer than several hours) experimental times [53,60–63].

4.2. EXPERIMENTAL

The experimental setup used for the trickle flow experiments is similar to that described in Chapter 3 for the upflow experiments. Figure 4.1 shows a process flow diagram of the experimental setup. The noteworthy changes in the apparatus and operation are described in this section.

4.2.1. TRICKLE BED

The trickle bed (1) was a 27 mm inner diameter, 1 m long PEEK tube. The tube was filled randomly with glass beads with a mean diameter of 5 mm. The bed was tapped at each addition of 10 cm of particles, to ensure a close random packing. The trickle bed was run in the co-current downward configuration, with both gas and liquid entering the vessel at the top. The liquid used was deionised water doped with 1.32 mmol/L Gd^{3+} ions to reduce the T_1 time to

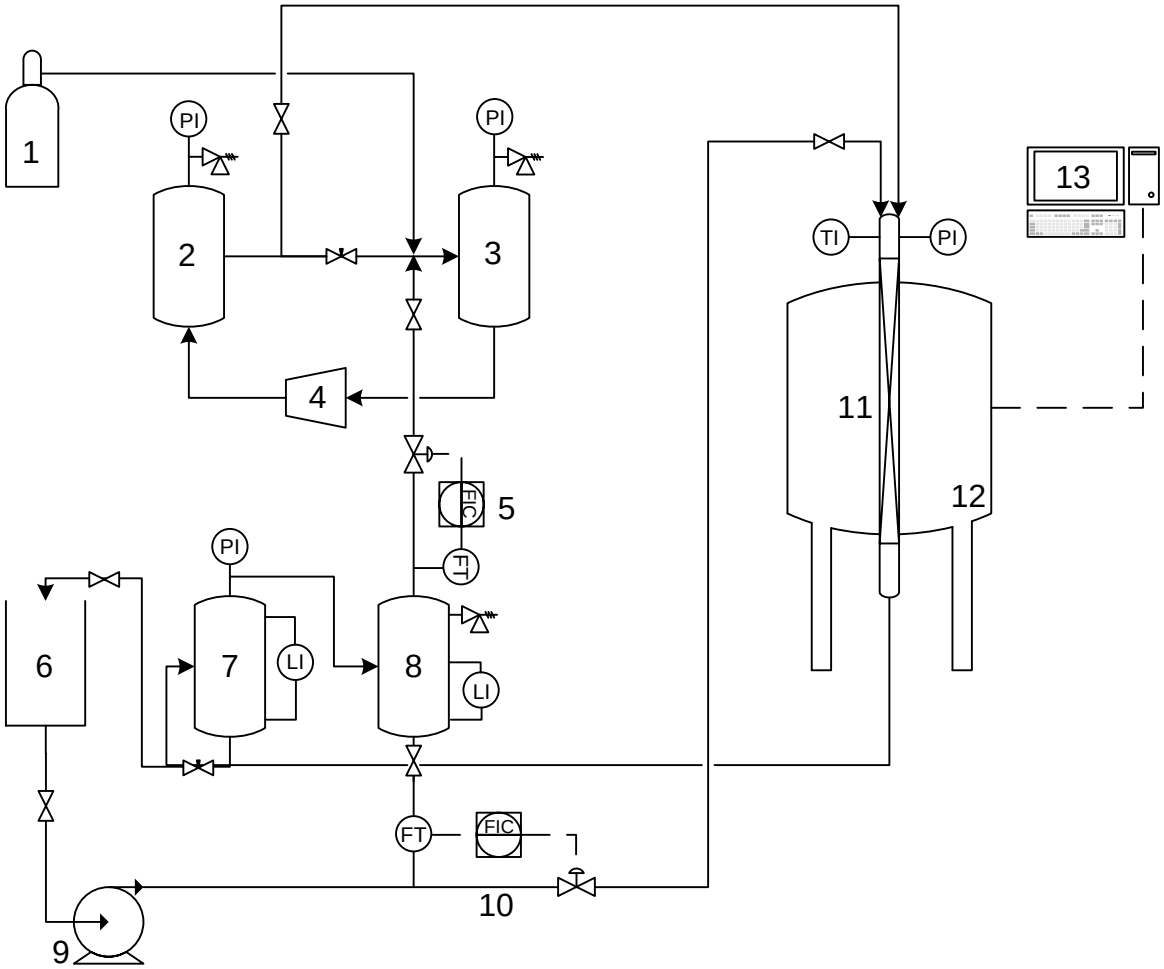

Figure 4.1: Process flow diagram of the experimental trickle bed system. Key equipment is labelled as follows 1: SF_6 cylinder, 2: high pressure gas receiver vessel, 3: low pressure gas receiver vessel, 4: SF_6 compressor, 5: gas mass flow controller, 6: water feed tank, 7: stage 1 gas-liquid separator vessel, 8: stage 2 gas-liquid separator vessel, 9: liquid water centrifugal pump, 10: liquid mass flow controller, 11: PEEK trickle flow packed bed vessel, 12: superconducting MRI magnet, 13: controller computer for NMR setup and software.

53 ms which reduces the time between successive MR excitations. SF_6 gas was supplied at a purity of 99.9% from BOC® in 20 bar cylinders.

The flow of gas to the bed was supplied using the same gas circulation as described previously in Chapter 3 consisting of units (2),(3) and (4). In the experiments the gas pressure was kept at 6.75 bara. The liquid was supplied using the same pump (9) as Chapter 3, and the gas-liquid separation was undertaken in the same way using the vessels (7) and (8). The liquid flow rate was controlled using a Bronkhorst Cori-Flow M55C4-AAD-22-K-C mass flow controller (10). Twelve gas and liquid velocity images were acquired at four gas superficial velocities of 0.70 cm s^{-1}, 1.33 cm s^{-1}, 1.95 cm s^{-1} and 2.57 cm s^{-1}; and liquid superficial velocities of 0.23 cm s^{-1}, 0.35 cm s^{-1}, 0.46 cm s^{-1} and 0.69 cm s^{-1} which corresponds to the low-interaction trickle bed regime (LIR).

The bed was prepared for imaging by operating it in the pulsing regime at a liquid superficial velocity of 1.04 cm s^{-1} and a gas superficial velocity of 2.57 cm s^{-1} for 15 minutes. This ensured that the beads were adequately pre-wetted. The desired gas and liquid velocities were then set and the bed was left to stabilise for a further 30 minutes.

4.2.2. MAGNETIC RESONANCE SETUP

Magnetic resonance experiments were conducted using the same vertical bore superconducting magnet (12) and r.f. coil as described in Chapter 3. The magnet was however located in a different building than the experiments in Chapter 3, was tuned to a frequency of 199.7 MHz in order to image the ^{1}H signal from the water, and a frequency of 188.3 MHz to image the ^{19}F nucleus in the SF_6 gas. The same gradient set was used for imaging experiments as in Chapter 3. All experiments were performed using the Bruker TopSpin™ software on a standard desktop computer (13).

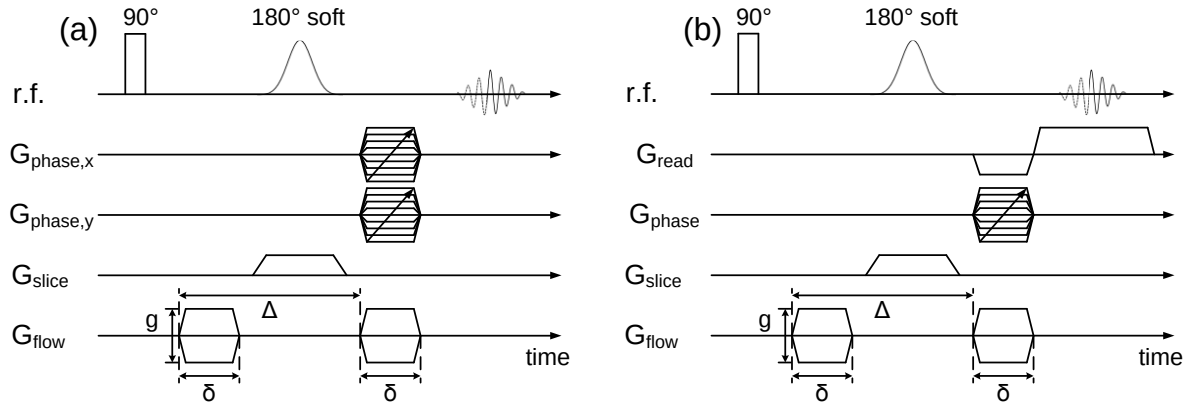

Figure 4.2: Pulse sequences used for velocity imaging of (a) the gas phase and (b) the liquid phase. In (a) a single-point imaging pure phase encoding approach is used to enable compressed sensing. In (b) a standard spin-echo frequency encoding sequence is used.

The 2D velocity maps of both phases were acquired as transverse sections of the bed of slice thickness 1 mm. Two pulse sequences were used. The first, shown in Figure 4.2 (a), was a single-point-imaging (SPI) phase-encoded spin-echo sequence which was used for the gas phase. The second was a spin-warp frequency-encoded sequence which was used on the liquid phase. The SPI sequence was chosen for the gas phase to increase signal-to-noise in combination with compressed sensing reconstruction. It is also ideal for compressed sensing, as the acquisition itself allows sparse sampling of both spatial dimensions. The compressed sensing approach allowed a 20% random under-sampling of a full 128 × 128 matrix to be undertaken. This meant a total of 3278 measurements were made, reducing the time for acquisition from potentially 8 hours to 100 minutes, using 16 averages.

The parameters used for the pulse sequences in Figure 4.2 are found in Table 4.1.

Table 4.1: Constants used in MRI velocity-encoding pulse sequences for gas and liquid velocity imaging

Parameter	**Gas**	**Liquid**
Field-of-view	30 mm × 30 mm	30 mm × 30 mm
Resolution	236 μm	180 μm
Slice thickness	1 mm	1 mm
Pulse sequence	SPI spin echo	Frequency encoded spin echo
Observation time (Δ)	1.92 ms	3.10 ms
Flow encoding gradient time (δ)	589 μs	995 μs
Echo time (τ)	3.60 ms	6.0 ms
Field of flow	1.22 m s^{-1}	0.5 m s^{-1}
Experiment time	100 minutes	14 minutes
Number of averages	16	16

4.3. RESULTS

The effect of varying the liquid velocity was analysed by studying the series of experiments at constant gas superficial velocity V_G = 0.70 cm s^{-1} and liquid superficial velocities of V_L = 0.23 cm s^{-1}, 0.35 cm s^{-1}, 0.46 cm s^{-1} and 0.69 cm s^{-1}. Conversely, the series at a constant liquid velocity of V_L = 0.46 cm s^{-1} and gas velocities of V_G = 0.70 cm s^{-1}, 1.33 cm s^{-1}, 1.95 cm s^{-1} and 2.33 cm s^{-1} was used to assess the effects of varying the gas flow. The series of axial velocity images at constant gas flow is reproduced in Figure 4.3.

The data in Figure 4.2 are shown using a fixed colour scale as shown on bottom right of the figure. This is done to assess the inception and development of flow effects as the liquid velocity is increased. Immediately apparent is the high degree of spatial inhomogeneity observed in both the gas and liquid phase velocity maps. A large portion of the flow of both phases is visibly near to zero, indicating that most of the in-plane liquid and gas is almost static. This result has been observed elsewhere for both single-phase [9,10] flow and flow in trickle beds [10,47].

Several noteworthy effects are apparent when studying the increase in liquid flow from left to right, and are indicated as the pores labelled (i-vii). Firstly, the additional liquid flow manifests

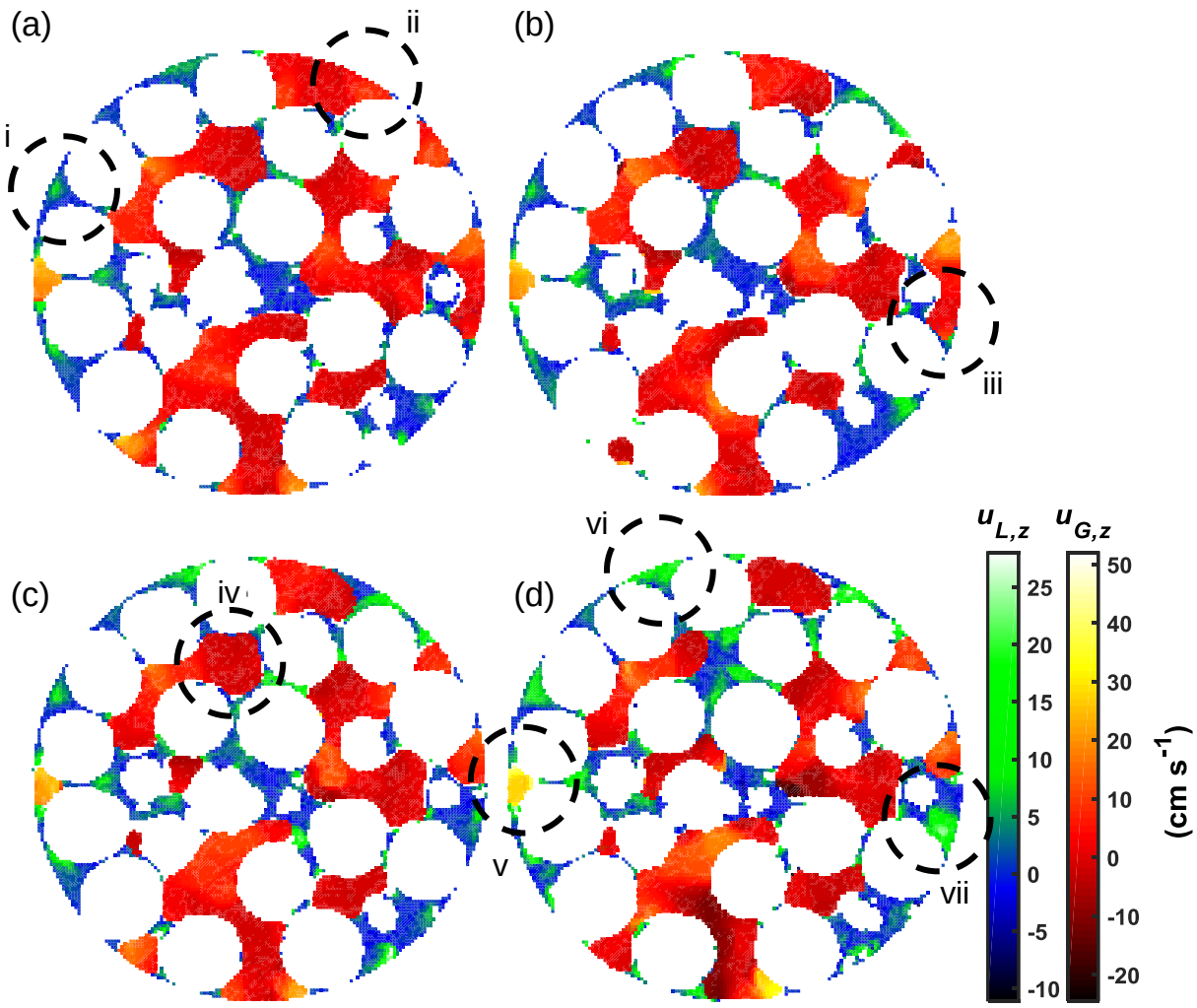

Figure 4.3: 2D axial velocity maps of the trickle bed at a constant gas superficial velocity of V_G = 0.70 cm s^{-1} and four liquid superficial velocities V_L = (a) 0.23 cm s^{-1}, (b) 0.35 cm s^{-1}, (c) 0.46 cm s^{-1} and (d) 0.69 cm s^{-1}. The maps are shown on a single colour scale axis as shown on the far right. The field-of-view for each acquired image is 30 mm × 30 mm, the slice thickness is 1 mm and the diameter of the trickle bed is 27 mm with 5 mm glass beads. Regions which are blank represent regions which contain neither gas nor liquid signal, and are thus either outside the vessel or are the solid phase region. The dotted circles labelled (i-vi) indicate pores which have noteworthy flow effects.

predominantly by increasing the individual liquid velocities of existing high-flow regions. Increasing the liquid superficial velocity does not increase in the average flow of the whole field and does not cause the creation of many more high-flow pores but will instead add to pores which are already flowing with high localised velocity. This effect is visible particularly in pore (i) and pore (vi). Cases of the creation of new pores include pore (vii), which not only sees the development of a new high-flow liquid pore, but additionally the removal of a previously gas-bearing region. This is seen in a few instances, namely pore (ii) where a primarily stagnant region of the gas-carrying pore becomes liquid-bearing from (a) to (b). Additionally, pore (iv) shows gas in (c) but acquires a significant amount of liquid flow in (d) which also shows high local liquid velocity. It is noted that these regions are nearly stagnant

and that no pores of gas which carry high local velocities were impinged upon by increasing liquid flow. Indeed, due to a reduction of overall available area for gas flow, the gas pores showing high flow such as (v) were found to flow at higher velocities with increasing overall liquid flow.

The extent of the inhomogeneity of the velocity field can be assessed using a number of different metrics. Furthermore, the effects of varying the gas and liquid flows on these metrics can be studied. Figure 4.4 (a) and (b) show the maximum deviation from the mean inter-pore velocity within a given flow image expressed as the ratio $|u_{max}|/u_{mean}$. In the case of the liquid,

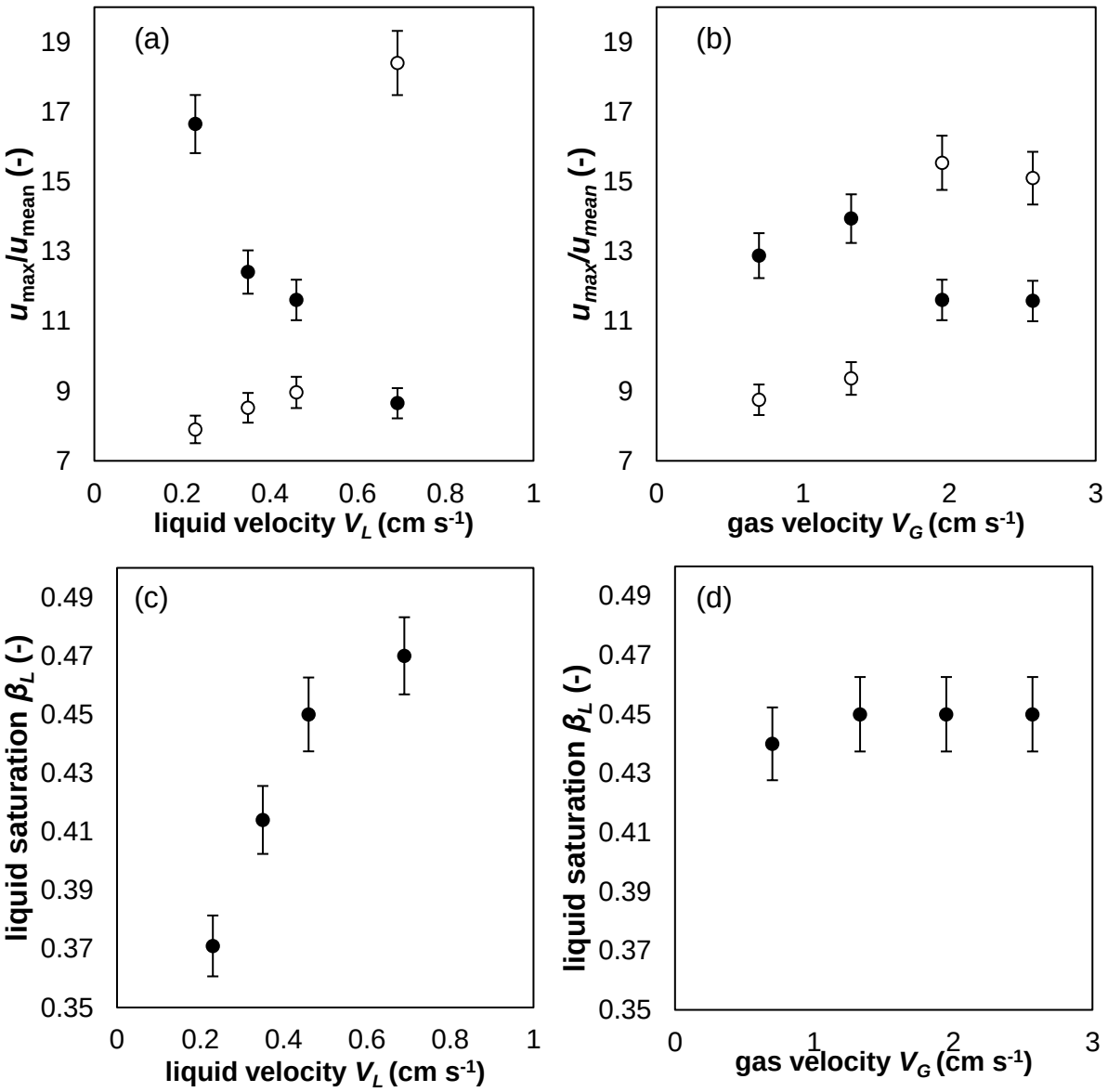

Figure 4.4: The deviation of the highest recorded absolute velocity divided by the mean interstitial velocity u_{max}/u_{mean} shown as a function of both liquid flow rate at constant gas flow (a) and gas superficial velocity at constant liquid flow (b) for both the liquid [●] and gas [○] phases. Also shown is the liquid saturation β_L as a function of the liquid superficial velocity (c) and gas superficial velocity (d). Error bars denote the standard error calculated at the 95% confidence limit.

the maximum velocity was found to vary between approximately 9 and 17 times larger than the average velocity. For the gas, the maximum velocity varied between approximately 8 and 19 times larger than the average figure. In (a), where the gas superficial velocity was held constant at 0.7 cm s^{-1}, the ratio for the liquid phase was found to decrease, indicating that the mean and maximum velocity became closer with increased flow rate. Conversely for the gas phase, the ratio increased which suggests that the field became less homogenous with increasing liquid flow. A less well-defined relationship is demonstrated for the case of constant liquid and varying gas flow in (b). On average the ratio for the gas phase increases with increasing gas flow, and the converse is found for the liquid which shows a slight decrease. The behaviour is much less pronounced than in the case of varying liquid flow, indicating that the homogeneity of both the gas and liquid fields is a stronger function of the liquid flow.

In Figure 4.4 (c) and (d), the in-plane liquid saturation β_L is plotted. This is defined as the fraction of available interstitial pore space occupied by the liquid phase and is important in trickle bed design. In (c), liquid saturation is shown as a function of liquid superficial velocity. Liquid saturation is clearly seen to increase with increasing liquid superficial velocity. This effect was observed qualitatively in Figure 4.3, with several of the regions which at lower flow contained gas being occupied by liquid at higher liquid flow. It can thus be inferred that whilst the additional liquid flow obtained by increasing the superficial velocity is carried mostly by existing high velocity pores, a fraction of the extra flow does serve to increase the cross section of liquid flow regions within the bed through additional catalyst wetting (Figure 4.8) and rivulets. Figure 4.4 (d) shows the liquid saturation as a function of gas flow rate, and shows that saturation is relatively insensitive to increasing the gas flow. This is due to increasing gas flow adding to existent high flow pores, but also at higher flow rates due to the instability of the liquid film close to the transition to pulsing flow.

The pore structure of the slice was analysed using a morphological thinning algorithm similar to that developed by Baldwin [64,65]. This was used to discretise the pore space based on the natural hydraulic radii obtained from the thinning process. The space was discretised into 37 separate pores, which are used for the following analysis. Figure 4.5 shows a parametric plot of $Q(p)/Q(0)$ which is the fraction of the total volumetric flow carried by pores with a flow greater than p plotted as a function of the fraction of the pores carrying this flow for the liquid (solid markers) and gas (white markers).

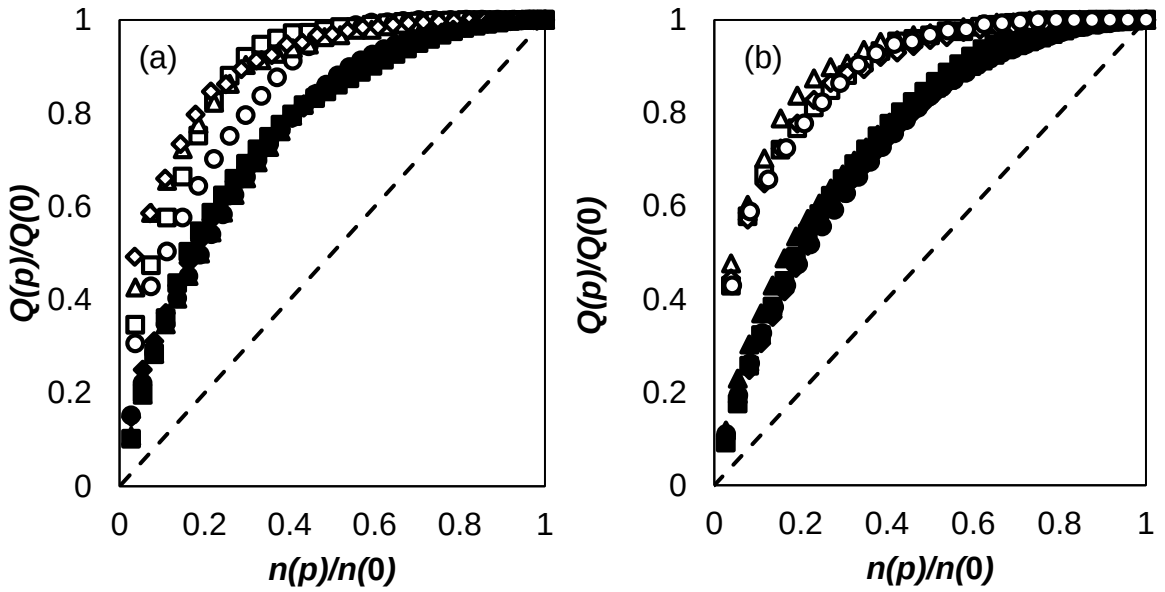

Figure 4.5: Fraction of total flow shown for both the gas phase (white-filled markers) and liquid phase (black solid markers) as a function of the fraction of pores carrying a flow greater than the parametric variable *p* for (a) constant gas superficial velocity V_G = 0.70 cm s^{-1} and (b) constant liquid superficial velocity V_L = 0.46 cm^{-1}. The liquid velocities in (a) are, for gas and liquid data respectively V_L = [○,● 0.23 cm s^{-1}, □,■ 0.35 cm s^{-1}, △,▲ 0.46 cm s^{-1}, ◇,◆ 0.69 cm^{-1}]. The gas velocities in (b) are, for gas and liquid data respectively V_G = [○,● 0.70 cm s^{-1}, □,■ 1.33 cm s^{-1}, △,▲ 1.95 cm s^{-1}, ◇,◆ 2.57 cm^{-1}].

If the flow were ideally and evenly distributed, this parametric curve would lie along the *y=x* line indicated by the dotted line on the axes. The deviation from this ideal line therefore characterises the degree of inhomogeneity of the flow fields. It can thus be observed that both the gas and liquid flow fields show a significant deviation from evenly spatially distributed flow. Figure 4.5 (a) is shown for flow at constant gas and varying liquid velocities, and Figure 4.5 (b) is plotted for constant liquid flow and varying gas flow. The liquid flow rate curve in (a) is relatively insensitive to the changes in liquid flow rate, whilst the gas curves get progressively further from the ideal *y=x* line with increasing liquid flow. This indicates that increasing the liquid flow rate leads to a greater degree of inhomogeneity in the gas field – a result observed in Figure 4.4 (a). It also suggests that the added flow volume is spatially distributed in the same manner as at lower flow rates, which was qualitatively observed in Figure 4.3. In (b) it is observed that both the flow curves are relatively insensitive to changes in the gas flow rate, with the gas curve showing some increase in inhomogeneity but the effect being essentially negligible on the liquid flow distribution.

Figure 4.5 can be used to highlight the extreme lack of homogeneity in the flow fields. For example, in (a) around 50% of the liquid volumetric flow is carried by only 20% of the available pores, and further that 90% of the flow accounts for only 50% of the pore space. For the gas in (a), 50% of the flow is carried by little as 4% and at most 11% of the pore space, indicating

that the vast majority of pores carry low or stationary flow and that only a few pores carry a large amount of the gas. This was qualitatively seen in the images in Figure 4.3. Figure 4.5 (b) illustrates similar levels of inhomogeneity in both flows, with just over 4% of the available pore space carrying approximately 50% of the gas flow at all gas flow rates.

The filling fractions, defined as the cross sectional area of each pore occupied by the liquid χ_L and gas χ_G, respectively called the liquid and gas filling fractions, can be determined for each of the discrete pores. Figure 4.6 shows the liquid (a) and gas (b) filling fraction distributions across the slice as a function of gas flow at constant liquid flow.

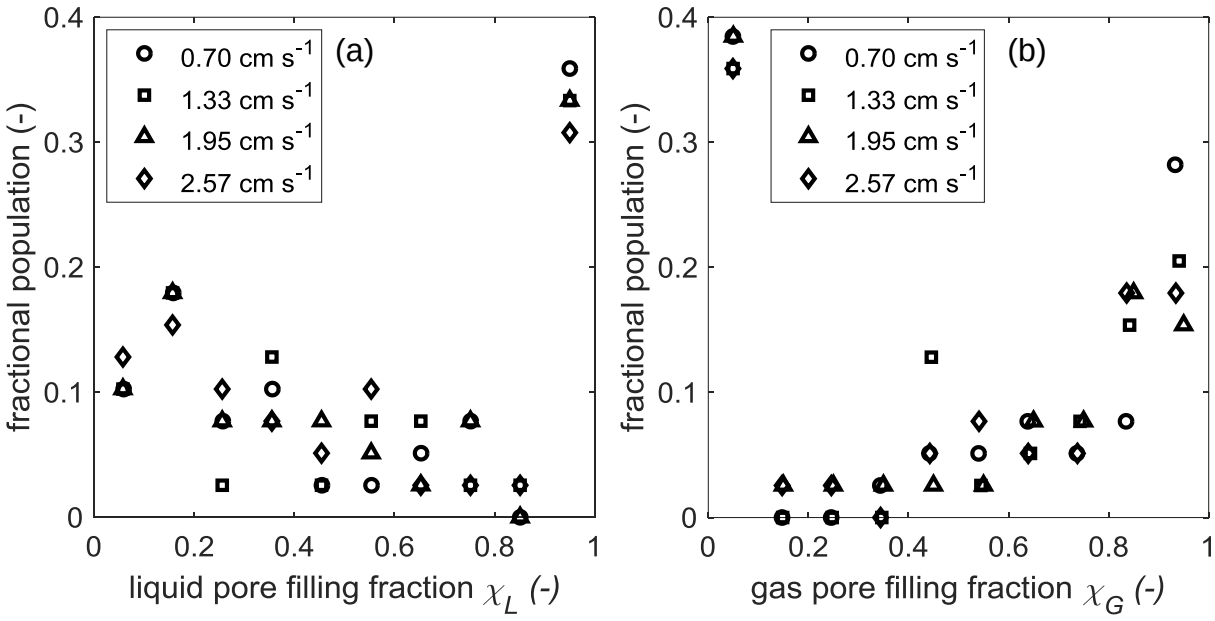

Figure 4.6: Distribution of pore filling fraction shown for both the liquid (a) and gas (b) phases at a constant liquid superficial velocity of V_L = 0.46 cm $^{-1}$ and gas superficial velocities of V_G = [○ 0.70 cm s^{-1}, □ 1.33 cm s^{-1}, △ 1.95 cm s^{-1}, ◇ 2.57 cm^{-1}].

It is noted that it is not strictly true that the gas and liquid fraction sum to unity due to certain areas of the bed lacking signal from either phase. Comparing the liquid and gas distributions reveals that opposite trends are observed in the magnitude of the phase filling fractions. Analysing only pores with both phases present, i.e. filling fraction not equal to unity and zero, it is seen that it is less likely to encounter pores with predominantly liquid flow than predominantly gas flow. Contrary to this trend however, most pores which were filled with one phase were liquid-filled, indicated by the strong peak at one in the liquid distribution (a) and at zero in the gas distribution (b). No strong relationship is observed for changing the gas flow rate in either phase. The series of filling fractions as a function of liquid velocity is given in Figure 4.7.

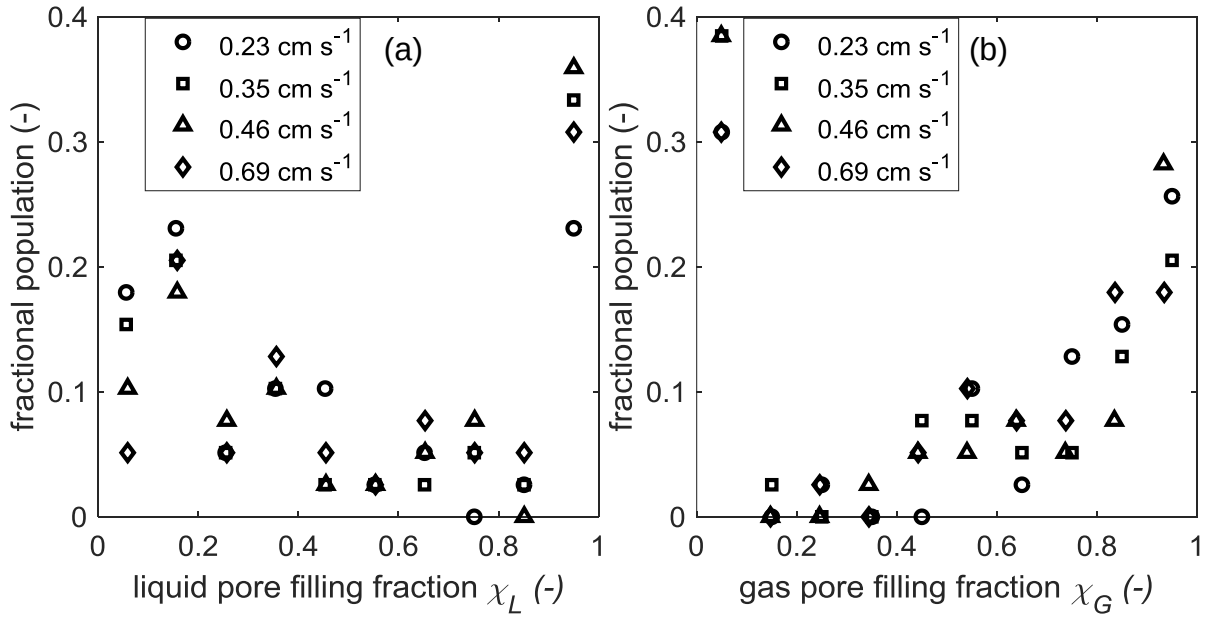

Figure 4.7: Distribution of pore filling fraction shown for both the liquid (a) and gas (b) phases at aconstant gas superficial velocity of V_G = 0.70 cm $^{-1}$ and liquid superficial velocities of V_L =[○ 0.23 cm s^{-1}, □ 0.35 cm s^{-1}, △ 0.46 cm s^{-1}, ◇ 0.69 cm^{-1}].

Similar inverse trends to those observed in Figure 4.6 are seen in the shapes of the distributions when the liquid and gas data are compared. In general, when single-phase filled pores are ignored, fewer pores filled with predominantly liquid were encountered. It is also evident that most pores were entirely liquid filled. As in Figure 4.6, no obvious relationship with the liquid superficial velocity is observed for either phase filling fraction.

An additional method of characterising the degree of solid surface coverage is by calculating the fractional solids wetting efficiency η_W. This parameter is defined as the fraction of total external solids surface area which is covered by the liquid film. In the slice it was calculated by determining which voxels belonged to the solid phase, followed by isolating the surface solid voxels and determining which portion of these were adjacent to voxels which contained signal from the liquid phase. This method has previously been used on MRI data to calculate the wetting efficiency [35,66]. The results of this calculation are shown in Figure 4.8 for the series of experiments at varying liquid superficial velocities (a) and varying gas superficial velocities (b).

It is noted that all wetting efficiencies are found to be higher than 0.68. This can be attributed to the pre-wetting technique of operating the bed in the pulsing regime before data acquisition. In Figure 4.8 (a), the wetting efficiency is found to scale linearly with liquid superficial velocity. This result is consistent with many previous studies [35,67] using MRI and other

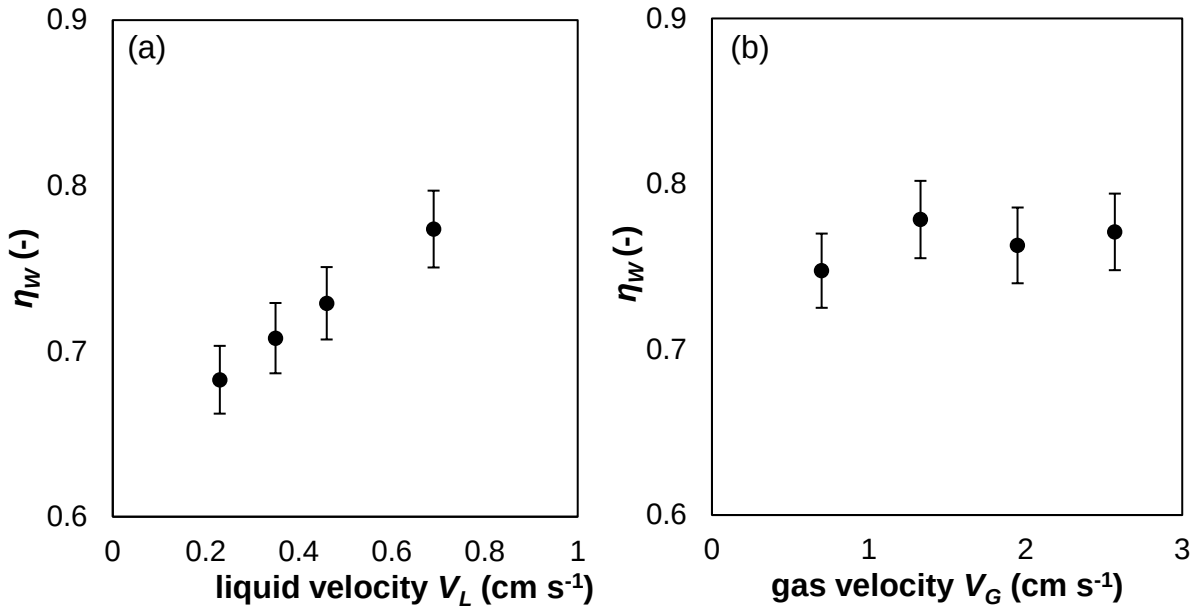

Figure 4.8: Variation of fractional solids wetting efficiency in the slice with liquid (a) and gas (b) superficial velocity. The constant gas velocity for the data in (a) is V_G = 0.70 cm s^{-1} and the constant liquid superficial velocity in (b) is V_L = 0.46 cm s^{-1}. Error bars denote the standard error calculated at the 95% confidence limit.

methods to determine wetting efficiency. In (b), the wetting efficiency is shown as a function of gas superficial velocity. It is evident that the solids wetting efficiency is not a strong function of gas superficial velocity, as the data show no noteworthy change and are mostly constant at ~ 0.75. This result strengthens the argument that the bed hydrodynamics are primarily a function of the liquid superficial velocity, and that the gas flow has a comparably negligible effect on the flow fields, distribution of flow and distribution of solids wetting due to the negligible momentum exchange on behalf of the gas phase.

The full axial velocity distributions are shown in Figures 4.9 and 4.10. In Figure 4.9 (a), the liquid velocity data are shown as a function of varying gas superficial velocity, and correspondingly for Figure 4.9 (b) the gas velocity data are shown for varying liquid superficial velocity. These are presented to show the insensitivity of the liquid flow field to changes in the gas flow, and the insensitivity of the gas flow field to changes in the liquid flow. The distributions are seen to approximately overlap, indicating that the fields are statistically very similar for changes in the corresponding phase flow rate. In Figure 4.10, the liquid flow data are given as a function of varying liquid rate in (a) and (c) and the gas flow data are given as a function of changing gas flow rate in (b) and (d). In Figure 4.10, the curves are shown as a function of local velocity u in (a) and (b) and are also plotted as a function of dimensionless velocity u/V where V is the phase superficial velocity in each case. The liquid axial velocity distribution is consistent with previous results from two-phase flow, showing a strong peak at zero, a long positive tail and a noteworthy portion of backflow. The peak at zero is indicative

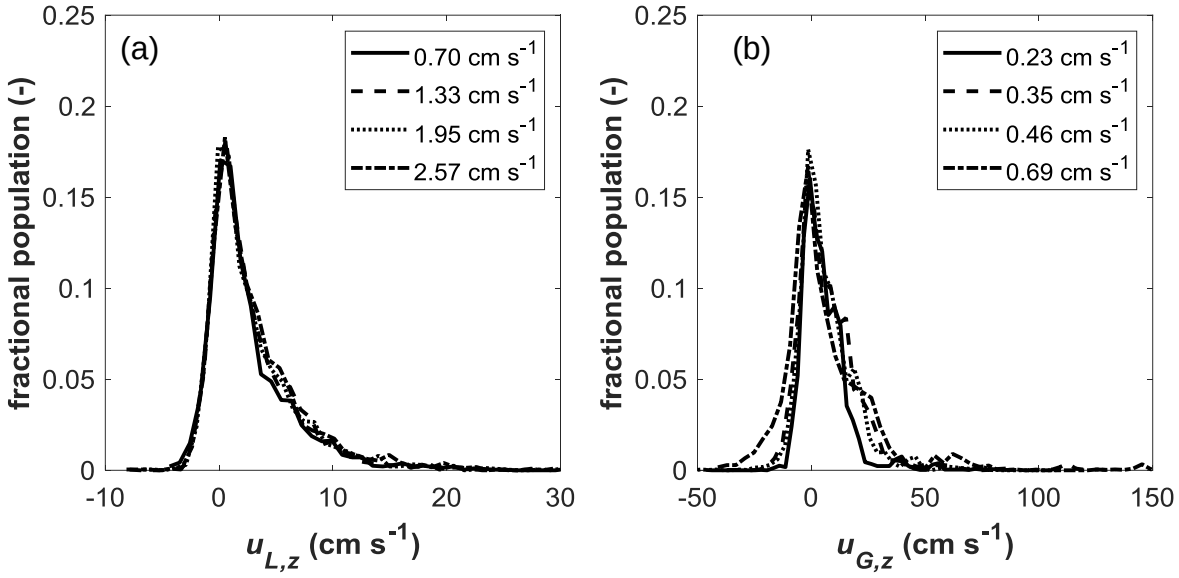

Figure 4.9: Axial local velocity fractional frequency distributions for the (a) liquid as a function of varying gas superficial velocity V_G = 0.70 cm s^{-1}, 1.33 cm s^{-1}, 1.95 cm s^{-1}, 2.57 cm s^{-1} (constant liquid velocity of V_L = 0.23 cm s^{-1}), and (b) gas as a function of varying liquid superficial velocity V_L = 0.23 cm s^{-1}, 0.35 cm s^{-1}, 0.46 cm s^{-1}, 0.69 cm s^{-1} (constant gas velocity of V_G = 0.70 cm s^{-1}).

of the fact that most of the flow in the slice is stationary. It has been previously suggested [43] that the long positive tail fits a double-exponential curve, which indicates the different flow regimes present in the bulk flow and rivulets (and other slow-flowing features). However, in this dataset a noisier tail is observed which has increased fluctuations as the superficial flow is increased. The effect of increasing liquid flow is mainly to broaden the velocity distribution, with an increased frequency of higher flow rates and a reduction of the zero-peak height. Increasing the liquid flow does not strongly affect the degree or shape of the back-flow distribution.

For the gas, a noisier distribution is recorded compared to the liquid axial flow. All four superficial velocities demonstrate a bimodal distribution, with a large peak at zero flow indicating stagnant voxels, and a second peak at just below 10 cm s^{-1}. The presence of this second peak is likely due to the existence of a few discrete gas pores which possess a relatively flat velocity profile. The distributions also show a noteworthy degree of back-flow, most prominently at the V_G = 2.57 cm s^{-1} where another peak emerges at negative flow.

The data from Figure 4.10 (a) and (b) are re-plotted as a function of the dimensionless velocity in (c) and (d). In (c), the liquid axial velocity data clearly collapse onto the same curve, indicating that the flow field scales with the particle Reynolds number in this regime and that the underlying structure of the flow field is consistent across superficial velocities. When analysing the gas, it is evident that the same consistency of structure is not present at all flow

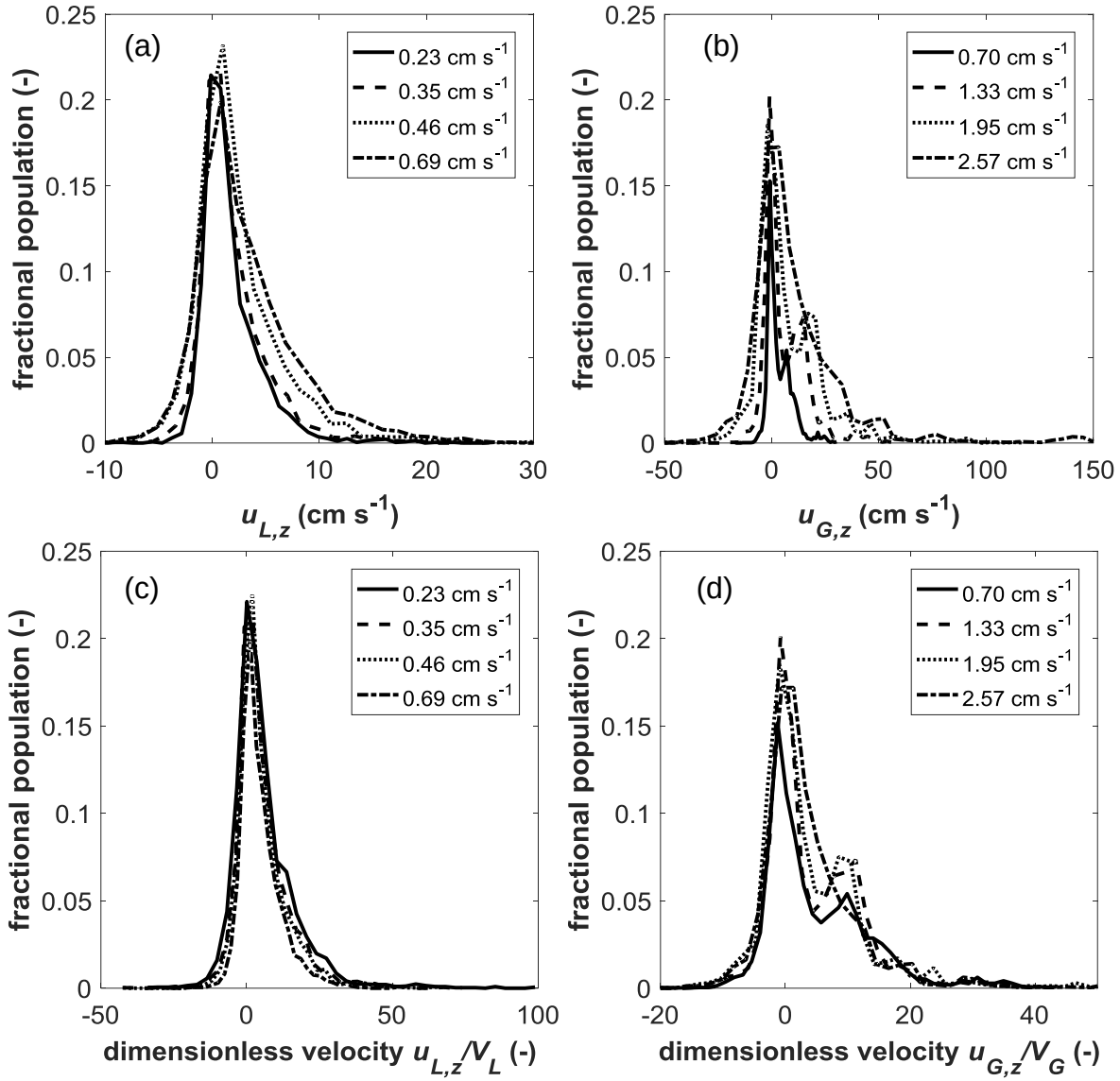

Figure 4.10: Axial local velocity fractional frequency distributions for the (a) liquid as a function of varying liquid superficial velocity V_L = 0.23 cm s^{-1}, 0.35 cm s^{-1}, 0.46 cm s^{-1}, 0.69 cm s^{-1} and (b) gas as a function of varying gas superficial velocity V_G = 0.70 cm s^{-1}, 1.33 cm s^{-1}, 1.95 cm s^{-1}, 2.57 cm s^{-1}. (c) and (d) show the same axial velocity distributions plotted in (a) and (b) but normalised by the superficial velocity in each case to yield the dimensionless velocity distributions.

rates. Notably, the curves from the first three flow rates 0.70 cm s^{-1}, 1.33 cm s^{-1} and 1.95 cm s^{-1} are relatively close in that their zero peaks and secondary peaks align well. The curve at 2.57 cm s^{-1} shows a different structure, notably in the velocity range between the zero and secondary positive peaks of the other curves. Beyond the secondary peak the curves show relatively close agreement. Close agreement is also found in the back-flow region. The difference at this higher gas flow could be due to the onset of flow regime change, as it lies on the border of the low interaction regime and further increase of velocity may see the onset of different pore behaviour and flow profiles in the gas phase.

4.4. DISCUSSION

4.4.1. FLOW VELOCITY IMAGES

Many of the classic features of flow in trickle beds identified and discussed by Al-Dahhan [1] can be directly observed in the images in Figure 4.3. In the centre of the bed, the large connected liquid feature which is predominantly stationary is clearly an example of a stagnant filament. This is confirmed by the images of the radial velocity components. Although these are not reported, the radial *x* and *y* velocity images are also predominantly stationary. Regions like the stagnant filament and pockets observed here are thus truly stationary as flow is not present in any direction. Several stagnant liquid pockets are also present. Fast-flowing liquid films can also be observed, notably in (iv) over the solid surface of the particle. In terms of pore effects, pore (i) demonstrates high flow across all flow rates and is entirely liquid-filled. Pore (ii) loses a portion of its gas flow in raising the liquid velocity from (a) to (b). The same effect is observed in pore (iii) which becomes a region of particularly high liquid flow as seen in (vii). The pore shown in (v) is the most significant gas flow pore, showing particularly high flow consistently and a flat velocity profile. It is also noted that the adjacent liquid at the gas-liquid interface of this pore is also high. These types of features and the overall appearance of the two-phase velocity maps has been recorded previously using MRI [43,47].

Because of this observed non-ideal flow behaviour, transport properties such as heat and mass transfer which are both enhanced by higher fluid velocities will be greatly impeded in most of the slice. This will lead to localised heat and mass transfer rates which are significantly lower from the average values. In a reaction vessel, this would cause differential catalyst utilisation and deactivation rates, as well as channelling of unreacted products. This leads to problems regarding industrial scale-up, as it has been routinely noted that larger vessels exhibit poorer isotropy of transport properties [21]. Here we demonstrate perhaps the only available technique for the recording of local fluid transport information, which could be used for improved design and modelling of catalysts and packing from the perspective of hydrodynamics.

4.4.2. STATISTICS OF INHOMOGENEITY

The objective of the metrics plotted in Figure 4.4 (a) and (b) is to assess the interaction effects of each phase on the statistical homogeneity of the corresponding flow field. Many techniques are incapable of capturing such information inside opaque media non-invasively. It is seen that the liquid flow field effectively becomes slightly more even as the difference between mean

and maximal values decreases with increasing liquid flow. Correspondingly the gas field becomes more uneven, with greater observed deviations between mean and maximal values with increasing liquid rate. This suggests an interaction between the phases on the statistical nature of the corresponding flow fields. This result is consistent with the fact that the liquid has the potential for larger momentum exchange and has more significant viscous and momentum transfer potential than the gas phase. It is thus expected that the hydrodynamic behaviour of the trickle bed is universally affected more by changes in the liquid flow than the gas.

Other workers have employed an X-ray digital industrial radiography (DIR) technique to record local velocities and distributions in trickle bed reactors [68]. This uses an intrusive particle tracking time-of-flight method to record the overall local velocity vector in 2D of various injected tracer particles in a packed bed. They found local deviations in velocity of up to 51 times the superficial liquid velocity. In the present work, deviations as high as 100 times the superficial flow rate for the liquid, as evidenced by the upper bound of the dimensionless velocity axis of Figure 4.6. It was found, as in the study by Salleh *et al.* [68], that this ratio generally decreased for higher superficial velocities. Ratios as high as 48 were recorded for the gas phase.

The changes observed for the gas velocity are suggestive of the approach to flow regime change. A jump in the relative spread of velocities present is observed in the gas phase and a corresponding reduction for the liquid phase. At these mutually high gas and liquid flow values the bed is close to the border of the pulsing regime. The onset of pulsing has previously been used to explain the reductions of liquid saturation observed for increasing gas flow [69]. Here the suggestion is made that approaching the trickle-to-pulse regime boundary causes the observed discontinuity due to the localised onset of film instabilities of some regions causing effects as observed in Figure 4.4 (a). The stabilisation thereafter is possibly attributed to the regime border. It is noted that for both increasing gas and liquid velocity, the flow of the gas field appears to become more inhomogeneous and the liquid appears to become more homogeneous.

4.4.3. LIQUID SATURATION

The total fractional liquid saturation is one of the primary design variables used in trickle bed analysis. It is critical to both design in itself, as it greatly affects aspects of catalyst and hydraulic design, and is frequently used as a correlating parameter in several models and empirical correlations for trickle bed analysis [11]. Saturation can sometimes be expressed in

terms of total liquid holdup, which differs by the void fraction of the bed as holdup is per unit volume of reactor. The amount of liquid present can be measured with a variety of methods [70] including classical gravimetric determinations and tomographic methods using ionising radiation [31]. MRI can provide spatially-resolved local measurements and the data in Figure 4.4 are shown for the slice investigated. In principle this data can be acquired using MRI throughout a 3D space in a single experiment, giving the axial and radial liquid saturation profiles.

Saturation and holdup, as staple measurements of trickle bed analysis, have been recorded by a vast number of workers [69,71–73] and simulated with good accuracy using both phenomenological [74] and numerical approaches [75,76]. The data reported in the literature qualitatively agree with the findings of the present study, in that liquid saturation is seen to increase with liquid flow rate, with the rate of increase slowing at higher liquid superficial flux rates. Similarly, the saturation is shown to decrease with increases in gas superficial flow. The rate of decrease is also shown to diminish, due to the approach of the pulsing regime transition boundary. At this point temporal instabilities in the liquid films cause localised reductions in the liquid present within pores which cause a localised saturation reduction in the area of interest. MRI offers a unique advantage in being able to assess the variations in localised liquid saturation with high spatiotemporal resolution and offer insights into the nature of the trickle-to-pulse regime transition point [14,77].

This is additional evidence for the claim made previously, which is that changing the gas flow has a comparably less significant effect on the hydrodynamics of the bed than changing the liquid flow due to the shear imparted by the gas being orders of magnitude lower than that of the liquid.

4.4.4. PORE-BASED VELOCITY ANALYSIS

Traditional modelling and design of trickle beds has made use of the assumption of plug flow in either the full flow field, for models which treat the phases as a single continuum, or for the individual fluid phases. Even in more sophisticated cases, the flow is simplistically related to the radial porosity distribution in the so-called effective porous medium approach. The majority of these models have not been able to produce the complex flow patterns which have been observed experimentally. This is due to the inability of models which treat properties as continuous spatial functions to predict the complex three phase interactions of the intra-pore space. Figure 4.5 illustrates the extent of this complexity, as it is shown that strong deviations

from plug flow are found for both the gas and the liquid phase, and that the gas phase showed a greater deviation from plug flow than the liquid phase. In a reactive system this implies that there would be a strong degree of spatial anisotropy rates of transport for both heat and mass, with certain pores carrying as much as 10% of the flow individually.

This type of deviation has previously been recorded using MRI velocimetry for single-phase flow, with authors recording that 50% of liquid flow is carried by 12% [65], and 18% [78] of the pores by number. In the latter study, the authors found the distribution of pore volumetric flow rates to compare very favourably with results obtained on the same geometry using lattice-Boltzmann simulations. In a study on two-phase trickle flow, Sankey [79] reported a value of 11% of the pores by number being responsible for 50% of the liquid volumetric flow through the bed. In the present work a value of approximately 20% of the pore space is recorded, which suggests the liquid field is actually slightly better distributed that previously reported. This may be due to the pre-wetting procedure employed or the column to particle diameter ratio, as this is expected to be a strong function of particle size. MRI is possibly the only method which can be readily employed to investigate distributions of this nature, and therefore few studies reporting experimental pore scale statistics of this nature are in the open literature.

4.4.5. FILLING FRACTION PORE ANALYSIS

The classical slit models [74,80] and model by Attou *et al.* [73] for trickle bed flow indirectly make assumptions regarding the extent and distribution of pore filling fraction. The double slit model accounts for potentially dry pores however most approaches assume a stable liquid film which coats the exterior solid surface. Therefore these approaches assume a uniform distribution of pore filling fraction to eliminate the complexity of introducing a distribution of filling fractions. Whilst these models are useful for determining global hydrodynamic behaviour, for the advancement of computational simulations and future design techniques a more sophisticated understanding of the pore-scale statistics is required.

For reaction vessels requiring a heterogeneously catalysed reaction, the ideal scenario would be an even spatial distribution of filling fraction which would give a uniform distribution of reaction kinetics. The precise nature of the desired filling fraction (annular liquid, partial wetting, highly dispersed phase), would be entirely a function of the nature of the reaction itself, the existence of homogenous side reactions and whether reactions were gas-liquid or gas-solid mass transfer limited. It is therefore problematic to encounter a distribution of filling fractions as recorded in Figures 4.6 and 4.7, as this implies that different pores might contain

vastly different reaction schemes and rates. This contributes strongly to the formation of hot spots in exothermic trickle bed systems. The majority of recorded pores were entirely liquid-filled pores, which in this system would restrict gas access to the solid catalyst surface. Similarly we encounter more frequently majority gas-filled pores, which in a three phase reaction would also lead to performance losses. Furthermore, if gas solubility was a key consideration, having mostly single-phase pore flow would dramatically limit the gas-liquid interface to pore necks, which would lead to lower dissolved gas concentrations than if this interfacial area were larger within pores. It is observed in Figure 4.3 that the gas-liquid interface most often occurs at pore necks, or constrictions connecting discrete pores. In this figure the division in filling fractions can also be observed, with several large gas filled pores observable, and connected liquid regions which occupy individual liquid-filled pores. Only a few identified pores, as in Figure 4.3 pore (vii), have a visible gas-liquid, or gas-liquid-solid interface. It is it almost never encountered that pores have an annular liquid structure.

Pore filling fraction distributions have previously been reported which show a similar bimodal form [79,81] with peaks at ~0.2 and ~0.9. In Figure 4.6 and Figure 4.7 of the liquid curves this form is found, with peaks occurring just below 0.2 and 1.0. This is attributed to the existence of surface wetting and rivulets respectively. However in these previous studies the surface wetting peak was found to be larger than the rivulet fraction, which is not the case in the data reported here. In Gladden and Sederman [81] the effect of increasing liquid flow rate was to increase the filling of pores to form rivulets, which is also observed in the current data but to less of an extent.

4.4.6. WETTING EFFICIENCY

Wetting fraction, or solids wetting efficiency, is one of the classical design variables for trickle bed reactors, and the influence of various parameters (temperature, pressure, flow rate, catalyst design and loading) on this quantity has been extensively reviewed and studied [3,5]. Measurement of wetting has been undertaken directly using photographic techniques and coloured dyes [82], MRI [35] and indirectly through reactive studies and residence time distribution estimates [83–86]. The extent of catalyst wetting will dramatically affect access to the catalyst pores in reactive systems, and localised variations will therefore potentially lead to spatially inhomogeneous product distributions where reaction kinetics are determined by the availability of compounds in either phase. Many models assume a uniform distribution of

perfect catalyst wetting but experimental studies universally show that catalyst wetting is almost universally imperfect [73,87].

The data in Figure 4.8 show that wetting efficiency scales positively with liquid macroscopic flow [35,66,67]. This result has been universally observed and is attributed to a corresponding increase in the liquid saturation level with higher liquid flow rates. The error in wetting efficiency determination is primarily related in MRI to the level of gating used in determining which voxels are adjacent to the solid matrix, which Sederman and Gladden [35] found to be on the order of 1%. Although the data appear to scale linearly with liquid flow rate, the actual relationship when tested over a greater range of conditions is found to be sub-linear and several power law correlations have previously been suggested [17,66,67,82]. The effect of gas velocity is not very well studied in open literature [67,74], but it is noted that due to a typical reduction in liquid saturation with increasing gas flow, it is expected that over a greater range of conditions it may be seen that wetting efficiency decreases with increasing gas velocity, certainly at near the onset of pulsing as liquid films become less stable. In this study however, it is seen that gas flow rate within the tested range has minimal effect on the extent of solid wetting, which is expected due to the lower extent of interaction on behalf the gas phase observed.

4.4.7. AXIAL FLOW RATE DISTRIBUTIONS AND FLOW FIELD HOMOGENEITY

The axial velocity distributions of both phases show a strong peak at zero velocity, implying that the flow is predominantly static for both phases. Ideal plug flow would be represented by an σ-function at the mean interstitial velocity. The long positive tail and short negative tail indicate that significant inhomogeneity is present. This sort of form has previously been reported using MRI for both single-phase [46,65,81,88] and two-phase [47,79] flow. It is shown that the zero peaks for two-phase flow are sharper, i.e. sub-exponential, than that of single-phase flow, suggesting a greater degree of stationary flow for two-phase. The fact that the distributions scale with Reynolds number is not surprising, as in the low interaction regime the same structure of flow field is expected within a bed of the same packing length scale in both phases.

Although MRI is unique as a technique which can non-invasively probe spatially resolved velocity distributions in packed beds, Salleh *et al.* [68] presented velocity distributions in trickle beds using an X-ray particle tracking method. These differ from the type presented in the present study which are of the axial component. It is noted that radial distributions were

recorded, and that these were found to be identical and symmetrical on the zero velocity which is expected. The type recorded by Salleh *et al.* [68] are 2D magnitude values, and thus the distributions show no negative values and are strictly positive. These distributions show modal values at the mean interstitial speed of the liquid phase. However upon inspecting the crude streak marks of the particles in their data, it can be seen that a large proportion of the streaklines are horizontal or very small in size. It can thus be inferred that if the axial component were isolated, it would result in a similar form to that observed in the data of this study with a peak close to or at zero axial velocity.

4.5. CONCLUSIONS

This study presents quantitative, spatially encoded velocity maps of the gas and liquid flow fields in a packed bed operated in trickle flow obtained by magnetic resonance. The first in-depth pore-scale analysis of both the gas and liquid velocity fields is undertaken, with the effects of varying the macroscopic flowrates being assessed. These data demonstrate the ability of MR techniques in assessing multiphase flow behaviour in packed beds occurring on length scales less than 200 μm.

The images show the extent of flow maldistribution in multiphase vessels, as the majority of fluid of either phase was found to have near stationary velocity. Small spatial regions of very high flow are responsible for the transport of most of the fluid through the bed. This was confirmed quantitatively using a pore-scale analysis. The gas phase volumetric flow was more poorly distributed than that of the liquid, with sometimes 4% of the available pores responsible for as much as 50% of the gas flow. For the liquid, 50% of the volume was carried by at most 20% of the pores. It was found that the maldistribution in velocity became more pronounced as both the flow of gas and liquid were increased. The gas flow was found to have a smaller effect than that of the liquid due to greater momentum exchange for liquids.

Standard design parameters for trickle beds, including the solids wetting efficiency, liquid saturation and pore filling fraction were calculated. The results for varying gas and liquid flow were consistent with the existing theories, with the liquid flow showing a greater effect on liquid saturation and wetting efficiency. The population of filling fractions showed that most pores were entirely liquid filled, but that probabilities of pores filled with mostly, but not entirely, gas were higher than that for the liquid. It was shown that neither macroscopic flow rate had a significant effect on filling fraction.

These data and subsequent analysis represent the first in-depth characterisation of the liquid and gas velocity fields in a gas-liquid-sold trickle bed reactor. It is unique in providing quantitative, spatially resolved velocity distributions recorded non-invasively. It has been shown using several calculations and representations of the axial flow data that trickle beds in the low interaction regime demonstrate a significant degree of velocity maldistribution, and that this lack of homogeneity can lead to dramatically reduced performance of reaction vessels. These findings show that idealised models assuming even flow across the bed area would lead to dramatically overestimated performances in design.

These results are presented with the aim of improving understanding and visualisation of trickle bed hydrodynamic phenomena. Further investigations are encouraged for constructing and validating more accurate analytical and phenomenological models.

NOMENCLATURE

ABBREVIATIONS

1D, 2D, 3D	one, two or three dimensional
FOV	field-of-view
r.f.	radiofrequency
MRI	magnetic resonance imaging
NMR	nuclear magnetic resonance
TBR	trickle bed reactor

SYMBOLS

G_{read}	read direction magnetic field gradient	T m^{-1}
G_{phase}	phase direction magnetic field gradient	T m^{-1}
G_{slice}	flow encoding magnetic field gradient	T m^{-1}
g	velocity gradient increment	T m^{-1}
n	number of pore	-
p	dimensionless parameter	-
Q	volumetric flow rate	cm^3 s^{-1}
u_L	local liquid velocity	cm s^{-1}
u_G	local gas velocity	cm s^{-1}
$u_{max/mean}$	maximum or mean local velocity	cm s^{-1}
V_L	superficial liquid velocity	cm s^{-1}
V_G	superficial gas velocity	cm s^{-1}
y,x,z	standard cartesian coordinates	-

GREEK LETTERS

β_L	total liquid saturation	-
Δ	observation time for velocity measurement	s
δ	flow encoding gradient pulse time	s
η_W	solids wetting efficiency	-
τ	echo time	s
χ_L	liquid pore filling fraction	-
χ_G	gas pore filling fraction	-

REFERENCES

[1] Al-Dahhan, M.H., Larachi, F., Dudukovic, M.P., Laurent, A. High-Pressure Trickle-Bed Reactors: A Review. *Ind. Eng. Chem. Res.* 1997;36: pp. 3292–314.

[2] Ng, K.M., Chu, C.F. Trickle-bed reactors. *Chem. Eng. Prog.;(United States)* 1987;83.

[3] Gianetto, A., Specchia, V. Trickle-bed reactors: state of art and perspectives. *Chem. Eng. Sci.* 1992;47: pp. 3197–213.

[4] Duduković, M.P., Larachi, F., Mills, P.L. Multiphase catalytic reactors: a perspective on current knowledge and future trends. *Catal. Rev.* 2002;44: pp. 123–246.

[5] Gianetto, A., Baldi, G., Specchia, V., Sicardi, S. Hydrodynamics and solid-liquid contacting effectiveness in trickle-bed reactors. *AIChE J.* 1978;24: pp. 1087–104.

[6] Kolb, W.B., Melli, T.R., De Santos, J.M., Scriven, L.E. Cocurrent downflow in packed beds. Flow regimes and their acoustic signatures. *Ind. Eng. Chem. Res.* 1990;29: pp. 2380–9.

[7] Krieg, D.A., Helwick, J.A., Dillon, P.O., McCreedy, M.J. Origin of disturbances in cocurrent gas-liquid packed bed flows. *AIChE J.* 1995;41: pp. 1653–66.

[8] Holub, R.A., Dudukovic, M.P., Ramachandran, P.A. Pressure Drop, Liquid Holdup, and Flow Regime Transition in Trickle Flow. *AIChE J.* 1993;39: pp. 302–21.

[9] Sederman, A.J., Johns, M.L., Bramley, A.S., Alexander, P., Gladden, L.F. Magnetic resonance imaging of liquid flow and pore structure within packed beds. *Chem. Eng. Sci.* 1997;225: pp. 2239–50.

[10] Mantle, M., Sederman, A.J., Gladden, L. Single- and two-phase flow in fixed-bed reactors: MRI flow visualisation and lattice-Boltzmann simulations. *Chem. Eng. Sci.* 2001;56: pp. 523–9.

[11] Ranade, V., Chaudhari, R., Gunjal, P. Trickle Bed Reactors: Reactor Engineering & Applications. 2011.

[12] Lim, M.H.M., Sederman, A.J., Gladden, L.F., Stitt, E.H. New insights to trickle and pulse flow hydrodynamics in trickle-bed reactors using MRI. *Chem. Eng. Sci.* 2004;59: pp. 5403–10.

[13] Gladden, L.F., Anadon, L.D., Lim, M.H.M., Sederman, A.J., Stitt, E.H. Insights into the mechanism of the trickle-to-pulse transition in trickle-bed reactors. *Ind. Eng. Chem. Res.* 2005;44: pp. 6320–31.

[14] Anadon, L.D., Sederman, A.J., Gladden, L.F. Rationalising MRI, conductance and pressure drop measurements of the trickle-to-pulse transition in trickle beds. *Chem. Eng. Sci.* 2008;63: pp. 4640–8.

[15] Gladden, L.F., Anadon, L.D., Dunckley, C.P., Mantle, M.D., Sederman, A.J. Insights into gas-liquid-solid reactors obtained by magnetic resonance imaging. *Chem. Eng. Sci.* 2007;62: pp. 6969–77.

[16] Anadon, L.D., Lim, M.H.M., Sederman, A.J., Gladden, L.F. Hydrodynamics in two-phase flow within porous media. *Magn. Reson. Imaging* 2005;23: pp. 291–4.

[17] Mills, P.L., Duduković, M.P. Evaluation of liquid-solid contacting in trickle-bed reactors by tracer methods. *AIChE J.* 1981;27: pp. 893–904.

[18] Hanratty, P.J., Duduković, M.P. Detection of flow maldistribution in trickle-bed reactors via tracers. *Chem. Eng. Sci.* 1992;47: pp. 3003–14.

[19] Bieberle, A., Schubert, M., da Silva, M.J., Hampel, U. Measurement of liquid distributions in particle packings using wire-mesh sensor versus transmission tomographic imaging. *Ind. Eng. Chem. Res.* 2010;49: pp. 9445–53.

[20] Ravindra, P. V, Rao, D.P., Rao, M.S. Liquid flow texture in trickle-bed reactors: An experimental study. *Ind. Eng. Chem. Res.* 1997;36: pp. 5133–45.

[21] Schwartz, J., Weger, E., Dudukovic, M.P. A New Tracer Method for Determination of Liquid-Solid Contacting Efficiency in Trickle- Bed Reactors. *AIChE J.* 1976;22: pp. 894–904.

[22] Azzopardi, B.J., Abdulkareem, L.A., Zhao, D., Thiele, S., Da Silva, M.J., Beyer, M., *et al.* Comparison between electrical capacitance tomography and wire mesh sensor output for air/silicone oil flow in a vertical pipe. *Ind. Eng. Chem. Res.* 2010;49: pp. 8805–11.

[23] Tsochatzidis, N.A., Karabelas, A.J., Giakoumakis, D., Huff, G.A. An investigation of liquid maldistribution in trickle beds. *Chem. Eng. Sci.* 2002;57: pp. 3543–55.

[24] Schubert, M., Khetan, A., Da Silva, M.J., Kryk, H. Spatially resolved inline measurement of liquid velocity in trickle bed reactors. *Chem. Eng. J.* 2010;158: pp. 623–32.

[25] Reinecke, N., Mewes, D. Tomographic imaging of trickle-bed reactors. *Chem. Eng. Sci.* 1996;51: pp. 2131–8.

[26] Hamidipour, M., Larachi, F. Characterizing the liquid dynamics in cocurrent gas–liquid flows in porous media using twin-plane electrical capacitance tomography. *Chem. Eng. J.* 2010;165: pp. 310–23.

[27] Nakamura, M., Mori, H., Hori, F., Kitao, T., Adachi, Y., Toyama, S. Visualization of liquid flow in trickle bed reactor by X-ray computed tomography method. Proc. Int. Conf. Multiph. flows '91 Tsukuba, 1991.

[28] Kantzas, A. Computation of holdups in fluidized and trickle beds by computer-assisted tomography. *AIChE J.* 1994;40: pp. 1254–61.

[29] Toye, D., Marchot, P., Crine, M., L'Homme, G. Analysis of liquid flow distribution in trickling flow reactor using computer assisted X-ray tomography. *Chem. Eng. Res. Des.* 1995;73: pp. 258–62.

[30] Toye, D., Marchot, P., Crine, M., L'Homme, G. Modelling of multiphase flow in packed beds by computer-assisted x-ray tomography. *Meas. Sci. Technol.* 1996;7: pp. 436.

[31] Toye, D., Marchot, P., Crine, M., Pelsser, A., M., L'Homme, G. Local measurements of void fraction and liquid holdup in packed columns using X-ray computed tomography. *Chem. Eng. Process. Process Intensif.* 1998;37: pp. 511–20.

[32] van der Merwe, W., Nicol, W., de Beer, F. Trickle flow distribution and stability by X-ray radiography. *Chem. Eng. J.* 2007;132: pp. 47–59.

[33] van der Merwe, W., Nicol, W., de Beer, F. Three-dimensional analysis of trickle flow hydrodynamics: computed tomography image acquisition and processing. *Chem. Eng. Sci.* 2007;62: pp. 7233–44.

[34] Basavaraj, M.G., Gupta, G.S., Naveen, K., Rudolph, V., Bali, R. Local liquid holdups

and hysteresis in a 2-D packed bed using X-ray radiography. *AIChE J.* 2005;51: pp. 2178–89.

[35] Sederman, A.J., Gladden, L.F. Magnetic resonance imaging as a quantitative probe of gas-liquid distribution and wetting efficiency in trickle-bed reactors. *Chem. Eng. Sci.* 2001;56: pp. 2615–28.

[36] Gladden, L.F., Sederman, A.J. Magnetic Resonance Imaging and Velocity Mapping in Chemical Engineering Applications. *Annu. Rev. Chem. Biomol. Eng.* 2017;8: pp. 227–47.

[37] Gladden, L.F. Magnetic resonance: ongoing and future role in chemical engineering research. *AIChE J.* 2003;49: pp. 2–9.

[38] Gladden, L.F. Recent advances in MRI studies of chemical reactors: ultrafast imaging of multiphase flows. *Top. Catal.* 2003;24: pp. 19–28.

[39] Gladden, L.F. Applications of In Situ Magnetic Resonance Techniques in Chemical Reaction Engineering. *Top. Catal.* 1999;8: pp. 87–95.

[40] Gladden, L.F., Akpa, B.S., Anadon, L.D., Heras, J.J., Holland, D.J., Mantle, M.D., *et al.* Dynamic Mr Imaging of Single- and Two-Phase Flows. *Chem. Eng. Res. Des.* 2006;84: pp. 272–81.

[41] Sederman, A.J., Mantle, M.D., Dunckley, C.P., Huang, Z., Gladden, L.F. In situ MRI study of 1-octene isomerisation and hydrogenation within a trickle-bed reactor. *Catal. Letters* 2005;103: pp. 1–8.

[42] Akpa, B.S., Mantle, M.D., Sederman, A.J., Gladden, L.F. In situ 13C DEPT-MRI as a tool to spatially resolve chemical conversion and selectivity of a heterogeneous catalytic reaction occurring in a fixed-bed reactor. *Chem. Commun. (Camb).* 2005: pp. 2741–3.

[43] Gladden, L.F., Abegão, F.J.R., Dunckley, C.P., Holland, D.J., Sankey, M.H., Sederman, A.J. MRI: Operando measurements of temperature, hydrodynamics and local reaction rate in a heterogeneous catalytic reactor. *Catal. Today* 2010;155: pp. 157–63.

[44] Kirillov, V.A., Koptyug, I. V. Critical phenomena in trickle-bed reactors. *Ind. Eng. Chem. Res.* 2005;44: pp. 9727–38.

[45] Lysova, A.A., Koptyug, I. V. Magnetic resonance imaging methods for in situ studies in heterogeneous catalysis. *Chem. Soc. Rev.* 2010;39: pp. 4585–601.

[46] Kutsovsky, Y.E., Scriven, L.E., Davis, H.T., Hammer, B.E. NMR imaging of velocity profiles and velocity distributions in bead packs. *Phys. Fluids* 1996;8: pp. 863.

[47] Sankey, M.H., Holland, D.J., Sederman, A.J., Gladden, L.F. Magnetic resonance velocity imaging of liquid and gas two-phase flow in packed beds. *J. Magn. Reson.* 2009;196: pp. 142–8.

[48] Newling, B., Poirier, C.C., Zhi, Y., Rioux, J.A., Coristine, A.J., Roach, D., *et al.* Velocity Imaging of Highly Turbulent Gas Flow. *Phys. Rev. Lett.* 2004;93: pp. 154503.

[49] Newling, B. Gas flow measurements by NMR. *Prog. Nucl. Magn. Reson. Spectrosc.* 2008;52: pp. 31–48.

[50] Albert, M.S., Balamoreb, D. Development of hyperpolarised noble gas MRI. *Nucl. Instruments Methods Phys. Res. A* 1998;402: pp. 441–53.

[51] Bouchard, L.-S., Burt, S.R., Anwar, M.S., Kovtunov, K. V., Koptyug, I. V., Pines, A. NMR Imaging of Catalytic Hydrogenation in Microreactors with the Use of para-Hydrogen. *Science (80-.).* 2008;319: pp. 442–5.

[52] York, A.P.E., Watling, T.C., Ramskill, N.P., Gladden, L.F., Sederman, A.J., Tsolakis, A., *et al.* Visualization of the Gas Flow Field within a Diesel Particulate Filter Using Magnetic Resonance Imaging. SAE Technical Paper; 2015.

[53] Ramskill, N.P., York, A.P.E., Sederman, A.J., Gladden, L.F. Magnetic resonance velocity imaging of gas flow in a diesel particulate filter. *Chem. Eng. Sci.* 2017;158: pp. 490–9.

[54] Koptyug, I. V, Altobelli, S.A., Fukushima, E., Matveev, A. V, Sagdeev, R.Z. Thermally polarized 1H NMR microimaging studies of liquid and gas flow in monolithic catalysts. *J. Magn. Reson.* 2000;147: pp. 36–42.

[55] Boyce, C.M., Ozel, A., Rice, N.P., Rubinstein, G.J., Holland, D.J., Sundaresan, S. Effective particle diameters for simulating fluidization of non-spherical particles: CFD-DEM models vs. MRI measurements. *AIChE J.* 2017;63: pp. 2555–68.

[56] Boyce, C.M., Rice, N.P., Ozel, A., Davidson, J.F., Sederman, A.J., Gladden, L.F., *et al.* Magnetic resonance characterization of coupled gas and particle dynamics in a bubbling fluidized bed. *Phys. Rev. Fluids* 2016;1: pp. 74201.

[57] Boyce, C.M., Rice, N.P., Sederman, A.J., Dennis, J.S., Holland, D.J. 11-interval PFG pulse sequence for improved measurement of fast velocities of fluids with high diffusivity in systems with short T 2∗. *J. Magn. Reson.* 2016;265: pp. 67–76.

[58] Boyce, C.M., Rice, N.P., Davidson, J.F., Sederman, A.J., Dennis, J.S., Holland, D.J. Magnetic resonance imaging of gas dynamics in the freeboard of fixed beds and bubbling fluidized beds. *Chem. Eng. Sci.* 2016;147: pp. 13–20.

[59] Kuethe, D.O., Pietraß, T., Behr, V.C. Inert fluorinated gas T1 calculator. *J. Magn. Reson.* 2005;177: pp. 212–20.

[60] Holland, D.J., Gladden, L.F. Less is More: How Compressed Sensing is Transforming Metrology in Chemistry. *Angew. Chemie Int. Ed.* 2014;53: pp. 13330–40.

[61] Holland, D.J., Malioutov, D.M., Blake, A., Sederman, A.J., Gladden, L.F. Reducing data acquisition times in phase-encoded velocity imaging using compressed sensing. *J. Magn. Reson.* 2010;203: pp. 236–46.

[62] von Harbou, E., Fabich, H.T., Benning, M., Tayler, A.B., Sederman, A.J., Gladden, L.F., *et al.* Quantitative mapping of chemical compositions with MRI using compressed sensing. *J. Magn. Reson.* 2015;261: pp. 27–37.

[63] Gladden, L.F., Sederman, A.J. Recent advances in flow MRI. *J. Magn. Reson.* 2013;229: pp. 2–11.

[64] Baldwin, C., Sederman, A.J., Mantle, M.D., Alexander, P., Gladden, L.F. Determination and characterization of the structure of a pore space from 3D volume images. *J. Colloid Interface Sci.* 1996;92: pp. 79–92.

[65] Sederman, A.J., Johns, M.L., Alexander, P., Gladden, L.F. Structure-flow correlations in packed beds. *Chem. Eng. Sci.* 1998;53: pp. 2117–28.

[66] Gladden, L.F., Lim, M.H.M., Mantle, M.D., Sederman, A.J., Stitt, E.H. MRI

visualisation of two-phase flow in structured supports and trickle-bed reactors. *Catal. Today* 2003;79–80: pp. 203–10.

[67] Al-Dahhan, M.H., Duduković, M.P. Catalyst wetting efficiency in trickle-bed reactors at high pressure. *Chem. Eng. Sci.* 1995;50: pp. 2377–89.

[68] Salleh, K.A.M., Lee, H.K., Al-Dahhan, M.H. X-ray Digital Industrial Radiography (DIR) for local liquid velocity (VLL) measurement in trickle bed reactors (TBRs): Validation of the technique. *Rev. Sci. Instrum.* 2014;85.

[69] Larachi, F., Laurent, A., Midoux, N., Wild, G. Experimental study of a trickle-bed reactor operating at high pressure: two-phase pressure drop and liquid saturation. *Chem. Eng. Sci.* 1991;46: pp. 1233–46.

[70] Clements, L.D., Schmidt, P.C. Dynamic liquid holdup in two-phase downflow in packed beds: air-silicone oil system. *AIChE J.* 1980;26: pp. 317–9.

[71] Larachi, F., Laurent, A., Wild, G., Midoux, N. Some Experimental Liquid Saturation Results in Fixed-Bed Reactors Operated under Elevated Pressure in Cocurrent Upflow and Downflow of the Gas and the Liquid. *Ind. Eng. Chem. Res.* 1991;30: pp. 2404–10.

[72] Benkrid, K., Rode, S., Midoux, N. Prediction of pressure drop and liquid saturation in trickle-bed reactors operated in high interaction regimes. *Chem. Eng. Sci.* 1997;52: pp. 4021–32.

[73] Attou, A., Boyer, C., Ferschneider, G. Modelling of the hydrodynamics of the cocurrent gas-liquid trickle flow through a trickle-bed reactor. *Chem. Eng. Sci.* 1999;54: pp. 785–802.

[74] Iliuta, I., Larachi, F. The generalized slit model: Pressure gradient, liquid holdup & wetting efficiency in gas–liquid trickle flow. *Chem. Eng. Sci.* 1999;54: pp. 5039–45.

[75] Lopes, R.J.G., Quinta-Ferreira, R.M. CFD modelling of multiphase flow distribution in trickle beds. *Chem. Eng. J.* 2009;147: pp. 342–55.

[76] Lopes, R.J.G., Quinta-Ferreira, R.M. Three-dimensional numerical simulation of pressure drop and liquid holdup for high-pressure trickle-bed reactor. *Chem. Eng. J.* 2008;145: pp. 112–20.

[77] Anadon, L.D., Sederman, A.J., Gladden, L.F. Mechanism of the Trickle-to-Pulse Flow Transition in Fixed-Bed Reactors. *AIChE J.* 2006;52: pp. 1522–32.

[78] Mantle, M.D., Sederman, A.J., Gladden, L.F. Single- and two-phase flow in fixed-bed reactors: MRI flow visualisation and lattice-Boltzmann simulations. *Chem. Eng. Sci.* 2001;56: pp. 523–9.

[79] Sankey, M. Velocity Mapping in Trickle-Bed Reactors and Multiphase Systems Using MRI. University of Cambridge, 2008.

[80] Iliuta, I., Larachi, F., Al-Dahhan, M.H. Double-slit model for partially wetted trickle flow hydrodynamics. *AIChE J.* 2000;46: pp. 597–609.

[81] Sederman, A.J., Gladden, L.F. Magnetic resonance visualisation of single-and two-phase flow in porous media. *Magn. Reson. Imaging* 2001;19: pp. 339–43.

[82] Baussaron, L., Julcour-Lebigue, C., Wilhelm, A.M., Delmas, H., Boyer, C. Wetting Topology in Trickle Bed Reactors. *AIChE J.* 2007;53: pp. 1850–60.

[83] Colombo, A.J., Baldi, G., Sicardi, S. Solid-liquid contacting effectiveness in trickle bed reactors. *Chem. Eng. Sci.* 1976;31: pp. 1101–8.

[84] Herskowitz, M., Carbonell, R.G., Smith, J.M. Effectiveness factors and mass transfer in trickle-bed reactors. *AIChE J.* 1979;25: pp. 272–83.

[85] Schwartz, J.G., Weger, E., Duduković, M.P. A new tracer method for determination of liquid-solid contacting efficiency in trickle-bed reactors. *AIChE J.* 1976;22: pp. 894–904.

[86] Llano, J.J., Rosal, R., Sastre, H., Díez, F. V. Determination of Wetting Efficiency in Trickle-Bed Reactors by a Reaction Method. *Ind. Eng. Chem. Res.* 1997;36: pp. 2616–25.

[87] Holub, R.A., Duduković, M.P., Ramachandran, P.A. A phenomenological model for pressure drop, liquid holdup, and flow regime transition in gas-liquid trickle flow. *Chem. Eng. Sci.* 1992;47: pp. 2343–8.

[88] Sederman, A.J., Johns, M.L., Alexander, P., Gladden, L.F. Visualisation of structure and flow in packed beds. *Magn. Reson. Imaging* 1998;16: pp. 497–500.

CHAPTER 5 – GAS AND LIQUID VELOCITY AND SHEAR STRESS AT THE PHASE INTERFACE

5.1. INTRODUCTION AND THEORY

Trickle-bed reactors are fixed-bed reactors with a co-current down-flow of liquid and gas. They are the most widely used three-phase reactors in industrial practice and find application in large-scale petrochemical processes such as hydrotreating and hydrocracking, as well as in hydrogenation and oxidation reactions for the synthesis of fine chemicals, and oxidative wastewater treatment [1]. Trickle-bed reactors are known to exhibit significant heterogeneity in reaction rate owing to spatial variations in the fluid flow in the reactor [2,3]; this may result in a reduction in catalyst effectiveness, and hence an increase in energy demand of the process. Chapter 4 in this thesis showed that the degree of heterogeneity of two-fluid reactor vessels is higher than that in single-phase flow through porous beds. There is, therefore, much interest in developing analytical, experimental and numerical tools to optimise the design of trickle bed reactors. Several approaches have been employed which attempt to describe the important TBR design variables of pressure drop, liquid holdup and flow regime transition. This task is inherently challenging due to the complexity and in some cases inherent nonlinearity of the physical processes at work which govern two-phase flow within a bed of packed solids. Early models include the relative permeability model of Saez and Carbonell [4], the slit models [5–7] and the two-fluid interaction model [8,9]. These phenomenological approaches attempt to overcome the complexity of the system by either treating the anisotropy in porosity and tortuosity statistically, through averaged lumped parametrisation, or by describing phase behaviour through macroscopic parameters. The permeability and slit models in particular use an Ergun-like approach as a building block for establishing the pressure drop. The slit model [5,6] and slit model extensions [7,10] model the complex geometry of the inter-pore space by an inclined-slit approximation. As models have become more sophisticated, they have moved from the realm of purely being used to predict macroscopic behaviour such as pressure drop, and are being used to gain insights into the physics of trickle flow.

Numerical simulations have also been used successfully to describe fluid flow in trickle beds, and to analyse existing designs for diagnostic purposes [11–16]. In all cases, a key closure problem lies in deciding the extent to which the phases all physically interact with one another. This is particularly tricky in the case of the influence of the gas phase on the liquid. In the

earliest models, essentially no interaction was assumed, in particular no shear stress at the gas-liquid interface. This assumption was considered justifiable in the low interaction regime, which by definition includes mutual flow rates for both fluids which are said not to cause significant interfacial interaction. This assumption was found to be justified for a number of experimental and lab-scale studies whose data were tested against the model at atmospheric conditions [17,18]. However, systematic under-prediction of the pressure drop at elevated pressures and gas flow rates was quickly observed when experimentation allowed these conditions to be studied [19–23]. These studies suggested that the amount of interaction on behalf of the gas phase on the liquid phase was significant, and posited this as the reason for deviations observed in the early models which neglected this interaction. It was clear that under certain conditions, it was necessary to account for the non-negligible momentum transfer at the interface between the gas and liquid, and further the effect of the gas phase flow and pressure on the solid-liquid momentum exchange terms.

Following these suggestions, Al-Dahhan *et al.* [22] proposed a modified version of the slit model, including the so-called "slip factors" which accounted for varying levels of interaction between the phase velocity and shear stress fields. These factors in themselves do not have a direct physical meaning but represent an average of the spatio-temporal interaction of the phases across the bed. Clearly this represents an oversimplification of naturally complex behaviour, however a useful improvement was achieved and allowing for this interaction is clearly an improvement on a model which does not allow any interaction. Additionally, Attou and Ferschneider [8,24] developed the two-fluid interaction model which developed estimates for the drag coefficients between all the phases and provided an improvement for predicting macro-scale parameters at elevated conditions. Furthermore in numerical studies employing the Euler-Euler approach, the momentum balances require a closure model to describe the drag at the gas-liquid interface. The problem of phase closure and coupling is thus important and much remains to be understood about this question, as well as the role of the stability of the interface in phase transition.

The slip factors were originally defined as the ratios of gas and liquid velocities u and shear stresses τ at the interface by Holub *et al.* [6]:

$$f_v = \frac{u_{G,i}}{u_{L,i}}, \tag{5.1}$$

$$f_\tau = \frac{\tau_{L,i}}{\tau_{G,i}}. \tag{5.2}$$

In the model by Al-Dahhan *et al.*[22], the slip factors were found through empirical correlation and dimensional analysis for a limited range of experimental data. Iliuta *et al.* [18] undertook a more thorough treatment and performed a neural network estimation of slip factors based on a more extensive database. These showed further improvements of the predictive capability of the original and extended Holub models, in which slip factors account for phase interaction. Until now however, the extent and nature of phase interaction in a trickle bed reactor has never been directly experimentally assessed. The primary objective of this study is to demonstrate the ability of MRI to provide validation for interaction forces, as this chapter presents the first quantitative, direct measurement of phase behaviour at the interface of a trickle bed at high spatial resolution. The localised physical validity of the slip relations is assessed at the phase interface – the proposed location for phase interaction. This is done by isolating the phase interface and estimating the spatial correlation in velocity and shear stress.

Magnetic resonance imaging (MRI) is very well suited to probe this localised motion of fluids in a non-invasive manner [25–28]. MRI is well-established as a technique for measurement of local liquid velocity distributions and to study structure flow-relationships for single-phase flow in packed beds [29–32]. Imaging of the liquid distributions during gas-liquid, two-phase flow in packed beds has been used to characterise flow patterns and to measure wetting efficiency in trickle-flow [33]. More recently the Gladden group [28,34] has extended the technique to velocity imaging two-phase flows and demonstrated the acquisition of 3D liquid velocity maps for all three spatial velocity components for two-phase flow in a packed bed at an isotropic resolution of 266 μm.

Velocity imaging of gas flow is considerably more challenging than velocity imaging of liquid flow because the typical nuclear spin density, and hence MR signal available, of gases is 100 - 1000 times lower than that of liquids. Further, the diffusivity of gases is faster than liquids. Both of these effects act to decrease the spatial resolution of gas phase images compared to their liquid counterparts. A common method to overcome the low signal-to-noise ratio resulting from the low nuclear spin density of gases is enhancement of magnetization through hyperpolarisation techniques [35–37]. However, hyperpolarised gases are either expensive or impractical to produce at high flow rates such as those required for use in trickle-beds. In

addition, the hyperpolarisation is short-lived and often destroyed when the hyperpolarised species contact interfaces and quantification of the acquired signal is not straightforward. Therefore, methods to obtain sufficient signal for gas phase imaging from thermally polarised gases have been reported [38–41]. The present study uses thermally-polarised pressurised SF_6 gas for its favourable characteristics described in Chapter 4. Sankey *et al.* [34] acquired the first combined maps of gas and liquid distribution and velocity in trickle-flow by imaging water and SF_6 employing ^{1}H and ^{19}F NMR, respectively. However, the in-plane spatial resolution of the gas velocity map was limited to 708 μm × 708 μm (48 × 48 volume elements, or voxels) compared to the spatial resolution of the liquid velocity map which was 176 μm × 176 μm (256 × 256 volume elements, or voxels). Thus, it was not possible to perform a quantitative analysis of the gas and liquid velocities at the gas-liquid interface within the fixed bed. To overcome this problem, compressed sensing (CS) MRI is used to enable an increase of the achievable spatial resolution of the gas phase velocity image. CS is becoming increasingly popular as a method for reconstructing high quality images from undersampled datasets; the approach is not limited to MR data acquisition [42–44]. In application to MR flow imaging, Holland *et al.* [45] have previously demonstrated that it is possible to significantly increase the spatial resolution in images of single-phase flow by undersampling the data by 70 % and reconstructing with CS. It was shown that this approach led to an error in the flow rate measurement of <3 % - a threefold improvement over conventional acquisition techniques.

The aim of the present work is to acquire gas and liquid velocity maps of two-phase flow in a trickle-bed at a high enough spatial resolution to unambiguously identify the gas-liquid interface and to measure the velocities of both phases at the interface. To do this a CS MRI technique has been implemented to reduce the acquisition time of gas phase imaging by 80 %. This increase in data acquisition rate allows greater signal averaging over a given total data acquisition time, thereby enabling acquisition of gas phase velocity maps at significantly higher spatial resolution than has previously been reported [34]. The resulting gas and liquid velocity maps are then analysed in order to validate and inform the use of slip factors on a local level for the modelling of multiphase flow interactions in TBRs. The data are presented at several gas and liquid flow rates to assess the sensitivity of the flow fields to the changes in macroscopic flow conditions and probe interactions. The present techniques can hypothetically be extended to investigate reactive trickle beds under considerably higher pressures and gas and liquid throughput rates which are relevant to industrial conditions. The techniques may in principle be used to validate any suggested phenomenological multiphase closure model.

5.2. EXPERIMENTAL

The experimental setup and operating procedures have previously been described in detail in Chapter 4, with additional equipment details specified in Chapter 3. The apparatus and operating procedures were identical to those described in Chapter 3.

5.2.1. METHOD OF IDENTIFYING PHASE INTERFACES

The phase interfaces were identified by initially applying a binary gating strategy to the spatially-encoded intensity images. It is important to consider the signal level at which binary gating is chosen, as the voxels in an MRI image may exist in a region of space which contains, due either to geometry or the nature of the system, a partial amount of either phase. The gating level chosen will influence whether each discrete voxel is therefore assigned to either the gas or the liquid phase, or both. This is especially true at the phase edges or interface, as curves in the system phase boundary geometry lead to so-called "partial volume" effects which account for diminished signal intensity in these regions. The binary gate assigns voxels containing liquid signal above the chosen threshold a value of unity, whilst all other voxels below this threshold are assigned a nil value. The distribution of intensity of an MR image typically yields a bimodal distribution with a peak which is Rayleigh-distributed representing the noise at lower intensity than the true signal, a normally-distributed peak. A threshold value sufficient to eliminate all the noise voxels is typically required, and in this thesis a value equal to four standard deviations above the noise mean is used to ensure all true velocity signal is retained.

The binary intensity map of each phase is then subject to further analysis to identify the edges. The morphological thinning algorithm as detailed by Baldwin [46] was implemented to identify these voxels. In this, any voxels which are 4-connected to a value of zero are "thinned" or shed away and in the following step of the iteration assigned a value of zero. Thus, only the first step of this iterative process is required, and the indices of these voxels are retained and identified as the edge of each phase. This process is illustrated in Figure 5.1 in which the edges identified by the first step of the Baldwin thinning algorithm are shown in black for the liquid (Figure 5.1 (a)) and gas (Figure 5.1 (b)). It is noted that in several cases, voxels for both the gas and liquid images are assigned values of unity. In these, the phase interface is either running through the voxel, or there is overlap of phases in the vertical direction due to the use of an excitation slice of finite thickness. These regions are expected to have occurred due to rivulets of liquid flowing over a particle located immediately under the slice. These are therefore

included in the phase interfacial region calculations. They are however excluded for the calculations of the shear stress, as this calculation is made to determine the component of the vertical shear which lies perpendicular to each phase boundary.

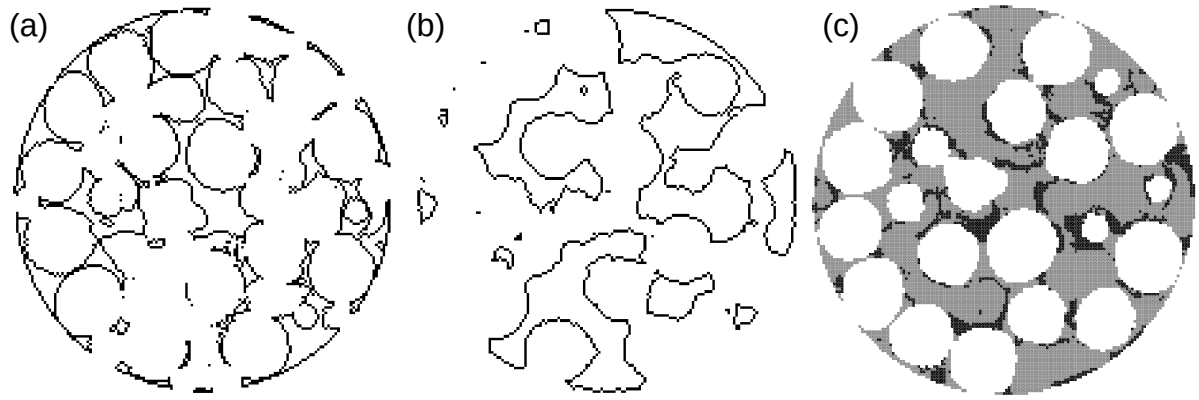

Figure 5.1: Illustration of phase interface identification using a morphological thinning algorithm. The liquid edges are shown in (a), gas edges in (b) and in (c) the regions of phase overlap caused using a finite thickness slice excitation are shown by the black regions. Grey regions in (c) are the filled inter-pore space and the white regions belong to the solid phase or are outside the bed.

5.2.2. CALCULATION OF THE SHEAR STRESS

The procedure for calculating the phase shear stresses is illustrated in Figure 5.2.

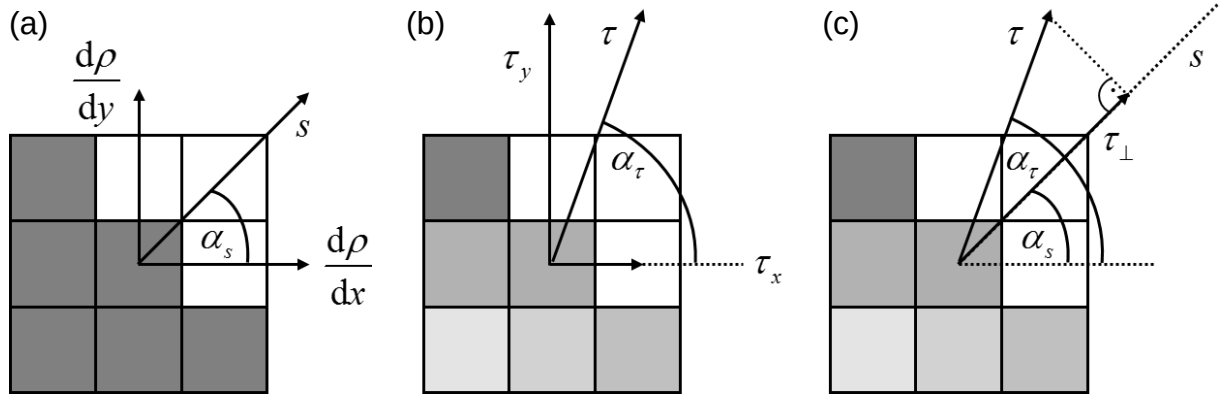

Figure 5.2: Illustration of the calculation of the surface orientation normal vector *S* via numerical differentiation of the intensity image (a), and numerical differentiation of the velocity fields to determine the orthogonal Cartesian components of the stress tensor (b), in order to calculate the component of the in-plane shear stress perpendicular to the phase surfaces $\tau_\perp$.

The shear stress τ is defined as:

$$\tau_{ij} = \mu \frac{du_i}{dx_i}, \tag{5.3}$$

where μ is the fluid viscosity, u the velocity and x the special dimension for a 1D stress calculation. The full shear stress tensor for all three spatial dimensions i and velocity components j would require the acquisition of a 3D volume image of the u_x, u_y and u_z components of the flow rather than just a 2D slice. However, the component of the shear stress tensor of particular interest in axial fixed bed design is the component of the shear stress within

the horizontal plane that is perpendicular to the main flow direction (i.e., vertically oriented surfaces). To estimate the magnitude of the shear stress component normal to the interface in the complex geometry inside the packed bed, the orientation of the interface was calculated from the binary phase map as shown in Figure 5.2 (a). The local orientation angle was calculated from the gradient of the phase distribution map in both the *x*- and *y*-direction over an area of 3 × 3 voxel. The surface orientation angle α_s was then defined as:

$$\alpha_s = \operatorname{atan}\left(\frac{d\rho}{dy}\Big/\frac{d\rho}{dx}\right). \tag{5.4}$$

In each gas- or liquid-filled voxel the shear rate in the *x*-direction caused by axial flow was calculated using a finite difference approximation of the velocity partial derivative surfaces in the orthogonal Cartesian directions *x* and *y*. The modulus $|\boldsymbol{\tau}|$ and angle α_τ of the in-plane shear stress vector were calculated from the *x*- and *y*-components of the Cartesian shear stresses, shown in Figure 5.2 (b). As illustrated in Figure 5.2 (c), the component of the shear stress perpendicular to the surface was then calculated using:

$$\tau_\perp = |\boldsymbol{\tau}| \cos(\alpha_\tau - \alpha_s). \tag{5.5}$$

5.3. RESULTS AND DISCUSSION

5.3.1. INTERFACIAL VELOCITY DISTRIBUTIONS

In Chapter 4 the velocity distributions of the liquid and gas phases flowing in a packed bed slice were analysed, however in the present chapter those exclusively at the phase interfaces are characterised. The axial velocity distributions of the gas and liquid phases at the gas-liquid interface are given in Figure 5.3. Here, changes in the distribution are studied both as a function of changing liquid and gas superficial velocity. Figure 5.3 (a) and (b) give the axial (*z*-component) velocity distributions of the liquid phase as a function of liquid superficial velocity at two different gas superficial velocities, 0.70 cm s^{-1} and 1.95 cm s^{-1} respectively. Figure 5.3 (c) and (d) give the distribution of gas axial velocities at different gas superficial velocities for two different liquid superficial velocities, 0.23 cm s^{-1} and 0.46 cm s^{-1} respectively. The distributions are similar in shape to those previously observed for the overall velocity distribution of fluids in trickle flow. Each has a strong peak at zero, indicating that the majority of interfacial flow for both phases is static. Each distribution has a long positive tail, with a smaller negative tail which is indicative of some backflow at the phase boundary. It has

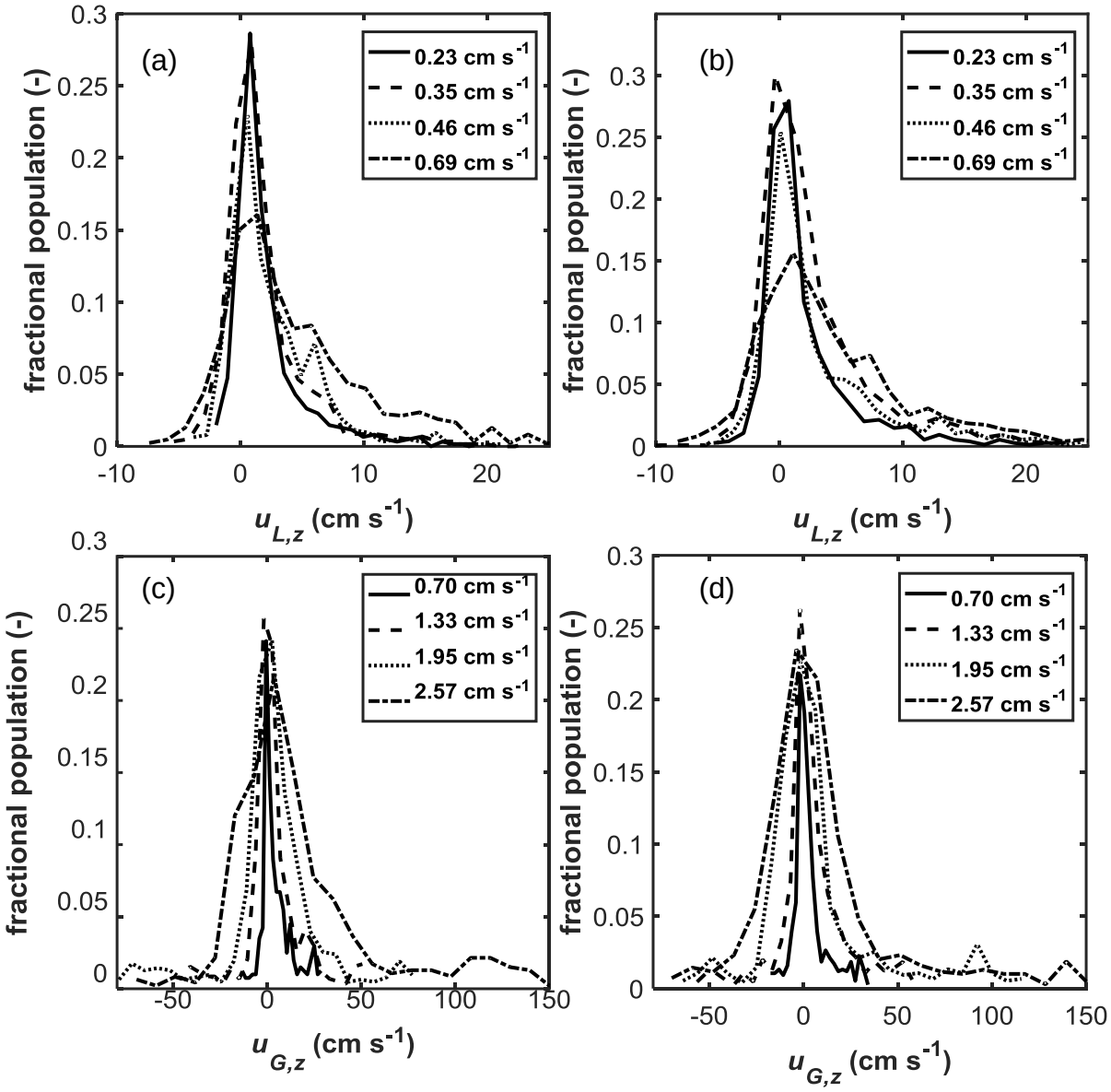

Figure 5.3: Population distributions of phase surface axial velocities at the gas-liquid interface for; the liquid phase as a function of liquid phase macroscopic velocity at a constant gas velocity of (a) 0.70 cm s^{-1} and (b) 1.95 cm s^{-1}, and for the gas phase as a function of gas phase macroscopic velocity at a constant liquid velocity of (c) 0.23 cm s^{-1} and (d) 0.46 cm s^{-1}.

previously been suggested that the tails of the distribution follow exponential decays, with the number of components indicative of the different flow regimes present in the field. In these however, any assertion of this behaviour beyond a liquid flow of 0.23 cm s^{-1} would be tenuous, as the tails are observed to deviate substantially from an exponential shape, particularly with increasing flow of both gas and liquid. The distributions are also seen to become noisier with increasing rate, which is possibly due to a reduction of signal-to-noise ratio attributed to voxel in-flow or out-flow effects at these high flow rates. In Figure 5.3 (a), the distribution is observed to spread out in both the positive and negative direction with increasing liquid flow rate. The proportion of interfacial flow which is static does not substantially diminish until a flow of

0.69 cm s^{-1}, for both gas flow rate assessed. This is suggestive that the flow behaviour enters a different sort of interfacial regime as more available flow area at the interface is recruited to carry the additional flow. Additionally, a small peak is observed at ~ 6 cm s^{-1} in the curve at 0.46 cm s^{-1}, and 0.69 cm s^{-1}. This is suggestive of a comparatively large section of flow which exists at this velocity, perhaps as a result of a localised constriction of the interface.

Figure 5.3 (b) shows that the liquid velocity field at the interface spreads out slightly more as the peaks become broader at the elevated gas velocity of 1.95 cm s^{-1} than in Figure 5.3 (a). The same broadening of the tails with increasing liquid superficial flow is observed, but to a larger extent than in (a). The second peak seen in the curve at 0.46 cm s^{-1} is however not observed. A similarity in peak magnitude as a function of flow is observed however, with the most dramatic reduction in the static peak magnitude is observed when transitioning to 0.69 cm s^{-1}. This is further evidence to suggest a difference in the physical nature of the interfacial flow at this high flow rate.

In the case of the gas axial velocity, the distributions differ from those seen for the overall velocity fields in Chapter 3. Particularly at low gas rates, the zero peaks are very narrow and sharp. This indicates that to a greater extent than in the liquid, most of the flow is static on the gas side of the phase interface. This does however change more so than in the case of the liquid, with a pronounced broadening of the distribution with increased gas flow rate. The distributions spread approximately monotonically with increasing superficial gas flow, and broaden proportionally much more than those for the liquid phase, such that the curve at the highest gas rate 2.57 cm s^{-1} is substantially broader than that at the lowest gas rate of 0.70 cm s^{-1}. The gas curves are additionally slightly noisier than the liquid curves due to an inherently lower signal-to-noise ratio.

For the gas curves at the higher liquid velocity of 0.46 cm s^{-1}, the data show a similar increased spreading indicating greater interaction between the phases at elevated superficial flow rates of the corresponding phase. The curves also appear slightly smoother than at the lower gas flow rate in Figure 5.3 (c), indicating perhaps a slightly more well defined and smooth flow pattern indicative of true trickle flow rather than being slightly at the border of either bubble or spray flow. Individual smaller peaks observed at the extremes of the distributions are attributed to localised regions of extreme flow possibly due to localised constrictions of the interface surfaces captured in the slice.

The similarity of these distributions to those for the overall flow indicates that the interface is a region of flow for both phases which is relatively representative of the physics of the overall flow in packed beds. No fundamentally different phenomena are present at the interface in particular, and flow occurs at a variety of rates – including elements of back-flow. The effect of varying the macroscopic flow on each phase is revealed as introducing more interaction between the phases, introducing a broader distribution of velocities in the corresponding phase even at the interface. This has important consequences for inter-phase mass transfer, as enhanced rates of flow at the surface of the phases will lead to enhanced transfer of reactive species between the two-phases and thus higher rates of dissolved reactants in the liquid and reaction at a solid catalyst surface.

5.3.2. INTERFACIAL VELOCITY SCATTER PLOTS AND CORRELATION INVESTIGATION

The so-called "closure" between the gas and liquid phases in modelling packed bed reactors is required to adequately model the interaction between phases at the interface. In order to locally validate a form of closure which uses linear slip factors to relate the phases, the axial velocity of each phase in connected voxels is plotted on a scatter plot in Figure 5.4. Earlier work [22] has proposed linear or constant correlations between these quantities. This phenomenological approach seeks to average out complex behaviour and apply a relation which can be used to calculate other fixed bed properties. However it is clearly apparent from Figure 5.4 that no such elegant correlation is observed in the data between the gas and liquid interfacial velocities.

The data are scattered over a broad area of corresponding velocities. Figure 5.4 (a) shows the velocity points in the gas interface as a function of the velocity of the liquid interface at a constant gas velocity of 0.70 cm s^{-1}. The most notable feature is that the points are predominantly clustered around the origin. Whilst there are multiple deviations from this, it is observed that for each liquid superficial velocity assessed, the density of points is highest around the point (0,0). Further to this, it is seen that the points lie mostly clustered on the axes, meaning that either the liquid or the gas velocity is stationary and that points which are mutually high in velocity are comparatively rare. There is a greater density of mutually high positive velocities than mutually high regions of backflow (negative velocity) at the interface. Density of points is also seen to increase in the positive quadrant as velocities both approach zero, suggesting that the interface is not typically a region where high flow is encountered. The points in Figure 5.4 (a) are more spread out along the liquid axis, which is unsurprising as it is the liquid superficial velocity being varied, which gives a similar range of gas interfacial velocities

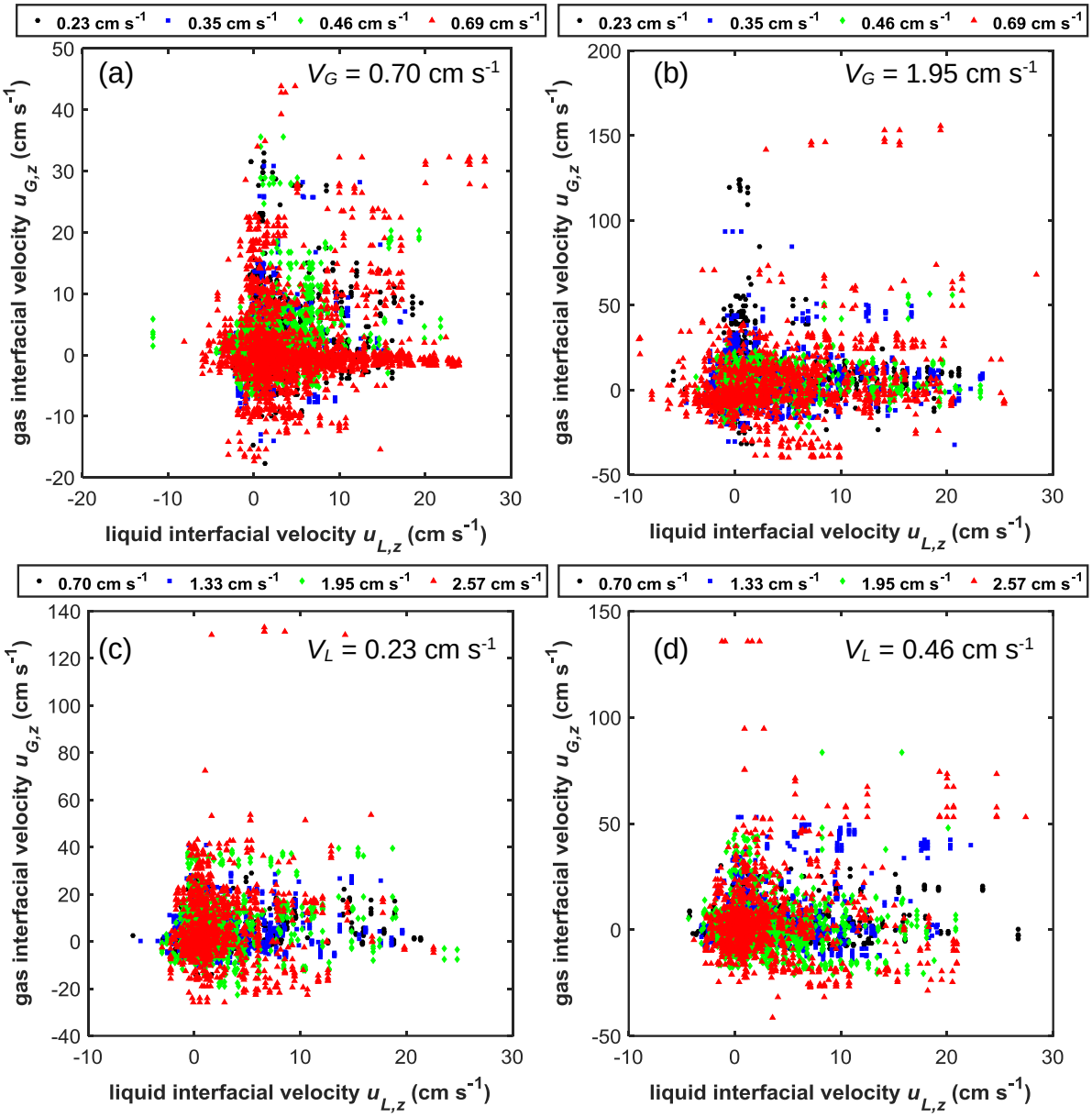

Figure 5.4: Scatter plots of the interfacial gas velocity as a function of the interfacial liquid velocity at the gas-liquid interface shown as; a function of liquid phase macroscopic velocity at a constant gas velocity of (a) 0.70 cm s^{-1} and (b) 1.95 cm s^{-1}, and a function of gas phase macroscopic velocity at a constant liquid velocity of (c) 0.23 cm s^{-1} and (d) 0.46 cm s^{-1}. Marker colour is indicated by the legend above each chart. Positive velocity denotes axial flow in the downward vertical direction. These scatter plots are provided to assess the extent of linear correlation as suggested by Holub *et al.* [6].

observed across all liquid superficial velocities investigated. Furthermore, the effect of increasing liquid superficial velocities is in general to spread the data further out in all directions but particularly for that of the liquid phase, which was also observed by analysing the velocity distributions at the interface. Due to an increase in the liquid holdup within the slice, reported previously using direct measurements [28], the size of the interface is also shown to increase with increasing liquid velocity.

Figure 5.4 (b) shows the same liquid superficial velocities assessed in (a) but for an elevated gas superficial velocity of 1.95 cm s^{-1}. Similar behaviour is observed to that in (a), with most of points for all liquid velocities clustered around the origin or spread out along the axes. Again, greater spreading is observed along the liquid axis, with a similar range of gas superficial velocities seen across the different liquid superficial velocities. However, the distribution of gas velocities observed in (b) is much larger and over a greater range than in (a), which was observed in the interfacial distributions in Figure 5.3 and is expected at the elevated gas velocity. Mutually high velocities are again in the minority, which almost no mutually negative liquid and gas velocities. Fewer points are observed along the gas axis, indicating that fewer points of zero liquid velocity and various gas velocity were observed.

Figure 5.4 (c) shows the interfacial velocity measurements as a function of gas superficial velocity at a fixed liquid superficial velocity of 0.23 cm s^{-1}. Once again the most notable aspect of the data is their pronounced density at the origin. As in the case of varying liquid velocity causing spreading of the points along the liquid axis, spreading of the data along the gas axis in this case is observed. The spreading is less pronounced, indicating that the gas interfacial behaviour is slightly less sensitive to phase macroscopic flow rate than the liquid. A similar range of both gas and liquid velocities is observed as a function of gas superficial flow rate, indicating a lower degree of interaction on behalf of the gas phase than the liquid, and that the spread of interfacial velocities is not a strong function of gas velocity. The relative absence of mutually negative velocities is again noted, but there is a prominent presence of mutually high positive values. Furthermore, there are a few data points with much higher than zero values (~140 cm s^{-1}) for the gas phase, and near zero values for the liquid-side velocity. This is indicative of where a high flow gas pore is adjacent to a quiescent liquid pore.

Figure 5.4 (d) shows the interfacial velocities at the same gas superficial velocities as Figure 5.4 (c), but at the elevated liquid superficial velocity of 0.46 cm s^{-1}. The data show a strong clustering around the origin, and are mostly confined to the mutually positive quadrant. More spreading along both the zero gas and liquid velocity lines is shown here than in Figure 5.4 (c), particularly along the liquid axis at this elevated liquid velocity, meaning more positive liquid velocities are present than at the lower liquid velocity. Some high gas rates (~140 cm s^{-1}) corresponding with near zero liquid velocity are observed once again as in (c), indicative of a very high gas flow pore next to a liquid interface with stationary flow. The density of mutually positive interfacial velocities diminishes significantly when moving away from the origin, which is behaviour observed in all the plots in Figure 5.4.

5.3.3. INTERFACIAL BIVARIATE DISTRIBUTION CURVES

For greater clarity, and to move the discussion in a more statistical direction, the data in Figure 5.4 are plotted in an alternative fashion in Figure 5.5. Here, the bivariate histogram of the scattered data was constructed as a surface. The discrete bins were then interpolated to smooth the data on a higher resolution grid. Equivalent frequency contours can then be constructed for these probability distributions, however to observe the behaviour with more clarity, only a single contour for each distribution which contains 80% of the highest frequency velocities was plotted. These single contours form a boundary in which 80% of the interfacial velocity points for adjacent voxels at each flow rate are contained. In this way, the effect of changing flow rate can be observed directly, and moreover the statistical behaviour of the interfacial flow can be observed.

In Figure 5.5 it is apparent that all of the distributions are centred at the origin, which is behaviour observed in Figure 5.4. This suggests that the modal value of interfacial velocity across all superficial velocities investigated is either identically or very close to zero. Figure 5.5 (a) shows the effect of changing liquid superficial velocity at low gas velocity. It is observed that the perimeter of the 80% threshold expands with increasing liquid velocity, which is expected and was seen also in the scatter plots. It is not monotonically true however, and in some regions movement of the border inwards is recorded. Most notably however the shape is relatively round except for the highest liquid velocity of 0.69 cm s^{-1}. Here the distribution has lobes which extend significantly onto the positive liquid axis, and minimally along the positive and negative gas velocity axis. This indicates that several interfacial measurements are of zero gas velocity and positive liquid velocity, and also of zero liquid velocity and have a non-zero corresponding gas velocity. The distributions are confined to an almost hyperbolically bounded region with no significant portion of the interface velocities lying away from the axes.

At the elevated gas superficial velocity of 1.95 cm s^{-1} similar behaviour is recorded. At lower liquid superficial velocities, the 80% region takes on a similar form to that in Figure 5.5 (a). It spreads out along the liquid axis with increasing liquid superficial velocity indicating that the liquid interface takes on a greater range of velocities at higher liquid velocities. This behaviour is exaggerated for the case of the highest liquid velocity of 0.69 cm s^{-1}. In this case, the distribution spreads significantly along the liquid velocity axis, with a smaller lobe extending along the negative axis and larger lobe on the positive side. The significantly enlarged area of the distribution at V_G,V_L = (1.95 cm s^{-1},0.69 cm s^{-1}) is potentially indicative of an overall flow

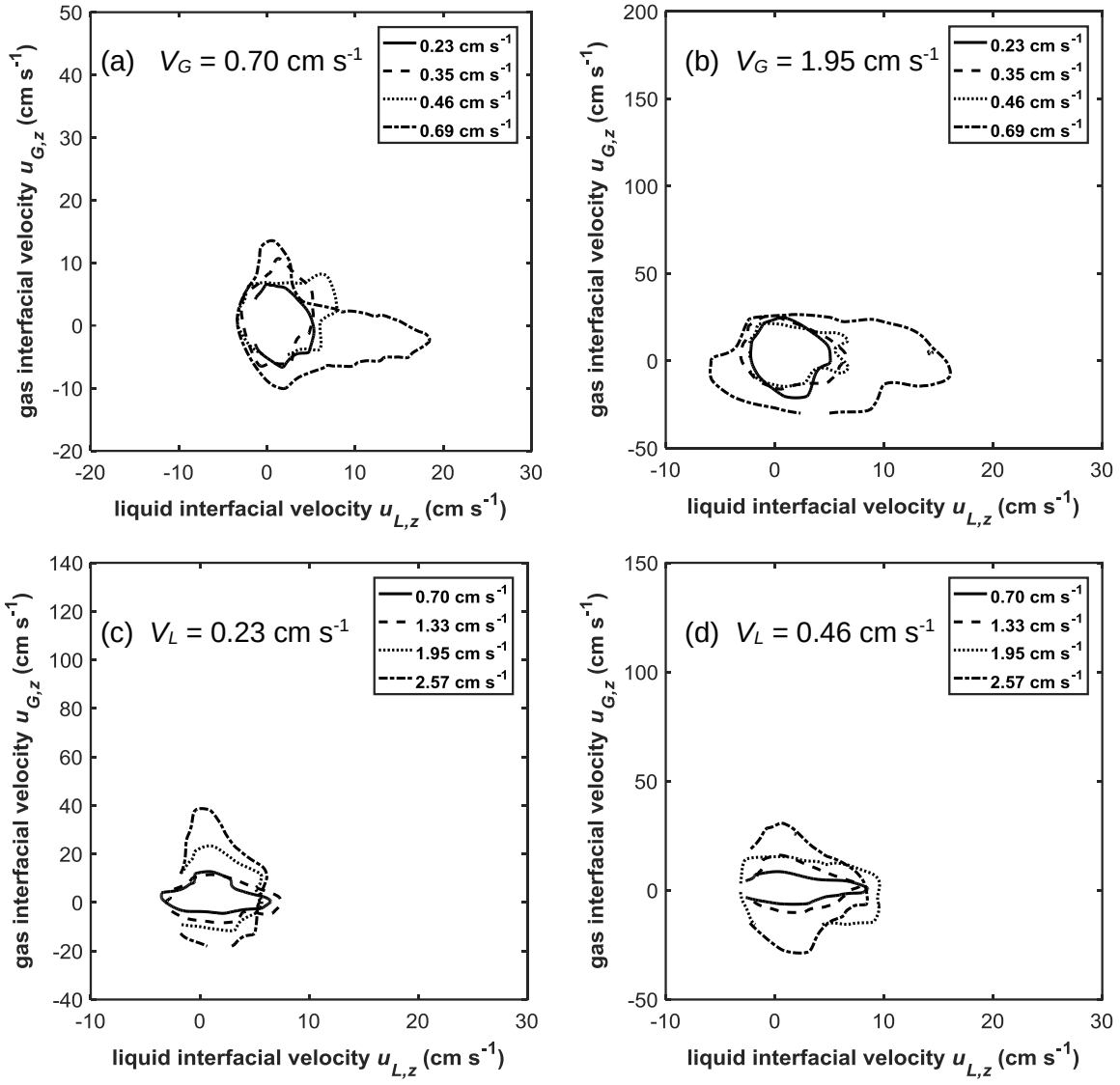

Figure 5.5: Thresholded bivariate density histograms for the interfacial phase velocity data in Figure 5. The lines shown are single value contours of the bivariate histogram surface at a value which contains 80% of the correlated velocity points in Figure 5.4. The data are shown on the same axes as in Figure 5.4, and for the same series of fluid velocities; for varying liquid velocities and a constant gas velocity of (a) 0.70 cm s^{-1} and (b) 1.95 cm s^{-1}, and varying gas velocity and a constant liquid velocity of (c) 0.23 cm s^{-1} and (d) 0.46 cm s^{-1}. Where the lines are broken shows the limits of the domain of the acquired data.

regime change, as it was recorded at the highest gas and liquid superficial velocity which is approaching the transition to pulsing flow. Further, this is suggestive that the macroscopic flow regime has a representative effect on the flow at the interface, i.e. the interfacial flow is not under a different flow regime in general.

Figure 5.5 (c) presents the 80% probability distribution threshold curves as a function of gas superficial velocity at a constant liquid velocity of 0.23 cm s^{-1}. Here, spreading of the distribution outwards along the gas velocity axis is noted, which is expected as the gas velocity is being varied. The range of the liquid velocities at the interface remains approximately the

same across all gas velocities. The curves are again centred approximately at the origin, indicating that varying gas flow rate causes the range of velocities encountered at the gas interface to increase but the modal mutual velocity is zero. The degree to which the distribution spreads along the gas axis also increases with increasing gas flow, with smaller increases observed for lower flow rates and a relatively large increase observed when going to the highest gas flow rate of 2.57 cm s^{-1}.

Figure 5.5 (d) gives the distribution curves for the elevated liquid flow rate of 0.46 cm s^{-1} as a function of the same gas superficial velocities shown in (c). It is again noted that the liquid velocity range within the 80% border remains approximately constant across the different gas velocities, which is expected at constant liquid superficial velocity. The curves are centred approximately at the origin, with the modal velocity recorded zero. Spreading of the curves outward along the gas velocity axis is observed as in (c), with lobes of each curve extending along the zero liquid velocity and zero gas velocity axes. This indicates that most of the velocities recorded in both phase interfaces are zero. Additionally, mutually high velocities are very rare, i.e. a case where adjacent interface voxels of both phases have velocities significantly nonzero. Once again the most significant degree of spreading is shown for the highest gas velocity investigated, 2.57 cm s^{-1}. This is as both the liquid and gas velocities are relatively high within the trickle regime. The sections of the curves which lie off the axes take on an approximately hyperbolic form, illustrative of the observation that most of the points lie on the axes as discussed previously.

The outcome of these measurements is to suggest that there is no simple phenomenological or analytical model of the mutual phase behaviour at the gas-liquid interface in this system. It is the author's proposal that the observed scatter is not due to a lack of resolution or experimental limitations. On a finer resolution it may be possible to observe what is occurring at the phase boundary layer, but in the majority of numerical simulations relevant to engineering it would be unreasonable to attempt to model the system with boundary-layer scale resolution even on an adaptive grid. It is thus suggested that modelling a fixed bed with the type of interfacial behaviour observed in the present study on a similar resolution would produce favourable results for these materials. The two observed facts of 1) the modal velocity in each case being approximately (0,0) for the gas and liquid respectively, and 2) that there does not exist a simple correlation with which the gas-liquid interaction can be modelled at the interface are in fact unsurprising. In terms of observation 1, it has previously been shown [28,33,34] in both multiphase and single-phase packed beds under trickle flow that the majority of recorded flow

is zero for both phases. It is therefore not surprising that the interfaces of each phase are representative of the bulk flow field. In this chapter it has been shown that the distributions of velocities extracted from the interface are qualitatively similar to those reported for the full flow fields. Regions of strong deviation from zero are almost always found adjacent to pores which exhibit high flow conditions. This illustrates that the interfacial flow behaviour is not in a fundamentally different regime and, on the resolution of this experiment, is governed by the same forces as the macroscopic flow field.

Furthermore for observation 2), the argument of continuity or closure at the interface depends on the phases having a degree of interaction with one another at the observation resolution (where that be experimentally or numerically). However, these experiments are conducted all within the low interaction regime (LIR) which is defined entirely by the phases having minimal interaction with one another. It is therefore unsurprising that no strong interaction is observed. It is noted that interaction may be present on a smaller scale at the interface, in a flow regime in which there is significant phase interaction due to momentum exchange at the phase surface or wave-like instabilities. In stable trickle flow for reasonable numerical simulations of this system, it would be practical to assume a distribution of velocities according to the ones observed here at the interface for each phase and treat them independently. In terms of the literature slip models by Holub [6] and Iliuta [18], the data imply that the velocity slip factor under the conditions considered here is best estimated at zero. A similar suggestion is made for the shear stress values obtained through numerical estimation from the recorded velocity fields.

5.3.4. SHEAR STRESS DISTRIBUTIONS

The shear stress field can be estimated based on the numerical techniques described previously. In the absence of 3D data and thus the ability to assess the entire shear stress tensor, analysing the component of the shear stress which is perpendicular to the phase interface surface (i.e. parallel to the normal vector to the phase interface) which is due to flow in the vertical direction, denoted $\tau_{\perp z}$, is expected to be the most significant component and also most indicative of any potential interaction between the phases. It is estimated as a function of varying liquid and gas superficial velocity. As can be expected, a distribution of shear stress values is encountered at the interface for each phase, denoted $\tau_{\perp z,L,i}$ at the liquid side of the phase interface, and $\tau_{\perp z,G,i}$ for the gas side of the phase interface.

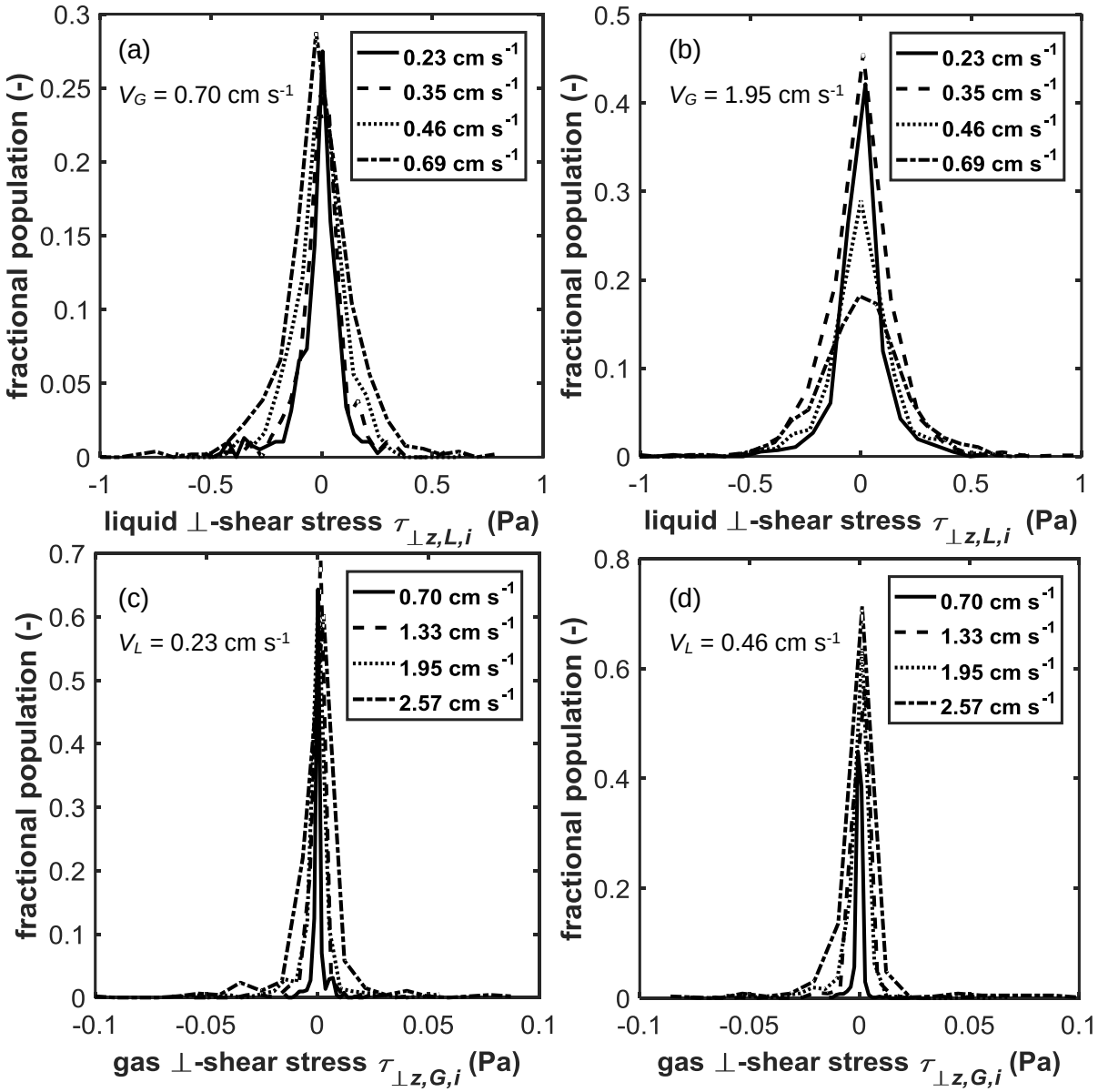

Figure 5.6: Population distributions of phase shear stresses at the gas-liquid interface for; the liquid phase as a function of liquid phase macroscopic velocity at a constant gas velocity of (a) 0.70 cm s^{-1} and (b) 1.95 cm s^{-1}, and for the gas phase as a function of gas phase macroscopic velocity at a constant liquid velocity of (c) 0.23 cm s^{-1} and (d) 0.46 cm s^{-1}. The shear stress shown here is the component of the stress due to vertical flow projected onto a vector normal to the phase interface, denoted ⊥-stress to indicate the normal is perpendicular to the phase surface.

Figure 5.6 gives the estimated shear stress distributions for each side of the interface. It was observed that the liquid phase interfacial shear stress distribution was insensitive to changes in gas phase velocity, and that the gas phase shear stress was insensitive to changes in the liquid phase velocity so these curves are not shown. Instead, Figure 5.6 (a) and (b) give the liquid shear stress distributions as a function of changes in liquid superficial velocity at gas velocities of 0.70 cm s^{-1} and 1.95 cm s^{-1} respectively. Similarly, Figure 5.6 (c) and (d) give the gas phase

interfacial shear stress distributions as a function of varying gas superficial velocity, at liquid superficial velocities of 0.23 cm s^{-1} and 0.46 cm s^{-1} respectively.

Figure 5.6 (a) shows that the distribution of perpendicular shear stresses in the liquid phase is approximately symmetrical about the value zero, with a modal shear stress value of zero. The tails appear to be diminishing exponentially in both the positive and negative directions. This behaviour is observed across the full range of liquid superficial velocities assessed, with slight noise observed in the tails at lower velocities. The net effect of increasing the liquid superficial velocity is to spread the distribution of shear stresses out about the origin. This effect is most noteworthy when transitioning to a gas flow rate of 0.69 cm s^{-1}, as the distribution becomes notably broader and to a greater extent than transitioning to the lower superficial liquid velocities. The curves at 0.23 cm s^{-1} and 0.35 cm s^{-1} are very similar, with some spreading out observed at 0.46 cm s^{-1} and significantly seen at 0.69 cm s^{-1}.

The same series of liquid velocities are assessed at a gas superficial velocity of 1.95 cm s^{-1} and these data are shown in Figure 5.6 (b). The distributions have a similar form to Figure 5.6 (a), centred at a value of zero with approximately symmetric near-exponentially diminishing tails. The spreading of these distributions with increasing liquid flow rate is more pronounced that at the lower gas velocity of 0.70 cm s^{-1} in (a). As the curves spread out, the modal frequency at a shear stress of zero decreases. The shear stress at the interface of the liquid phase is thus more sensitive to changes in liquid flow rate when the gas flow rate is higher.

In the case of changing gas flow rate, the gas phase shear stress is given in Figure 5.6 (c) and (d) as a function of gas superficial velocity. It is initially noted that the gas phase shear stress distributions are particularly narrow and centred on zero shear stress. This is expected, as the shear stress for the gas phase is an order of magnitude lower than the liquid phase due to the much lower viscosity of the gas. Increasing the gas superficial flow rate causes the distributions to broaden around the peak at zero shear stress.

At the elevated liquid flow rate of 0.46 cm s^{-1} in (d), the curves are very similar in shape, size and behaviour to those at the lower liquid velocity given in (c). The shear stress distribution is again centred on zero, with tails which rapidly diminish towards larger positive and negative shear stress values. The effect of increasing gas flow is again to cause the distributions to spread and broaden around the zero peak. However, in contrast with the liquid curves, the degree and nature of the broadening is very similar to that observed at the lower liquid flow rate. This suggests that the gas phase interfacial sheer stress behaviour is relatively insensitive to changes

in the liquid overall flow rate, within the range of superficial velocities studied presently. In both gas phase cases, the modal frequency seems to increase with increasing gas flow, which is in contrast to the liquid where the modal frequency decreases with increasing liquid flow. This suggests that the proportion of the flow at the interface which is stationary increases marginally with increasing liquid flow rate.

5.3.5. SHEAR STRESS CORRELATION

The closure laws typically used for trickle bed modelling also make consideration for relating the shear stress of the liquid phase to the gas phase at the interface. This is analogous to their treatment of velocity, as shear slip factors are introduced which attempt to model the magnitude and direction of interaction between the phases. The shear stress is of particular importance, as the existence of a linear shear slip factor would imply the shearing of one phase as a result of the momentum and viscous forces of the other phase.

As can be expected from the distributions of velocity previously presented and discussed, the shear stresses of the gas and liquid phases do not seem to be spatially correlated with a simplified linear relation, as can be seen on the scatter plots presented in Figure 5.7. Perhaps unsurprisingly, with a velocity field which is both macroscopically and at the interface predominantly static, the shear stresses are predominantly zero and the points are significantly concentrated around the origin, as in the case of velocity. Unlike velocity however, the shear stress plots are approximately symmetrical along both the liquid and gas velocity axes. This is due to the distribution of interfacial surface direction normal vectors being randomly distributed in all directions within a slice of packing.

Figure 5.7 shows the perpendicular shear stress of the gas interface on the ordinate axes and the liquid interface shear stress on the abscissa for varying liquid superficial velocities (different marker shapes and colours as indicated on the legend) for a constant gas superficial velocity of (a) 0.70 cm s^{-1} and (b) 1.95 cm s^{-1}, and varying gas superficial velocity at a constant liquid velocity of (c) 0.23 cm s^{-1} and (d) 0.46 cm s^{-1}. The distribution of data is concentrated significantly at the origin, and spreads most notably out along the liquid shear stress axis, suggesting that a broader range of liquid shear stress is encountered than gas shear stress for all experiments. This is somewhat surprising as even in the cases of varying the gas superficial velocity (c) and (d) show a greater range of liquid shear stresses at the zero gas shear stress line. This suggests that the shear stress in the gas side of the interface is more concentrated at zero than that of the liquid phase. As in the case of velocity, it is expected that spreading occurs

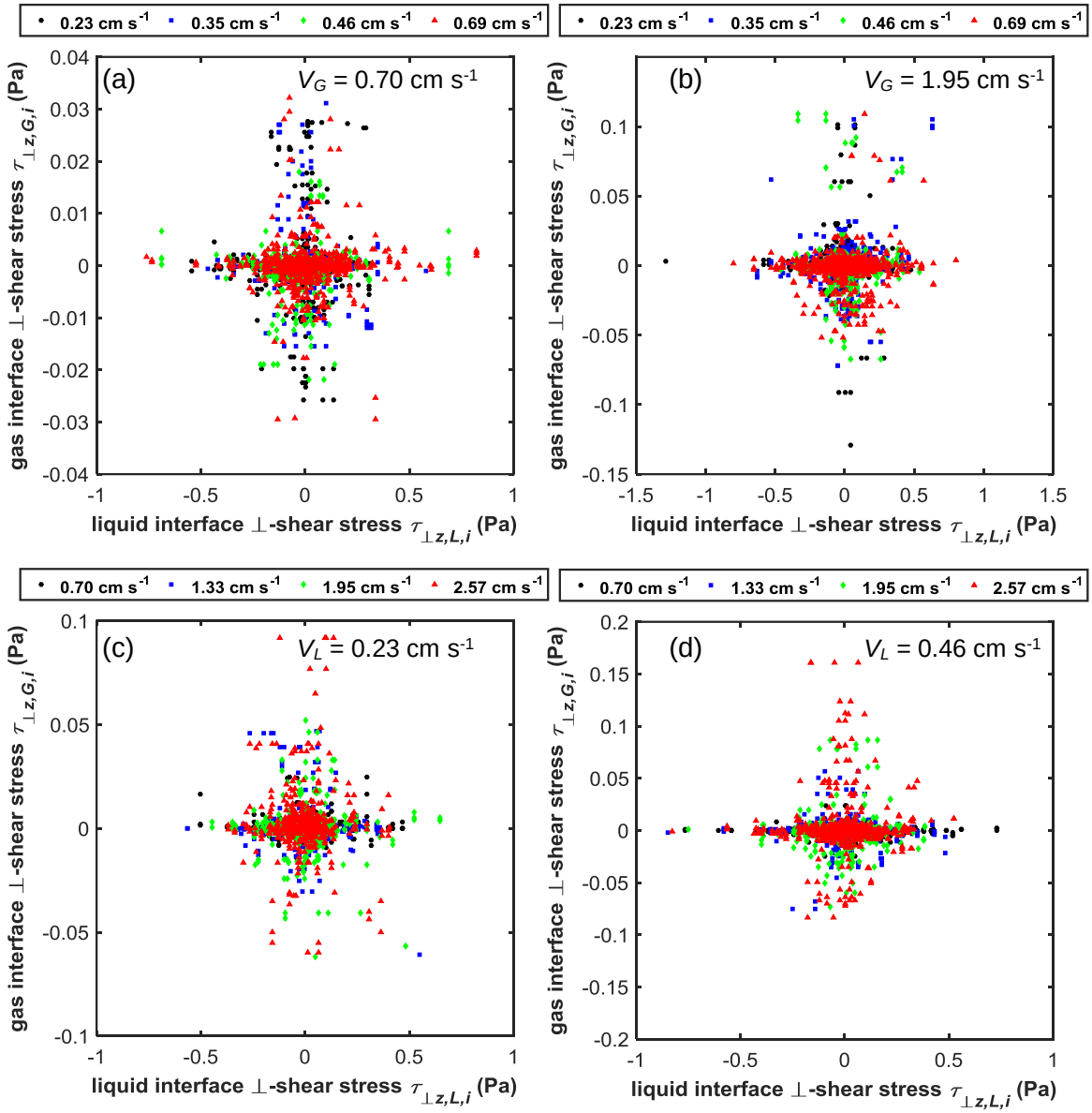

Figure 5.7: Scatter plots of the interfacial perpendicular shear stress components as; a function of liquid phase macroscopic velocity at a constant gas velocity of (a) 0.70 cm s^{-1} and (b) 1.95 cm s^{-1}, and a function of gas phase macroscopic velocity at a constant liquid velocity of (c) 0.23 cm s^{-1} and (d) 0.46 cm s^{-1}. Marker colour is indicated by the legend above each chart. Positive velocity denotes axial flow in the downward vertical direction. These scatter plots are provided to validate the extent of linear correlation as suggested by Holub [6].

along the axis of the phase whose superficial velocity is being varied. However it is shown in the case of shear stress that more spreading is universally observed along the liquid axis, indicating the liquid shear stress is of pronounced significance in magnitude compared to the gas shear stress.

The effect of increasing both the liquid flow rate, in (a) and (b), and the gas flow rate in (c) and (d), is to cause the observed distribution of shear stresses to spread out about the origin, however once again it is noted that there is a stark rarity of points with mutually high absolute values. That is to say, points which have a large distance from the origin off the axes are

virtually non-existent, and the observation that the data are mostly enclosed in an envelope bounded by hyperbola is again made. The extent of overlap in the data in close vicinity with the origin is so significant that once again for clarity, the bivariate histogram is calculated, interpolated and thresholded at a contour value which encompasses 80% of the density of shear stress data points. These data are shown in Figure 5.8.

As in Figure 5.5, the plots in Figure 5.7 illustrate by use of a single contour, the boundary inside which 80% of the shear stress data lie on the plane. These boundaries are relatively regularly shaped, and as in the case of velocity, are centred approximately at the origin and spread outwards in size with increasing superficial fluid velocity for both phases. In the case of Figure 5.8 (a), the contours are elliptical in shape and have their major axis along the liquid shear stress line indicating a greater range of liquid shear stresses. The degree of spreading in this case is not significant, as the range of both the gas and liquid shear stresses remains approximately constant for all liquid velocities investigated. Interestingly, the bottom boundary appears to shrink initially from 0.23 cm s^{-1} to 0.35 cm s^{-1}, and then expand finally for the largest velocity of 0.69 cm s^{-1}. This is perhaps due to the disappearance of a particular gas phase pore which has a significant portion of negative shear stress which later re-emerges at the liquid flow rate of 0.69 cm s^{-1}. This sort of pore hysteresis is documented in trickle bed reactors [47,48]. A slight peak is also observed at 0.23 cm s^{-1} at zero liquid shear stress and outwards along the positive gas shear stress axis.

Figure 5.8 (b) shows the same series of liquid superficial velocities as (a) but at a higher gas superficial velocity of 1.95 cm s^{-1}. Only subtle sensitivity to changing liquid superficial velocity is observed until the highest value of 0.69 cm s^{-1}. The threshold remains similar in size and shape, centred at the origin for the lowest three liquid velocities. It then spreads symmetrically about the gas shear axis along the liquid shear axis to become elongated and elliptically shaped. This sharp change has been observed in the velocity distribution data, and is suggestive of the approach to a regime change. This is due to the fact that it is the highest combination of gas and liquid velocities investigated within this series and is approaching the border of the low interaction regime. Similar transitional behaviour is suggested in the gas velocity series in Figure 5.8 (d).

Figure 5.8 (c) illustrates the series of shear stress threshold contours as a function of gas superficial velocity at a constant liquid velocity of 0.23 cm s^{-1}. The range of liquid shear stress values measured is not a strong function of gas superficial velocity. Significant spreading is

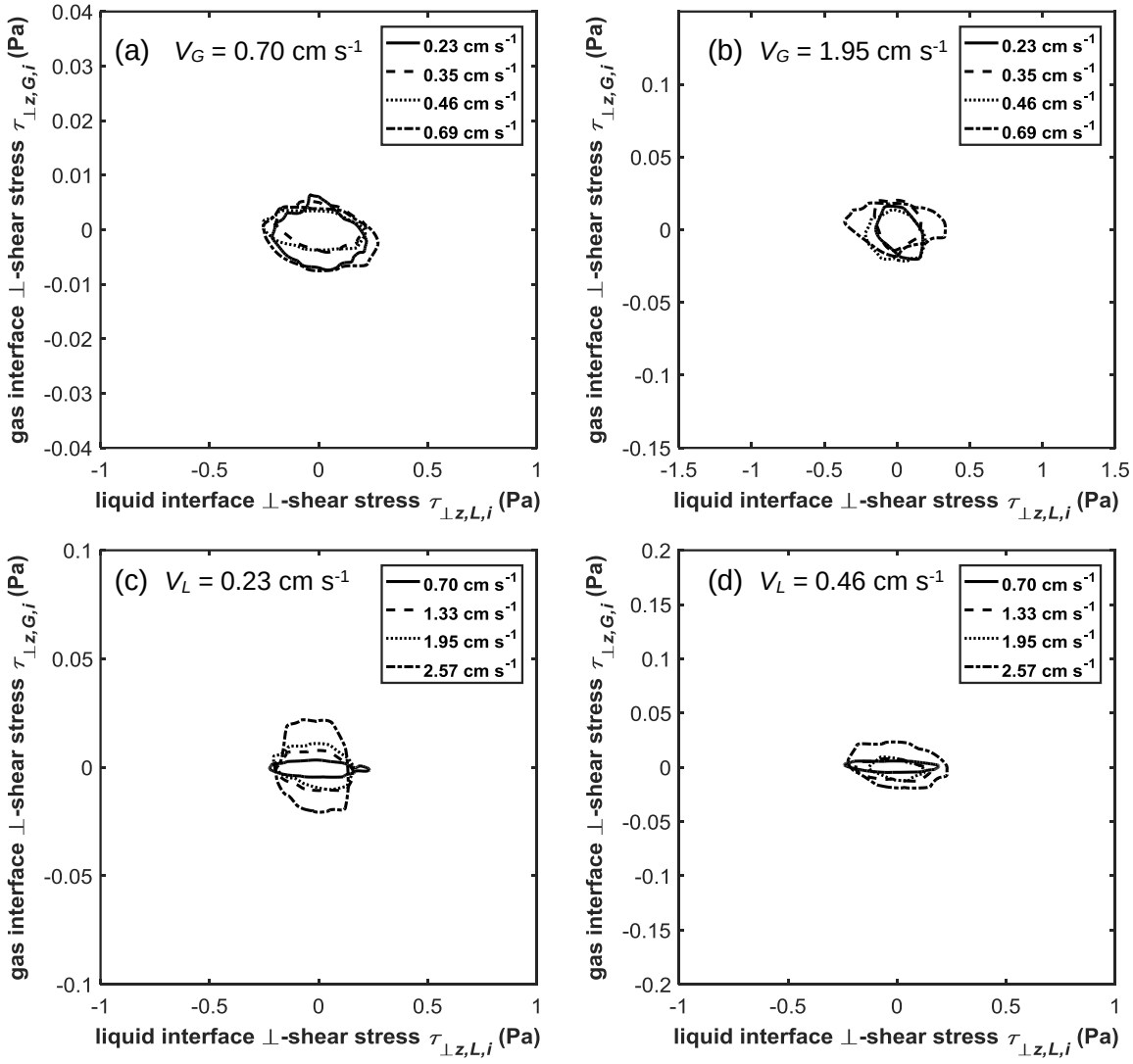

Figure 5.8: Thresholded bivariate density histograms for the interfacial phase perpendicular shear stress data in Figure 5.7. The lines shown are single value contours of the bivariate histogram surface at a value which contains 80% of the spatially correlated shear stress data in Figure 5.7. The data are shown on the same axes as in Figure 5.7, and for the same series of fluid velocities; for varying liquid velocities and a constant gas velocity of (a) 0.70 cm s^{-1} and (b) 1.95 cm s^{-1}, and varying gas velocity and a constant liquid velocity of (c) 0.23 cm s^{-1} and (d) 0.46 cm s^{-1}. Where the lines are broken shows the limits of the domain of the acquired data.

however recorded in the gas shear stress direction, with a pronounced increase in broadness encountered when transitioning to the highest gas velocity tested. The borders in the gas direction monotonically spread out along the gas axis, however very significant spread is shown at 2.57 cm s^{-1}, which is somewhat expected as the gas rate is being increased giving rise to an increase in activity in the gas flow field.

Figure 5.8 (d) shows the same gas velocity series presented in (c) however at a higher liquid superficial velocity of 0.46 cm s^{-1}. The effect on the gas-varying behaviour of the shear stress distribution of increasing the liquid superficial flow rate is not remarkable. A slightly broader

range of liquid shear stress is encountered, but again this remains approximately constant across the range of gas velocities. The behaviour as a function of gas superficial velocity is also very similar, with monotonic spreading of the boundary along the gas axis with increased gas velocity. A gradual spread is recorded aside from the curve at 2.57 cm s^{-1}, in which a pronounced increase is observed. This is suggestive of the potential for encountering a macroscopic flow regime change, as observed in Figure 5.8 (b).

In a similar way to the velocity distributions, these data reveal negligible interaction between the gas and liquid phases at the interface with the majority of shear stress values perpendicular to the interface being zero. Together with the outcome of the study on velocity, this suggests that the assumption of earlier research regarding the lack of interaction between phases is valid at low-to-moderate pressures using the presently studied materials. The interaction between phases is principally observed on a global level, through varying the macroscopic flow rates which cause changes to the overall shear stress and velocity distributions. Local interactions at the interface are difficult to glean from the present data. However, for flows in the high interaction regime, surface instabilities and temporal variation of the interface location would make MRI experiments very challenging or impossible to gather quantitative data such as those presented here. A non-zero linear slip factor for shear stress would be of limit use in modelling this bed. It is nevertheless noted that if most of flow in each phase is near zero (as found in the present chapter and Chapter 4), the value of both the velocity and shear stress slip factors would be of little consequence in modelling the current set of materials and conditions.

5.3.6. SOLID-LIQUID SHEAR STRESS

Another significant phase momentum interaction which affects the performance of trickle bed reactors is the solid-liquid interface. The momentum transfer at this interface significantly impacts the transport of reactants/products to/from the surface of a reactive or catalytic solid and is thus an important consideration in trickle bed design and analysis. The solid-liquid shear stress distributions on the liquid side of the solid-liquid interface are therefore calculated. The distributions are investigated as a function of both the liquid and gas superficial velocities to assess the extent of interaction between the phases on this shear stress field. Figure 5.9 shows the resulting solid-liquid shear stress distributions.

Figure 5.9 (a) and (b) show the solid liquid shear stress probability distribution as a function of varying liquid flow rate for constant gas flows of (a) 0.70 cm s^{-1} and (b) 1.95 cm s^{-1}. It is again observed that a strong peak at zero shear stress is encountered, which is not unusual for a liquid

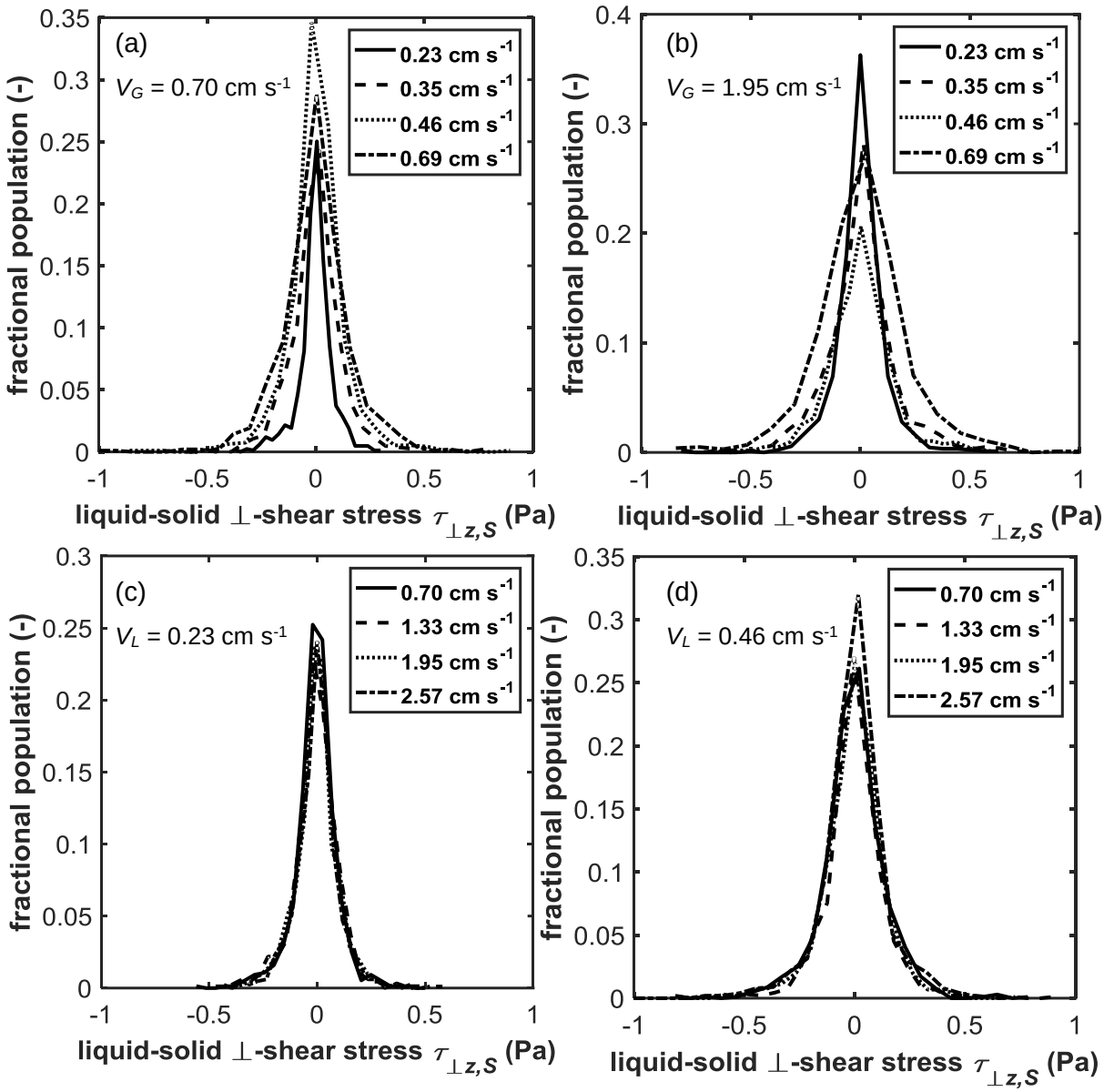

Figure 5.9: Population distributions of solid-liquid shear stress at the solid surface for; the liquid phase as a function of liquid phase macroscopic velocity at a constant gas velocity of (a) 0.70 cm s^{-1} and (b) 1.95 cm s^{-1}, and as a function of gas phase macroscopic velocity at a constant liquid velocity of (c) 0.23 cm s^{-1} and (d) 0.46 cm s^{-1}. The shear stress shown here is the component of the stress due to vertical flow projected onto a vector normal to the solid surface, denoted ⊥-stress to indicate the normal is perpendicular to the solid interface.

flow field which is both across the slice and at the interface mostly stationary. The distribution then takes on a familiar form, tailing off smoothly and sub linearly towards higher positive and negative shear stress values. This form is found for all of the solid-liquid shear stress curves recorded. It is seen that the effect of increasing the liquid velocity is to spread the solid-liquid distribution outwards symmetrically about the peak at zero shear stress. The spread is approximately monotonic, in that each successive curve at higher velocity encompasses the curves at lower liquid velocities.

For the curve at elevated gas velocity in (b), it is noted that on the same horizontal scale, the curves are universally broader than those in (a), indicating an interactive effect due to increasing gas velocity. It is also seen that for the lowest three liquid velocities the curves are relatively close together. However, at the highest velocity of 0.69 cm s^{-1}, a proportionally broader degree of spreading is observed. This is further suggestion of the fact that the regime at the interface, here at the solid-liquid interface, is approaching regime change as a result of interaction between the gas and liquid phases.

The curves are given also as pure functions of gas velocity at two different liquid velocities in (c) and (d). In (c), at a liquid velocity of 0.23 cm s^{-1}, the curves predominantly lie on top of one another, and thus represent approximately the same distribution of shear stresses. The distribution takes on a familiar form centred with a pronounced zero peak, with symmetrical tails towards both higher positive and negative shear stress. Similarly, at the elevated liquid velocity of 0.46 cm s^{-1} the distributions once again lie on top of one another indicating essentially negligible direct effect of changing gas velocity on the solid-liquid shear stress. The curves are however slightly broader, which is unsurprising since the solid-liquid shear stress has been shown here to be more sensitive to the liquid macroscopic flow rate.

It can therefore be inferred that the gas superficial velocity has negligible direct effect on the behaviour at the liquid-solid interface, however the interaction of the phases causes a greater sensitivity to changes in liquid flow rate, as demonstrated by the change in behaviour observed between Figure 5.9 (a) and (b).

5.3.7. SLICE-AVERAGED VELOCITY RELATIONS

In a further effort to observe the interactive effects between the phases on the interfacial flow fields, the phase interfacial velocities at the interface for both the gas and liquid phases were averaged over the entire image slice and plotted as a function of the macroscopic flow rates for both phases and at different constant values of the corresponding phase macroscopic flow rate. Figure 5.10 presents this data for varying liquid superficial velocity at a constant gas flow rate of 0.70 cm s^{-1} [(a) and (c)] and for varying gas superficial velocity at a constant liquid flow of 0.46 cm s^{-1} [(b) and (d)]. These charts show the average axial and radial components (*z*- ,*x*- and *y*-components) for the slice (indicated by different markers as per the legend provided).

In (a) the axial interfacial velocity component is an approximately linear function of the liquid superficial velocity. This is expected as it is the liquid velocity being varied, however the

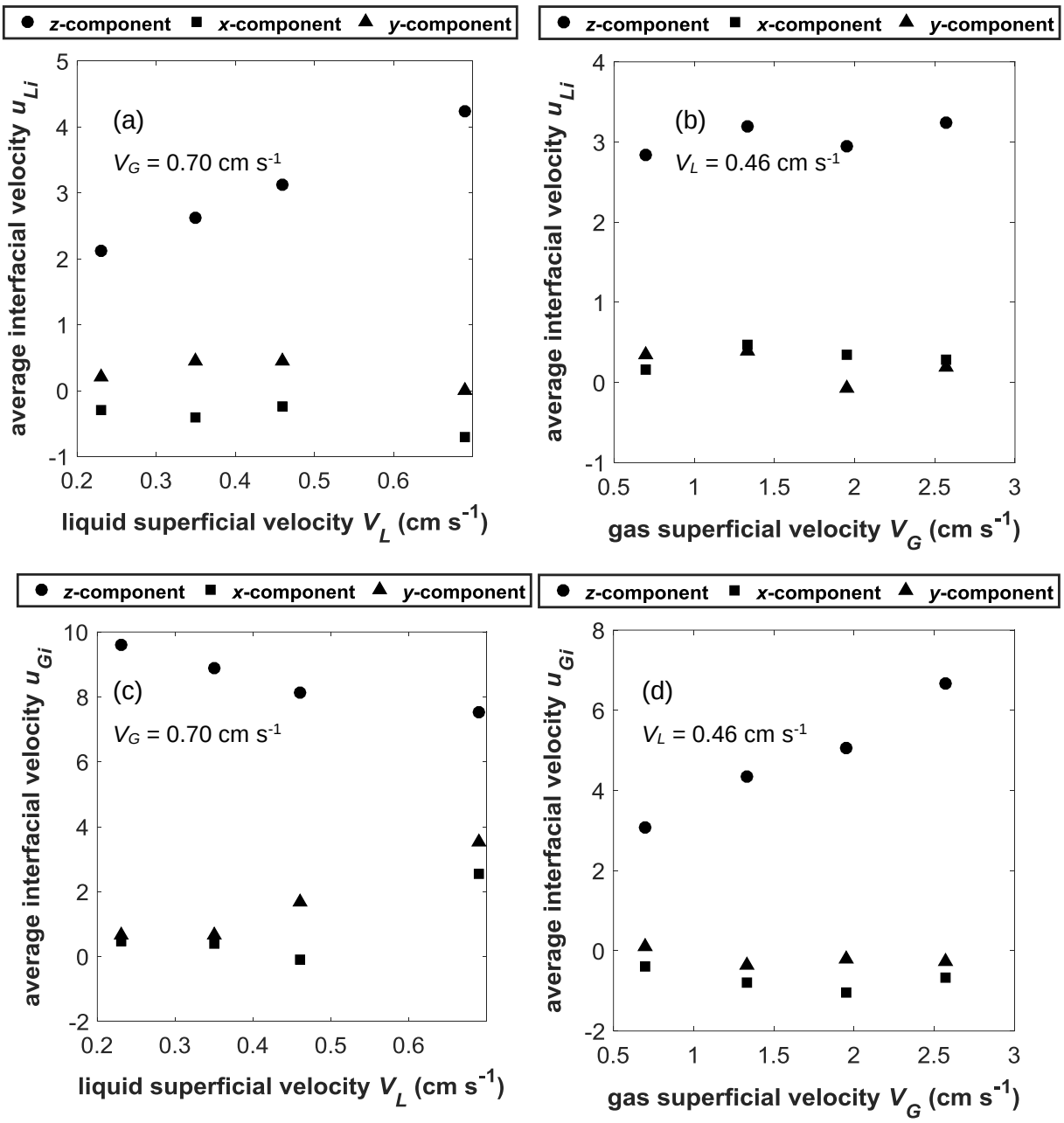

Figure 5.10: Interfacial velocities for the gas and the liquid phases averaged over the full slice in each experiment for; the liquid phase as a function of the (a) liquid macroscopic velocity at a fixed gas velocity of 0.70 cm s^{-1}, and (b) gas macroscopic velocity at a fixed liquid velocity of 0.46 cm s^{-1}, and the gas phase as a function of (c) the liquid macroscopic velocity at a gas velocity of 0.70 cm s^{-1}, and (d) gas macroscopic velocity at a fixed liquid velocity of 0.46 cm s^{-1}.

linearity confirms that the flow regime at the measured interface scales identically with the macroscopic flow rate. As expected, the radial in-plane components fluctuate slightly around a value of zero, which is expected as no net flow within the plane can occur with the impenetrable walls of the bed.

In (b) there is very little influence on behalf of the gas macroscopic flow rate on the liquid flow field at the interface, which is an expected result in the low interaction regime. Both the axial

and radial components remain essentially constant across the gas velocities investigated. In (c) the gas interfacial average velocities are plotted as function of the liquid superficial flow. A slightly decreasing trend is observed in the gas axial flow rate, indicating that increasing the liquid flow causes a slight reduction in the average gas flow at the interface. The radial components are also seen to rise slightly, which is possibly due to the inception and growth of a section of the flow field which lies directly above or below a particle in the plane, which causes lateral flow to be positive. This behaviour is seen to be enhanced slightly by increasing the liquid flow.

Figure 5.10 (d) shows the averaged velocity components as a function of the gas macroscopic flow rate. The axial gas flow component is an approximately linearly increasing function for increasing macroscopic flow. This is expected and was also observed for the liquid phase, and further confirms that the interfacial flow does not scale in a different way to the overall flow field. The radial components remain approximately constant around zero, which is expected as in the case of the liquid, as no net axial flow is possible. Deviations from this within the slice are due to sloping surfaces intersecting the plane causing the local flow to be slightly nonzero, however when integrated over the full bed length this value would be identically zero.

It is observed that the liquid phase has a greater interaction potential than the gas phase for the average velocities at the interface, and further that the interfacial flow field subset behaves in the same fashion as the macroscopic flow field. It is also seen that local deviations in the radial plane can be enhanced by phase interaction.

5.4. CONCLUSIONS

This study has demonstrated the ability of MRI to provide a non-invasive, quantitative, and spatially-resolved assessment of the extent and nature of phase interaction in a packed bed operating in gas-liquid trickle flow. The velocity fields of both the SF_6 gas and liquid water phases were recorded using a compressed sensing technique and phase-encoded NMR experiments, and the interface was unambiguously identified using a morphological thinning algorithm.

The velocity measurements at the interface show that the distribution of both gas and liquid velocities at the interface are in a similar regime of flow to that of the bulk phase flow fields. Most of the flow under the present experimental conditions is stationary, with large positive decaying tails and a small amount of back-flow. The effect of increasing the macroscopic flow

rate of the liquid and gas, was in turn, to broaden the velocity distributions of the liquid and gas interfacial velocities respectively. Minor global interaction effects were shown, with slightly more broadening recorded in the case of higher gas flow on the liquid flow curves, and vice versa but the effect was not dramatic.

The extent of correlation between both interfacial velocities and shear stresses was assessed using the bivariate probability density functions. It was observed that the overwhelming number of spatially adjacent voxels of both velocity and shear stress lay clustered very near the origin, indicating minimal phase interaction. This is expected for the low interaction regime, and reinforces the validity of the assumption of negligible phase interaction at moderate-to-low pressures made in early models of trickle flow. In the framework of Iliuta *et al.* [18], this indicates a zero value for the shear and velocity slip factors, which would be a justifiable implication for modelling a trickle bed of these materials and conditions. It is suggested that isolating regions which show higher flow and shear (thereby negating the contribution by the majority-static flow), or by using a TBR at higher pressures and in more vigorous flow regimes may be used to further validate the linear slip or other closure relationships using this method.

The primary advantage of the present study is to demonstrate the capability of MRI to obtain detailed spatially-resolved measurements of phase interaction effects. Furthermore, these measurements can be analysed in terms of existing literature models, such as the slip models [6,18,22], to determine under which conditions these models are valid. The data reveal minimal interaction between the phases within the low interaction regime assessed in the experiments. At higher flow rates, interaction becomes more significant in the form of surface temporal instabilities and wave structures. To the authors knowledge, no analytical treatments of these conditions have been produced in the literature. The fact that these structures are temporally variable means such conditions would be practically very difficult to study using MRI. In summary, the data presented here suggest the interaction between phases is minimal, and that for this system the linear slip models are of limited physical significance on a localised interfacial basis. The interaction effects observed are related more to global macroscopic flow rate changes.

NOMENCLATURE

ABBREVIATIONS

1D, 2D, 3D	one, two or three dimensional
FOV	field-of-view
r.f.	radiofrequency
MRI	magnetic resonance imaging
NMR	nuclear magnetic resonance

SYMBOLS

f_v	velocity slip factor	-
f_τ	shear stress slip factor	-
S	normal vector/surface	-
u_L	local liquid velocity	cm s^{-1}
u_G	local gas velocity	cm s^{-1}
V_L	superficial liquid velocity	cm s^{-1}
V_G	superficial gas velocity	cm s^{-1}
y,x,z	standard cartesian coordinates	-

SUBSCRIPTS

i	interfacial/i^{th} component	-
j	j^{th} component	-
$\perp$	perpendicular	-
y,x,z	standard cartesian direction	-

GREEK LETTERS

α_s	interface surface angle	rad
α_τ	angle of shear stress	rad
Δ	observation time for velocity measurement	s
μ	viscosity	Pa s
$\boldsymbol{\tau}$	shear stress vector	Pa
$\tau_{\perp z,L}$	liquid vertical shear stress normal to interface	Pa
$\tau_{\perp z,G}$	gas vertical shear stress normal to interface	Pa

REFERENCES

[1] Duduković, M.P., Larachi, F., Mills, P.L. Multiphase catalytic reactors: a perspective on current knowledge and future trends. *Catal. Rev.* 2002;44: pp. 123–246.

[2] Ren, X., Stapf, S., Blümich, B. Magnetic resonance visualisation of flow and pore structure in packed beds with low aspect ratio. *Chem. Eng. Technol.* 2005;28: pp. 219–25.

[3] Yuen, E.H.L., Sederman, A.J., Sani, F., Alexander, P., Gladden, L.F. Correlations between local conversion and hydrodynamics in a 3-D fixed-bed esterification process: An MRI and lattice-Boltzmann study. *Chem. Eng. Sci.* 2003;58: pp. 613–9.

[4] Sáez, A., Carbonell, R.G. Hydrodynamic Parameters for Gas-Liquid Cocurrent Flow in Packed Beds. *AIChE J.* 1985;31: pp. 52–62.

[5] Holub, R.A., Duduković, M.P., Ramachandran, P.A. A phenomenological model for pressure drop, liquid holdup, and flow regime transition in gas-liquid trickle flow. *Chem. Eng. Sci.* 1992;47: pp. 2343–8.

[6] Holub, R.A., Duduković, M.P., Ramachandran, P.A. Pressure Drop, Liquid Holdup, and Flow Regime Transition in Trickle Flow. *AIChE J.* 1993;39: pp. 302–21.

[7] Iliuta, I., Larachi, F., Al-Dahhan, M.H. Double-slit model for partially wetted trickle flow hydrodynamics. *AIChE J.* 2000;46: pp. 597–609.

[8] Attou, A., Ferschneider, G. A two-fluid model for flow regime transition in gas–liquid trickle-bed reactors. *Chem. Eng. Sci.* 1999;54: pp. 5031–7.

[9] Attou, A., Boyer, C., Ferschneider, G. Modelling of the hydrodynamics of the cocurrent gas-liquid trickle flow through a trickle-bed reactor. *Chem. Eng. Sci.* 1999;54: pp. 785–802.

[10] Iliuta, I., Larachi, F. The generalized slit model: Pressure gradient, liquid holdup & wetting efficiency in gas–liquid trickle flow. *Chem. Eng. Sci.* 1999;54: pp. 5039–45.

[11] Augier, F., Koudil, A., Royon-Lebeaud, A., Muszynski, L., Yanouri, Q. Numerical approach to predict wetting and catalyst efficiencies inside trickle bed reactors. *Chem. Eng. Sci.* 2010;65: pp. 255–60.

[12] Gunjal, P.R., Kashid, M.N., Ranade, V. V., Chaudhuri, R. V. Hydrodynamics of trickle bed reactors: experiments and CFD modeling. *Ind. Eng. Chem. Res.* 2005;44: pp. 6278–94.

[13] Jiang, Y., Khadilkar, M.R., Al-Dahhan, M.H., Dudukovic, M.P. CFD of multiphase flow in packed-bed reactors: I. k-fluid modeling issues. *AIChE J.* 2002;48: pp. 701–15.

[14] Jiang, Y., Khadilkar, M.R., Al-Dahhan, M.H., Dudukovic, M.P. CFD of multiphase flow in packed-bed reactors: II. Results and applications. *AIChE J.* 2002;48: pp. 716–30.

[15] Lappalainen, K., Manninen, M., Alopaeus, V. CFD modeling of radial spreading of flow in trickle-bed reactors due to mechanical and capillary dispersion. *Chem. Eng. Sci.* 2009;64: pp. 207–18.

[16] Lopes, R.J.G., Quinta-Ferreira, R.M. CFD modelling of multiphase flow distribution in trickle beds. *Chem. Eng. J.* 2009;147: pp. 342–55.

[17] Al-Dahhan, M.H., Duduković, M.P. Pressure drop and liquid holdup in high pressure

trickle-bed reactors. *Chem. Eng. Sci.* 1994;49: pp. 5681–98.

[18] Iliuta, I., Larachi, F.F., Grandjean, B.P.A. Pressure Drop and Liquid Holdup in Trickle Flow Reactors: Improved Ergun Constants and Slip Correlations for the Slit Model. *Ind. Eng. Chem. Res.* 1998;37: pp. 4542–50.

[19] Wammes, W.J.A., Westerterp, K.R. The influence of the reactor pressure on the hydrodynamics in a cocurrent gas-liquid trickle-bed reactor. *Chem. Eng. Sci.* 1990;45: pp. 2247–54.

[20] Wammes, W.J.A., Westerterp, K.R. Hydrodynamics in a pressurized cocurrent gas-liquid trickle-bed reactor. *Chem. Eng. Technol.* 1991;14: pp. 406–13.

[21] Larachi, F., Laurent, A., Midoux, N., Wild, G. Experimental study of a trickle-bed reactor operating at high pressure: two-phase pressure drop and liquid saturation. *Chem. Eng. Sci.* 1991;46: pp. 1233–46.

[22] Al-Dahhan, M.H., Khadilkar, M.R., Wu, Y., Duduković, M.P. Prediction of Pressure Drop and Liquid Holdup in High-Pressure Trickle-Bed Reactors. *Ind. Eng. Chem. Res.* 1998;37: pp. 793–8.

[23] Larachi, F., Laurent, A., Wild, G., Midoux, N. Some Experimental Liquid Saturation Results in Fixed-Bed Reactors Operated under Elevated Pressure in Cocurrent Upflow and Downflow of the Gas and the Liquid. *Ind. Eng. Chem. Res.* 1991;30: pp. 2404–10.

[24] Attou, A., Ferschneider, G. A two-fluid hydrodynamic model for the transition between trickle and pulse flow in a cocurrent gas–liquid packed-bed reactor. *Chem. Eng. Sci.* 2000;55: pp. 491–511.

[25] Boyce, C.M., Rice, N.P., Sederman, A.J., Dennis, J.S., Holland, D.J. 11-interval PFG pulse sequence for improved measurement of fast velocities of fluids with high diffusivity in systems with short T 2∗. *J. Magn. Reson.* 2016;265: pp. 67–76.

[26] Boyce, C.M., Rice, N.P., Ozel, A., Davidson, J.F., Sederman, A.J., Gladden, L.F., *et al.* Magnetic resonance characterization of coupled gas and particle dynamics in a bubbling fluidized bed. *Phys. Rev. Fluids* 2016;1: pp. 74201.

[27] Boyce, C.M., Rice, N.P., Davidson, J.F., Sederman, A.J., Dennis, J.S., Holland, D.J. Magnetic resonance imaging of gas dynamics in the freeboard of fixed beds and bubbling fluidized beds. *Chem. Eng. Sci.* 2016;147: pp. 13–20.

[28] Rice, N.P., Schmaus, C., Sederman, A.J., Gladden, L.F. Investigation of the effects of macroscopic velocity on the extent of flow maldistribution in a gas-liquid trickle bed using MRI [in preparation]. 2018.

[29] Johns, M.L., Sederman, A.J., Bramley, A.S., Gladden, L.F., Alexander, P. Local transitions in flow phenomena through packed beds identified by MRI. *AIChE J.* 2000;46: pp. 2151–61.

[30] Nesbitt, G.J., De Groot, A., Fens, T.W., Bonnie, J.H.M. Towards validation of porous media models using NMR imaging and image-analysis techniques. *Magn. Reson. Imaging* 1991;9: pp. 779–87.

[31] Rajanayagam, V., Yao, S., Pope, J.M. Quantitative magnetic resonance flow and diffusion imaging in porous media. *Magn. Reson. Imaging* 1995;13: pp. 729–38.

[32] Sederman, A.J., Johns, M.L., Alexander, P., Gladden, L.F. Structure-flow correlations

in packed beds. *Chem. Eng. Sci.* 1998;53: pp. 2117–28.

[33] Sederman, A.J., Gladden, L.F. Magnetic resonance visualisation of single- and two-phase flow in porous media. *Magn. Reson. Imaging* 2001;19: pp. 339–43.

[34] Sankey, M.H., Holland, D.J., Sederman, A.J., Gladden, L.F. Magnetic resonance velocity imaging of liquid and gas two-phase flow in packed beds. *J. Magn. Reson.* 2009;196: pp. 142–8.

[35] Albert, M.S., Cates, G.D., Driehuys, B., Happer, W., Saam, B., Springer, C.S., *et al.* Biological Magnetic Resonance Imaging Using Laser-Polarized 129Xe. *Nature* 1994;370: pp. 199–201.

[36] Bouchard, L.-S., Burt, S.R., Anwar, M.S., Kovtunov, K. V., Koptyug, I. V., Pines, A. NMR Imaging of Catalytic Hydrogenation in Microreactors with the Use of para-Hydrogen. *Science (80-.).* 2008;319: pp. 442–5.

[37] Brunner, E., Haake, M., Kaiser, L., Pines, A., Reimer, J.A. Gas flow MRI using circulating laser-polarized 129Xe. *J. Magn. Reson.* 1999;138: pp. 155–9.

[38] Codd, S.L., Altobelli, S.A. A PGSE study of propane gas flow through model porous bead packs. *J. Magn. Reson.* 2003;163: pp. 16–22.

[39] Koptyug, I. V, Altobelli, S.A., Fukushima, E., Matveev, A. V, Sagdeev, R.Z. Thermally polarized 1H NMR microimaging studies of liquid and gas flow in monolithic catalysts. *J. Magn. Reson.* 2000;147: pp. 36–42.

[40] Newling, B., Poirier, C.C., Zhi, Y., Rioux, J.A., Coristine, A.J., Roach, D., *et al.* Velocity Imaging of Highly Turbulent Gas Flow. *Phys. Rev. Lett.* 2004;93: pp. 154503.

[41] Prado, P.J., Balcom, B.J., Mastikhin, I. V, Cross, A.R., Armstrong, R.L., Logan, A. Magnetic Resonance Imaging of Gases: A Single-Point Ramped Imaging with T1 Enhancement (SPRITE) Study. *J. Magn. Reson.* 1999;137: pp. 324–32.

[42] Candès, E.J., Romberg, J., Tao, T. Robust uncertainty principles: Exact signal reconstruction from highly incomplete frequency information. *IEEE Trans. Inf. Theory* 2006;52: pp. 489–509.

[43] Donoho, D.L. Compressed sensing. *IEEE Trans. Inf. Theory* 2006;52: pp. 1289–306.

[44] Lustig, M., Donoho, D., Pauly, J.M. Sparse MRI: The application of compressed sensing for rapid MR imaging. *Magn. Reson. Med.* 2007;58: pp. 1182–95.

[45] Holland, D.J., Malioutov, D.M., Blake, A., Sederman, A.J., Gladden, L.F. Reducing data acquisition times in phase-encoded velocity imaging using compressed sensing. *J. Magn. Reson.* 2010;203: pp. 236–46.

[46] Baldwin, C., Sederman, A.J., Mantle, M.D., Alexander, P., Gladden, L.F. Determination and characterization of the structure of a pore space from 3D volume images. *J. Colloid Interface Sci.* 1996;92: pp. 79–92.

[47] Benkrid, K., Rode, S., Midoux, N. Prediction of pressure drop and liquid saturation in trickle-bed reactors operated in high interaction regimes. *Chem. Eng. Sci.* 1997;52: pp. 4021–32.

[48] Gunjal, P.R., Ranade, V., Chaudhari, R. Liquid Distribution and RTD in Trickle Bed Reactors : Experiments and CFD Simulations. *Can. J. Chem. Engneering* 2003;81: pp. 821–30.

CHAPTER 6 – INJECTION OF REPRODUCIBLE BUBBLES INTO AN INCIPIENTLY GAS-SOLID FLUIDISED BED

6.1. INTRODUCTION AND THEORY

The previous chapters of this thesis have described the fluid mechanics encountered when fluids are allowed to flow through the interstitial spaces of a solid matrix in which the solid particles are kept stationary. In this chapter, the solid phase is no longer static and the relative motion of both the solid and the fluid phase is studied.

If the fluid is passed upwards through the bed of particles, for low fluid velocities the bed behaves essentially the same as a fixed bed. Upon increasing the fluid flow, the friction acting on the particles causes them to move apart slightly and oscillate in spatially restricted zones. If however the fluid velocity is increased further, a point is reached at which the upward drag force on the particles due to vertical fluid flow becomes equal to their weight in the fluid. At this point, there ceases to be a compressive vertical force between particles in the bed, and they become suspended in the fluid stream. The bed is termed a fluidised bed. Thus the pressure drop becomes equivalent to the weight of the particles per unit area of the bed. This point is termed incipient fluidisation, and the fluid superficial velocity at which it occurs is known as the minimum fluidising velocity U_{mf}.

The behaviour of the bed upon further increases in fluid velocity depends on the physical properties of the solid-fluid combination. In liquid-solid systems, a regime of so-called smooth fluidisation is typically encountered. The bed remains relatively homogeneous in solids concentration, and increases in size with an observable rate of expansion in height. Whilst this regime of particulate, or homogeneous smooth fluidisation can be seen in gas-solid systems, it is restricted to dense gases at high pressure fluidising fine solid particles. Gas-solid systems much more typically exhibit aggregative fluidisation, which is a more chaotic regime in which large voids of fluid are found in the fluidised bed. As we shall see in subsequent chapters and discussions, the behaviour of these voids in the bed can be analogous to gas bubbles rising through liquids. The superficial fluid velocity at which bubbles first form in the bed is termed the minimum bubbling velocity U_{mb}.

The extent and severity of bubbling is a function of the fluid velocity, with greater velocities generally corresponding with a more vigorous bubbling regime. At very high fluid velocities,

physical transport of the solids out of the vessel is possible. This strategy is sometimes employed deliberately, as in the regeneration of catalyst particles in circulating fluidised beds. Under certain conditions, for example with very fine powders, high fluid velocities can lead to slugging behaviour in which large alternating regions of fluid-rich and particle-rich rise through the bed and collapse near the top. The regions occupy a diameter approximately equal to the diameter of the containing vessel.

An interesting and important characteristic of fluidisation is the formation and presence of rising bubbles within fluidised beds. Bubbles occur under certain conditions in fluidised beds during the aggregative fluidisation regime, in which two distinct phases can be observed within the bed of solids. There is a dense particulate phase which consists mainly of the solid bed material with interstitial fluid flow, and a lean phase of bubbles consisting mostly of the fluidising medium. These bubbles are distinct from bubbles formed in liquids most notably due to the lack of surface tension within the particulate medium and the fact that in liquids, the less dense fluid within bubbles does not readily undergo exchange with the denser liquid other than through diffusive mass transport. Despite this, bubbles in fluidised beds share many of the same characteristics as the analogous phenomenon found in true fluids. Fluidised bed bubbles readily rise to the surface with a defined velocity and erupt into the freeboard region. Additionally, they demonstrate and maintain a well-defined and in some cases predictable shape. The rise characteristics and velocity of bubbles in fluidised beds is perhaps most important, as it is this which has a large influence on particle and gas mixing behaviour in the bed. In one respect, it is the presence of bubbles which gives the particulate phase excellent mixing and heat and mass transfer. Conversely, the possibility of significant gas bypass in catalytic beds is an undesirable consequence of a bubbling bed and would result in an under-reacted gas stream. The ability to predict and model bubbling phenomena in fluidised bed reactors is therefore of critical importance, and has been the subject of intense academic scrutiny for many decades. Much progress has been made towards understanding bubble shape and structure, rise velocity and gas and particle dynamics, but a fundamental understanding of the phenomena still eludes many systems. This is often related to the difficulty of experimentally probing the optically-opaque media in fluidised beds.

The rise velocity of bubbles is an extremely important parameter to have knowledge of as it dictates the regime of gas interchange between phases as will be described later. The simplest relation investigated by Davies and Taylor [1] is based on experimental results for gas bubbles rising in columns of inviscid liquids and is as follows:

$$U_{b,\infty} = \frac{2}{3}\sqrt{gR_b}. \tag{6.1}$$

In Equation 6.1 U_b is the rise velocity of an isolated bubble and g is the acceleration due to gravity. In continuously bubbling and slugging beds, Davidson and Harrison [2] propose the following modification:

$$U_b = U - U_{mf} + U_{b,\infty}. \tag{6.2}$$

The $U - U_{mf}$ term is added to account for bubble interactions, but its inclusion has been contested by Müller [3] for freely bubbling beds, but must indeed be added to slugging beds.

Bubble size is a key parameter which can be estimated using a variety of empirical correlations. In general, all workers have found that bubble size increases with column height above the distributor, and thus all correlations contain a height factor. A popular and simple correlation by Rowe [4] is given by:

$$D_b = \frac{(U - U_{mf})^{\frac{1}{2}}(h + h_0)^{\frac{3}{4}}}{g^{\frac{1}{4}}}. \tag{6.3}$$

In this expression, D_b is the bubble diameter, or the diameter of the region of the bubble with the largest chord, h is the height above the distributor and h_0 is a characteristic constant for a distributor. Many other versions for this form exist, mostly having different values of the exponents for each term in Equation 6.3.

Both the academic and industrial examination of bubbling in fluidised beds have been centred on describing bubbling in terms of the bubble size distribution, rise velocity and bubbling frequency. Several different experimental strategies have been employed to describe the effect of bed physical parameters on these parameters, and subsequently infer the effects on bed performance. For predictive purposes, many historic studies have attempted to develop empirical correlations to describe bubble size, rise velocity and frequency for different combinations of fluid and particles. Bubble formation at the distributor has also been of central interest, as well as the coalescence behaviour of bubbles which come together higher up in the bed.

Bubble size and rise behaviour, being intimately related to overall bed physics, is a function of the classification of the bed materials according to Geldart [26]. A summary of several studies

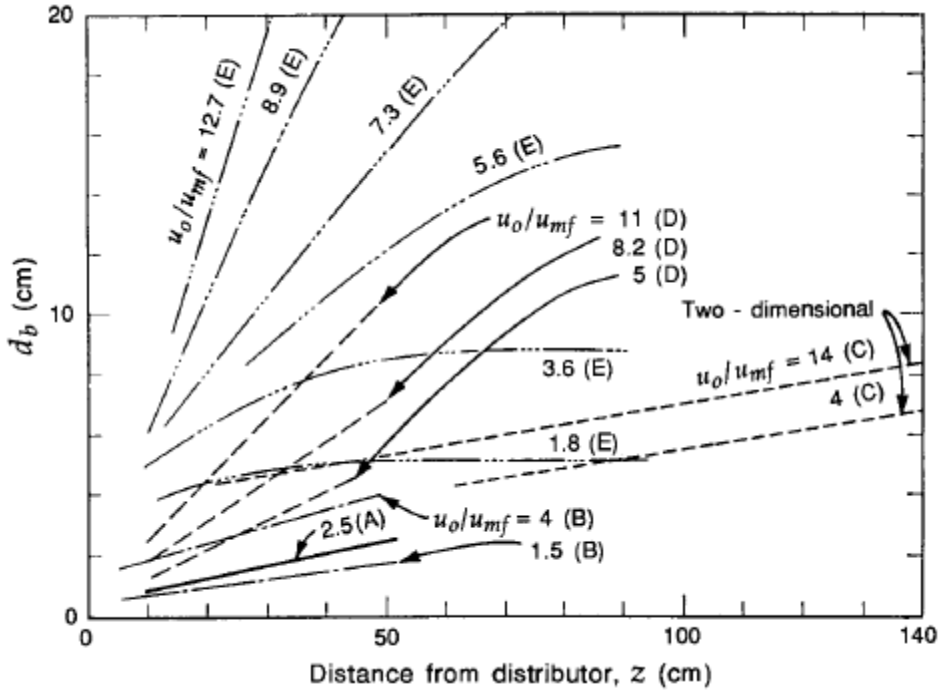

Figure 6.1: Bubble size as a function of bed height for different solid and fluid combinations in various beds by several authors. Reproduced from Kunii and Levenspiel [5]: (A) Yasui and Johanson [6]; (B) Toei *et al.* [7]; (C) Hiraki *et al.* [8]; (D) Kobayashi *et al.* [9]; (E) Hiraki *et al.* [8].

investigating the influence of height above the distributor, Geldart [26] classification and excess fluid flow on the size of bubbles is reproduced in Figure 6.1.

Bubble frequency at a given plane, defined as the rate at which bubbles pass through a planar location in the bed is only weakly influenced by the excess fluid velocity, which has been shown experimentally. Frequency at locations further away from the distributor is strongly related to the extent of bubble coalescence. Two primary models of bubble coalescence consider leading-following coalescence between bubbles which are axially aligned, and side-by-side coalesce of bubbles in the same radial plane. Due to coalescence, bubble frequency diminishes with height away from the distributor.

The dynamics of fluidised beds is difficult to analyse due to the opaque nature of particulate systems. Workers have used several techniques to study bubbling in fluidised beds including the use of invasive optical sensors [6,10], capacitance probes [11,12] and pressure sensors. Non-invasive methods are preferable as their effect on the fluidisation physics are minimal. Such methods use ionising radiation (X-rays or γ-rays), and tomographic or photographic techniques for image reconstruction. Positron emission particle tracking has also successfully been employed. This method uses tracer particles which contain positron sources, and γ-ray detectors to determine the spatial location of the tracer particle. Both electrical capacitance and

resistance tomography have been used to examine fluidisation behaviour. These methods make use of the spatial variation in capacitance and resistance within a sample, and use electrodes which record changes in these properties. Complex numerical methods are then employed to reconstruct data into images or useful signals. Non-invasive optical methods including planar laser induced fluorescence (PLIF) and particle image velocimetry (PIV) have also been widely implemented to gain insights into particle and fluid motion. For fluidisation studies, these methods often rely on the use of spatially-limited, pseudo-2D fluidised beds which have flat, transparent walls. They are therefore of limited accuracy when attempting to extend observations to industrially accurate 3D units of realistic dimensions.

Magnetic resonance imaging is able to be used non-invasively and on 3D, cylindrical fluidised beds and has been established as a powerful method for the analysis of bubbling dynamics [3,13–15]. As bubbles in fluidised beds typically have rise velocities up to 1 m s^{-1}, a technique which possesses high temporal resolution is ideal. As MRI requires the switching of large electrical coils to acquire different parts of the image signal, typical imaging sequences have relatively poor temporal resolution which would be unable to capture the structure or dynamics of fluidised bed bubbles. This is particularly true for any attempt to record fluid velocities, and especially fluids like gases which have low inherent NMR signal. Rapid imaging techniques such as FLASH and RARE have been used, and recently UTE [13,14]. With the aim of being able to record the fluid dynamics around an isolated bubble in a fluidised bed, a different experimental approach is required.

MR experiments, especially imaging in multiple dimensions, have inherently low temporal resolution owing to the need to traverse **k**-space. The fact that **k**-space is traversed in time means that significant motion-induced artefacts can result if motion is present in a sample. Various fast imaging strategies, such as FLASH and RARE, have allowed image acquisition times to be significantly reduced. These are used at the expense of signal-to-noise ratio, which is the second significant challenge presented. The low signal-to-noise associated with gases and solids necessitates the use of multiple scans which further reduces the temporal resolution.

If one could therefore eliminate the motion in some way, and thus acquire multiple scans of the same phenomenon over time, **k**-space could be built up and an image acquired. The idea is thus to have a reproducible phenomenon, such that the motion could be frozen in some way and the temporal variation of a single event effectively eliminated. One strategy for imaging single bubbles is to eliminate the randomness of a freely bubbling bed by creating reproducible

bubbles using an additional mechanism. In this way, the size, location and shape of bubbles could be controlled. If the generation of bubbles was also temporally predictable, the acquisition of images could in theory be timed appropriately to capture the reproducible bubble at the same point in space.

A similar approach and idea was followed in the study by Han *et al.* [16] which describes NMR imaging measurements of reproducible water droplets falling in air. In this study, a pipette was used to create a stream of predictably similar droplets. Each droplet spent only ~10 ms in the RF coil, thus a full 3D image of a single droplet event was impossible to capture. The authors thus resolved to make very similar droplets and acquire each scan for an image from a different droplet to build up the eventual image. The spectrometer acquisition was triggered using an infrared photosensor placed below the pipette tip to register when drops were released. The authors were able to capture the internal velocity field of the liquid within the droplet.

Several researchers have successfully introduced single bubbles via fluid injection into an incipiently fluidised bed. These typically involve the introduction of a nozzle for bubble injection which is placed centrally in the fluid distributor. Gas is allowed to pass through this nozzle from timed valve openings often employing a solenoid valve and timer. The time the valve spends open governs the volume of gas injected and thus the size and shape of the bubble as per Equation 6.3. Levy and Lockwood [17] used a pseudo 2D bed of dimensions 0.3 × 0.6 × 2.4 m to study freeboard flow characteristics following bubble injection and eruption. The bed material used was sand and the fluidising medium was humidified air. Their setup used a nozzle located at the centre of the distributor covered with mesh to prevent particles from falling in the nozzle. Bubble size was calibrated against the nozzle geometry, injection delivery pressure and solenoid valve opening time. The nozzle tube was passed upwards through the windbox which served to even the main fluidising flow prior to entering the bed. The authors were able to produce highly regular bubbles which were released with the main air supplying the bed at the minimum fluidisation velocity. The same setup was used in the counterpart paper to study particle elutriation characteristics which also saw the bubble injector introduction into a 3D bed (Levy *et al.* [17]).

Yorquez-Ramirez and Duursma [18] followed a very similar procedure using a nozzle tube placed slightly above the distributor of a cylindrical 3D bed with injections controlled by a solenoid valve. The distributor material used was a sintered metal disc. The main flow through the rotameter was again maintained at the minimum fluidisation velocity. The authors were

able to produce predictable bubble injections. Solimene *et al.* [19] conducted a PLIF experiment examining flow structures in the freeboard induced by erupting bubbles in a cylindrical 3D bed. They injected tracer-filled bubbles from a nozzle connected to a solenoid valve. The source of bubble fluid was a pressurised vessel containing the acetone tracer necessary for PLIF. The injection nozzle was passed through the windbox and was placed centrally in the fluid distributor. Further PLIF studies were undertaken by Hartung *et al.* [20] making use of a single bubble injection method to introduced traced bubbles into the fluidised bed. The bed used was a square cross-sectional vessel with a central nozzle for bubble injection. The bed was maintained at incipiently fluidised conditions while bubbles were injected. A solenoid valve was used to convey controlled volumes of acetone-rich air as bubbles into the bed. Bubbles were controlled by varying the pressure of the injection system and the opening time of the solenoid valve. These authors were able to produce a regular stream of bubbles for the study of time-averaged flow profiles in the freeboard of the fluidised bed. This exact experimental rig and results obtained from it were used in the other papers (Müller *et al.* [15]; Third & Müller [21]). Vun *et al.* [22] used two injection nozzles placed around the centre of a rectangular 2D fluidised bed. Their PIV study was also supported by CFD modelling results which confirmed the theory behind single bubble formation from an orifice into a bed at minimum fluidisation.

In the present study, it is required to inject reproducible bubbles into a fluidised bed which is set up for study using MRI. To make the phases sensitive to MRI, oil-containing seeds for the solid phase and compressed SF_6 gas are chosen as the materials. Therefore, the aim of the present study is to investigate the spatiotemporal reproducibility of bubbles injected into the SF_6-poppy seed fluidised bed. Employing an experimental approach like that of Han *et al.* [16] requires a high degree of reproducibility. To accomplish this, 1D signal profiles (representing a spatial average in the radial direction) of the bed are acquired. These experiments have a much higher temporal resolution (~10 ms) than 2D imaging sequences and thus the technique can study the behaviour of individual bubbles in the bed. This approach has previously been used to assess the bubble size, rise velocity and coalescence behaviour of bubbles in fluidised and fixed beds using MRI [14,23,24]. In this study, the size, rise velocity, general behaviour and statistical reproducibility of bubbles will be assessed using 1D profiles and compared to previous observations using other techniques and theory. Additionally, these techniques together with conventional pressure drop measurements will be used to assess the existence of a homogeneous, smooth fluidisation state previously speculated for this fluidised bed [25].

6.2. EXPERIMENTAL

6.2.1. FLUIDISED BED

The experimental system is schematically depicted in Figure 6.2.

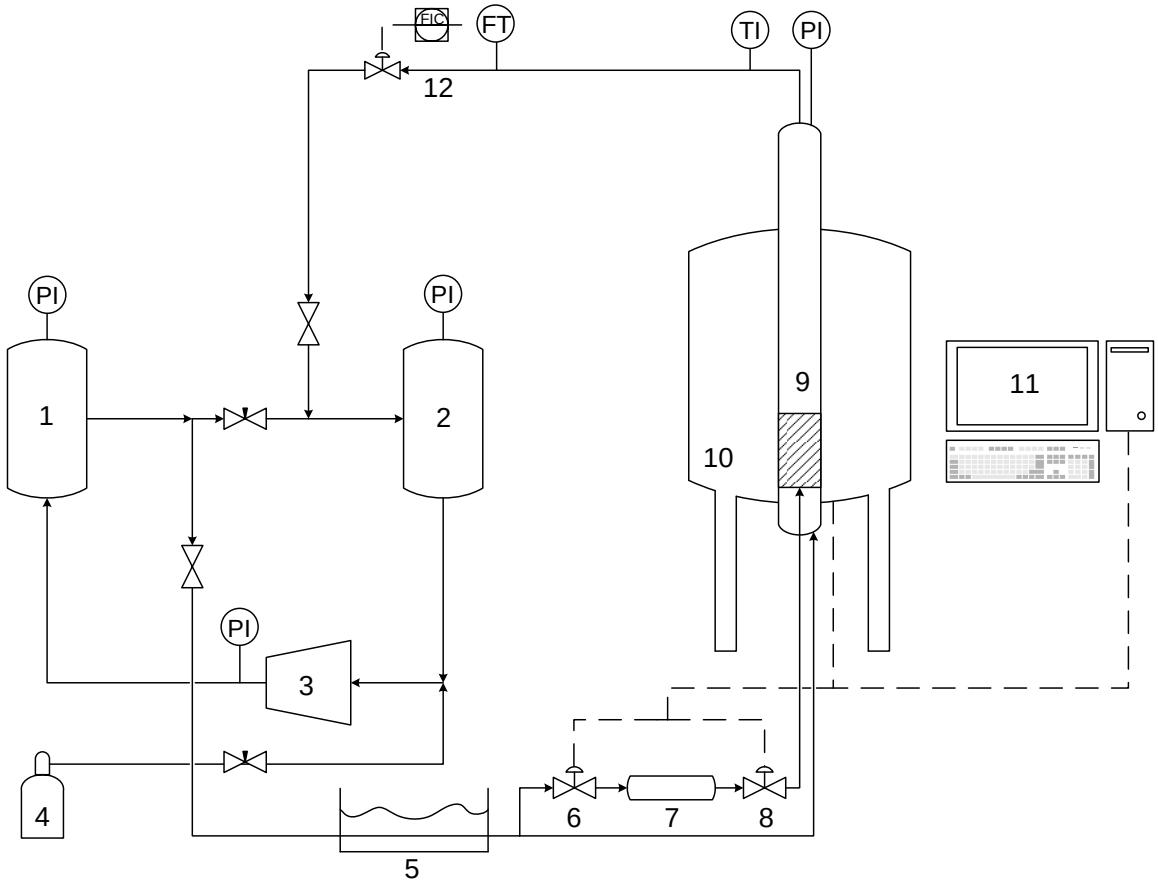

Figure 6.2: Process flow diagram of the single-bubble injector and fluidised bed apparatus inside the MRI magnet. Key equipment is labelled as follows 1: high pressure receiver vessel, 2: low pressure receiver vessel, 3: SF_6 compressor, 4: SF_6 cylinder, 5: cooling water bath, 6: injection reservoir refill valve, 7: injection reservoir, 8: bubble injection valve, 9: PVC fluidised bed, 10: superconducting MRI magnet, 11: controller computer for NMR software and valve injector, 12: SF_6 mass flow controller. Abbreviations: TI: temperature indicator, PI: pressure indicator, FT: flow transducer, FIC: flow indicator-controller.

The experimental fluidisation setup was modified from an earlier system which has previously been reported by Boyce [25]. In this study, a mechanism for the injection of single bubbles through the fluid distributor system was added and optimised. The vessel (9) was a 52 mm inner diameter, 2.0 m long PVC tube. A collar was used to set the vertical position of the vessel within the magnet. Gas was fed through a 60 cm long wind box filled with glass ballotini 5 mm in diameter. A sintered bronze disc served as the distributor which had a pressure drop higher than that across the bed of particles at minimum fluidisation. The flow to the bed was split into two lines. The first line supplied gas to keep the bed slightly above the minimum fluidisation velocity. In parallel with this line was a system designed to inject single gas bubbles into the

bed. Two electrically-actuated solenoid valves (Burkert 6011) units (6) and (8) with fast switching times (7-12 ms) were placed either side of a 300 mL holding vessel (7). This served to store gas for the injections at a constant vessel pressure while not disrupting the fluidising gas stream. Valve (8) was used to inject bubbles and (6) was closed to allow the injection system to be isolated during injection. Between injections (6) was opened to replenish the pressure in the tank (7). The injection line ran through the plenum chamber and terminated in a nozzle threaded into the sintered bronze distributor. This was covered by a thin wire mesh to prevent particles from entering the gas line. In this setup, the pressure drop for the main fluidising flow was 400 times larger than for the bubble injection line, ensuring that bubbles would be injected at high pressure. This arrangement has been used previously for the injection of single bubbles into fluidised beds [17–20]. The solenoid valves were controlled electronically using a computer. Poppy seeds were used as fluidised particles with a settled bed height of 100 mm. The particles were sieved to a mean size of 1.2 ± 0.15 mm. The sphericity of the poppy seeds was found gravimetrically to be 0.86 ± 0.02. The system was classified as Group D by the classification of Geldart [26].

Due to its nonzero nuclear spin, 100% natural abundance of the NMR-active nucleus ^{19}F and inertness, SF_6 gas was used to conduct the gas phase MRI experiments. It was supplied at a purity of 99.999% from Air Liquide® in a 20 bar cylinder labelled (4) in Figure 6.2. SF_6 has an extremely high global warming potential (~22,800), therefore a recirculation system was used to minimise the release of gas.

The flow of gas to the fluidised bed was supplied using a circulation system consisting of a compressor (3), a high-pressure receiver tank (1) and a low pressure tank (2). The compressor used was a specialised SF_6 unit by Dilo® which handles suction pressures of ~0.5 bara and delivers a compression ratio of 24 typically to give gas pressures of 10-12 bara. The compressor provided a pressure gradient between (1) and (2). Gas was then able to flow through the fluidised bed (9). A needle valve was used to control the pressure gradient by allowing an amount of gas to bypass the fluidised bed. SF_6 gas was fed into the system from cylinder (4) using a valve when required. A k-type thermocouple was used to measure the gas temperature in the bed. A thermal mass flow controller labelled (12) (Bronkhorst EL-FLOW® Select) was used to control the flow rate through the bed and provide quantitative measurements of the mass flow rate of the SF_6 gas. The gas from the high pressure tank was passed through 2 m of metal tubing immersed in a water bath (5) held at room temperature to cool the gas from the compressor and provide temperature control.

Table 6.1: Operating parameters of the experimental fluidised bed

Bed Parameter	Value
Inner diameter	52 mm
Tapped bed height	100 mm
Particle type	Poppy seeds
Gas	Sulphur hexafluoride
Particle diameter	1.2 ± 0.15 mm
Particle density	1040 kg/m^3
Particle sphericity	0.86 ± 0.02
Gas density	56 kg/m^3
Geldart's grouping	D
Pressure	7.5 barg
Temperature	25.0 ± 3.0 °C
Gas viscosity	16 µPa.s
U_{mf}	0.088 m s^{-1}
U_{mb}	0.088 m s^{-1}
Distributor type	Porous sintered bronze disc

With this system, the temperature of the gas in the fluidised bed was maintained at 25.0 ± 2.0 °C when the system was run over periods of up to 7 hours. The key parameters of the fluidised bed are summarised in Table 6.1.

6.2.2. MAGNETIC RESONANCE SETUP

Magnetic resonance experiments were conducted using a vertical bore Bruker Spectrospin DMX 200 superconducting magnet (10) with field strength of 4.7 T (200 MHz Larmor frequency for ^{1}H) and bore diameter of 149 mm. The magnet was tuned to a frequency of 199.7 MHz in order to image the ^{1}H signal from the poppy seeds, and a frequency of 187.9 MHz to image the ^{19}F nucleus in the SF_6 gas. This frequency separation is sufficiently large such that no interference between the two phases is observed. The radiofrequency coil used was of the birdcage type with an inner diameter of 64 mm. The gradient set used was a Bruker Mini 0.36 shielded gradient with a maximum gradient strength of 13.88 G cm^{-1} in all three orthogonal spatial directions. All experimental data were recorded using the Bruker TopSpin^{TM} software on a standard desktop computer (11).

6.2.3. 1D PROFILES OF PARTICLE PHASE

The NMR data presented in this chapter consists of 1D images of the bed acquired in three orthogonal directions. A schematic diagram illustrating the method and application to fluidised bed bubbling is provided in Figure 6.3. An absence of ^{1}H nuclei, as in a void or bubble travelling through a fluidised bed, will manifest as a depression in the signal intensity. This is illustrated in Figure 6.3 by showing the bubble and the corresponding 1D profile which shows a signal depression radially in line with the bubble. As the bubble moves up in the bed, the depression in signal intensity will be recorded at a location in the profile which corresponds to higher positions. Figure 6.3 (c) shows a series of profiles acquired as a single bubble rises

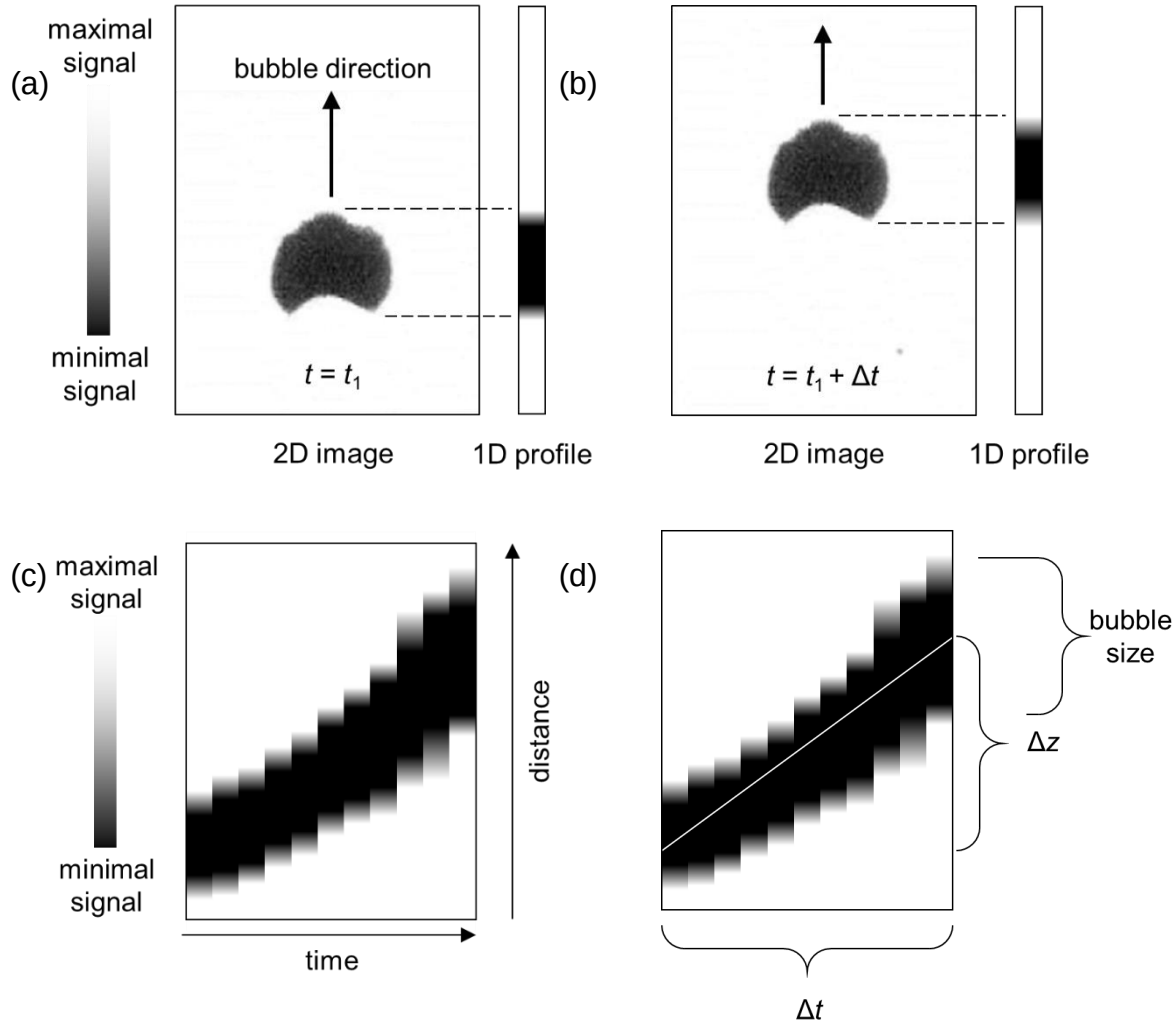

Figure 6.3: The capture of bubble motion and behaviour by the recording of 1D signal intensity images of the fluidised bed. (a) illustrates the position of a bubble at time *t*, (b) shows this same bubble later $t + \Delta t$. The transit of the bubble upwards is indicated by the directional arrow. The 1D image profile is indicated on the right, which shows a darkened region which is representative of the bubble. This profile is an average of the signal intensity originating from the poppy seeds in the radial direction. (c) shows a series of these profiles taken over time, from which the trajectory of the bubble can be assessed. (d) indicates how, from knowing the field-of-view of the profile the vertical bubble size can be inferred and the average bubble rise velocity (shown by the white line on the image) can be calculated from the gradient of bubble travel distance over the time between profiles.

through the bed, tracing out its trajectory. The vertical size dimension can be calculated if the MRI field-of-view is known, and the rise velocity can be determined by the ratio of the average displacement of the bubble in the time between any two profiles, both calculations are illustrated in Figure 6.3 (d). As was explained in detail previously, when a spatial gradient of known shape is applied to a population of nuclei which have been excited by an r.f. signal of the correct frequency, their precessional frequencies will vary along the gradient according to the magnitude of the magnetic field at a point. In the present study, a single MRI gradient is applied in each orthogonal spatial direction at a time, which imparts a spatial encoding of the signal. Upon Fourier transformation of the signal, a spatial map is acquired which represents the distribution of magnetic spins at each frequency (or point in space). Since the gradient application and signal acquisition process for a 1D image is relatively fast in MRI *O*(ms), this experiment is useful for studying fast physical processes, such as the rise of bubbles through fluidised beds.

This method is first employed to assess the existence and behaviour of single injected bubbles into the fluidised bed. By including an electronic trigger which simultaneously opens the bubble injection solenoid valve and starts the NMR pulse sequence, the experiment can be calibrated to capture signal from the fluidised bed with a defined delay between bubble release and signal acquisition. The delay time can either be fixed to capture information about the bubble at the same location in the bed, or varied to assess the rise behaviour of the bubbles. Acquiring successive profiles of bubble injections was employed to investigate the following aspects of bubble injection:

1) Whether the bubble injection system functions as intended
2) To what degree bubble size can be related to injected gas volume
3) The spatiotemporal reproducibility of the bubble injection process
4) The effects on the produced bubbles of:
    a. injection pulse time
    b. frequency of bubble injection
5) Rise velocity and rise behaviour
6) Bubble size.

To assess the statistical reproducibility of the bubble injector, the average standard deviation between successively recorded profiles will be used as a metric to determine which variables

give the most reliably reproducible bubbles. Key experimental parameters for the 1D profiles are tabulated in Table 6.2.

Table 6.2: Experimental parameters used in 1D profile images of the particle phase

Parameter	Value
Field-of-view (*z*,*x*,*y*)	100 mm, 60 mm, 60 mm
Resolution (*z*,*x*,*y*)	1.25 mm, 0.470 mm, 0.470 mm
Pulse sequence	Spin echo
Recycle time	40 ms
Experiment time	700 ms
Number of profiles	128

6.2.4. MEASUREMENT OF U_{MF} AND U_{MB}

As the bubbles require injection into an incipiently fluidised bed, it is crucially important to have an accurate determination of the minimum fluidisation velocity and the minimum bubbling velocity. For gas-fluidised beds, these values typically coincide with one another and a state of homogeneous fluidisation in which bed expansion occurs is not observed. It was previously supposed that due to the high density of SF_6 gas and relatively large nature of the seeds, a homogeneous fluidisation state did exist for this group of materials, however using a combination of techniques in the present study it is conclusively shown that this is not the case and that the fluidisation behaviour is as expected for Geldart's Group D particles.

The point of minimum fluidisation is determined using the traditional method of measuring the pressure drop across the bed at various superficial gas velocities. Before the drag force acting on the particles is sufficient to overcome their weight in the fluid, the bed behaves as a fixed bed and the pressure drop is governed by a quadratic relation as in the Ergun equation. It should be noted that particles can exist in different levels of compaction. Upon the application of vibrations or tapping, particles can "jam" together to form a more tight state of packing than if they could rest simply at their points of natural contact. Therefore, at or even slightly above minimum fluidisation, the pressure drop may rise to a value higher than the theoretical weight of the bed per unit bed cross sectional area. Once fluidised however, the pressure drop will be equal to a constant value of the weight per unit bed area. Due to equipment limitations pressure probes could not be inserted directly above and below the bed, and thus the baseline system

curve without any particles present was recorded and subtracted from the pressure drop measurements made with the particles inside the vessel.

The bed was routinely tapped at each velocity to correctly distinguish between the fluidised and unfluidized states, as MRI measurements were simultaneously taken to identify signs of bed expansion or bubbling. This method allows the fluidisation state to be unambiguously identified. The pressure drop was recorded at 20 linearly spaced superficial velocities at a bed pressure of 7.5 barg and 21 °C. The gas flow was initially incremented in a positive direction, and then lowered incrementally to identify hysteresis. The point at which the upward and downward curves intersect is the point of minimum fluidisation, as it is free from the influence of particle jamming.

The minimum bubbling velocity was calculated from acquiring a series of 1D profiles at each superficial velocity. When static, the difference between successive profiles in time would be minimal. Therefore, by taking the standard deviation across the time dimension of a series of profiles and plotting this as a function of superficial velocity, a sudden increase in the standard deviation – indicative of rapid changes in the bed particle density – would be able to unambiguously identify the onset of bubbling in the fluidised bed. Together these two measurements, the pressure drop and 1D MRI profiles, will be able to identity U_{mf} and U_{mb} conclusively and indicate whether any difference in their values suggests the existence of a homogeneous, smooth fluidisation regime with bed expansion.

6.3. RESULTS

6.3.1. MEASUREMENT OF U_{MF} WITH MRI AND COMPARISON WITH PRESSURE MEASUREMENTS

Three distinct metrics were used to unequivocally determine the location of the point of incipient fluidisation U_{mf}. This is due to unexpected observed behaviour for the combination of SF_6 gas and poppy seeds at pressure. For all three types of measurements, the bed was subjected to gas flow increasing upwards in magnitude, and then downwards in what is henceforth referred to as the "up" and "down" runs respectively. For clarity, the mode of operation is given a numerical designation provided in Table 6.3, which includes the use of tapping as described in the experimental section.

Table 6.3: Designations for running modes used to assess the existence of the homogeneous fluidisation state. Tapping was performed to unjam particles and provide an unambiguous bed height. Up- and down-sweeps are typically performed to identify the point of incipient fluidisation in the pressure drop curve.

Designation	Mode of operation
I	Up-sweep with tapping
II	Down-sweep with tapping
III	Up-sweep (no tapping)
IV	Down-sweep (no tapping)

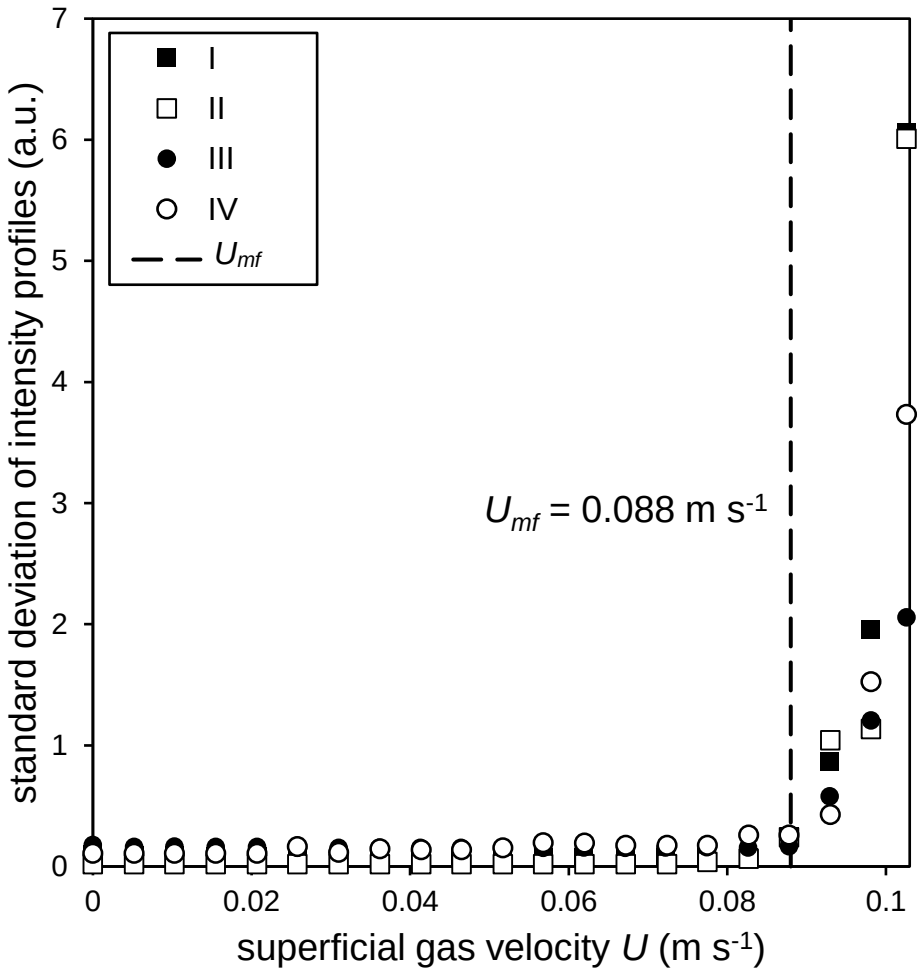

Figure 6.4: The standard deviation between successive MRI 1D profiles recorded in time as a function of the gas superficial velocity flowing through the bed. The signal intensity acquired when a single vertical gradient is applied between successive temporal profiles of a temporally steady system should differ only by the noise level. Any deviation greater than this is indicative of temporal instabilities and movement in the sample. Here the average temporal standard deviation is shown for both sweeping up (solid black markers) and down (empty white markers) gas velocity, and for both experiments in which the bed was tapped (squares) and not tapped (circles) to study the effect of particle jamming. Also shown is a dashed vertical line indicating the velocity of minimum fluidisation as determined using all three measurements presented in this section.

Early measurements and bed observations [25] suggested the possible existence of a state of homogeneous fluidisation for this system, despite no such state being reported previously for Geldart Group D particles. Homogeneous fluidisation is only typically observed in liquid systems. Figure 6.4 shows a plot of the average standard deviation between a series of profiles recorded in time as a function of gas velocity. If the bed is spatially steady at a gas velocity, it is expected that profiles recorded at different times will only have differences amounting to the experimental noise. Above the point of minimum fluidisation therefore, when particles are free to move, we expect a clear increase in the standard deviation across time of the signal. For all operational modes (I-IV), the temporal standard deviations are approximately zero below a gas superficial velocity of U = 0.088 cm s^{-1}. Above this point, the standard deviation increases sharply with increasing superficial velocity in each case but displaying different responses for each velocity. It is not expected that the standard deviation displays an analytical relationship beyond the point of minimum fluidisation, as the amount of random fluctuation beyond this point is not directly related to the superficial velocity.

The height of the bed is also monitored using MRI profiles by assessing the location of the bed surface relative to a fixed point in space. These data are shown as a function of gas superficial velocity in Figure 6.5. The bed was loaded with sufficient particles for a resting bed height of approximately 100 mm. For modes of operation (I), (III) and (IV), the data show roughly constant bed height of 100-105 mm and no effect of increasing or decreasing the superficial gas velocity. The fluidised bed height for (I) is seen to be slightly less than (III) and (IV), which is expected as the particles are in a tighter arrangement. It is also seen that it is more constant than the other cases. At a velocity of ~ 0.088 m s^{-1} the behaviour changes, as the bed heights for all runs converge and are shown increasing with increasing superficial velocity. Above this velocity, it is shown that both the effect of tapping the bed and increasing or decreasing the superficial velocity has no effect on the bed height. This insensitivity to tapping and lack of hysteresis with respect to fluid velocity is indicative of fluidisation. Below this point therefore the bed is not fluidised. Run (II) displays markedly different behaviour, with a gradual and continuous contraction to a final bed height of ~ 85 mm at a velocity 0.06 m s^{-1}. This experiment was repeated, and the same behaviour was observed.

Fluidisation behaviour is traditionally characterised using pressure drop measurements of the bed. Where the pressure drop remains constant at a value equal to the weight of the bed per unit area the bed is said to be fluidised. The pressure drop as a function of gas superficial

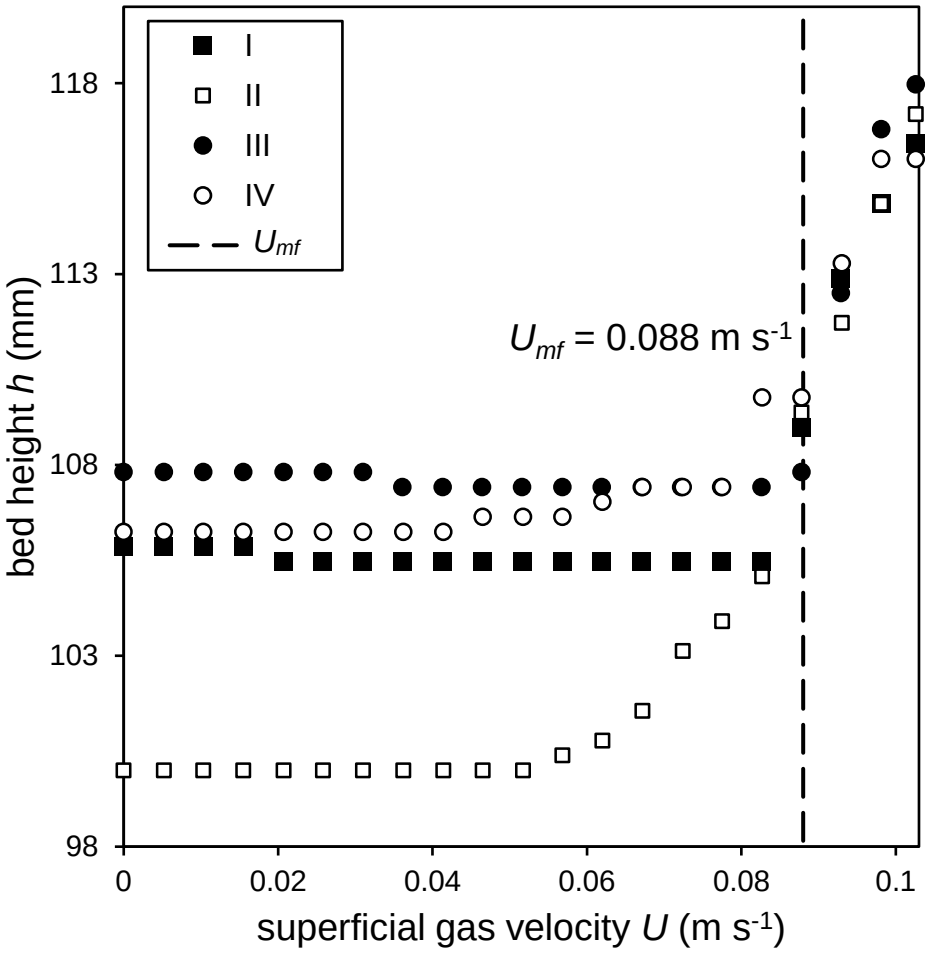

Figure 6.5: Measurement of the height of the bed *h* as a function of gas superficial velocity *U*. These heights are determined using a centimetre scale on the side of the bed which is relative to the known height of the distributor. The height is monitored using MRI profiles. A sharp depression in signal intensity signifies the bed surface, and its movement up and down relative to a fixed point can be determined quantitatively knowing the field-of-view of the profile. The bed is initially positioned such that its surface is central in the image field-of-view. Bed height is plotted here for both sweeping up (solid black markers) and down (empty white markers) gas velocity, and for both experiments in which the bed was tapped (squares) and not tapped (circles) to study the effect of particle jamming. Also shown is a dashed vertical line indicating the velocity of minimum fluidisation as determined using all three measurements presented in this section.

velocity is presented in Figure 6.6. The data shown are typical for a fluidised bed, with a parabolic increase in pressure indicative of fixed bed behaviour below a velocity of ~ 0.088 m s^{-1}. At precisely this point, some spread in the data is recorded between modes (I-IV). This is due to different extents of particle jamming and thus different pressure drops at the point of fluidisation. At higher superficial velocities, within a single data set the pressure remains constant – indicating fluidisation. There is some difference between tapped (I and II), and non-tapped (III and IV) runs with (I) and (II) having a slightly lower pressure drop. Below minimum fluidisation, it is noted that the up-sweep (I and III) has consistently higher pressure drop than the down-sweep (II and IV), and (III) and (IV) have slightly higher pressure drop at each point than (I) and (II).

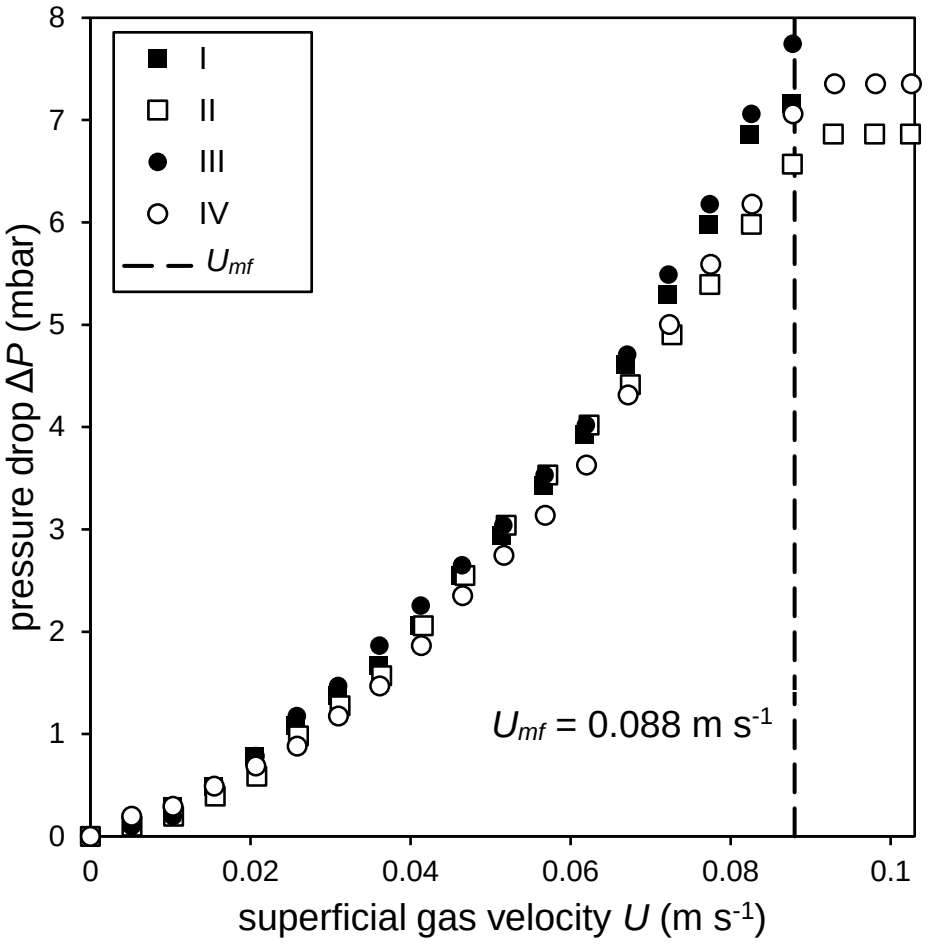

Figure 6.6: Pressure drop across the bed ΔP as a function of gas superficial velocity U. Pressure drop is shown for both sweeping up (solid black markers) and down (empty white markers) gas velocity, and for both experiments in which the bed was tapped (squares) and not tapped (circles) to study the effect of particle jamming. Also shown is a dashed vertical line indicating the velocity of minimum fluidisation as determined using all three measurements presented in this section.

6.3.2. INJECTION OF GAS AND EFFECT ON INTENSITY PROFILE

Figure 6.7 illustrates the fluidised bed under different conditions of bubbling. Initial imaging employed 1D profile measurements due to their high temporal resolution compared with 2D imaging schemes. Figure 6.7 (a) shows the bed under static conditions, prior to fluidisation. The intensity of the bed profile varies only by the experimental noise level between successive profiles, which indicates that the particle phase is spatially static. Any deviation from this would be evident in the form of regions of reduced signal within the bed. This is shown in Figure 6.7 (b), in which the bed was made to freely bubble above U_{mf}. Here the deviations in signal intensity between successive profiles are significant, indicating the passage of bubbles, regions of varying particle density which pass through the bed. It is noted that no discernible temporal patterns are identified as can sometimes be found in fluidised beds under the present conditions, and that the nature of the fluidisation of this system appears notably chaotic.

In the final image Figure 6.7 (c), the bed has been brought to the point of incipient fluidisation and the single bubble injector has been triggered to inject individual bubbles. As the imaging region is 50 mm above the gas distributor and injector nozzle, the acquisition of MRI signal is deliberately delayed by a set delay time which can be varied. In this image, the delay was increased by 0.0159 s between profiles, which allowed the bubble trajectory to be captured as the bubble was displaced between successive profiles by an amount equal to its rise velocity multiplied by the time increment between profiles. The bubble is identified by the region of depressed signal showing a rising trajectory through the bed.

It is noted that at a point approximately 40 mm above the distributor, the bubble trajectory displays an inflection as the bubble is seen to slow down. As time advances it is seen that injected bubbles become increasingly variable in terms of size and spatial location.

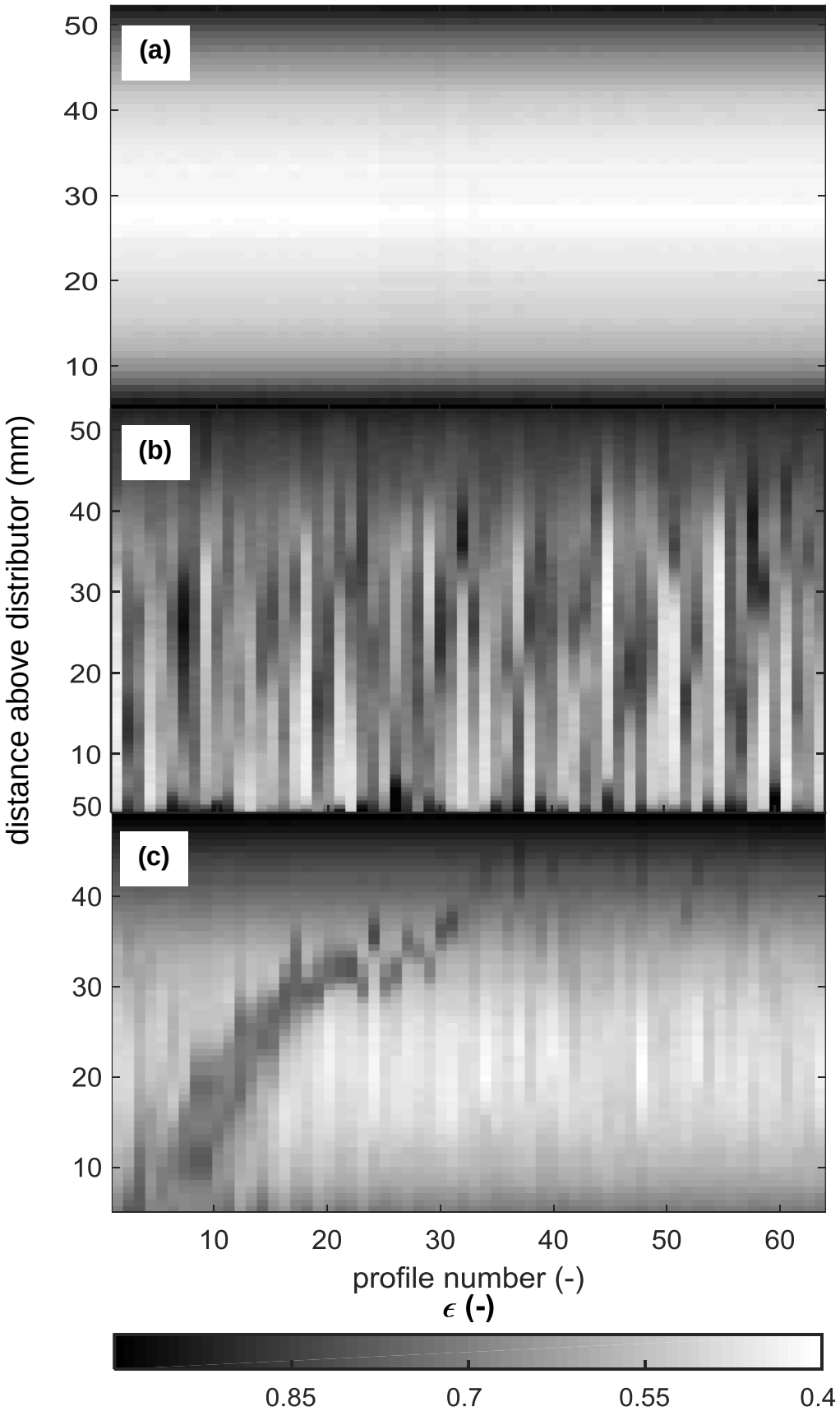

Figure 6.7: 1D MRI profile series shown for (a) an unfluidised non-bubbling bed, (b) a freely bubbling chaotic bed and (c) a stack of 1D profiles of controlled single bubble injections showing distinct individual bubbles captured at increasing delay between bubble injection and profile acquisition. As per the colour scale, regions which are rich in particles are indicated by increased signal strength or white, and regions which are black indicate lack of ^{1}H signal. The colour bar indicates void fraction.

6.3.3. BUBBLE RISE BEHAVIOUR

The injected rising single bubbles shown in Figure 6.7 (c) are observed to undergo atypical rise behaviour which can be broadly classified into three different regimes or regions. These are shown in Figure 6.8 (a) as region (i), (ii) and (iii) divided by the red lines.

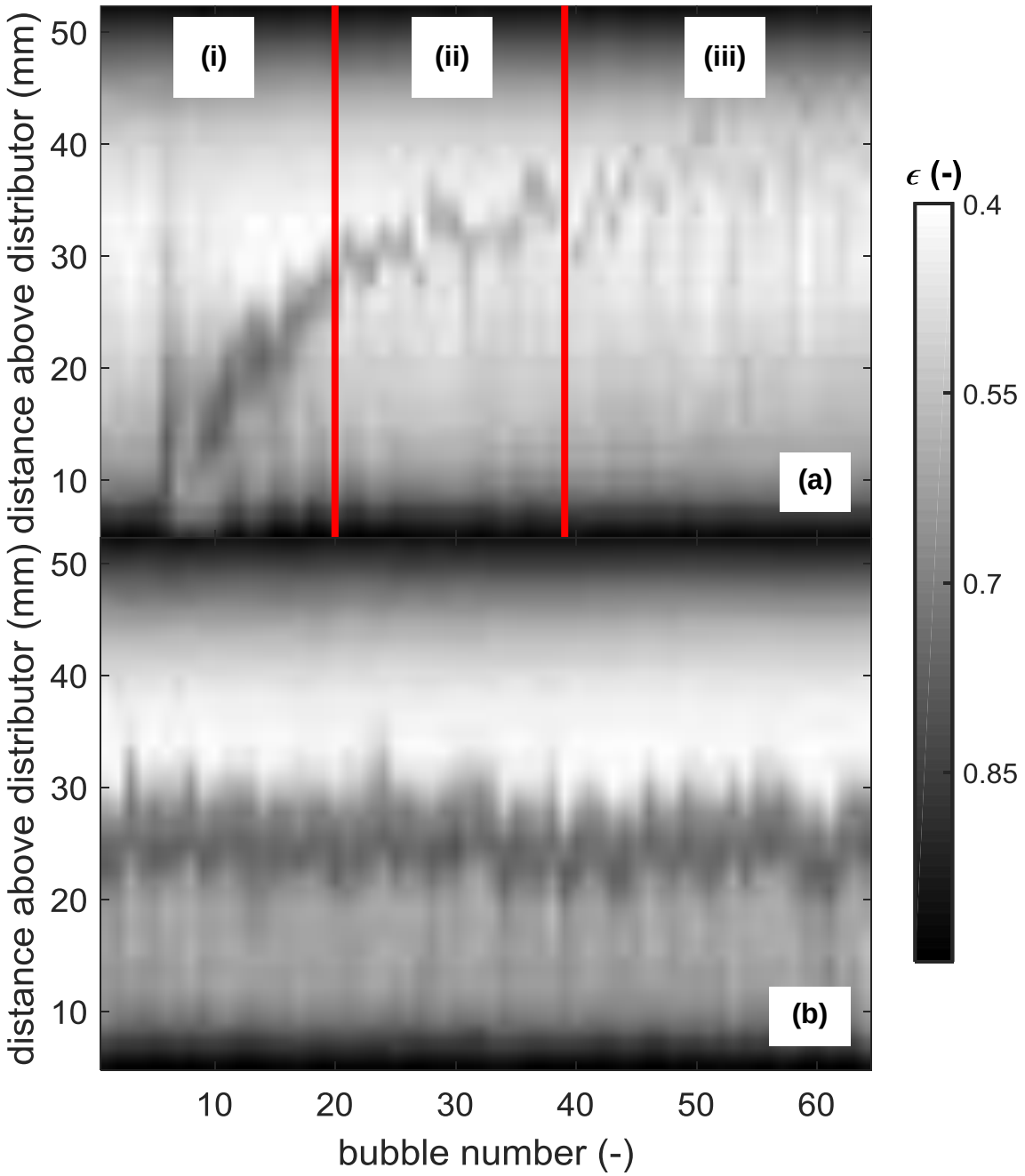

Figure 6.8: Time series of 64 1D MRI profiles illustrating in (a) the different regimes (i, ii and iii) found for rising single bubbles at increasing delay times and (b) a series of 'frozen' bubbles, with each profile acquired at the same delay time (0.13 s) between injection and signal acquisition thus allowing the signal from the bubble to be acquired when it is in the same spatial position (~25 mm above the distributor). Red lines in (a) indicate the division between rise regimes. More detail about the regimes (i-iii) is provided in the main text.

In region (i) the bubble size and position are approximately consistent, and the rise trajectory is linear. At the border between (i) and (ii), an inflection in the rise trajectory is encountered and the bubble begins to slow its ascent. This point of inflection was observed to be a function of superficial flow, occurring typically between 30 mm and 40 mm above the distributor, with higher superficial flows showing a higher point of inflection. Region (ii) is where the bubble begins to exhibit atypical rise behaviour, as fluidised bed bubbles typically show increasing size and rise velocity through the bed before erupting at the bed surface. Instead in region (ii) we see that bubbles slow down, their size is diminished compared to region (i) and the position becomes slightly less predictable than in region (ii).

Region (iii) is identified as where the bubble behaviour becomes even more difficult to predict as the bubble is shown to disappear. The disappearance is attributed to the bubble collapsing. In region (iii), the injected bubbles become smaller and the observed average rise velocity in this region is lower than in regions (ii) and (i). The position of the bubble is shown to be more random than in region (ii), and certainly beyond this region above 50 mm in the bed, the bubble is shown to have totally dissipated. Despite this, it is shown that in Figure 6.8 (b), if the delay between bubble injection and 1D signal acquisition is held constant instead of linearly varied as in Figures 6.8 (a) and 6.7 (c), it is possible to acquire signal from the bubble in approximately the same vertical position with each profile. In Figure 6.8 (b) a depression in signal intensity representing the rising bubble is shown in each of the 64 acquired profiles at approximately the same spatial location 25 mm above the bed distributor. Some vertical movement is recorded, with the position of the vertical centroid of the bubble being recorded as 25 ± 2.5 mm. The vertical size of the injected bubble for constant injection parameters is seen also to be approximately constant at 15 ± 0.9 mm. The statistical reproducibility of the bubble size and position is assessed in the subsequent sections.

By adjusting the injection parameters of single bubbles, it is possible to alter the rise behaviour of the bubbles being studied. Figure 6.9 illustrates different rise behaviour for two different bubble injection parameters. For both experiments the superficial gas flow is held at the minimum fluidisation velocity, but in Figure 6.9 (a) the injection time is 100 ms which is double that for Figure 6.9 (b) of 50 ms. This shows that two bubbles of different volumes are injected into the bed. Figure 6.9 (a) shows a larger bubble, indicated by the relatively lower signal intensity in the void region. Figure 6.9 (b) shows a comparatively smaller bubble, which rises more slowly and begins to dissipate within the field-of-view as shown previously. The

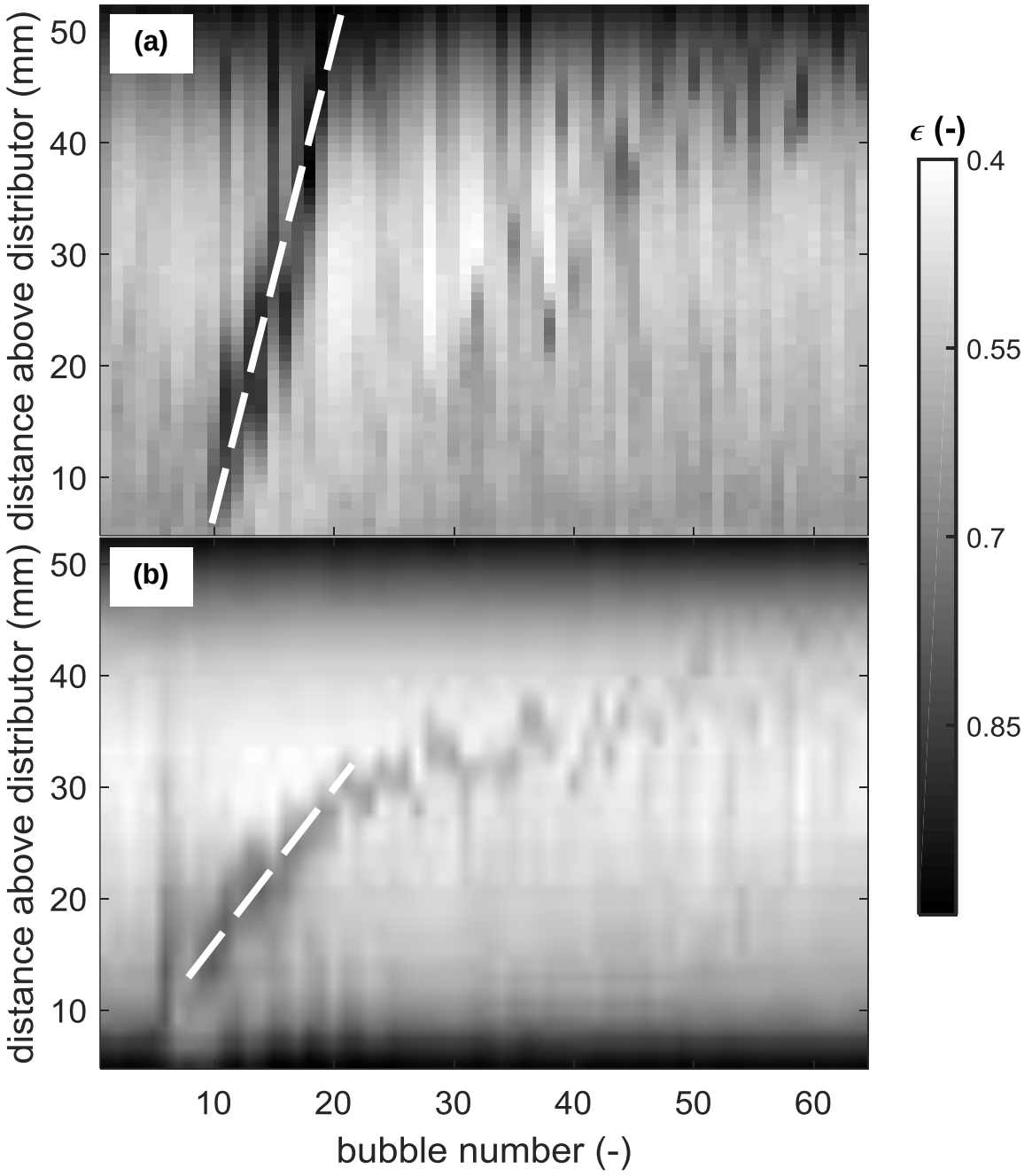

Figure 6.9: Time series of 1D MRI profiles showing two rising bubbles of different rise velocity. In (a) a fast-rising bubble is shown, and in (b) a bubble which rises more slowly and begins to dissipate. The injection pulse durations for the bubbles in these experiments are (a) 50 ms and (b) 100 ms. The part of the bubble's trajectory which is roughly linear is highlighted by the dashed white line which is overlaid onto the rising bubble. Note the gradient is much steeper in (a) than in (b). The rise velocity calculated in each case is (a) U_b = 23 cm s^{-1} and (b) U_b = 12 cm s^{-1}. (a) is indicative of a larger bubble which is deduced from the lower void signal intensity as compared to (b).

white dashed lines drawn over the linear region of the bubble rise are provided to illustrate the graphical difference in rise velocities and trajectories with a steeper gradient observed in the case of (a) and a shallower gradient shown for (b), as well as the method by which bubble rise velocities are calculated in this work. The gradient of this line through time and space is

identically the rise velocity. It is mentioned that only region (i) of the rise behaviour is taken to assess rise velocity, as it is only in this region in which the bubble behaves in the classical manner. By altering the volume of injected gas through the pulse duration, it is thus possible to produce bubbles of differing size and rise velocity. Figure 6.9 (a) additionally shows other minor bubbling events after the passage of the main bubble, associated with smaller bubbles which have potentially ejected or have broken off the injection of the main bubble.

Bubble rise velocity in both liquids and granular media is well known to be a function of the bubble geometry, specifically its volume and shape. It is established that fluidised bed bubbles typically obey the following relation, which is a generalisation of the work on rising spherical cap bubbles in inviscid liquids:

$$U_b = k\sqrt{gD_e}. \tag{6.4}$$

In Equation 6.4 U_b is the isolated bubble rise velocity, g is the acceleration due to gravity, D_e is the bubble equivalent diameter and k is an experimentally determined parameter which is affected by bubble geometry and particle rheological behaviour. As the bubble approaches an ideal spherical cap, and the fluid behaviour approaches that of an inviscid liquid, these parameters should approach those determined by Davies and Taylor [1]. For fluidised beds, k is typically found to be in the range of 0.57-0.85 [27]. In the present work, bubble volume was estimated using the actual bubble diameter D_b which was quantitatively determined using horizontally-acquired 1D MRI profiles. The bubble volume is then determined by assuming they are spherical in shape. This assumption is shown later as being justified by 2D images in the axial and radial directions (see Figures 6.12, 7.2, 7,3 and 7.4). In this bubble geometry, a cap of a certain fraction 'removed' from the bubble volume at the rear of the bubble, known as the wake fraction:

$$V_B = (1 - f_w)\frac{\pi}{6}D_b^3\ . \tag{6.5}$$

In Equation 6.5, f_W is the wake fraction of the bubble, and is simply the fraction of bubble volume removed from an ideal sphere. This quantity was determined in the present experiments by comparing the MRI signal acquired from a real bubble in the bed to a numerically integrated perfect sphere of the same size and centroid location. This comparison is illustrated in Figure 6.10. The bubble is shown to have a nearly spherical front, with the lines in close agreement above the bubble equator. Some particle signal is recorded around the bubble equator which

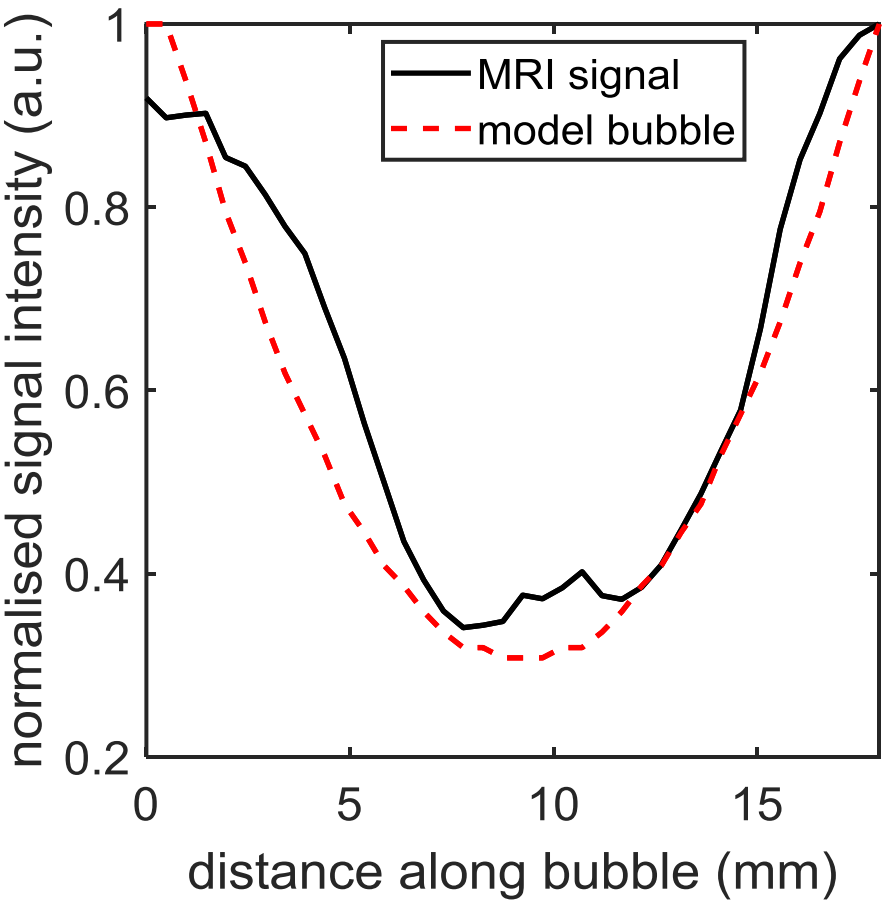

Figure 6.10: The vertical profile of a single bubble acquired using a 1D MRI experiment (sold black line) compared with a numerically integrated perfect sphere with the same centroid (red dashed line). This is used to compare the shape of the bubble front and to calculate a quantitative value for the wake fraction of the bubble.

may indicate the presence of falling particles inside the bubble. Below the equatorial position we see a difference in the line shapes which indicates the presence of the particle wake. The total signal is integrated and the ratio between the two will be equivalent to the wake fraction. In the present experiments the wake fraction was found to be 0.12 ± 0.012. The bubble volume calculated from Equation 6.5 is then used to determine the equivalent diameter D_e of a sphere of equivalent volume. Equivalent volume has been shown to be a correlating dimension for bubble rise velocity owing to the analogous behaviour of fluidised bed bubbles with bubbles rising in inviscid liquids [5,28]. The results of plotting the measured rise velocity as a function of the bubble equivalent diameter are provided in Figure 6.11.

In Figure 6.11 a scatter of several measurements of rise velocity and bubble size. Error bars denote the standard error for each experiment, defined as the standard deviation divided by the mean. The model for bubble rise Equation 6.4, shown by the dotted line, was fitted to the data using the method of least squares. Slightly more scatter is observed in the rise velocity than that of the bubble size. Agreement between the recorded data and model is however good, with

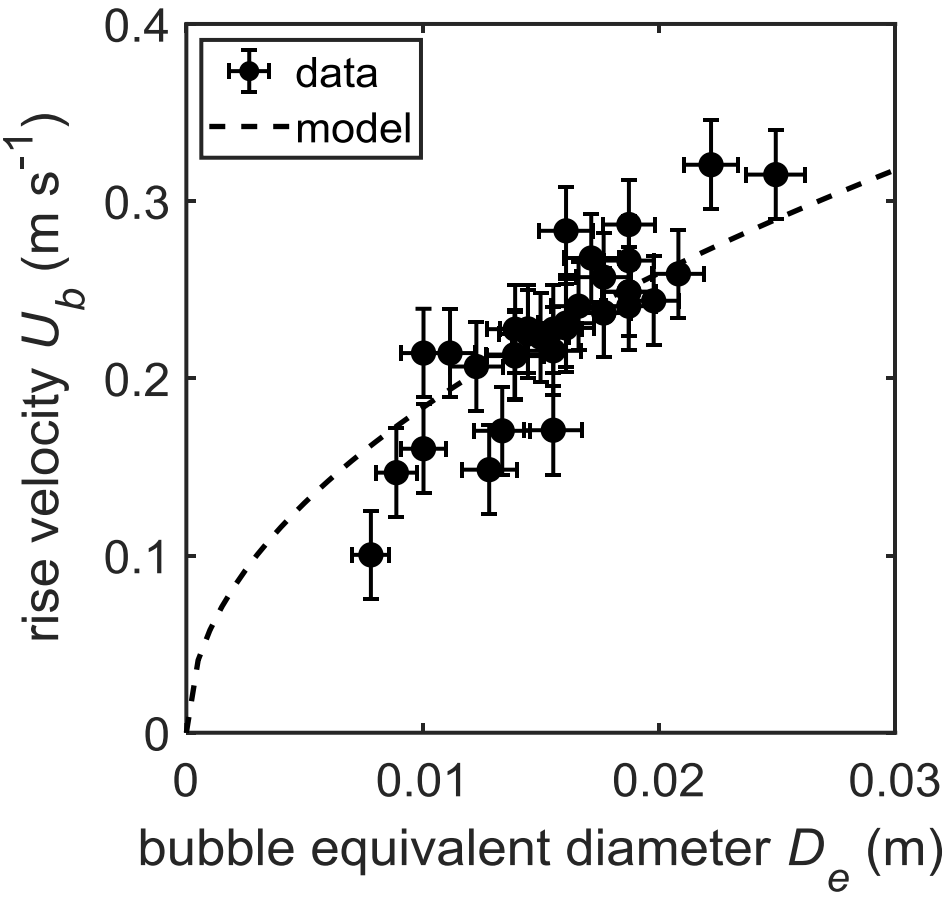

Figure 6.11: Measured bubble rise velocity given on the ordinate as a function of the equivalent bubble diameter determined from measured bubble diameters on the abscissa. The data are presented as black dots and are compared with model predictions based on inviscid bubble flow given by the dashed line. Equation 6.4 has been fitted using an adjustable parameter *k* which gives insight into bubble geometry and particulate viscosity. Error bars denote the standard error at the 95% confidence level.

the power law relationship being followed across the range of data tested. Particularly the region between 0.012 m and 0.018 m shows good quantitative agreement and shows the predictive power of the model. For these data, the rise velocity coefficient *k* was calculated to be 0.57, which is within the range previously assessed for fluidised beds.

Further information can be gleaned from analysing the horizontal 1D profiles. These are used here to measure bubble diameter but can furthermore give insight into the rise behaviour and also provide rise velocity information. Figure 6.12 shows a series of 64 slice-selective 1D intensity profiles acquired over the same range of time as those shown previously with the same time intervals. The slice is located 25 mm above the distributor. A slice which is 2 mm thick is excited in the NMR experiment, and thus what is being observed is the signal within that same vertical slice as time progresses. If objects were to rise through the slice, successive profiles would illustrate the passing of this object through this slice and would give a more 3D picture of the nature of the passing object. It is similar to taking tomographic slices of an object,

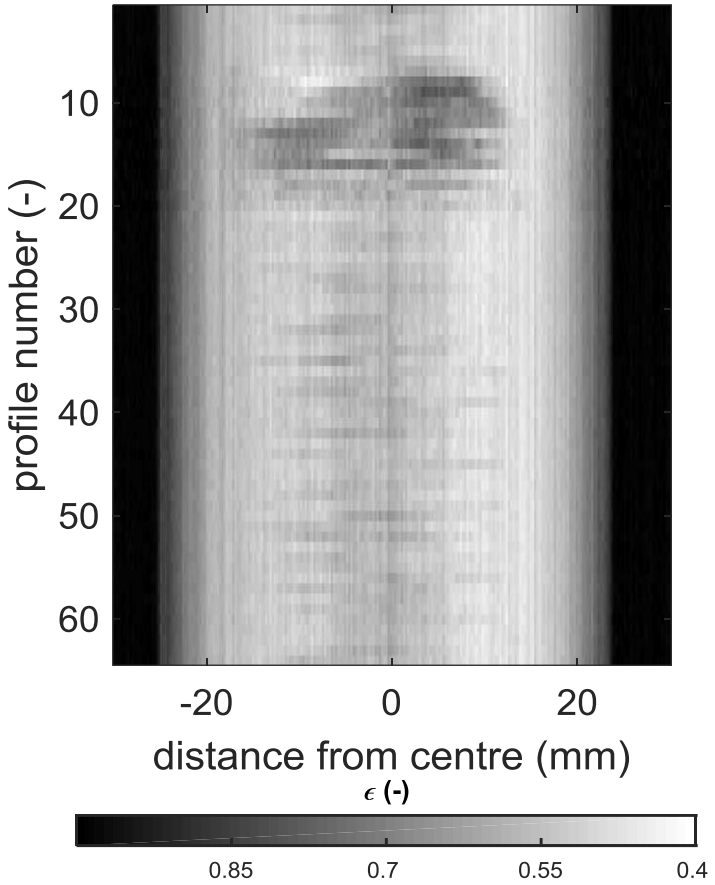

Figure 6.12: Series of 64 1D profiles recorded in the horizontal *x*-plane. Signal depression representative of a rising bubble is first seen in profile 7 and continues to outline the rising bubble as time progresses until profile 16. The slices are acquired at a fixed point in space, but from the vertical travel of the bubble it is seen that they form the classical spherical cap shape as the bubble moves through this fixed plane 25 mm above the distributor.

however it is the object moving in this example and not the instrument. The data in Figure 6.12 are noisier than the vertical profiles, owing to the fact that it is a thin slice being excited which necessarily has less signal present.

Figure 6.12 shows a clear depression in signal between bubble number 10 and 18 (corresponding to a rise time of 0.12 s). This confirms the previously calculated rise velocity of approximately 20 cm s^{-1} of a bubble to this slice 25 mm above the distributor. It is seen that the width of the depression approaches a maximum at around slice 12 and begins to become narrower once again. This indicates that the passing signal depression is approximately ellipsoid in shape. After the depression is clear of the slice, only minor variations in signal intensity are observed. The slices together show a bubble with a diameter of approximately 18 mm passing through the slice, with a vertical length of approximately 16 mm. These values are deduced by using the field-of-view, the time between successive profile acquisitions and the measured rise velocity. When studied closer despite the noise, a spherical cap shape can be deduced from the recorded signal.

6.3.4. INJECTION CALIBRATION

To be able to image the velocity characteristics of an isolated bubble, the reliability of the injection process needs to be assessed against the injection parameters. Of primary concern is the relationship between bubble size and the injection pulse time. The type of solenoid valve used in this study opens with times between 12 ms and 3 s reliably. To establish how bubble size is affected by injected volume, the bubble diameter as measured using 1D MRI profiles is plotted as a function of the injection pulse duration in Figure 6.13.

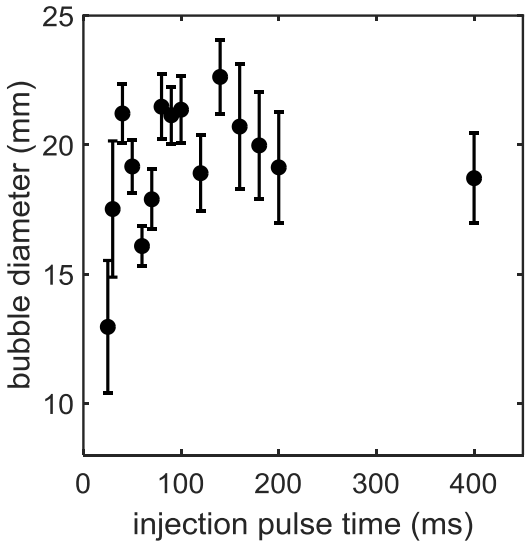

Figure 6.13: Injected bubble diameter as measured using 1D MRI profiles as a function of the injection pulse duration in milliseconds. Bubble diameter rises initially until 60 ms, undergoes a slight decrease and begins again to rise to a near-constant value of 20 mm at an injection time of 100 ms. This continues to injection times of up to 400 ms. Error bars here denote the standard error of each experiment between 64 successive bubble injections at the 95% confidence level.

The bubble size is shown to rise quickly from approximately 13 mm at a pulse time of 25 ms, to just above 20 mm at a pulse injection of 40 ms. From here, it oscillates slightly about 20 mm reaching a local minimum at 60 ms. From 60 ms to 100 ms it is roughly constant around a mean of 20 mm. At 140 ms however a local maximum of 23 mm is recorded, which is then seen to reduce to just below 20 mm for times longer than this. The error bars denote the standard error at the 95% confidence level and were found to be larger at shorter injection pulse times. Pulse durations between 25 ms and 100 ms were used in the previous section to vary the volume of bubbles to study their rise behaviour.

It is also important to assess the effects of the injection parameters on the spatiotemporal reproducibility of the injected bubbles. Figure 6.14 gives the normalised standard deviations over time of a series of profiles with the delay time set constant to capture the bubble in a set place in space. The smaller the standard deviation metric, the more similar successive profiles

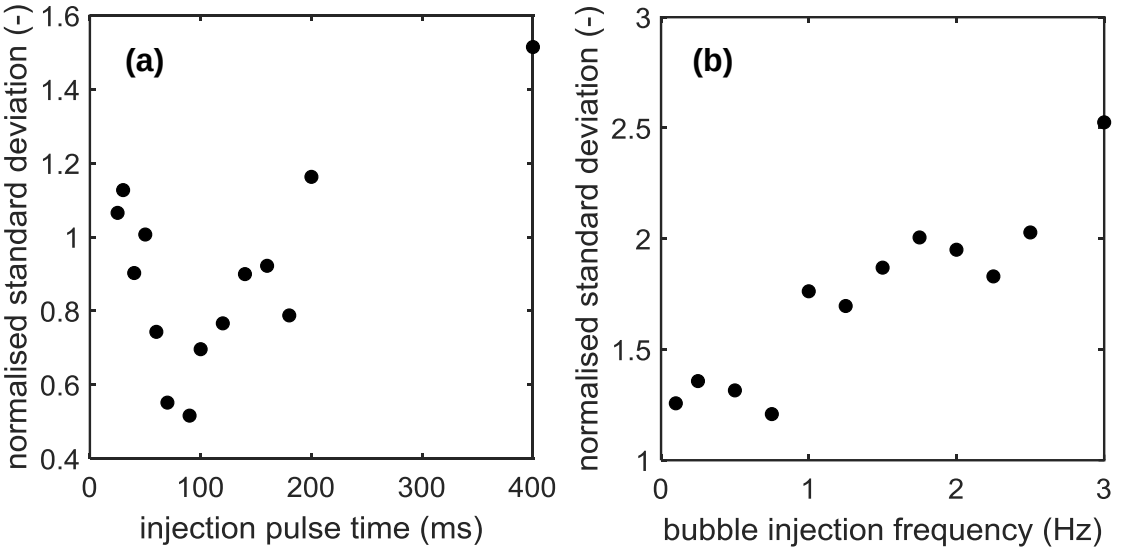

Figure 6.14: Graphs illustrating the optimisation of (a) injection pulse time, and (b) bubble injection frequency in terms of the reproducibility of bubble position in space. Bubble position is assessed by summing the standard deviations over time of 1D MRI profiles, represented by the normalised standard deviations shown in these graphs. Injection pulse time exhibits a minimum standard deviation just below a pulse time of 100 ms. The frequency at which bubbles are injected shows i) a step change at approximately 1 Hz, ii) a plateau between 1-2.5 Hz and iii) a further increase at 3 Hz. These profiles are normalised to a standard non-fluidised experiment.

are and thus the more reproducible a set of parameters. On the left axes the standard deviation is plotted as a function of the injected pulse duration in the same range as given in Figure 6.13. The standard deviation falls from a local maximum at 30 ms to a minimum value at 90 ms. This is confirmed through visual inspection of the 64 profiles at 90 ms, which show the most reproducible set of bubbles. This can be seen in Figure 6.17 (a). The standard deviation of injection pulses longer than 90 ms rises monotonically until 160 ms after which a local minimum is observed, and subsequently rises rapidly beyond 180 ms. For the purposes of further study, injection pulses of 80 ms and 90 ms are used for the most reproducible bubbles.

The rate at which bubbles are injected is also a controlled parameter. It is advantageous in terms of experimental time to have a higher rate of injection, but the effect of injecting at very high rates on the reproducibility of the bubbles, as well as the potential for bubble coalescence would limit this, in addition to the limitation posed by the internal switching time limit of the valves. The standard deviation is plotted as a function of bubble injection frequency (in bubbles per second, or Hertz) on the right axes of Figure 6.12. The standard deviation is shown to increase with increased bubble injection frequency. Standard deviation is approximately constant in the range 0.1 – 0.8 Hz, and then jumps to another approximately constant value between 1 Hz and 2.5 Hz. At 3 Hz it is seen to increase further. These two plateau values are relatively similar, at approximately 1.25 normalised value on the lower plateau and 1.8 at the higher plateau.

6.3.5. REPRODUCIBILITY

The spatiotemporal reproducibility can be assessed in all three orthogonal spatial dimensions by analysing the statistical nature of 1D MRI profiles in the *x*-, *y*- and *z*-directions. Figure 6.15 provides an illustration of the 'frozen' bubble experiments, in which the series of profiles in each direction is averaged along the time dimension. These are plotted against a no-flow control in each direction, which illustrates the difference observed in intensity and that the presence of a bubble can confidently be identified. The time-averaged intensity profile in each case is given by the solid black line, and the stationary control (also time-averaged) is plotted in a red dashed line.

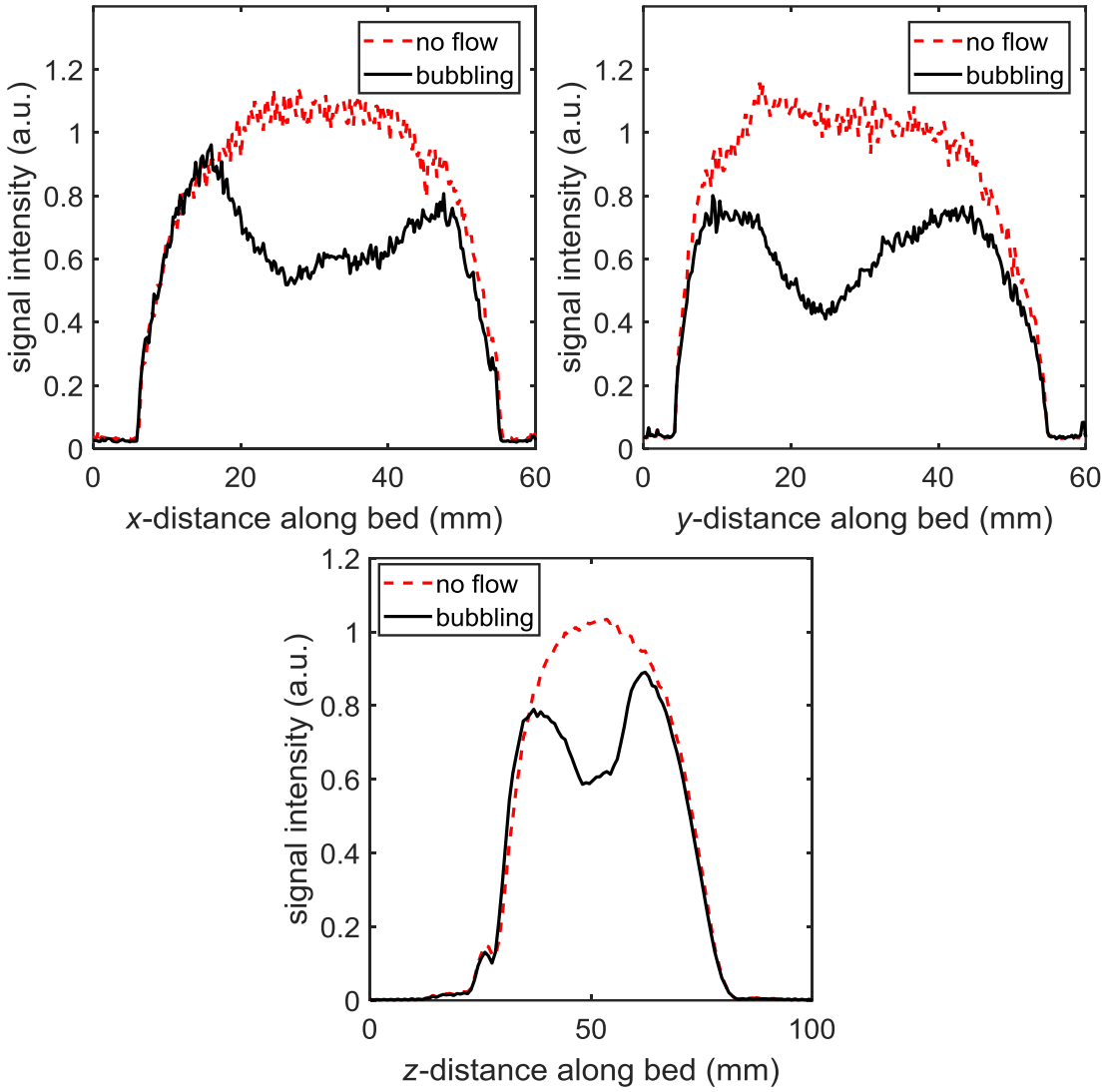

Figure 6.15: Time-averaged 1D MRI profiles in each orthogonal direction (*x*-, *y*-, and *z*-) illustrating the presence of 'frozen' bubbles with reference to the control of no flow through the bed. It is clearly observed that a significant difference in signal intensity is observed between when bubbles are injected or not injected. The no-flow cases in each direction are given by the red dashed line, and the time-averaged bubble injections over 64 bubbles are given by the solid black profiles. The effect of the presence of the bubble is illustrated by the signal depression in the centre of the field-of-view in each case.

In the *x*- and *y*-directions, the profiles display greater noise, because their signal-to-noise ratios are lower than the vertical direction as slice-selection is employed. In each direction, a clear depression in signal intensity is recorded approximately in the centre of the field-of-view in each case. This confirms that the generated stream of bubbles occurs mostly in the centre of the bed. The shape of the profiles is slightly different between the *x*- and *y*-directions, however as these experiments were conducted on an instrument with imperfect shim particularly between the horizontal gradients, these differences can be attributed to imperfect B_0 homogeneity. The size of the depression in signal is slightly larger than the injected bubble diameter of 20 mm, indicating some radial variation in position. In the *z*-direction, a similar observation of clear signal depression is recorded, however the size of the depression is closer to the individually recorded bubbles of approximately 18 mm – indicating less variation in axial position and thus less time-averaged induced blurring.

The degree of expected motion-induced blurring can be quantified and assessed by plotting these time-averaged profiles in each direction, along with an envelope of statistical confidence. This envelope is obtained by calculating the standard deviation of each voxel's intensity over time, and by creating a profile of these quantities at the 95% confidence level. This assessment is provided in Figure 6.16 for each orthogonal direction. The average profile is again shown in solid black, and the average plus and minus twice the standard deviation across time is plotted in red and blue dashed lines respectively. These envelopes represent the region which is expected to contain 95% of the bubble intensity at the investigated injection parameters of 1.5 Hz and 90 ms. The *x*- and *y*- profiles show a small increase in particle intensity in the centre of the bubble, indicative of the particle wake in each case. It is seen that the left-right boundaries of the bubble envelopes in the horizontally-acquired profiles are not dissimilar, indicating that the bubble is overwhelmingly found in the same horizontal position. The same is true, but to a slightly lesser degree in the vertical profile, which indicates that the dimension of most positional variation is the vertical direction. Quantitatively therefore, we can expect the degree of motion-induced blurring on the image intensity to be predominantly less than 17% in the case of both horizontal directions, and less than 10% in the vertical case. This intensity blurring would be likely to occur at the bubble perimeter. The effects on the recorded geometry of the bubble could be minimised through careful choice of imaging gating level

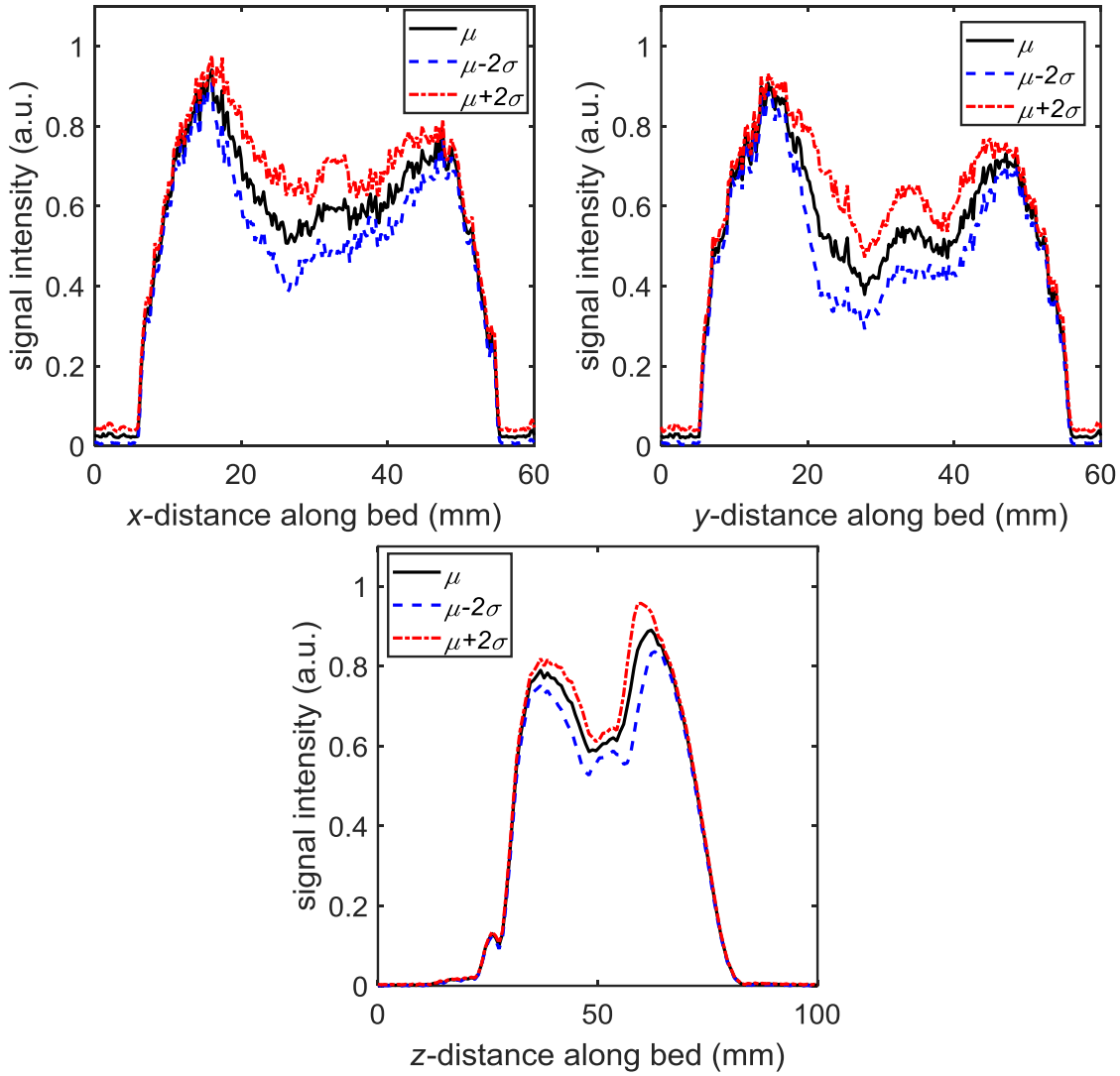

Figure 6.16: Time-averaged 1D MRI profiles of 64 bubbles in each orthogonal direction (x-, y-, and z-) showing the spatial statistical reproducibility of the bubble's position. For each direction, the time-averaged profile is given by the solid black line, whilst the blue and red dashed lines in each case show twice the standard deviation subtracted and added to the average respectively. Plotting these profiles gives an indication of the extent of blurring which can be expected in each orthogonal direction. The 95% confidence envelope of position is illustrated by the dashed lines in each case, showing a) how much variation can be expected in this direction and b) where in the envelope the mean (black line) is located.

therefore, choosing it such that blurred regions may be eliminated and the true geometry of the bubble captured. Furthermore, the effect on recorded signal phase would be to smooth spatial regions slightly. It is seen however that the degree of spatial smoothing at the edges of the bubble are minimal, particularly in the horizontal directions.

6.3.6. OTHER OBSERVATIONS

Some further features are noted in the recording of profiles of injected bubbles in Figure 6.17. Firstly, the extent of reproducibility under the optimised conditions of pulse injection time,

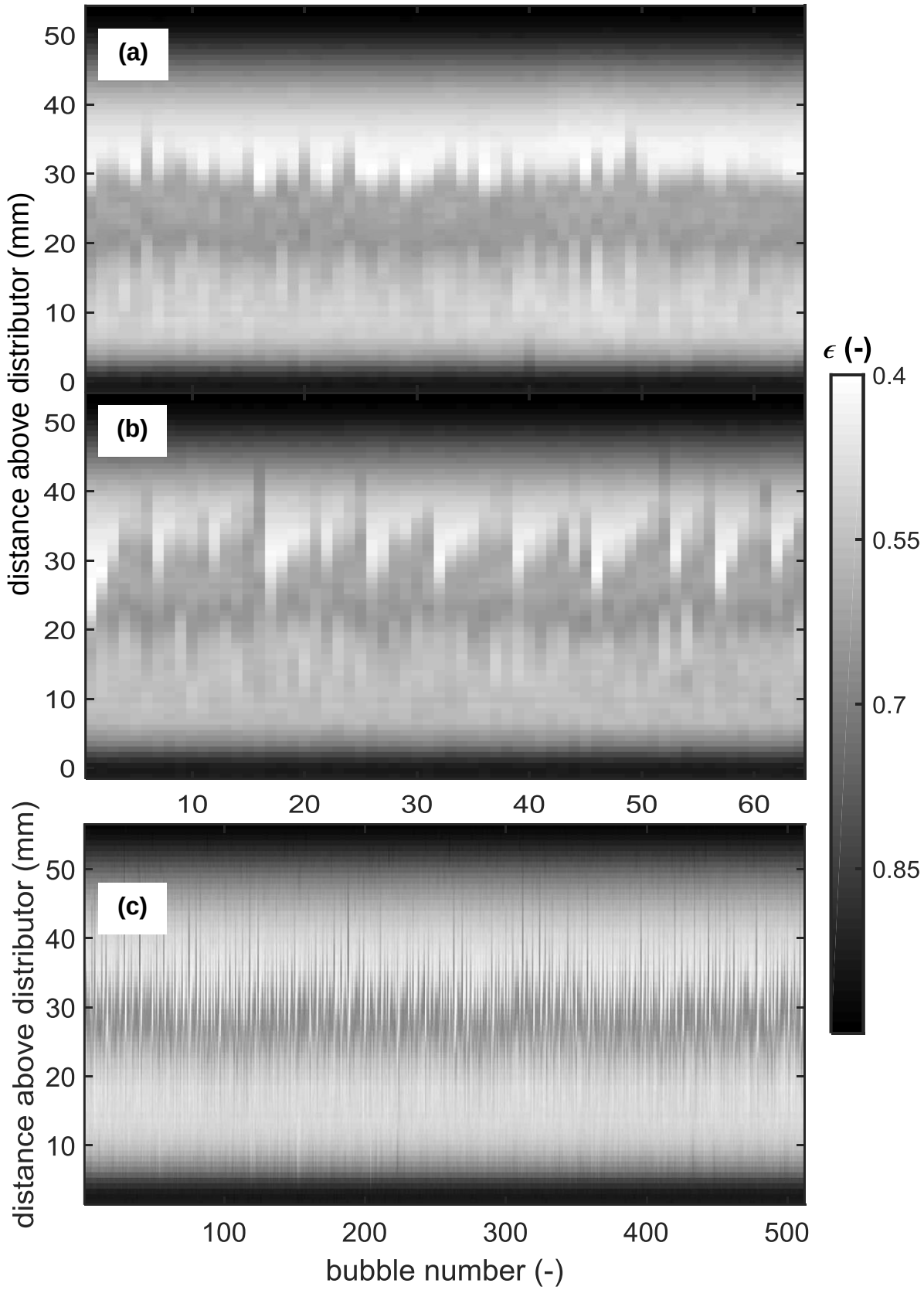

Figure 6.17: 1D MRI profiles in time illustrating (a) a typical series of 64 bubbles injected at the experimental frequency of 2.5 Hz, (b) a periodic size 'growth' and 'decay' pattern identified at a frequency of 3 Hz (c) a time series of 512 bubbles injected at a higher frequency of 3.5 Hz.

frequency and fluid velocity is illustrated in Figure 6.17 (a). Here we see a highly reproducible set of 64 bubbles injected at 2.5 Hz, with the signal depression associated with the bubble occurring in the same region of the profile 25 mm above the fluid distributor.

Figure 6.17 (b) illustrates an unusual periodic variation in bubble size, which was obtained at an injection frequency of 3 Hz and injection pulse duration of 400 ms. Here we see the bubble size increase almost linearly from 4 mm to 20 mm over the course of 6 profiles, or two seconds and rapidly reduce again. This pattern is seen to repeat approximately 11 times over the course of the experiment and is quite regular in nature. This sort of behaviour is not observed under any other experimental conditions assessed.

Figure 6.17 (c) is an illustration of the limit of the injection process, with a high injection frequency of 3.5 Hz used to inject 512 bubbles (injection pulse = 90 ms) over the course of just under 3 minutes. Over the course of 512 bubbles more vertical variation is observed than for the 64 injected at 2.5 Hz in Figure 6.17 (a), but nevertheless looking at the mean location of the signal depression it is approximately the same at 25 mm above the distributor. No periodic behaviour is seen; however, it is noted that bubbles which are significantly away from the centre of the field-of-view more often occur above the plane of interest than below. Experiments for velocity measurements and imaging were all conducted using parameters giving much more reproducible bubble streams than this.

6.4. DISCUSSION

When this system was studied previously by Boyce [25] it was concluded using a combination of MRI measurements of bed bubbling and surface height, that because there was a region of superficial velocities in which bed height was seen to change with superficial velocity, but no bubbling was observed in the intensity profile, that a possible homogeneously fluidised state may exist despite these materials being Geldart's D classified. Smooth fluidisation is most often associated with liquid systems and Geldart's group A particles, so it was surprising to have potentially identified this state existing in the poppy seed-SF_6 system. This required more careful examination in these experiments as bubbles would need to be injected into a bed which is either incipiently fluidised or operating very slightly below fluidisation.

The data in Figures 6.4-6.6 should therefore be viewed together as they complete the argument for the conclusive identification of the minimum fluidisation velocity at U_{mf} = 0.088 m s^{-1} and dispel any confusion about the existence of a homogeneous fluidisation regime. It is clearly

observed that for velocities above 0.088 m s^{-1} in Figure 6.4, there is a marked increase in the standard deviation across time of the 1D profiles. This would indicate particle motion of some form, and it was previously unclear as to whether this was due simply to smooth motion or bubbling. The key piece of new information reported here comes from observing that under different conditions of environmental vibration, the bed was able to exist in different states of packing and thus possess very different bed heights.

To eliminate this effect, the bed was reproducibly tapped at each velocity point. This allows the particles, if unfluidised, to attain a state of stable close packing. When granular media are static, they can be consolidated by the application of vibrations. The increase of packing density is well known and is attributable to grains attaining a state of closer, tighter packing which sees a reduction of the void fraction in the bed. This is especially true for particles of irregular shape, as they can obtain a more stable physical state by changes experienced in their orientation relative to one another. In this system the poppy seeds are mostly kidney-bean shaped and are also polydisperse in size. It is therefore unsurprising to identify that more stable packing states are achievable upon the application of vibrations to the bed.

When particles are fluidised, several important definitions should be valid. Within a fluidised bed:

1) The surface of the bed behaves as that of a liquid surface, and should be orthogonal to the direction of gravitational acceleration
2) For a given superficial velocity, the bed height should be constant and unaffected by vibrations
3) Objects with a mean density less than that of the mean density of the bed should rise to the surface, and likewise more dense objects should sink
4) The pressure drop across the bed is constant and equal to the weight of the bed divided by the cross sectional area.

It is the application of point (2) from above which effectively led to the confident identification of the point of minimum fluidisation. Figure 6.5 gives the bed height as measured using MRI for up- and down-sweeps in velocity for both tapped and untapped beds. It can firstly be observed that tapping has a dramatic effect on the unfluidised bed, which is unsurprising as the particles are achieving more stable states of packing. Above 0.088 m s^{-1} however, for both up- and down-sweeps in velocity, as well as for tapped and untapped, the bed is at the same height. This invariance with respect to tapping means that the bed is certainly fluidised beyond this

point. What is interesting however, is that for the tapped down-ward velocity sweep, a smooth and monotonically decreasing bed height is recorded. This behaviour is attributed to the possibility that when bringing the bed down after being fluidised, the poppy seed particles attain a hydrodynamically stable position. It is conceivable that this position is positionally anisotropic, and that because of the stability of one position caused by differential drag on a seed, when the bed is lowered after being fluidised there may exist a spatially anisotropic particle orientation within the bed. This may lead to the scenario observed, in which this anisotropy is maintained hydrodynamically as the velocity is lowered, creating the most stable packing arrangement possible. This would lead to the denser bed observed, and thus the lowest bed height, and is seen to monotonically decrease as the flow is decreased due to greater fractions of the bed achieving this state as velocity is lowered.

Identifying U_{mf} in Figure 6.5 is confirmed by looking at the standard deviation in Figure 6.4, with increases in the standard deviation observed from 0.088 m s^{-1}. It was finally confirmed by measuring U_{mf} using the classical method of pressure drop. The pressure drop curves in Figure 6.6 show a typical peak at U_{mf} particularly for the tapped bed, which is expected as the particles are jammed together, hence giving a higher than expected pressure drop. Removing this hysteresis using up- and down-sweeps for both the tapped and untapped beds allows the point of inflection to be confidently identified as 0.088 m s^{-1}. The intensity fluctuations present in Figure 6.4 are thus attributable solely to the onset of bubbling, and it is concluded that $U_{mf} = U_{mb}$ and that bubbles are formed as soon as the bed is fluidised.

Figure 6.7 demonstrates graphically the different behaviours of the bed under the conditions tested, with 6.7 (a) illustrating the control state of flow prior to fluidisation and thus prior to the onset of bubbling. The temporally-stable signal is due to the lack of macroscopic movement of the particle phase. Bubbling and fluidisation is achieved for velocities above U_{mf}, illustrated by the random fluctuation in intensity in Figure 6.7 (b). It would be impossible to glean useful velocity information from these random bubbles, and a velocity map would yield simply time-averaged behaviour about no particular event. For this, single injections are required. The injection of single bubbles is shown to be successful in Figure 6.7 (c), meaning that the pressure differential between the reservoir of gas and the injection nozzle tip is sufficient to impart a pulse of flow required to generate a fluidised bed bubble if the bed is held very slightly below the minimum fluidisation velocity.

The fact that the system is of Geldart's group D makes it relatively difficult to study, as ideally the bed would be fluidised into which injections are made. But if the bed is fluidised, it will have random bubbling and thus not exist in an experimentally controllable state with respect to bubble generation. This situation means it is run slightly below U_{mf} which leads to the atypical temporal development of the bubble as illustrated in Figure 6.7 (c), and highlighted in Figure 6.8 (a). The three regimes identified highlight that the behaviour of the injected bubbles is different from what one might expect of a freely bubbling bed. The fact that the velocity diminishes with time is unusual, and that eventually the bubble is structurally unsound and begins to collapse is a situation which has not been studied in the open literature. Due to this, further studies of the flow of the materials around an isolated bubble are restricted to regime (i) in which the rise velocity is approximately linear, and the size of the bubble is constant. The bubble structure begins to change in regime (ii) and is shows frequent collapse in regime (iii). This behaviour is attributed to the fact that the bed may be slightly defluidised, and that the energy of pulse injection initially is sufficient to cause a pressure wave and bubble to form, but that this energy dissipates as the bubble rises.

Bubble geometry is entirely dependent on the flow of gas through the roof of the bubble, which supports the particles on the bubble front and causes rise behaviour. If this flow becomes insufficient, the bubble will collapse by the wake "catching up" to the roof, and the relative velocities of the roof and wake particles not being in equilibrium. This situation clearly develops here beyond 40 mm above the distributor plate. This scenario is worth investigating in more detail with respect to stability criteria, but this is left for future work. Clearly, the bubble is rising reproducibly before this point in regime (i), a situation which if captured several times is reliably reproduced in Figure 6.8 (b).

Further evidence of this collapse hypothesis is gleaned from Figure 6.9. Here we see two different pulse durations produce two bubbles of different diameter. A 100 ms pulse produces a bubble which rises at 23 cm s^{-1}, whilst a 50 ms pulse produces a bubble which rises at 12 cm s^{-1}. In addition to the visibly different rise velocities, illustrated by the different gradients of lines following the bubble trajectories, the larger bubble is extant for a greater distance up the bed. This is attributed to a greater amount of energy imparted to the fluidised bed in the case of the larger bubble, and thus the equilibrium supporting the bubble's geometry can exist for a longer period.

The rise behaviour is assessed in more detail by considering the injected bubble geometry relative to an idealised sphere rising in a bed of the same dimensions in Figure 6.10. The signal from the model bubble is numerically integrated to give a simulated profile. The shape of the injected bubble differs most noticeable in the wake region, towards the left of the axes. This is expected, as fluidised bed bubbles are most commonly of the spherical cap form, in which particles are entrained in the wake like large bubbles rising through columns of quiescent liquids. The shape of the bubble front is much closer to that of an ideal sphere, so it is expected that the rise behaviour resembles established studies. Rise dynamics are governed primarily by bubble geometry (front shape, wake size and total volume) and thus established models which assume or have been based on spherical cap bubbles are expected to perform relatively well when modelling the rise behaviour of the bubbles in the present study.

The fraction by which the volume differs from an ideal sphere may be found by summing the total signal of particles present in the bubble and taking this as a ratio of the signal in the model bubble. Wake fraction for these experiments was found to be 0.12. This information allows the rise velocity behaviour to assessed as in Figure 6.11. The model proposed by Davies and Taylor [1] is quasi-analytical and is based on a spherical front. The data in Figure 6.11 show behaviour which is explained by the power law relationship, with no dramatic deviations from this behaviour. Notable exceptions include only the smallest bubbles and largest bubbles, with intermediate sizes showing good agreement with this common form. The velocity coefficient was determined to be $k = 0.57$. Velocity coefficient was found by Rowe and Partridge [28] to be a function of particle physical properties, notably the particle size and shape, as well as the void fraction at minimum fluidisation. They found that velocity coefficient increases for decreases in particle size and decreases for increases in wake size. Further work is encouraged for the direct examination of wake and velocity coefficient behaviour with different sizes of poppy seeds.

Rowe and Partridge [28] measured the velocity coefficient between 0.8 and 1.2, which is higher than was found here. This indicates that comparatively slower rise velocities for similar sized bubbles were recorded in the present study. It can also be concluded from Figure 6.11 that due to the good agreement between data and the model, the particulate phase is behaving similarly to an inviscid liquid, which is one of the critical assumptions for simplified fluidised bed modelling. The true relationship for the poppy seed-SF_6 system and velocity coefficient is left for future studies, as the value here being comparatively low is no doubt due to the granular rheological behaviour, as well as particle geometry and characteristics at minimum fluidisation.

In addition to being useful for measuring the true bubble diameter D_b, the horizontal 1D profiles acquired in a slice in the *x*- and *y*-directions can yield information regarding the shape, rise behaviour and spatial reproducibility of the injected bubbles. Figure 6.13 provides the first effective analyses of the 3D shape of the injected bubbles by acquiring rapid 1D profiles of the bubble passing through the fixed slice in space. The signal depression recorded between profiles 10 and 18 is clearly the rising bubble, with the cap of the bubble passing through the slice first followed by the wake. The depression consists of two lobes which are approximately symmetrical about the bed centre, which clearly resembles the spherical cap shape. The rise velocity and bubble diameter assessed using this method are 23 cm s^{-1} and 18 mm. Despite the signal-to-noise ratio being low for this single slice, it is encouraging that the shape can be determined in this way and is a verification of the fact that in the region of interest the injected bubbles are behaving as expected.

Calibration of the size and reproducibility of injected bubbles is important for the next step of investigation, which is to employ the methods developed here to image the flow fields of the fluids around a single bubble. In Figure 6.13 we see that generally longer pulse durations result in larger bubbles. However, the relationship is not linear nor monotonic. One may expect a linear relationship between injected gas volume and bubble volume. Rowe and Partridge [28] report a strong linear correlation between these quantities. They found that it was however mostly not true that these quantities were equal, rather that some linear relationship existed with a gradient equal to a pseudo transfer factor between injected gas and measured bubble volume and that this was a strong function of the superficial flow rate of gas through the bed. They attribute differences in excess gas to differing degrees of fluidisation and noted that for lower velocities near U_{mf} a certain threshold injection volume was needed for bubbles to form altogether. Similar behaviour is noted in this bed. These authors used a change in reservoir pressure to calculate injected volume.

The differences seen in this study in Figure 6.13 are primarily due to experimental apparatus limitations in that it was impossible to monitor reservoir pressure. This was due to limitations imposed on the pressure drop for fluidisation to occur in general in the gas recirculation system. It is therefore expected that injection delivery pressure in studies which show a linear relationship was more controllable and temporally stable than in this study. Injection pressure was non-linear in this study, and thus bubbles injected at pulses longer than ~ 120 ms, the injected volume and pressure remained effectively constant by the time the bubbles were generated. This may explain the plateau seen from 140 ms onwards, as the duration the

injection valve is open is not directly relatable to the injected volume at these extended injection times. The non-monotonically increasing behaviour of this curve is also attributed to more complex dynamics at the point of injection leading to bubbles which are either a different shape at shorter injection times, or coalesce or split up for longer injection times. Future work on this subject is recommended in which a separate SF_6 supply is used, enabling the use of a pressure gauge to monitor reservoir pressure before and after injection. Nevertheless, for the purposes of injection controlled isolated bubbles, the data in Figure 6.13 provide a useful calibration curve for controlling bubble diameter in the range of 10 mm to 23 mm.

Further evidence supporting the existence of this non-linear injection pressure and complexity of injection behaviour can be found in Figure 6.14, in which the most spatially reproducible bubbles around found at an injection pulse duration of 80-90 ms. Increases in spatial signal fluctuation either side of this time may indicate the formation of secondary bubbles, or bubbles which coalesce or split up which display non-controlled behaviour and for the purposes of the following experiments would be unsuitable. Here it is desired to establish the most reliable method of injecting single isolated bubbles. The frequency at which bubbles are injected is also important to produce isolated bubbles, as frequencies which are too rapid may result in bubble coalescence, and frequencies which are too long result in exorbitant experimental times. It is seen that a plateau between a frequency of 1 Hz and 2.5 Hz exists, in which the bubble production behaviour can be labelled as consistent. Beyond this, coalescence of injected bubbles may explain the increase in standard deviation. The step from 0.8 Hz to 1 Hz is explained as slightly more spatial variation in individual position owing to time taken for the particles to resettle after the passage of the previous bubble. With a typical rise velocity of 20 cm s^{-1}, all bubbles should be clear of the 100 mm bed up to a frequency of 2 Hz, despite only being spatially reproducible until 50 mm above the injection point.

The profile data in Figures 6.15 and 6.16 indicate that bubble injection is present and spatially reproducible in all three orthogonal directions. Bubbles can confidently and quantitatively be identified against the control of no-flow or no bubbles being present, and their shape, despite the poor magnetic field homogeneity, can be identified from the intensity line shapes as spherical cap. By taking the standard deviation of bubble positions in these directions across time, a sense of how significant the effects on spatial blurring in imaging experiments may be assessed. The spatial position envelopes in Figure 6.16 indicate that bubbles are highly spatially reproducible, with their centroid occurring at the same spatial location for most instances. This is truer in the horizontal directions, indicating that blurring is likely to be most significant in

the vertical plane because of slight variations in the rise velocity of bubbles. The edges of each bubble can be seen to occur at almost the same location in the *x*- and *y*-directions with the mean profile exhibiting the same edges as the standard deviation profiles in each case. The small rise in signal intensity seen in the centre of the profiles is no doubt due to the presence of the particle wake. The vertical direction profile shows slightly more spread in the edges of the bubble, but by using the statistical changes in intensity observed over these experiments the extent of the blurring can be expected to be well within experimental uncertainty. Figure 6.17 (a) illustrates the highly reproducible and optimised experimental parameters chosen, with a series of 64 bubbles injected using a 90 ms pulse at a rate of 2.5 Hz. This sort of reproducibility is expected to produce a good map of the bubble in two dimensions.

The pattern illustrated in Figure 6.17 (b) gives further weight to the argument that a non-linear injection reservoir pressure may be causing atypical behaviour in the injected bubbles. The periodicity and variation in different bubble sizes may be due to periodic bubble coalescence, or indeed due to an induced ordering of the fluidisation behaviour induced by forcing the system's flow at a particular resonance frequency. The effects of forcing order on fluidised systems using temporally oscillating flow rates is a subject of intensive study [29–32], in which the so-called "natural frequency" of the fluidised bed is exploited in order to introduce a greater degree of control and regularity. It is thought that at these elevated injection frequencies, it is certainly plausible that the pulsing of gas bubbles is approaching the natural frequency of this fluidised bed. However Figure 6.17 (a) indicates that 2.5 Hz and 90 ms pulses do not produce this behaviour, and the system is much more regular. The series of 512 bubbles indicates that even at highly elevated frequencies the system is mostly predictable, with the bubble occurring as expected. As the deviations in this behaviour are seen mostly to occur above 25 mm, it is suggested that these are primarily due to coalescence events creating much larger bubbles than expected (causing them to rise more rapidly), or due to frequency effects as 3.5 Hz is above the frequency at which the regular size differences were observed in Figure 6.17 (b). Despite these atypical behaviours, it is noted that the system is highly controllable with the optimised parameters as shown by Figure 6.17 (a), and that the parameters optimised in terms of reproducibility and bubble size can be used to confidently proceed with imaging experiments of isolated bubbles.

6.5. CONCLUSIONS

A combination of 1D MRI profiles and pressure drop measurements were used to unequivocally determine the fluid velocity at minimum fluidisation to be $U_{mf} = 0.088$ m s^{-1}. This finding dismissed earlier suppositions of the existence of a homogeneous fluidisation state and proved that $U_{mf} = U_{mb}$ and thus experiments introducing bubbles are to be run at incipient fluidisation, i.e. $1U_{mf}$. MRI was subsequently employed to distinguish between unfluidised beds, freely bubbling beds, and the bed into which isolated bubbles were injected at incipient fluidisation. 1D profiles in all three orthogonal directions identified the bubble as a rising depression in the particle signal – indicative of a void which is rising through the bed. The vertical profiles indicate that the bubble rises with atypical behaviour, slowing down in velocity and eventually collapsing at a position approximately halfway through the bed. Attempts to remedy this by raising the fluidising velocity resulted only in a freely bubbling bed, into which no controllable bubble could be injected without the influence of naturally occurring bubbles. This behaviour is typical of Geldart Group D particles where the bubbling and fluidising velocities are identical. Three different regions of behaviour were identified, with all remaining experiments conducted in regime (i) of the rise, in which bubbles were shown to remain the same size and rise with an approximately linear trajectory.

Injection pulse duration was shown to change the size of bubbles, although the relationship was not linear as the relationship between injected volume and bubble volume has previously been shown to be. This is attributed to a non-linear pressure in the injection reservoir, which for practical reasons could not be monitored. It was however seen that for pulse durations between 25 ms and 100 ms were able to vary bubble diameter sufficiently to study the relationship between rise velocity and bubble size. Rise velocity data was shown to obey a power law relationship with respect to bubble equivalent diameter, with a correlation velocity coefficient found to be $k = 0.57$ which is typical for slower rising bubbles in fluidised beds. The wake factor found using intensity data was determined to be $f_w = 0.12$ which is also typical for spherical cap bubbles. These facts lead to the conclusion that the bubbles are behaving similar to rising spherical cap bubbles in inviscid liquids, and their geometry approximates that of a spherical cap.

The injection parameters which produced the most spatially reproducible stream of bubbles were calibrated in terms of pulse duration and injection frequency. These were found to be a 80-90 ms pulse and, for efficient experimentation, a frequency of 1-2.5 Hz. These parameters

produced bubbles of approximately 20 mm in diameter which showed less than a 17% variation in intensity at the boundaries of the bubble in any orthogonal direction within the 95% confidence level. This was assessed by analysing the standard deviation envelopes across time for each profile, each of which showed a sufficiently narrow envelope for the bubble location. The profiles illustrate that the bubbles generated with ideal parameters are highly spatially reproducible in both their geometry and position.

NOMENCLATURE

ABBREVIATIONS

1D, 2D, 3D	one, two or three dimensional
CFD	computational fluid dynamics
FOV	field-of-view
r.f.	radiofrequency
MRI	magnetic resonance imaging
NMR	nuclear magnetic resonance
PLIF	planar laser induced fluorescence and
PIV	particle image velocimetry

SYMBOLS

D_b	isolated bubble diameter	m
D_e	isolated bubble diameter	m
d_b	bubble diameter in free bubbling bed	m
f_W	bubble wake factor	-
g	acceleration due to gravity	m s^{-2}
h	bed height	m
h_0	characteristic distributor length	m
k	bubble velocity coefficient	-
P	pressure	bar
R_b	bubble radius	m
t	time	s
U	superficial fluid velocity	m s^{-1}
U_{mf}	minimum fluidisation velocity	m s^{-1}
U_{mb}	minimum bubbling velocity	m s^{-1}
U_b	bubble rise velocity	m s^{-1}
V_b	volume of bubble	m^3
y,x,z	standard cartesian coordinates	-

GREEK LETTERS

μ	statistical estimate of mean based on sample	-
σ	sample standard deviation	-

REFERENCES

[1] Davies, R., Taylor, G. The mechanics of large bubbles rising through extended liquids and through liquids in tubes. *Proc. R. Soc.* 1950;200: pp. 375–90.

[2] Davidson, J.F., Harrison, D. Fluidised particles. vol. 3. Cambridge: Cambridge university press Cambridge, UK; 1963.

[3] Müller, C.R., Davidson, J.F., Dennis, J.S., Fennell, P.S., Gladden, L.F., Hayhurst, A.N., *et al.* Rise velocities of bubbles and slugs in gas-fluidised beds: Ultra-fast magnetic resonance imaging. *Chem. Eng. Sci.* 2007;62: pp. 82–93.

[4] Rowe, P. Prediction of bubble size in a gas fluidised bed. *Chem. Eng. Sci.* 1976: pp. 285–8.

[5] Kunii, D., Levenspiel, O. Fluidization Engineering. 2nd ed. Stoneham: Butterworth-Heinemann; 1991.

[6] Yasui, G., Johanson, L.N. Characteristics of gas pockets in fluidized beds. *AIChE J.* 1958;4: pp. 445–52.

[7] Toei, R., Matsuno, R., Kojima, H., Nagai, Y., Nakagawa, K., Yu, S. Behavior of bubbles in gas–solid fluidized beds. *Kagaku Kogaku* 1965;29: pp. 851.

[8] Hiraki, I., Yoshida, K., Kunii, D. Behavior of bubbles in a two-dimensional fluidized bed. *Chem. Eng.* 1966;4.

[9] Kobayashi, H., Arai, F., Chiba, T. Behaviour of bubbles in a gas-solid fluidized bed. *Kagaku-Kogaku (Abr. Ed)* 1966;4: pp. 147–50.

[10] Hailu, L., Plaka, F., Clift, R., Davidson, J.F. Measurement of gas flow through a two-dimensional bubble in a fluidised bed: particle processing. *Chem. Eng. Res. Des.* 1993;71: pp. 382–9.

[11] Werther, J., Molerus, O. The local structure of gas fluidized beds -I. A statistically based measuring system. *Int. J. Multiph. Flow* 1973;1: pp. 103–22.

[12] Werther, J., Molerus, O. The local structure of gas fluidized beds -II. The spatial distribution of bubbles. *Int. J. Multiph. Flow* 1973;1: pp. 123–38.

[13] Fabich, H.T., Sederman, A.J., Holland, D.J. Development of ultrafast UTE imaging for granular systems. *J. Magn. Reson.* 2016;273: pp. 113–23.

[14] Fabich, H.T., Sederman, A.J., Holland, D.J. Study of bubble dynamics in gas-solid fluidized beds using ultrashort echo time (UTE) magnetic resonance imaging (MRI). *Chem. Eng. Sci.* 2017;172: pp. 476–86.

[15] Müller, C.R., Holland, D.J., Sederman, A.J., Mantle, M.D., Gladden, L.F., Davidson, J.F. Magnetic Resonance Imaging of fluidized beds. *Powder Technol.* 2008;183: pp. 53–62.

[16] Han, S.-I., Stapf, S., Blümich, B. NMR Imaging of Falling Water Drops. *Phys. Rev. Lett.* 2001;87: pp. 144501.

[17] Levy, Y., Lockwood, F.C. Laser doppler measurements of flow in freeboard of a fluidized bed. *AIChE J.* 1983;29: pp. 889–95.

[18] Yorquez-Ramirez, M.I., Duursma, G.R. Study of the flow pattern above an erupting

bubble in an incipiently fluidised bed using image shifting. *Chem. Eng. Sci.* 2000;55: pp. 2055–64.

[19] Solimene, R., Marzocchella, A., Ragucci, R., Salatino, P. Laser diagnostics of hydrodynamics and gas-mixing induced by bubble bursting at the surface of gas-fluidized beds. *Chem. Eng. Sci.* 2007;62: pp. 94–108.

[20] Hartung, G., Müller, C.R., Hult, J., Dennis, J.S., Kaminski, C.F. Laser Diagnostic Investigation of the Bubble Eruption Patterns in the Freeboard of Fluidized Beds. 1. Optimization of Acetone Planar Laser Induced Fluorescence Measurements. *Ind. Eng. Chem. Res.* 2008;47: pp. 5686–97.

[21] Third, J.R., Müller, C.R. Bubble eruption patterns and gas dynamics in the freeboard of a gas-fluidized bed: A discrete element model (DEM) study. Mediterr. Combust. Symp., Cagliari: 2011, p. 1–10.

[22] Vun, S., Naser, J., Witt, P.J., Yang, W. Measurements and numerical predictions of gas vortices formed by single bubble eruptions in the freeboard of a fluidised bed. *Chem. Eng. Sci.* 2010;65: pp. 5808–20.

[23] Holland, D.J., Müller, C.R., Davidson, J.F., Dennis, J.S., Gladden, L.F., Hayhurst, A.N., *et al.* Time-of-flight variant to image mixing of granular media in a 3D fluidized bed. *J. Magn. Reson.* 2007;187: pp. 199–204.

[24] Collins, J.H.P., Sederman, A.J., Gladden, L.F., Afeworki, M., Kushnerick, J.D., Thomann, H. Characterising gas behaviour during gas–liquid co-current up-flow in packed beds using magnetic resonance imaging. *Chem. Eng. Sci.* 2017;157: pp. 2–14.

[25] Boyce, C.M. Fundamental Studies of the Physics of Gas-Solid Fluidization. University of Cambridge, 2014.

[26] Geldart, D. Types of gas fluidization. *Powder Technol.* 1973;7: pp. 285–92.

[27] Fan, L.T., Ho, T. -C, Walawender, W.P. Measurements of the rise velocities of bubbles, slugs and pressure waves in a gas-solid fluidized bed using pressure fluctuation signals. *AIChE J.* 1983;29: pp. 33–9.

[28] Rowe, P.N., Partridge, B.A. An x-ray study of bubbles in fluidised beds. *Chem. Eng. Res. Des.* 1997;75: pp. S116–34.

[29] Massimilla, L., Volpicelli, G., Raso, G. A study on pulsing gas fluidization of beds of particles. Chem. Eng. Prog. Symp. Ser, vol. 62, 1966, p. 63–70.

[30] Wong, H., Baird, M. Fluidisation in a pulsed gas flow. *Chem. Eng. J.* 1971;2: pp. 104–13.

[31] Coppens, M.-O., van Ommen, J.. Structuring chaotic fluidized beds. *Chem. Eng. J.* 2003;96: pp. 117–24.

[32] van Ommen, J.R., Nijenhuis, J., van den Bleek, C.M., Coppens, M.-O. Four Ways To Introduce Structure in Fluidized Bed Reactors. *Ind. Eng. Chem. Res.* 2007;46: pp. 4236–44.

CHAPTER 7 – PHASE DYNAMICS OF ISOLATED BUBBLES IN A GAS-SOLID FLUIDISED BED

7.1. INTRODUCTION AND THEORY

Fluidisation behaviour can be crudely categorised as particulate or aggregative. In the latter under certain conditions, bubbles of a lean phase consisting mostly of the fluidising fluid form and rise through the bed [1]. The presence of these bubbles in fluidised beds presents an interesting and challenging phenomenon both academically and industrially. In commercial fluidised beds, bubbling causes the vigorous mixing of solids responsible for the favourable heat and mass transfer in fluidised beds. Conversely it can lead to the negative effect of fluid bypassing a solid catalyst bed [2,3]. The formation and rise of these bubbles is interesting physically, because no surface tension exists in the particulate phase to stabilise the bubble structure. Much research has therefore been undertaken in the last 6 decades towards understanding the formation, propagation and structure of these bubbles [1,4,5].

One of the earliest attempts to model the behaviour of the fluid within aggregative fluidised beds was undertaken by Toomey and Johnstone [6]. This is known as the two-phase model of fluidisation, as it partitions the fluidised bed into two "phases" or regions. The particle and fluid properties and flow are then divided between these phases to aid modelling and design of fluidised beds. Despite its simplicity, it has remained an important model of fluidisation which researchers have scrutinised and developed since its introduction. The central assumption of two-phase theory is that any gas flow in excess of that required to minimally fluidised the bed is carried through the bed in the bubbling phase:

$$\frac{Q_b}{A} = U - U_{mf}. \tag{7.1}$$

In this equation, Q_b is the volumetric rate of gas carried by the bubble phase, A is the cross-sectional area of the bed, U is the fluid velocity and U_{mf} is the fluid velocity at minimum fluidisation. The bubble rate Q_b is sometimes called the "visible" bubble rate, as it is the rate of bubble rise which would be visible to an observer in the laboratory reference frame. In this theory, the bubble rise velocity is equal to:

$$U_b = \frac{Q_b}{A_b}, \tag{7.2}$$

where U_b is the bubble rise velocity and A_b is the cross-sectional area of bubbles in the bed. The particulate or "dense" phase is then treated as a bed at minimum fluidisation conditions, with the average void fraction being isotropically equivalent to the voidage at minimum fluidisation. Thus the velocity of the gas in the particulate phase is equal to:

$$U_p = \frac{U_{mf}}{\varepsilon_{mf}}, \tag{7.3}$$

where U_p is the fluid velocity in the dense phase and ε_{mf} is the voidage at minimum fluidisation. The cumulative gas flow through the bed is therefore:

$$UA = Q_b + Q_p, \tag{7.4}$$

where Q_p is the volumetric rate of the fluid in the dense phase. Several experimental studies [7–12] showed that the visible bubble rate differed from what was predicted by the theory however, and in general saw that the theory dramatically overpredicted the rise velocity. Authors [13] introduced the following form to accommodate these observations:

$$\frac{Q_b}{A} = U - KU_{mf} \tag{7.5}$$

where K is a fitted parameter which depends on the concentration and nature of the bubbles. K is most often positive, but in some cases can be negative. Other variants of this include the n-type theories, which use the following relation:

$$\frac{Q_b}{A} = U - (1 + ne_b)U_{mf} \tag{7.6}$$

where e_b is the fractional area occupied by the bubbling phase and n is a fitted property. Clearly the original two-phase theory is thus a special case of a broader theory with $n = 0$. The parameter n attempts to model either an increase in flow in the dense phase beyond that required for minimum fluidisation, or an increase in flow which traverses the bubble perimeter. This is an important conceptual development, as fluidised bed bubbles are naturally able to have gas pass into and out of their volume, unlike bubbles in a liquid. Through-flow through the bubbles is a critical development and was first considered in detail by Davidson and

Harrison [8]. They developed an analytical treatment which supported the idea of bubble through-flow, which will be considered later. Adding a through-flow component means the total flow through a planar section of the bed is given by:

$$UA = Q_b + Q_p + Q_{tf}, \tag{7.7}$$

where Q_{tf} is the volume of gas flowing through the bubble. It is now clear that this is distinct from the visible bubble flow, as many authors [5] were able to show experimentally that the gas flow through the bubble may in practice by much higher than the rise velocity only. In earlier modifications the flow in the particle phase was assumed still to be equal to that for incipient fluidisation [14,15]. Davidson and Harrison [8] were also the first to consider the effect of the particle velocity on the gas flow. Whilst it is true that, since no particles enter or exit the bed, the net vertical velocity of the particle phase is zero, locally the particle phase may exhibit different non-zero velocities even at minimum fluidisation. Accounting for this in the two-phase theory, the total velocity of the gas in the dense phase becomes:

$$U_p = \frac{U_{mf}}{\varepsilon_{mf}} + U_s, \tag{7.8}$$

where U_s is equal to the average particle velocity in the plane of interest. This led to improved estimations of the dense phase velocity which seemed in some cases to account for the deficit observed in the visible bubble rate. Locket *et al.* [15] developed an analytical expression for the through-flow based on the treatment of isolated bubbles by Davidson [16]. The simple modelling using potential flow around a spherical void showed that the flow through the bubble is substantially higher than the rise velocity. For 3D bubbles they showed that it is equivalent on average across the bubble area to:

$$U_{tf} = 3U_{mf}, \tag{7.9}$$

where U_{tf} is the bubble through-flow velocity. The authors therefore posited the following equation for the flow:

$$UA = (1 - e_b)AU_{mf} + Q_b + e_b A3U_{mf}, \tag{7.10}$$

where:

$$Q_{tf} = e_b A3U_{mf} \tag{7.11}$$

and:

$$Q_{br} = Q_b + Q_{tf} = U_b A_b + e_b A 3 U_{mf}. \tag{7.12}$$

In these expressions, Q_{br} is the total flow through the bubbling region which is a sum of the through-flow and the bubble rise (visible bubble) flow. The total area for two-phase models is clearly:

$$A = A_b + A_p, \tag{7.13}$$

where A_p is the cross-sectional area of the particulate dense region. Based on the discovery of recirculation-type patterns, other authors [17] have included other regions but these become unwieldy to apply, and are not easily compared due to the subjective identification of the various flow rates and regions.

Studying bubbling is challenging experimentally due to the opacity of fluidised beds, which limits the use of many optical techniques [5,18–20]. Other experiments require the use of radiation techniques which may be ionising and require complex reconstruction algorithms [21]. To avoid this, much of the experimental work has been undertaken in so-called two dimensional (2D) rectangular fluidised beds of minimal width [19,20,22,23], which do not accurately resemble industrial units. Numerical simulation of fluidised beds using either DEM-CFD [24], or the two-fluid model (TFM) [22,25–28] is useful but is still limited by a lack of *a priori* physical knowledge and are therefore limited in applicability or require experimental validation. This study presents quantitative measurements of the structure and flow behaviour of isolated bubbles in a dense gas-solid fluidised bed.

The earliest instance of an analytical treatment of bubbling was undertaken by Davidson [16] which treated the solid particles as an additional fluid phase with zero viscosity (inviscid flow) and constant voidage (incompressible). A spherical bubble was assumed such that the flow of the particulate phase could be treated as the flow over a sphere. The phases were linked using Darcy's law. Using potential flow theory, the following Stokes stream function for the fluidising fluid was obtained in a frame of reference which is stationary relative to the rising bubble:

$$\psi_f = \frac{r^2 \sin^2 \theta}{2} \left[\left(U_b - U_p\right) - \left(U_b + 2U_p\right) \frac{r_b^3}{r^3} \right]. \tag{7.14}$$

In Equation 7.14 ψ_f is the stream function of the fluidising fluid, r is the radial co-ordinate centred at the centroid of the spherical bubble, θ is the angular co-ordinate, U_b is the bubble rise velocity, U_p is the velocity of the fluid in the interstitial space, and r_b is the bubble radius. An important consequence of this function is the existence, provided $U_b > U_p$, of a zero value for the flow potential, and thus a radius around the bubble for which:

$$r = r_c = r_b \left(\frac{U_b + 2U_p}{U_b - U_p} \right)^{\frac{1}{3}}. \tag{7.15}$$

In Equation 7.15, r_c is the radius for which the flow is zero which occurs in a concentric "cloud" called the cloud radius. The implication is that for "fast" moving bubbles, a region of non-mixing with the bulk fluid phases exists around a rising bubble. The flow field is greatly influenced by the ratio $\alpha = U_b/U_p$. Four scenarios are typically studied, which are illustrated in Figure 7.1.

The situations depicted in Figure 7.1 (a) and (b) are rarely encountered practically, and bubble behaviour is typically a version of either (c) or (d). In scenario (c), the bubble moves slower than the interstitial fluid, and thus represents a region of lower resistance. Consequently, the field lines curve into the bubble at the bottom and out at the top, showing that gas channels preferentially through slow bubbles due to the reduction in flow resistance. In scenario (d), the bubble moves faster than the interstitial fluid and a vortex cloud around the bubble is predicted which does not mix with the bulk particulate fluid. Scenario (b) is a limiting case of this behaviour in which r_c extends to infinity.

This model gives insight into the existence and rise behaviour of bubbles. At all values of α the predicted flow patterns show upward flow through the bubble, explaining why the roof doesn't collapse due to the lack of a surface tension force in bubbles in granular media. Earlier theories postulated a "Roman arch" effect in which the particles at the bubble roof were thought to jam together to support the bubble [1]. By the classification by Geldart [29], beds of Group B and D typically demonstrate scenario (d) with the existence of clouds. Clouds are also encountered for large bubbles in beds of Group A and very rarely in fine particles of Group C. In order for the predictions of the Davidson model to have significance, the scale of the bubbling phenomena should be at least an order of magnitude larger than the mean particle size of the bed [30].

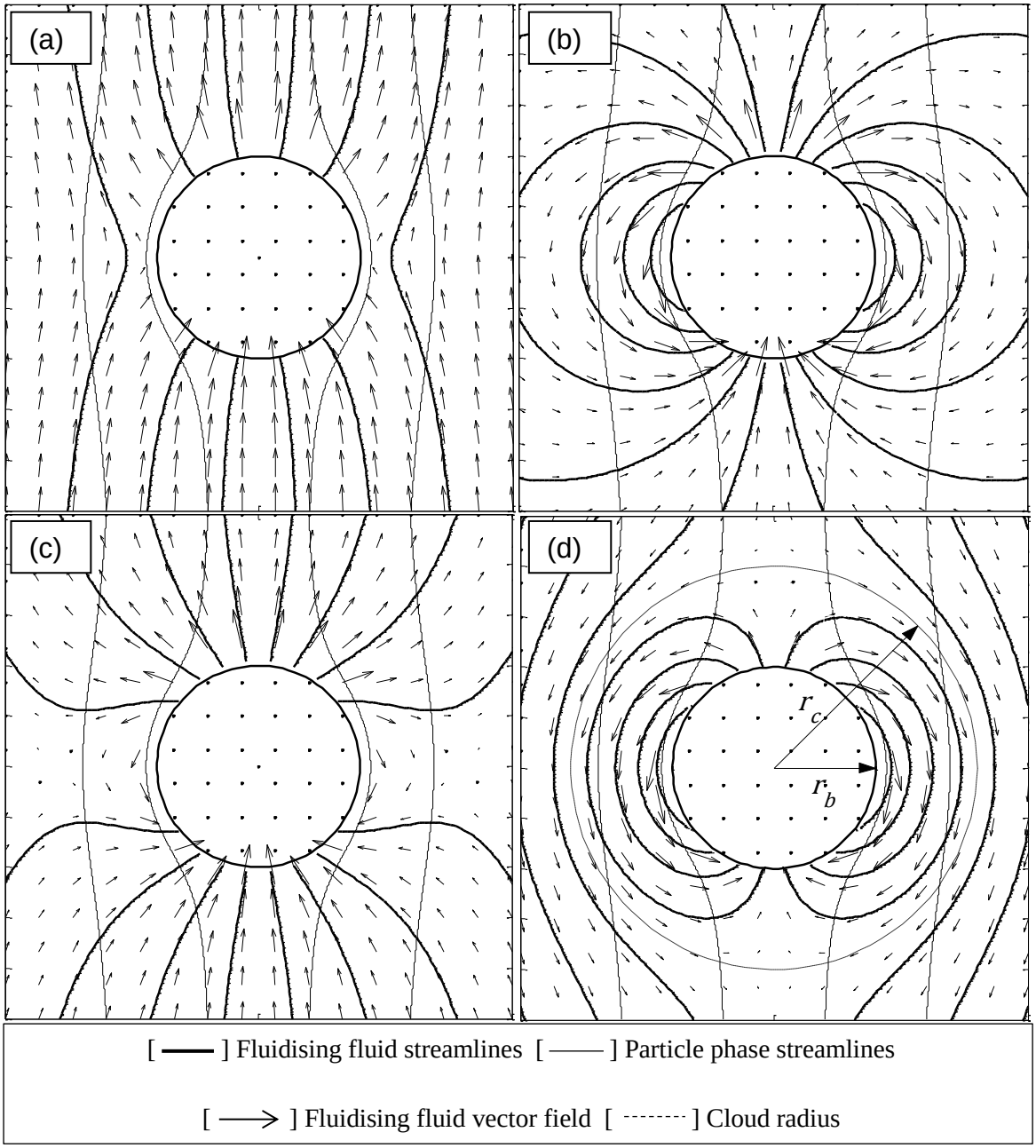

Figure 7.1: Schematic illustration of the Davidson bubble model showing the motion of the fluidising fluid and streamlines for fluid and particle flow around an isolated bubble in a fluidised bed at different vales of α. (a) $\boldsymbol{\alpha = 0}$, (c) $\boldsymbol{\alpha = 1}$, (c) $\boldsymbol{\alpha = 0.6}$ and (d) $\boldsymbol{\alpha = 1.67}$. In a fast bubble, as in (d), a cloud of radius $\boldsymbol{r_c}$ exists in which gas circulation occurs.

Other more complex models have been developed which better explain some observed phenomena. Jackson [31] developed equations for a spherical bubble which left the void fraction of the particulate phase free. These were treated as most accurate for the upper half of the bubble and showed an increasing voidage towards the bubble. This general trend was confirmed using combination of capacitance and optical measurements in the results by Lockett and Harrison [32], though the shape of the voidage increase mantle were different. The flow patterns predicted were roughly similar to that of Davidson. Murray [33] used Oseen's approximation on a spherical bubble to produce flow behaviour similar to that of Davidson,

with the centroid of vortex behaviour around the bubble shifting upwards to become asymmetric around the equatorial axis.

Collins [34] followed a similar development to these models, but performed analysis on the classic kidney bean-shaped spherical cap bubble geometry observed in experiments, and is thus expected to be more accurate in the wake region. Surprisingly, similar cloud behaviour and flow patterns were predicted for fast and slow moving bubbles. Stewart and Davidson [35] used a similar approach to extend the analysis to slugging beds and large bubbles. Collins [36] used a 2D bed to compare the differences in the models by Davidson and Murray, with special attention on the flow around slugs predicted by both. Interestingly, the models were found to give nearly identical predictions. The later models all predict a slightly smaller cloud than that of Davidson. The relative similarity of predictions made by all models is surprising and emphasises the elegance of the original model by Davidson. Due to its simplicity is the starting point of most contemporary analysis of isolated bubbles, including that of this study.

Testing these models is most often done with the use of 2D fluidised beds and optical measurements of bubble cloud size [18]. Rowe [19] *et al.* used injected bubbles of NO_2 (a visible brown gas) to show the existence of the cloud region in fast bubbles in a 2D bed using photography. The clouds differed in shape from the Davidson model, with radii closer to the later models by Murray and Jackson. The same study used NO_2 streaklines to show the passage of gas bending into an injected slow bubble, with patterns close to Figure 7.1 (c) revealed. Stewart [20] compared cloud sizes at different interstitial fluid velocities to various models and found that most experimental data fell within an envelope of the models by Davidson and Murray. Lignola [37] *et al.* and Hatano and Ishida [38] compared measurements of cloud size with the models, but the data showed significant scatter and thus conclusions on the suitability of any model could not be drawn.

Other studies have looked at the pressure distribution around bubbles using pressure probes inserted into the bed. Reuter's [39,40] measurements showed favourable agreement with all models but particularly with that of Davidson. Yates and Cheesman [41] and Yates [42] *et al.* measured particle concentrations near bubbles using X-ray and showed reduced particle volume fractions in the vicinity of bubbles. The results were compared in another study by Buyevich [43] *et al.* who suggest another model for the existence of this region and analysed its importance in the existence and propagation of bubbles in fluidised beds. Rowe and Partridge [21] made an extensive study of bubble size and rise characteristics using X-ray.

Computationally most studies assess the ability of CFD models to generate accurate representations of bubble motion and interaction in fluidised beds [22,24–28,44–48]. It has been found that both the two-fluid and discrete element method (DEM) give qualitatively similar results [24]. Recently, Almendros-Ibanez [45] *et al.* used results from particle image velocimetry (PIV) to generate a computation mesh to study fluid flow around bubbles in a 2D bed. They modified the use of Darcy's law in Davidson's model to include inertial effects in a quadratic term (Ergun equation). This did not produce significantly different results from the simple model. Boemer [46] *et al.* studied pressure distributions near bubbles and bubble flow patterns using the Eulerian approach which showed good agreement with the predictions of the model by Davidson. A review of various numerical schemes and approaches and their influence on predicted bubble characteristics is given by Guenther and Syamlal [25], who analyse the effect of numerical diffusion on bubble shape. They found that an upwind scheme produced elongated bubbles. Hernandez-Jimenez [22] study the interchange of gas in a 2D gas fluidised bed using TFM. They found good agreement between results and predictions made from the potential flow models, particularly in the case of the pressure profile which showed close agreement to the model by Davidson. Patil [48] *et al.* generated flow maps which should close qualitative agreement to the slow moving bubble case depicted in Figure 7.1 (c). Recently, Boyce [49] *et al.* used a CFD-DEM simulation to study a bed identical to that in this study. It is shown that the code predicts bubbles which are very similar in nature to those recorded here. They use the simulation results to compare with time-averaged MRI data on a lower spatial resolution, with good agreement being achieved.

Several experimental limitations exist for most of the classical studies on bubble dynamics. Firstly the use of a pseudo-2D fluidised bed introduces wall effects which may change the shape and behaviour of bubbles and flow behaviour. Secondly, the introduction of pressure probes and other invasive measurement devices could alter the dynamics of the system. Thirdly, measurements inferring the validity of the models have mostly been indirect through the estimation of gas cloud size. None of these techniques have been able to quantitatively probe the flow of fluid around isolated 3D gas bubbles. MRI is ideally suited to making non-invasive measurements of hydrodynamic phenomena and has recently been highlighted as being a valuable tool in chemical engineering research [50–52]. It has also been used with great success in studying other aspects of fluidisation hydrodynamics and behaviour [53–56].

Using MRI it is possible to acquire spatially-resolved velocity and velocity distribution information without using invasive probes. It is also possible to do this on realistic 3D systems.

To circumvent the traditionally poor temporal resolution of MRI experiments, a technique has been developed to acquire individual **k**-space data points for each bubble produced in the bed. The bubble injection method is therefore required to be highly reproducible in terms of the size, position and rise velocity of bubbles. This technique was inspired by a similar approach used to image the flow of liquid in individual water droplets using MRI [57]. This study reports the first use of MRI to study the instantaneous motion of fluid and particles around isolated bubbles in a 3D gas-solid fluidised bed.

7.2. EXPERIMENTAL

The experimental apparatus and magnetic resonance setup used in this chapter were identical to those described in detail in Chapter 6. What is provided in this section are the differences where appropriate, and the operating procedures and pulse sequences used.

7.2.1. SPATIALLY-RESOLVED VELOCITY IMAGES OF PARTICLE AND GAS VELOCITY

Images of the particle and gas velocity surrounding a bubble were acquired using a triggered pulse sequence variant of the type reported in Boyce *et al.* [58]. This sequence made it possible to measure accurate fluid velocities in particulate media despite the presence of considerable background gradients due to magnetic susceptibility differences. It was based on the earlier work by Cotts [59]. It consists of an 11-interval sequence, which in this study was modified with a pseudo-random under-sampling pattern chosen for use with compressed sensing. The sampling pattern is calculated using the routines by Lustig [60] to make use of incoherent signal addition. The images are reconstructed using a routine developed by Benning [61] for MRI. It makes use of a Tikhonov regularisation algorithm and employs a signal mask to improve the quality of the reconstruction by rejecting signal outside a region of the image known to contain signal. Single-point-imaging (SPI) with two phase-encoding gradients was chosen to minimise background gradients, as signal decay in frequency-encoding experiments was too severe. Two signal averages were acquired for an imaging time at an injection rate of 1 Hz of 4.5 hours for each 32 × 32 image. The image slice thickness was 2 mm. The modifications allowed images with double the spatial resolution as previous results [58] to be obtained in the same time.

Images were acquired in the horizontal plane with the bubble at five different spatial positions at a single superficial fluid velocity of 0.0931 m s^{-1}. All three orthogonal components of the velocity were acquired. Images were also acquired in a vertical slice with the same acquisition parameters as the horizontal slice. The details of the key MRI parameters used are given in

Table 7.1. The vertical positions of horizontal slices of the bubble relative the its equatorial locus are given in Table 7.2. The vertical slices are taken through the centre of the bed.

Table 7.1: Experimental parameters used in 2D gas velocity images of the gas/particle phase

Parameter	Value
Field-of-view	60 mm x 60 mm
Resolution	1.875 mm
Slice thickness	4 mm
Pulse sequence	Spin echo
Phase cycle	12-step cogwheel
Observation time (Δ)	6 ms
Flow encoding gradient time (δ)	100 μs
Echo time (τ)	360 μs
Field-of-flow	3 m s^{-1}
Recycle time	0.5 s
Experiment time	4.5 hours
Number of averages	2

Table 7.2: Vertical positions at which horizontal slice images were acquired in the fluidised bed relative to the bubble centre

Position	Vertical distance relative to bubble centroid
A	10 mm
B	5 mm
C	0 mm
D	-5 mm
E	-10 mm

7.2.2. OPERATING PROCEDURE

Referring to the system in Figure 6.2, the gas flow was initially started within the recirculation system between tanks (1) and (2). Gas flow was subsequently introduced into the fluidised bed (9), and the bed was run at a maximum achievable superficial velocity of 0.11 m s^{-1} to vigorously fluidise the particles. The pressure was brought to the desired value using the bypass valve between vessels (1) and (2), and the flow rate was then brought down to the desired value of 0.0931 m s^{-1} using the mass flow controller (12). In this time, valve (6) was left open for the pressure in tank (7) to equilibrate with the system and stabilise. The bed was run at the desired

flow for 20 minutes to allow steady state conditions to be established. After this, the image acquisition was initiated by starting the bubble injections at the desired frequency using valve (8). A set delay time between bubble release and signal acquisition from the magnet allowed each bubble to be acquired at the same spatial location for the duration of the image.

7.3. RESULTS

7.3.1. INTENSITY IMAGES

Figure 7.2 shows the 2D particle phase intensity images in the horizontal plane. In these images, the horizontal plane is fixed relative to the laboratory reference frame with the depicted bubble rise through the imaging plane achieved using increasing delay times. Image (a) shows the particle phase throughout the bed as having approximately the same solids fraction except for the central region where an approximately circular depression in signal intensity is seen. Surrounding this are local variations in intensity indicative of fluidisation, and edge effects on the bed perimeter due to the B_1 coil effects. The region of lower intensity in the centre is the nose of the bubble, as this image was acquired at a location 10 mm above the theoretical bubble equator. The solids fraction in the central region is larger than zero, owing to some motion blur effects and finite image slice thickness. Image (b) is acquired with the bubble 5 mm higher relative to the plane than image (a). It shows the region of lowered intensity has become enlarged to approximately 15 mm in diameter. The solids fraction is lower than in (a), and the shape is closer to that of an ellipse.

Image (c) is acquired through the predicted bubble equator, with its position 5 mm higher than in (b). The region of lowered particle concentration is again enlarged and is closer to being circular in shape. The solids fraction is approximately zero in the centre of the image. The diameter of the bubble in this image is 18.7 mm. Some local signal depressions are recorded in the annulus between the bubble and the walls of the bed. The bubble is pictured 5 mm higher relative to the static plane in (d), where the image is acquired 5 mm below the equatorial slice. Here the region of lowered signal takes on an annular shape, with a region of increased solids fraction seen in the centre of the bubble. A ring of decreased solids fraction is seen around this which is approximately radially symmetrical. Image (e) is acquired at the limit of the theoretical wake region of the bubble, 10 mm below the bubble equator. The ring of lowered solids fraction is seen to diminish in size and voidage relative to (d), and the region of increased solids fraction in the centre is seen to increase.

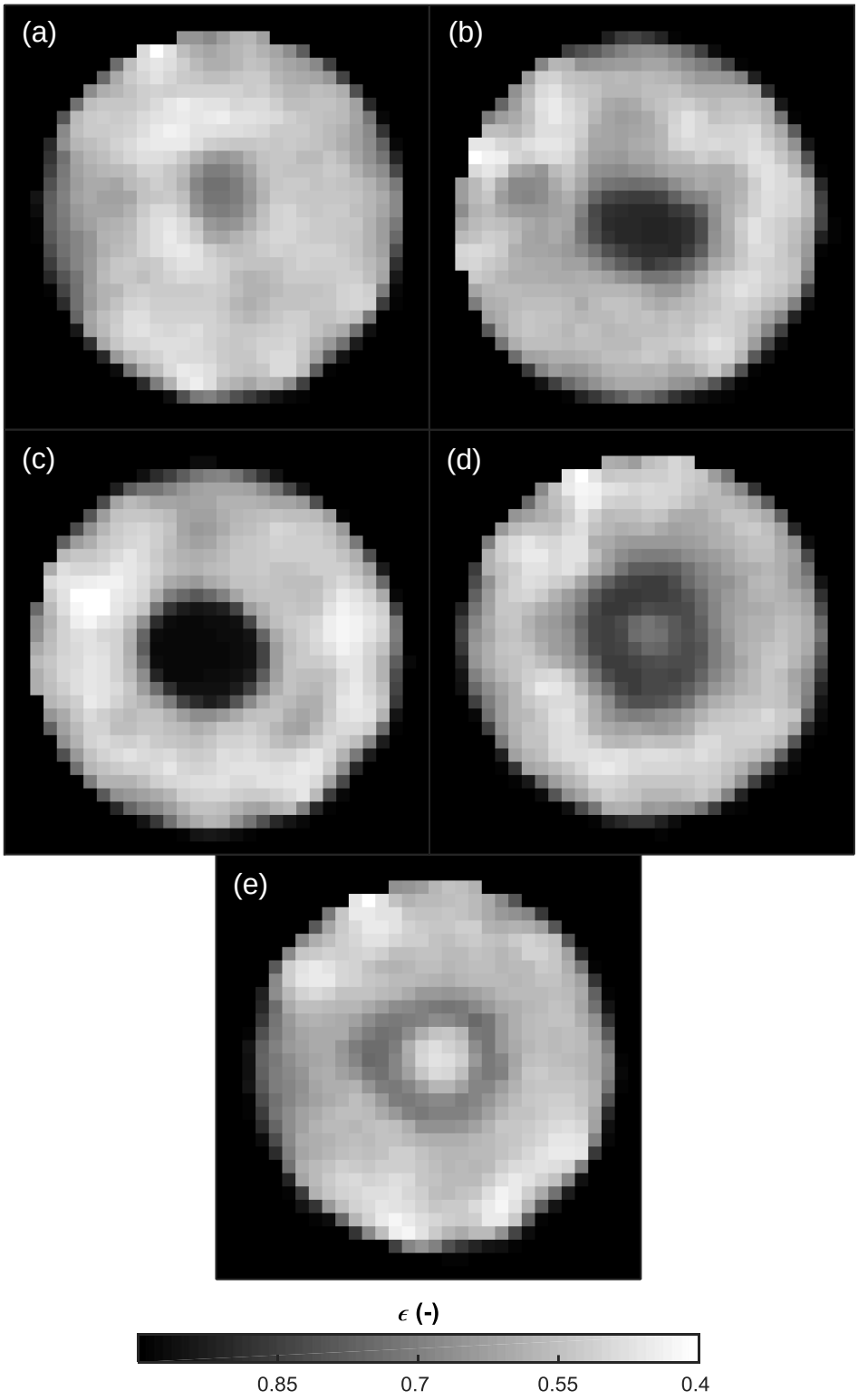

Figure 7.2: Signal intensity images in the horizontal plane for the solid particle phase showing the intensity of ^{1}H signal within the poppy seeds. The images are shown in a static horizontal plane (relative to the laboratory reference frame) with the bubble rising through the plane of imaging. Images (a)-(e) are shown as the bubble passes through showing slices which are 10 mm, 5 mm, 0 mm, - 5 mm and -10 mm relative to the bubble centroidal position. The field-of-view is 60 mm × 60 mm and the resolution is 1.875 mm × 1.875 mm, and the slice thickness is 2 mm. The colour bar denotes the void fraction of the bed.

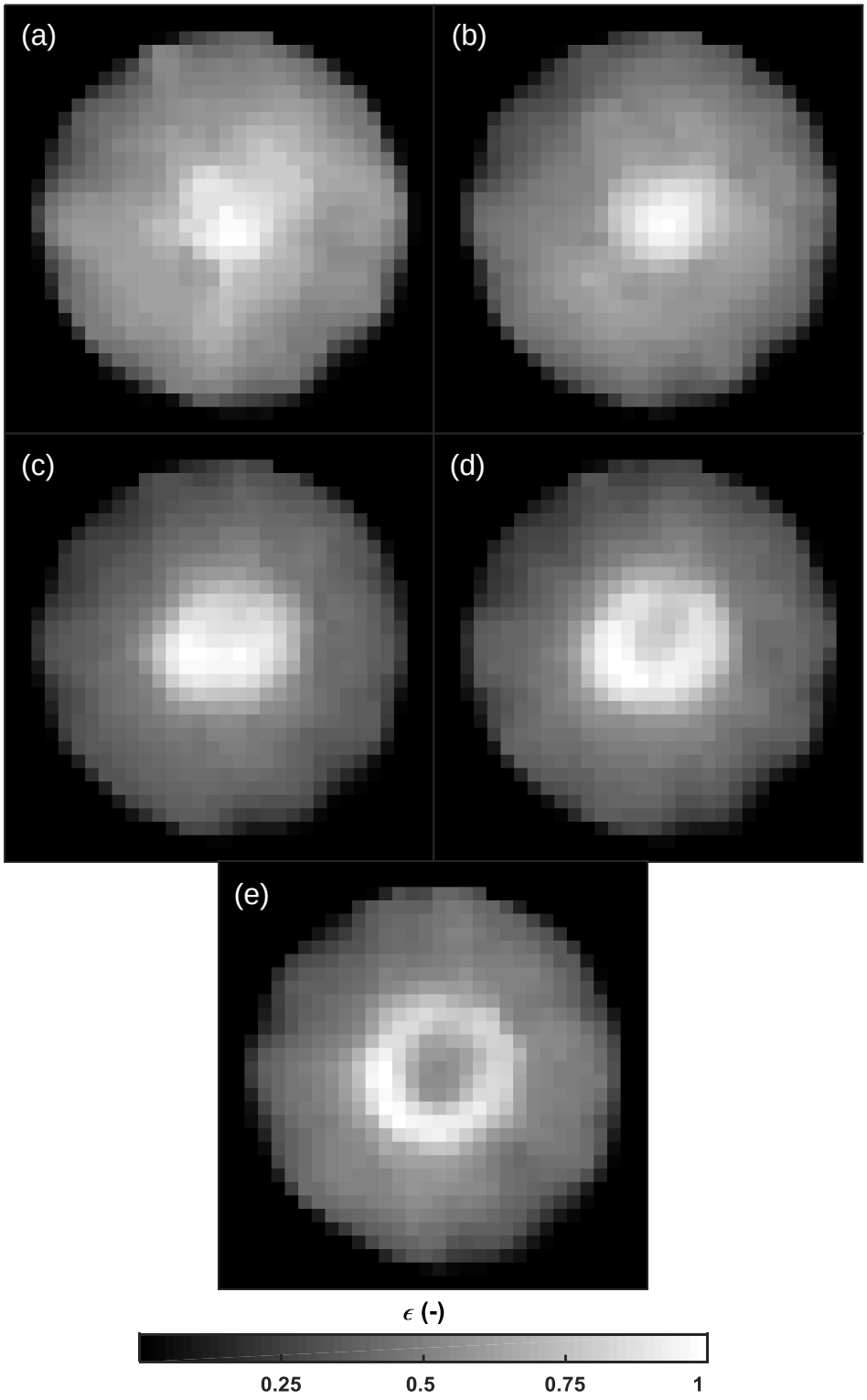

Figure 7.3: Signal intensity images in the horizontal plane for the gas phase showing the intensity of ^{19}F signal within the SF_6 gas. The images are shown in a static horizontal plane (relative to the laboratory reference frame) with the bubble rising through the plane of imaging. Images (a)-(e) are shown as the bubble passes through showing slices which are 10 mm, 5 mm, 0 mm, - 5 mm and -10 mm relative to the bubble centroidal position. The field-of-view is 60 mm × 60 mm and the resolution is 1.875 mm × 1.875 mm, and the slice thickness is 2 mm. The colour bar denotes the void fraction of the bed.

Figure 7.3 gives the gas phase intensity images for the same spatial locations relative to the bubble equator as in Figure 7.2. Image (a) shows a small region of increased gas concentration in the centre of the bed. The annular region between the bubble and the bed walls shows approximately constant gas fraction (which is equivalent to void fraction). Image (b) indicates that the bubble region has increased in size and void fraction relative to (a), as it shows the bubble 5 mm higher in the laboratory reference frame. The diameter of the bubble region is 15 mm. The bubble equatorial slice is given in image (c), which shows an approximately circular region of 18.7 mm in dimeter with void fraction of one. Image (d) shows an annular shape of increased gas concentration, with a central region of reduced void fraction. A similar shape is shown in (e), with a slightly larger annular ring shown, and a larger central area of reduced voidage. Both annuli are however radially symmetrical.

Figure 7.4 shows the particle (a) and gas (b) 2D intensity images in the vertical plane. These slices are acquired in the centre of the bed in the vertical direction. Image (a) shows a region of decreases signal intensity which takes on a kidney bean shape. It is approximately circular with an indentation at the bottom region. The diameter across the equator is 18.7 mm. Local variations and drop-off in signal intensity is recorded elsewhere in the bed, attributed to the motion of fluidisation and inhomogeneities in the magnetic field. Image (b) shows the gas phase, indicating a region of markedly increased gas concentration also in the shape of a kidney bean towards the centre of the bed. The same indented circular structure is shown, with the voxels within the region having a void fraction approaching unity. The diameter of the

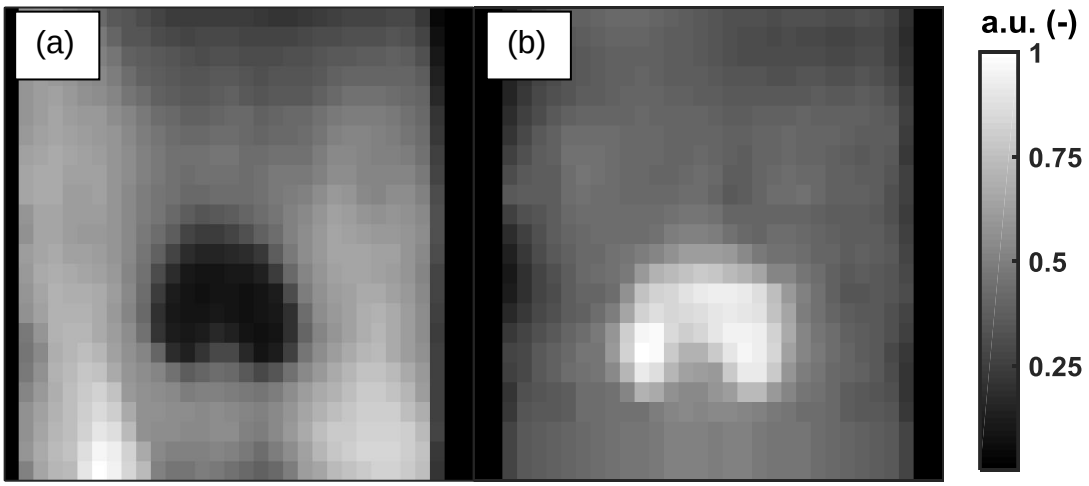

Figure 7.4: Vertical plane signal intensity images for the (a) solid particle phase (^{1}H signal) and (b) the gas phase (^{19}F signal) showing the bubble frozen in the slice. The field-of-view is 60 mm × 60 mm and the resolution is 1.875 mm × 1.875 mm, and the slice thickness is 2 mm. The colour bar denotes relative signal strength in fractional arbitrary units (a.u.) for both the (a) solid and (b) gas phases.

equatorial region is again approximately 18.7 mm. Local variations in the bed outside the bubble region are attributed to magnetic field inhomogeneities and the motion of the fluidised particles.

7.3.2. HORIZONTAL PLANE VELOCITY IMAGES

Figure 7.5 shows all three orthogonal velocity components for the solid particle phase in the horizontal slice with the bubble in the same five vertical locations as in Figures 7.3 and 7.4. The vertical velocity component (on the colour map) is shown in the bubble reference frame, with the positive direction indicating flow in the upwards direction. Image (a) shows most of the vertical flow of particles is approximately -0.23 m s^{-1} in the region between the centre and the bed walls. This is approximately equal to the bubble rise velocity in the downward direction, meaning that relative to the laboratory frame of reference the particulate phase around the bubble is static. A region of more positive particle velocity is seen in the centre, corresponding to the nose of the bubble. The radial components show particle flow outwards from the central region. Image (b) is similar, with radial outflow of the particles shown, and a central region of more positive velocity. The magnitude of the radial outflow of particles is higher in (b) than in (a). Image (c) is in the bubble equatorial position, which shows that the radial direction of particle flow has reversed and is now towards the bubble. As the particle concentration is zero inside the bubble, the gated imaging mask is annular in shape. The magnitude of the radial flow is less than in (a) and (b). The radial flow components in all images in regions away from the bubble (i.e. the bed centre) are approximately zero, indicating low net horizontal motion in the particle phase. The vertical component in (c) shows a ring of more-positive particle velocity surrounding the bubble in a ring-like structure. The structure of the field is radially-symmetrical around the bubble.

Images (d) and (e) are similar, showing radial flow towards the centre of the bed, i.e. towards the bubble. The locus of the centre of the radial flow direction is however different, with (d) being slightly off bed centre and (e) being almost identically in the centre of the bed. Both images show a region of more-positive flow in the vertical direction in the bed centre. This corresponds to the wake region and indicates that the particles in the wake region rise with the bubble or rise at a velocity higher than the bubble relative to the laboratory frame. An annular ring region of more negative flow is observed in both images, with surrounds the region of more positive flow. The magnitude of the inward-flow radial components in (e) indicates a

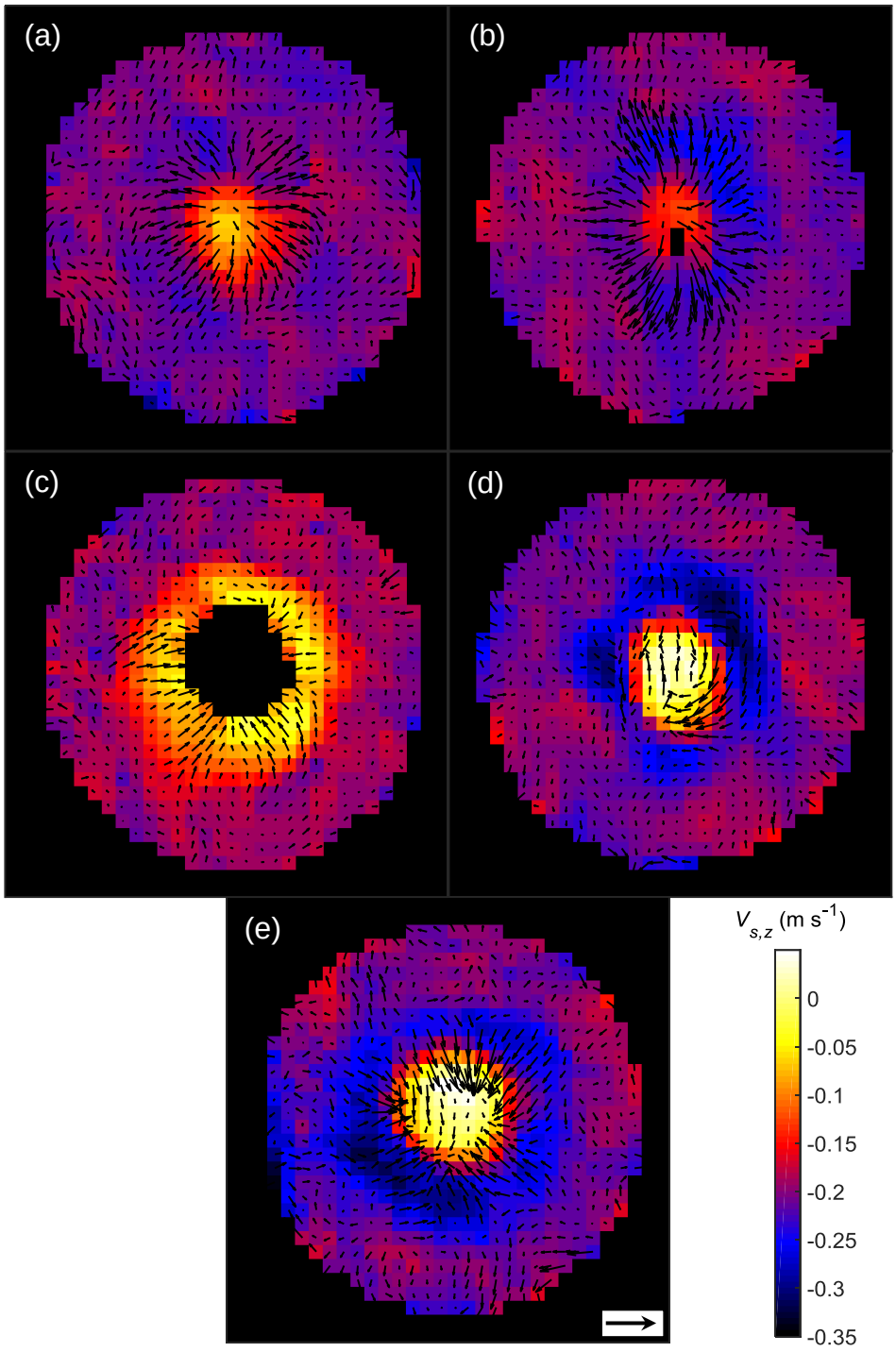

Figure 7.5: Velocity images for the solid particle phase shown for the same slice locations as in Figure 7.2. The vertical (axial) *z*-velocity component is shown on the same image colour axis, whilst the radial in-plane *x*- and *y*-components are indicated by the vector field. The colour axis for all images is shown alongside image (e) and the vector scale is indicated by the arrow representing a speed of 15 cm s^{-1} also shown on image (e). The field-of-view is 60 mm × 60 mm and the resolution is 1.875 mm × 1.875 mm, and the slice thickness is 2 mm. Images (a)-(e) denote the passage of the bubble in 5 mm spatial increments moving upwards.

high flow of particles towards the centre of the bed. The diameter of the more positive region in (d) and (e) is approximately equal to the bubble diameter of 18 mm.

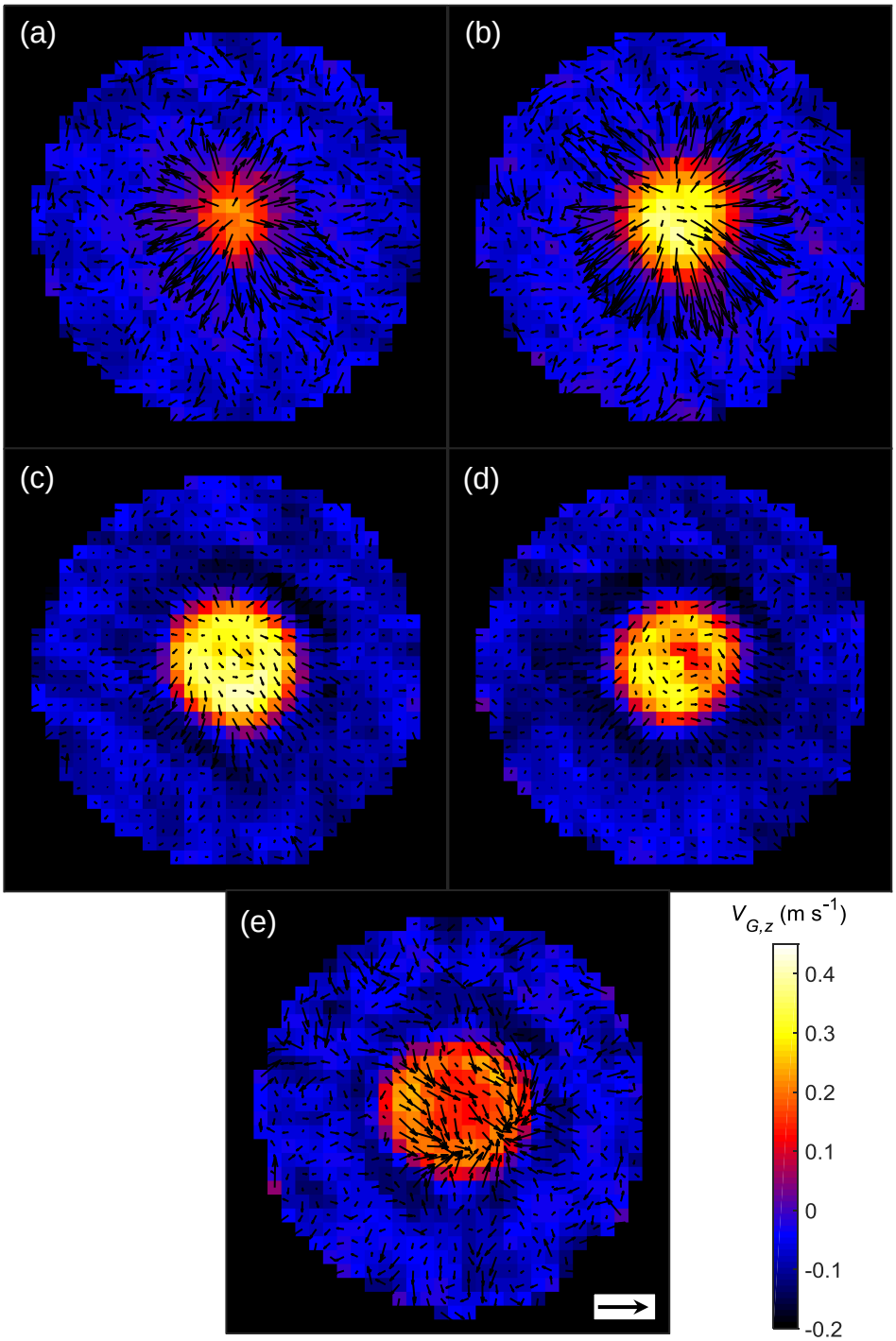

Figure 7.6: Velocity images for the gas phase shown for the same slice locations as in Figure 7.3. The vertical (axial) *z*-velocity component is shown on the same image colour axis, whilst the radial in-plane *x*- and *y*-components are indicated by the vector field. The colour axis for all images is shown alongside image (e) and the vector scale is indicated by the arrow representing a speed of 15 cm s^{-1} also shown on image (e). The field-of-view is 60 mm × 60 mm and the resolution is 1.875 mm × 1.875 mm, and the slice thickness is 2 mm. Images (a)-(e) denote the passage of the bubble in 5 mm spatial increments moving upwards.

The gas phase 2D horizontal slice velocity images showing all three orthogonal components are given in Figure 7.6. The vertical velocity images (on colour scale) are shown in the rising bubble reference frame. These are shown for the same spatial locations relative to the bubble

equator as Figures 7.2, 7.3 and 7.5. Image (a) shows that the gas in most of the particulate phase surrounding the bed centre is flowing at a vertical rate of -0.11 m s^{-1} relative to the bubble. The vertical velocity is reasonably constant in the annular region between the central bubbling section and the bed walls. A high-flow region of positive (upwards) velocity is indicated in the bed centre. At this location, the radial flow is seen to be high and shows an out-flowing pattern away from the bed centre. The radial flow in most of the bed away from the bubble is shown to be static. Image (b) shows the velocity of the central region has increased in magnitude, in both the vertical and radial directions. The diameter of the region is approximately equal to 15 mm and is radially symmetrical. The gas flow outwards is higher than in (a) and covers a larger area. In image (c) the flow is seen to be almost purely vertical, as the radial components in the bubble equatorial position are nearly zero. The central region shows high positive up-flow at a velocity of 0.47 m s^{-1}, which is approximately constant in the bubble region which has a diameter of 18.7 mm. An annular ring of high negative flow is seen surrounding the bubble region. The diameter of this ring is approximately 35-37 mm.

In image (d), the negative flow ring is again shown with a similar diameter. This indicates flow of gas in the downward direction relative to the rising bubble. The positive upflowing region in the centre of the bubble is diminished in magnitude compared to image (c). The radial as velocity components are approximately zero but show very slight outward flow from the bed centre. The profile of the high-flowing central regions of (d) and (e) is similar, showing an annulus of higher flow within the bubble region. In (e), the direction of the radial flow field is shown to reverse, now displaying an inward flowing pattern towards the bubble and bed centre. The annulus of high negative (downward) flow is visible in (e) but has reduced magnitude when compared to (c) and (d).

7.3.3. VERTICAL PLANE VELOCITY IMAGES

Figure 7.7 shows the velocity images of the two in-plane components (which are the vertical and *x*-direction component) in the vertical plane for both the gas (a) and the solid particles (b). These are shown as vector fields both superimposed onto the solid phase intensity image of the bubble for illustrative purposes. The out-of-plane component which is orthogonal to the page was also recorded, but it was found to be almost identically static in the centre of the bed slice. Image (a) shows immediately a recirculation-type pattern for the gas phase, in which the gas is seen around the bubble to circulate in two symmetrical vortex cells with the line of symmetry being the centre line of the bubble and bed. The gas in the particulate phase around the bubble

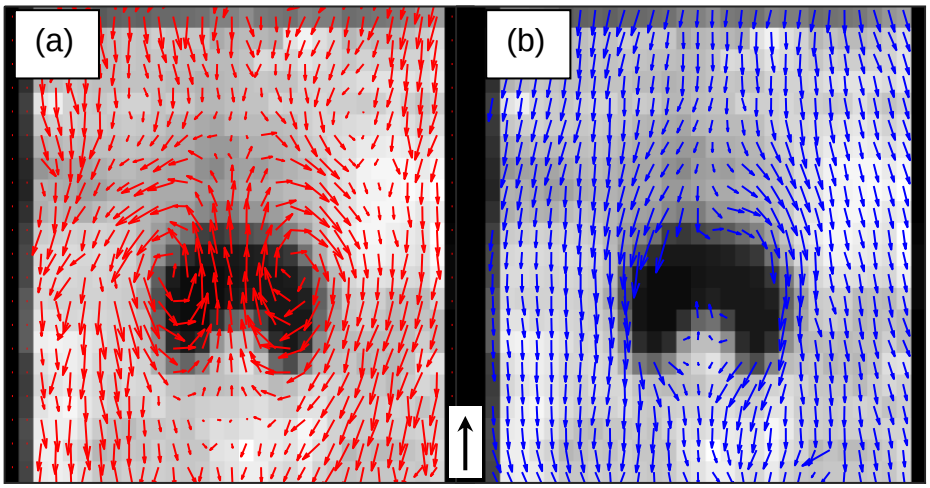

Figure 7.7: Combined velocity vector fields shown for (a) the gas phase (in red vectors) and (b) the particle phase (in blue vectors) shown on an intensity image for the particle phase showing the bubble. The velocity fields are shown relative to the bubble reference frame. A gas recirculation pattern is shown in image (a). The scale of the vector field is shown in the arrow, which for the gas represents a velocity of 0.2 m s^{-1} and for the particles a velocity of 0.1 m s^{-1}. The field-of-view is 60 mm × 60 mm and the resolution is 1.875 mm × 1.875 mm, and the slice thickness is 2 mm.

is seen to move downward relative to the rising bubble at a velocity of -0.11 m s^{-1}. This is an example of a recirculation cloud, which forms when the bubble rises faster in the bed than the gas in the particulate phase interstices. The diameter of the recirculation cloud is approximately 37.5 mm. Two static points are observed which are symmetric about the bubble equator, one at the bubble nose and the other at the lowest point of the bubble wake region.

Image (b) shows the particle phase. Most of the particles away from the bubble simply have a velocity equal to the negative of the rise velocity of the bubble. Near the bubble however, the particle phase is seen to "make way" for the rising bubble, moving down and outwards around the nose of the bubble and then back inwards towards the wake of the bubble. The wake region indentation of the bubble has a near-static velocity relative to the rising bubble. The particles at the top of the wake indentation are moving upward relative to the bubble. The particle flow around the bubble is more asymmetric than the gas flow field, with greater horizontal flow observed above the top right of the bubble than the top left.

7.3.4. COMPARISON WITH CLASSICAL FLUIDISATION THEORY

Tables 7.3 and 7.4 contain calculated data which are relevant for the comparison of the present experiments with classical fluidisation theories, including the two-phase theory of fluidisation. In Table 7.3, bubble geometric features were determined using the acquired images' resolution. Table 7.4 gives a comparison of various calculated values using the division of flow dictated

by the two-phase theory of fluidisation and its modifications by later authors. In each case, the bubble geometry and measured flow rates were used to calculate flow values in the various divisions of phases.

Table 7.3: Experimentally determined values for critical bubble parameters used to compare with analytical fluidisation theories

Bubble diameter D_b (mm)	18.7
Cloud diameter D_c (mm)	37.5
Wake angle (degrees)	140
Wake diameter (mm)	25
Particle region area fraction e_p (-)	0.111
Bubble region area fraction e_b (-)	0.889
Superficial velocity U (m s^{-1})	0.0931
Minimum fluidisation velocity U_{mf} (m s^{-1})	0.088
Excess gas velocity U - U_{mf} (m s^{-1})	0.0051
Bubble rise velocity (m s^{-1})	0.23
Voidage at minimum fluidisation ε_{mf} (-)	0.51
Mean voidage in particulate region ε_p (-)	0.52
Mean voidage in bubble region ε_b (-)	0.0

Table 7.4: Comparison of various flow values in regions of the fluidised bed with the classical theories of Toomey and Johnstone [6], Davidson and Harrison [14], Locket *et al.* [15] and the modelling and experimental values of Boyce *et al.* [49].

Metric	**This work**	**Toomey and Johnstone** [6]	**Davidson and Harrison** [14]	**Locket *et al.*** [15]	**Boyce *et al.*** [49]
Total flow through bed UA (cm^3 s^{-1})	197.7	197.7	197.7	197.7	220.9
Particulate region flow Q_p (cm^3 s^{-1})	111.6	166.1	145.2	166.1	131.7
Visible bubble flow Q_b (cm^3 s^{-1})	55.8	31.6	52.5	55.8	97.4
Bubble through-flow Q_{tf} (cm^3 s^{-1})	59.9	0.0	0.0	62.0	84.8
(UA-Q_t)	-29.6	0.0	0.0	-86.3	-93.0
Particulate region velocity U_p (m s^{-1})	0.11	0.173	0.151	0.173	0.14
Bubble rise velocity U_b (m s^{-1})	0.23	0.13	0.22	0.23	0.31
Bubble region velocity U_{br} (m s^{-1})	0.47	0.13	0.22	0.49	0.58
Through-flow velocity U_{tf} (m s^{-1})	0.24	0.0	0.0	0.26	0.27

7.4. DISCUSSION

7.4.1. INTENSITY IMAGES

The vertical slice intensity images allow the visualisation of the bubble shape in three dimensions by acquiring several slices of the bubble as it rises through a plane fixed in the laboratory reference frame. It is clear from Figure 7.2 that the bubble is approximately radially symmetrical and is injected and rises through the centre of the bed. Although some variation is observed, the slices show that the nose, equator and wake regions of the bubble are approximately circular in shape. The nose in Figure 7.2 (a) and wake region (e) are separated by approximately 20 mm, and the delay time difference between these slices was 0.08 s, meaning the rise velocity is 23-25 cm s^{-1} which compares well with previous measurements. Due to the finite slice thickness used of 2 mm, some of the bubble is still present in the slices of (a) and (e). Image (c) though the central equatorial plane shows that no particles are present in the central region of the bubble. Particles are however apparent in (d) and (e), indicating the presence of an indented bottom of the bubble in the wake region. The bubble wake forms an annular shape when intersected by the imaging pane. The variations in intensity away from the bubble in the particulate phase are attributed to small local fluctuations in the local void fraction, and B_1 effects due to the imaging coil being close to the fluidised particles.

The gas phase images in Figure 7.3 reveal nearly identical behaviour, and they can be seen to be an 'inverse' of the intensity images in Figure 7.2. This is because the signal now originates in the gas nuclei, and thus it is the bubble and fluidising gas being imaged. The shape and size of the bubble nose, equatorial and wake regions is seen to be identical in the gas images when compared to the particle phase images which is expected. This highlights the sensitivity of the NMR technique used. Much higher gas fraction is observed inside the bubble in the equatorial plane in image (c) than in the fluidising fluid, allowing the bubble to be confidently identified. The annular shape of the wake region is also revealed in images (d) and (e), with the annulus being of the same dimensions as those found by studying the particle images. The parity between the gas and particle images allows the shape of the bubble to be positively identified in 3D as being a spherical-cap type of bubble.

The vertical cross-sectional slices of the bubble in Figure 7.4 provide confirmation of the shape identified in Figures 7.2 and 7.3. The particle phase image in (a) shows a clear kidney-bean shaped bubble with an indented bottom in the wake region. The gas phase image in image (b)

is again an inversion of (a) with the higher intensity originating in the bubble itself. The diameter of the bubble across the equator is 18.7 mm and the vertical axis is approximately 17 mm neglecting the indented bottom. This implies that the bubble is not precisely a spherical cap and is ellipsoidal in shape with the major axis in the horizontal direction. The indented bottom is quite different from a spherical cap bubble, which for gas bubbles in liquids is sometimes seen to have a flat bottom corresponding to an infinite wake region radius. The lobes of the kidney-bean shape here are seen to be rounded, meaning the geometry more closely approximates the union of two ellipsoidal shapes rather than two spheres as is very often observed in gas bubbles rising in liquids. This kidney-bean type of shape has previously been shown in 2D fluidised beds by Collins [34] and Stewart [20]. For comparison with the classical models however, the geometry of the bubble was approximated by a spherical cap with a wake angle of 140°, a wake region radius of 25 mm and a wake fraction of 0.12.

7.4.2. HORIZONTAL PLANE VELOCITY IMAGES

To the author's knowledge this is the first time the motion of the both the fluidising fluid and particle phase has been quantitatively obtained around an isolated 3D fluidised bed bubble. The particle phase shows several slice positions on the bubble in Figure 7.5 relative to a plane moving vertically with the bubble. In both (a) and (b), the particles move away from the centre of the rising bubble towards the bed walls. The vertical component near the bubble is more positive than the rest of the particulate phase, meaning that the motion of the approaching bubble effectively 'slows' the flow of particles downward, relative to the rising bubble. Classical theories [16,31,33,34] predicted this flow pattern using analogies with gas bubbles rising in liquid columns. In the equatorial slice in (c), the particulate phase is seen to symmetrically become more positive, and hence 'slow' in the vertical downward direction towards the edge of the bubble. Importantly, an inversion is seen in the radial direction, where the flow of particles is now inward toward the bubble centre. This is again predicted by potential flow theory, in which the particle phase field lines curve around the rising bubble.

The principal difference between the theoretical particle flow field and the measured data is in the particle wake region, which has a central area of much more positive (upward) flow than the rest of the particulate phase. In the centre of the images in Figure 7.5 (c), (d) and (e), the flow is positive relative the bubble, meaning the particles are moving upwards faster than the bubble itself. This behaviour has been suggested as being necessary for the existence of the particle wake region [5,62], and in some cases the particles in the wake can rise much faster

than the bubble causing the bubble to become structurally unsound and collapse from the bottom up. The analytical treatment of Collins [34,63] is one of the more prominent to use a realistic bubble geometry with an indentation in the wake region. This theory shows regions in the wake where the streamlines are curved upwards or are horizontal, implying zero or positive vertical (upwards) flow in the particle region.

In the gas phase, the presence of the bubble clearly provides the gas with an energetically favourable path for flow due to its reduction in local solids fraction. In all images in Figure 7.6, strong upward gas flow is recorded in the centre of the bubble, showing that even relative to the upward-moving bubble there is a strong degree of bubble through-flow. The particle phase gas flow is relatively constant, aside from a ring of negative flow, which is observed in images (c), (d) and (e). This negative-flowing ring indicates the presence of a thin annular region of downward flowing gas relative the bubble. This is clearly a recirculation cloud, which displays a maximum downward flow in the identified region. In (a) and (b), the flow of gas is outwards from the centre of the bubble towards the bed walls, and this pattern is reversed when traversing the bubble equator as the gas is seen to flow towards the bubble again in (d) and (e). The radial field passes through a relatively static zone around the equatorial region in (c).

The recorded flow in the horizontal slices support the model that gas flow around the fluidised bubble exists in a recirculation cloud shape. This type of shape was first analytically discussed by Davidson [16], and suggests there is a radius r_c around the bubble into which the fluid from the surrounding fluidised bed does not penetrate. The radius of the region of negative flow seen in the horizontal slices is approximately 19 mm. From the measured values of the interstitial gas flow rate and bubble rise velocity the bubble is of the 'fast' type, which causes this recirculation cloud to exist. This is expected for Geldart Group D particles. A key advantage presented by these data is the ability to measure the fluidisation behaviour of a non-MRI visible solid particle phase by virtue of imaging the gas phase. In this way, the varying bubble and jet behaviour across different Geldart classifications may be probed. Previously this has been limited by the need for MRI-active solids such as poppy seeds.

7.4.3. VERTICAL PLANE VELOCITY IMAGES

To support the data from the horizontal slice measurements, the vertical cross-section through the centre of the bed in Figure 7.7 is analysed. These images are consistent with the observations in the horizontal slices presented previously. Image (a) for the gas phases shows a clear recirculation cloud of the type predicted by theory [16] for fast-rising bubbles. The

cloud diameter is measured at approximately 37.5 mm. This is slightly larger than the value predicted by Equation 7.15, which uses the Davidson model to predict a value of 29.1 mm for the cloud radius of this bed. Typically, real clouds have been found to be smaller than those predicted by the Davidson theory and closer to the work by Murray. The simulation of Boyce *et al.* [49] however found the cloud diameter of a nearly identical bed to be 40 mm, which is closer to the experimentally determined value here.

The particle phase shows similarly classic behaviour, with the particle field appearing to 'make way' for the rising bubble by moving outwards and downwards at the bubble nose and then back inwards towards the bubble wake. The wake region displays the most deviation from theory, as it has traditionally been troublesome to model the pressure distribution in the wake region accurately. The geometric differences of the indentation mean it is difficult to apply analytical theory in this region. The particles in the indentation are mostly static relative to the bubble, with those at the very top of the indentation showing slight upflow as seen before. This may explain the bubble geometry issues shown in Chapter 6, in which the bubble was seen to collapse about 60-75% of the way up the bed. If the particle phase in the wake moves much faster than the rising bubble, the structure will last only as long as it takes for these particles to 'catch up' with the bubble roof, causing bubble collapse.

7.4.4. COMPARISON WITH CLASSICAL FLUIDISATION THEORY

For the comparison with the existing fluidised bed theories, the geometry of the bed and bubble was used to divide the flow according to the assumptions made by Toomey and Johnstone [6], Davidson and Harrison [14] and Locket *et al.* [15]. It is clear from the experimental data that significant through-flow exists through the bubble. Through-flow is the primary shortcoming of the original two-phase theory, which assumed that all flow more than the minimum fluidisation flow would pass through the bed in the visible bubble flow rate. For clarity, despite the existence of a recirculation cloud the bubble is analysed only in terms of the bubble and the particulate phases. The flow upward through the bubble is compensated by flow downward within the cloud region which has previously been defined by some authors. However, the mass balance is still valid on an averaged basis across the current slice when only looking at the bubble and particulate phases.

In previous analyses, the motivation to improve the two-phase theory came mostly from the observation that it over-predicted the visible bubbling rate. In this example however, it is seen that it is under-predicted, with two-phase theory predicting a rise velocity of 0.13 m s^{-1} and a

measured value of 0.23 m s^{-1}. This is due to the measured value of the average velocity in the particulate phase measured to be less than U_{mf}/ε_{mf}. This is a surprising result as classical theory would dictate that these particles are no longer fluidised. This deficit may be due to the presence of the recirculation cloud which causes a local reduction in gas velocity around the bubble, as well as the relative particle velocity of -0.02 m s^{-1}. If both effects are compensated for, the particles are clearly in a fluidised environment. The motivation for the modification of the two-phase theory to include through-flow is however clear from these experiments, as the analytical work by Davidson shows through-flow to be a critical component of bubble geometry which is present under all relative rise/fluidising flow conditions.

The modification by Davidson and Harrison [14] considers the local velocity of the particle field in the particulate region. Using the average particle velocity measured by experiment the new particulate phase gas velocity predicted is 0.151 m s^{-1}. This is closer to the measured value than for two-phase theory, indicating that the relative local flow of gas and the particles is an important consideration for modelling. The model does not in itself allow for through-flow, and the rise velocity was determined from the balance of flow remaining after the particle flow in the particulate phase was accounted for. The rise velocity predicted is 0.22 m s^{-1} which is a significant improvement over pure two-phase flow even though the model doesn't allow for through-flow. These conditions imply a value for *K* of 0.78 (i.e. less than unity) and for *n* of -2 as per Equations 7.5 and 7.6, which has previously been observed but is rare [13].

The modification by Locket *et al.* [15] is based on the work by Davidson [16] which showed that the through-flow for the Davidson bubble is $3U_{mf}$. This is overwhelmingly the most accurate estimate of the through-flow, with the experimentally-determined rise velocity being added giving a total bubble region velocity of 0.49 m s^{-1} which compares favourably with the experimental value of 0.47 m s^{-1}. The through-flow velocity is 0.26 m s^{-1} which is consistent with the experimental value of 0.24 m s^{-1}. To be used in a predictive capacity, this model relies on an accurate assessment of the bubble rise velocity. Clearly the analytical treatment of the potential flow around a spherical bubble provides a very reasonable estimate of the through-flow. The particle-phase flow is still overestimated as it assumes it is equal to U_{mf}/ε_{mf}. Accounting for the relative flow of particles would improve this estimate however.

The results are also compared to the modelling study by Boyce *et al.* [49] which models a bed under very similar conditions using the same materials, the only noteworthy difference being the rate of fluidising gas through the bed. This is reflected in the higher value of *UA* in Table

7.4. This study also finds that the rate of flow through the particulate region is lower than U_{mf}/ε_{mf}. The bubble rise velocity compares well with a simulated value of 0.31 m s^{-1}. The through-flow rate compares particularly well with the present data. The predicted bubble region velocity is higher than measured here possibly due to the higher rate of fluidising gas. Nevertheless, the simulation indicates that the division of flow measured in the present experiments is very reasonable. In the models by Locket *et al.* [15] and the simulation by Boyce *et al.* [49] there is a deficit between the theoretical total flow through the bed and the calculated total flow based on the divided regions of the bed. This is also seen in the experimental results. Experimentally, this deficit may be due to the finite resolution of the images and partial volume effects, or due to the injection volume not being adequately accounted for. The second explanation is however less likely as the volume of injected gas is nearly negligible. It may also be due to localised variations in the solids fraction which are not accounted for in this type of analysis. The smallest deficit is however recorded for the experiments, and larger deficits are seen for the models and simulation data.

The inaccuracy of these models is no doubt due to their many simplifying assumptions which neglect the nuanced flow patterns observed in the gas and particle phases. Few studies have used pressurised 3D beds with a dense gas such as SF_6, so it is unsurprising that some novel effects have been observed. Furthermore, the type and geometry of the bubbles observed here (elliptical indented kidney bean) with wake regions of significant particle velocity means many of the modelling approaches would naturally fall short as none of this behaviour is accounted for.

7.5. CONCLUSIONS

Single isolated fluidised bed bubbles were successfully injected and imaged using MRI. The intensity images in both the horizontal plane and vertical plane were acquired. These were found qualitatively to be inverses of each other, with the regions of enhanced void fraction showing as regions of enhanced signal intensity for the gas images and diminished signal intensity for the particle phase. The horizontal images show the bubble rising through a static slice, affirming the rise velocity measured in Chapter 6 of 0.23 m s^{-1}. The bubble has a maximum diameter in the equatorial plane of 18.7 mm. Geometrically the bubble is an indented ellipsoid, or kidney-bean shape, which differs slightly from the idealised spherical cap. Using a spherical cap model however the wake angle was found to be 140°, the wake region radius

was 25 mm and the wake fraction was 0.12. The difference in bubble shape is attributed to the unusual combination of particles and dense gas.

MRI velocimetry measurements of each orthogonal velocity component in both the horizontal and vertical planes of both phases showed flow behaviour which is approximated by the classical theory of isolated bubble flow in fluidised beds. In the gas phase, a recirculation cloud was observed which is characteristic of 'fast' rising bubbles. The cloud diameter was 37.5 mm, inside which a vortex was observed. This is slightly larger than the cloud predicted by the Davidson model. The particles showed behaviour similar to that predicted by the potential flow around a spherical bubble, with important differences observed in the wake region. The indented wake region showed particles which were moving upwards relative to the bubble, which implies a lack of stability in the bubble structure. This explains why the bubbles were seen to collapse in Chapter 6, as the wake region overtakes the nose of the bubble.

One of the principle advantages of this study for the future of fluidisation research using MRI is the possibility to now probe different Geldart-classified materials, such as Groups A and B, by imaging exclusively the gas phase. In this way, any solid powder which need not be MRI-visible may be used together with an MRI-visible gas. The behaviour of jets and bubbles across the Geldart classification (different particle sizes and densities) can now be assessed by imaging the gas phase alone, thus opening several avenues of promising research.

Using the measured data, a quantitative comparison was made with classical two-phase fluidisation theory. The bubble through-flow was found to be significant, with a measured value of 0.24 m s^{-1}. Together with the rise velocity this gives a total bubble region flow velocity of 0.47 m s^{-1}. This compared well with the modified two-phase theory which accounts for 1) particle flow and 2) bubble through-flow using the Davidson bubble. The Davidson bubble therefore provides a good estimate of the through-flow velocity for first-pass design calculations. Good agreement was seen in the division of flow between the experimental data and the simulation data by Boyce *et al.* [49]. In all cases, the models were found to overestimate both the particulate phase flow rate and underpredict the bubble rise velocity. This is attributed to the different materials and operating conditions used in this study compared with typical fluidisation experiments in 2D beds using atmospheric air.

NOMENCLATURE

ABBREVIATIONS

1D, 2D, 3D	one, two or three dimensional
CFD	computational fluid dynamics
DEM	discrete element method
FOV	field-of-view
r.f.	radiofrequency
MRI	magnetic resonance imaging
NMR	nuclear magnetic resonance
TFM	two-fluid model

SYMBOLS

A	cross sectional area	m^2
A_p	particle region area	m^2
A_b	bubbling region area	m^2
D_b	bubble diameter	m
Dc	cloud diameter	m
e_b	fraction of bubbling area	-
f	bubble wake fraction	-
g	velocity gradient increment	$T\ m^{-1}$
g	acceleration due to gravity	$m\ s^{-2}$
K	bubble concentration coefficient	-
n	dimensionless fluidised bubble constant	-
Q	volumetric flow rate	$m^3\ s^{-1}$
Q_p	volume flow of gas in particle region	$m^3\ s^{-1}$
Q_b	volume flow of gas in bubbling region	$m^3\ s^{-1}$
Q_{tf}	through-flow volumetric rate	$m^3\ s^{-1}$
r_b	bubble radius	m
r_c	cloud radius	m
t	time	s
U	superficial/average velocity	$m\ s^{-1}$
U_{mf}	minimum fluidisation velocity	$m\ s^{-1}$

U_{mb}	minimum bubbling velocity	m s^{-1}
U_b	bubble rise velocity	m s^{-1}
U_s	average solids velocity	m s^{-1}
U_p	gas velocity in the bubbling region	m s^{-1}
U_{tf}	through-flow velocity	m s^{-1}
V_G	local gas velocity	m s^{-1}
V_S	local solids velocity	m s^{-1}
y,x,z	standard cartesian coordinates	-

GREEK LETTERS

α	ratio of bubble rise to particulate phase velocity	-
Δ	observation time for velocity measurement	s
δ	flow encoding gradient pulse time	s
ε	void fraction/voidage	-
ε_p	particulate region voidage	-
ε_{mf}	voidage at minimum fluidisation conditions	-
Ψ_f	fluid potential flow stream function	m^2 s^{-1}
Θ	angle	rad
τ	echo time	s

REFERENCES

[1] Jackson, R. The dynamics of fluidized particles. Cambridge University Press; 2000.

[2] Christensen, D., Nijenhuis, J., Van Ommen, J.R., Coppens, M.O. Influence of distributed secondary gas injection on the performance of a bubbling fluidized-bed reactor. *Ind. Eng. Chem. Res.* 2008;47: pp. 3601–18.

[3] Köksal, M., Vural, H. Bubble size control in a two-dimensional fluidized bed using a moving double plate distributor. *Powder Technol.* 1998;95: pp. 205–13.

[4] Kunii, D., Levenspiel, O. Fluidization Engineering. 2nd ed. Stoneham: Butterworth-Heinemann; 1991.

[5] Davidson, J.F., Harrison, D. Fluidised particles. vol. 3. Cambridge: Cambridge university press Cambridge, UK; 1963.

[6] Toomey, R.D., Johnstone, H.F. Gaseous fluidization of solid particles. *Chem. Eng. Prog.* 1952;48: pp. 220–6.

[7] Pyle, D.L., Harrison, D. An experimental investigation of the two-phase theory of fluidization. *Chem. Eng. Sci.* 1967;22: pp. 1199–207.

[8] Grace, J.R., Harrison, D. The behaviour of freely bubbling fluidised beds. *Chem. Eng. Sci.* 1969;24: pp. 497–508.

[9] Baumgarten, P.K., Pigford, R.L. Density fluctuations in fluidized beds. *AIChE J.* 1960;6: pp. 115–23.

[10] Geldart, D., Cranfield, R.R. The gas fluidisation of large particles. *Chem. Eng. J.* 1972;3: pp. 211–31.

[11] Geldart, D. The size and frequency of bubbles in two-and three-dimensional gas-fluidised beds. *Powder Technol.* 1970;4: pp. 41–55.

[12] Geldart, D. The effect of particle size and size distribution on the behaviour of gas-fluidised beds. *Powder Technol.* 1972;6: pp. 201–15.

[13] Grace, J.R., Clift, R. On the Two-Phase Theory of Fluidization. *Chem. Eng. Sci.* 1974;29: pp. 327–34.

[14] Davidson, J.F., Harrison, D. Behavior of a continuously bubbling fluidized bed. *Chem. Eng. Sci.* 1966;21: pp. 731–738.

[15] Lockett, M.J., Davidson, J.F., Harrison, D. On the two-phase theory of fluidisation 1967;22: pp. 1059–66.

[16] Davidson, J.F. Symposium on fluidization - discussion. *Trans. Inst. Chem. Eng.* 1961;39: pp. 230–2.

[17] Yacono, C., Rowe, P.N., Angelino, H. An analysis of the distribution of flow between phases in a gas fluidised bed. *Chem. Eng. Sci.* 1979;34: pp. 789–800.

[18] Davidson, J.F., Harrison, D. Fluidization. London: Academic press; 1971.

[19] Rowe, P.N., Partridge, B.A., Lyall, E. Cloud formation around bubbles in gas fluidized beds. *Chem. Eng. Sci.* 1964;19: pp. 973–85.

[20] Stewart, P.S.B. Isolated bubbles in fluidized beds - theory and experiment. *Trans. Inst.*

Chem. Eng. 1968;46: pp. 60–6.

[21] Rowe, P.N., Partridge, B.A. An x-ray study of bubbles in fluidised beds. *Chem. Eng. Res. Des.* 1997;75: pp. S116–34.

[22] Hernández-Jiménez, F., Gómez-García, A., Santana, D., Acosta-Iborra, A. Gas interchange between bubble and emulsion phases in a 2D fluidized bed as revealed by two-fluid model simulations. *Chem. Eng. J.* 2013;215–216: pp. 479–90.

[23] Hong, R., Ren, Z., Ding, J., Kawaji, M., Li, H. Bubble dynamics in a two-dimensional gas-solid fluidized bed. *China Particuology* 2007;5: pp. 284–94.

[24] Gera, D., Gautam, M., Tsuji, Y., Kawaguchi, T., Tanaka, T. Computer simulation of bubbles in large-particle fluidized beds. *Powder Technol.* 1998;98: pp. 38–47.

[25] Guenther, C., Syamlal, M. The effect of numerical diffusion on simulation of isolated bubbles in a gas-solid fluidized bed. *Powder Technol.* 2001;116: pp. 142–54.

[26] Lindborg, Hå., Lysberg, M., Jakobsen, H.A. Practical validation of the two-fluid model applied to dense gas-solid flows in fluidized beds. *Chem. Eng. Sci.* 2007;62: pp. 5854–69.

[27] Gidaspow, D., Seo, Y.C., Ettehadieh, B. Hydrodynamics of Fluidization: Experimental and Theoretical Bubble Sizes in a Two-Dimensional Bed With a Jet. *Chem. Eng. Commun.* 1983;22: pp. 253–72.

[28] Acosta-Iborra, A., Sobrino, C., Hernández-Jiménez, F., de Vega, M. Experimental and computational study on the bubble behavior in a 3-D fluidized bed. *Chem. Eng. Sci.* 2011;66: pp. 3499–512.

[29] Geldart, D. Types of gas fluidization. *Powder Technol.* 1973;7: pp. 285–92.

[30] Clift, R., Grace, J.R. Continuous bubbling and slugging. *Fluidization* 1985;78.

[31] Jackson, R. The mechanics of fluidized beds. Part 2. The motion of fully developed bubbles. *Trans. Inst. Chem. Eng.* 1963;41: pp. T22–30.

[32] Lockett, M.J., Harrison, D. The distribution of voidage fraction near bubbles rising in gas-fluidized beds. In: Drinkenburg A, editor. Proc. Int. Symp. Fluid., Amsterdam: Netherlands University Press; 1967, p. 257–67.

[33] Murray, J.D. On the mathematics of fluidization, Part 2: steady motion of fully developed bubbles. *J. Fluid Mech.* 1965;22: pp. 57–80.

[34] Collins, R. An extension of Davidson's theory of bubbles in fluidized beds. *Chem. Eng. Sci.* 1965;20: pp. 747–55.

[35] Stewart, P.S.B., Davidson, J.F. Slug flow in fluidised beds. *Powder Technol.* 1967;1: pp. 61–80.

[36] Collins, R. The effect of a bubble on gas flow in a plane fluidized bed of finite width: two theories compared. *Chem. Eng. Sci.* 1969;24: pp. 1291–307.

[37] Lignola, P.G., Donsi, G., Massimilla, L. Mass spectrometric measurements of gas composition profiles associated with bubbles in a two dimensional bed. AIChE Symp. Ser, vol. 79, 1983, p. 19–26.

[38] Hatano, H., Ishida, M. Study On The Cloud Radius And Interphase Mass-transfer Coefficient For A Gas-solid Fluidized-bed. *Kagaku Kogaku Ronbunshu* 1984;10: pp.

184–91.

[39] Reuter, H. Druckverteilung um Blasen im Gas-Feststoff-Fließbett. *Chemie Ing. Tech.* 1963;35: pp. 98–103.

[40] Reuter, H. Mechanismus der Blasen im Gas-Feststoff-Fließbett. *Chemie Ing. Tech.* 1963;35: pp. 219–28.

[41] Yates, J.G., Cheesman, D.J. Voidage variations in the regions surrounding a rising bubble in a fluidized bed. AIChE Symp. Ser., vol. 88, American Institute of Chemical Engineers; 1992, p. 34.

[42] Yates, J.G., Cheesman, D.J., Engineering, B. Experimental Observations of Voidage Distribution. *Chem. Eng. Sci.* 1994;49: pp. 1885–95.

[43] Buyevich, Y.A., Yates, J.G., Cheesman, D.J., Wu, K. A model for the distribution of voidage around bubbles in a fluidized bed. *Chem. Eng. Sci.* 1995;50: pp. 3155–62.

[44] Shi, Z., Wang, W., Li, J. A bubble-based EMMS model for gas-solid bubbling fluidization. *Chem. Eng. Sci.* 2011;66: pp. 5541–55.

[45] Almendros-Ibanez, J.A., Pallarest, D., Johnsson, F., Santana, D. Novel Approach to Characterize Fluidized Bed Dynamics Combining Particle Image Velocimetry and Finite Element Method. *Ind. Eng. Chem. Res.* 2009;48: pp. 5010–23.

[46] Boemer, A., Qi, H., Renz, U. Verification of Eulerian simulation of spontaneous bubble formation in a fluidized bed. *Chem. Eng. Sci.* 1998;53: pp. 1835–46.

[47] Shin, H.-S., Park, M.-G., Jung, J.-Y. Nutrient removal processes for low strength wastewater. *Environ. Technol.* 2001;22: pp. 889–95.

[48] Patil, D.J., van Sint Annaland, M., Kuipers, J. a. M. Gas Dispersion and Bubble-to-Emulsion Phase Mass Exchange in a Gas-Solid Bubbling Fluidized Bed: A Computational and Experimental Study. *Int. J. Chem. React. Eng.* 2003;1.

[49] Boyce, C.M., Ozel, A., Rice, N.P., Rubinstein, G.J., Holland, D.J., Sundaresan, S. Effective particle diameters for simulating fluidization of non-spherical particles: CFD-DEM models vs. MRI measurements. *AIChE J.* 2017;63: pp. 2555–68.

[50] Gladden, L.F. Magnetic resonance: ongoing and future role in chemical engineering research. *AIChE J.* 2003;49: pp. 2–9.

[51] Gladden, L.F. Recent advances in MRI studies of chemical reactors: ultrafast imaging of multiphase flows. *Top. Catal.* 2003;24: pp. 19–28.

[52] Gladden, L.F., Sederman, A.J. Recent advances in flow MRI. *J. Magn. Reson.* 2013;229: pp. 2–11.

[53] Pore, M., Chandrasekera, T.C., Holland, D.J., Wang, A., Wang, F., Marashdeh, Q., et al. Magnetic resonance studies of jets in a gas-solid fluidised bed. *Particuology* 2012;10: pp. 161–9.

[54] Fennell, P.S., Davidson, J.F., Dennis, J.S., Gladden, L.F., Hayhurst, A.N., Mantle, M.D., et al. A study of the mixing of solids in gas-fluidized beds, using ultra-fast MRI. *Chem. Eng. Sci.* 2005;60: pp. 2085–8.

[55] Wang, R., Rosen, M.S., Candela, D., Mair, R.W., Walsworth, R.L. Study of gas-fluidization dynamics with laser-polarized 129Xe. *Magn. Reson. Imaging* 2005;23: pp.

203–7.

[56] Pore, M., Ong, G.H., Boyce, C.M., Materazzi, M., Gargiuli, J., Leadbeater, T., et al. A comparison of magnetic resonance, X-ray and positron emission particle tracking measurements of a single jet of gas entering a bed of particles. *Chem. Eng. Sci.* 2015;122: pp. 210–8.

[57] Han, S.-I., Stapf, S., Blümich, B. NMR Imaging of Falling Water Drops. *Phys. Rev. Lett.* 2001;87: pp. 144501.

[58] Boyce, C.M., Rice, N.P., Sederman, A.J., Dennis, J.S., Holland, D.J. 11-interval PFG pulse sequence for improved measurement of fast velocities of fluids with high diffusivity in systems with short T 2∗. *J. Magn. Reson.* 2016;265: pp. 67–76.

[59] Cotts, R.M., Hoch, M.J.R., Sun, T., Markert, J.T. Pulsed field gradient stimulated echo methods for improved NMR diffusion measurements in heterogeneous systems. *J. Magn. Reson.* 1989;83: pp. 252–66.

[60] Lustig, M., Donoho, D., Pauly, J.M. Sparse MRI: The application of compressed sensing for rapid MR imaging. *Magn. Reson. Med.* 2007;58: pp. 1182–95.

[61] Benning, M., Gladden, L., Holland, D., Schönlieb, C.-B., Valkonen, T. Phase reconstruction from velocity-encoded MRI measurements–a survey of sparsity-promoting variational approaches. *J. Magn. Reson.* 2014;238: pp. 26–43.

[62] Richardson, J.F., Harker, J.H., Backhurst, J.R. Fluidisation. Coulson Richardson's Chem. Eng. Vol. 2 Part. Technol. Sep. Process. 5th ed., Oxford: Butterworth-Heinemann; 2002, p. 291–369.

[63] Collins, R. The rise velocity of Davidson's fluidization bubble. *Chem. Eng. Sci.* 1965;20: pp. 788–90.

CHAPTER 8 – CONCLUSIONS AND FUTURE RESEARCH

8.1. CONCLUSIONS

This thesis has presented an investigation into the complex multiphase interactions which occur inside fixed and fluidised beds. Magnetic resonance imaging and velocity measurement techniques were utilised on a non-reactive co-current upflow, trickle flow and fluidised bed to visualise the complex micro-scale phase interactions which make these units challenging to design optimally. MRI and experimental procedures were developed to address the goals of the thesis which were to: acquire spatially resolved quantitative gas flow information in a co-current upflow bed, assess the anisotropy in the flow of fluids in trickle flow and the degree to which fluids interact, and to image the flow around an isolated fluidised bed bubble and compare the findings to classical models. These phenomena were all identified as having a strong influence on the mass and heat transfer, and thus performance, of units of these types operating industrially.

In Chapter 3, it was first shown that the MRI velocity imaging methods developed for use with SF_6 gas and gadolinium-doped water were quantitative. This was done by measuring the velocity profiles of single-phase gas and liquid flow through a 52 mm tube. The profiles for the liquid phase approached that of ideal Poiseuille flow with a flattened centre. The gas phase also showed a flattened profile towards the tube centre. The average velocity measured using MRI agreed to at least 2% of the values obtained from the external mass-flow controllers, indicating that the chosen pulse sequences are quantitative. Low spatial resolution time-averaged velocity measurements were acquired in the packed bed. Liquid saturation within the slice was shown to increase as a function of liquid flow and decrease for increasing gas velocity. Liquid saturation and pressure drop (obtained using pressure gauges) showed reasonable quantitative agreement was shown with existing models. The spatially-resolved velocity maps showed a strong difference from single-flow, indicating the presence of liquid-rich rivulets towards the centre of the bed and gas-rich regions in pores indicative of bubbling behaviour towards the bed walls. The distribution of velocities enabled the identification of significant back-mixing in both phases, and the identification of static gas holdup which was insensitive to changes in either phase superficial velocity. These measurements show the ability of MRI to provide information on a range of traditional design considerations for co-current upflow beds.

In Chapter 4, velocity images were acquired of the temporally-stable state of trickle flow in a co-current downward flowing bed. The images showed that in both the gas and liquid phases, most of area occupied by each phase is static. This means that the axial flow is carried mostly be a few pores which have much higher than average flow rates. A pore-scale analysis showed that the gas phase flow field exhibits higher anisotropy than the liquid flow. For the gas, 4% of the available pore space was responsible for conveying as much as 50% of the flow through the slice. In the liquid phase, approximately 20% of the pore space conveyed around 50% of the flow in the slice. Maldistribution was also increased in both phases when the flow velocities of both the gas and liquid were increased, however the effects of the liquid flow were more pronounced on both phases than the gas flow. The design parameters of solids wetting efficiency, liquid saturation and pore filling fraction were calculated as a function of macroscopic flow rate. These were consistent with existing theories regarding how TBR operation is influenced by the macroscopic flow rates of gas and liquid. However, the calculation of pore-filling fraction distributions was only possible using a spatially-resolved non-invasive technique such as MRI.

Chapter 5 presented an analysis of the trickle-bed images based on the use of a morphological thinning algorithm which allowed the identification of the phase interfaces. This allowed the voxels at the interface to be isolated for both the gas and the liquid phases. The distributions of interfacial velocity were found to be like those obtained for the full slice for both the gas and the liquid. This indicates that the interface at the 180 μm scale does not behave in a fundamentally different way to the bulk fluid. Most of the interfacial voxels were static for both the gas and the liquid. Using the orientation of the phase surface, the component of the shear stress tensor in the vertical direction orthogonal to the surface was calculated for both phases. The shear stress distributions were found to be symmetrical around zero, indicating that a most of the voxels experience no shear in the vertical direction. In order to validate the slip-type closure laws for modelling, the interaction between both the velocity and the shear stress was assessed by determining if correlations between these quantities exist on a local spatial basis. It was shown that very little correlation could be determined, and therefore that minimal phase interaction is present in the trickle-flow regime for this system. Therefore, the inclusion of locally-interacting slip factor in models is of limited validity under the present conditions in systems such as the one studied here. Interaction between phases was observed more on a global basis due to macroscopic flow rate changes.

Chapter 6 presents the first data on the fluidised bed, where a combination of conventional pressure drop measurements and MRI 1D profiles was used to unequivocally determine the minimum fluidisation velocity to be equal to the minimum bubbling velocity at $U_{mf} = U_{mb} = 0.088$ m s^{-1}. This is characteristic of Geldart [1] Group D fluidisation behaviour. A special pulsing gas injection system was designed to inject high pressure SF_6 gas in controlled short pulses into the centre of the fluidised bed distributor. This system was used to inject single bubbles into an incipiently fluidised bed. The bubbles were found to rise with slightly anomalous behaviour, slowing down with vertical position and eventually collapsing above the halfway point in the bed. The bubble rise velocity was studied as a function of injected volume, which was consistent with existing theories. For the imaging experiments it was required that the injected bubbles be spatially reproducible. The reproducibility of the bubble was assessed using statistical methods, and the injection parameters were optimised. Using this approach, injections at 1-2.5 Hz of bubbles with 80-90 ms injection times were found to be the most reproducible. These parameters were found to give bubbles approximately 20 mm in diameter with less than 17% variation in the spatial position.

Chapter 7 gives the first spatially-resolved gas and liquid velocity images of the fluid flow surrounding an isolated bubble in a fluidised bed. The injection system was used to trigger pulses of the imaging experience to build up **k**-space using a single-point-imaging strategy from individual bubbles which were isolated at the same spatial location over the experimental duration. The bubble was successfully imaged in both the solid and gas phases, the density maps of which showed an indented ellipsoidal shape which resembles a kidney bean. The geometric characteristics of the bubble were found from the images, giving a wake angle of 140° and a bubble diameter of 18.7 mm. All three orthogonal velocity components were acquired for both phases in both the horizontal plane as a bubble rises through it, and in the vertical plane. The vertical plane image revealed a streamline pattern very similar to that predicted by the classical models by Davidson [2], Murray [3] and Jackson [4]. A recirculation cloud characteristic of fast bubbles was observed, with a cloud diameter of 37.5 mm. The bubble geometry was shown to change up the length of the bed, caused by the rapid motion of particles upwards in the bubble wake, which overtakes the nose of the bubble and causes it to collapse. The data compared well with a similar simulated bed by Boyce *et al.* [5], but differences were found in the division of gas flow between the regions in classical models such as the two-phase theory. The through-flow was found to be significant at 0.24 m s^{-1}, which was similar to the value predicted by Lockett *et al.* [6].

In conclusion, this thesis has demonstrated the successful application of MRI and MRI velocimetry techniques to study microscopic fluid dynamics in complex multiphase environments. The spatiotemporal characteristics of several pore-scale phenomena were observed for the first time in both the gas and the liquid phases of fixed and fluidised beds, and the physical interaction of the phases was probed. This demonstrates the ability of non-invasive experiments to analyse existing models and data, in addition to informing the development of new computational approaches for the design and optimisation of reaction vessels.

8.2. FUTURE RESEARCH

The work presented in this thesis raises some interesting questions and reveals several promising roads for future research. These are principally in the theme of validating computational simulations and improving the fundamental understanding of multiphase hydrodynamics for reaction engineering.

In terms of the co-current upflow experiments, the first improvement of the current work would be to increase the spatial resolution of the images. This has been shown in packed beds to enable the analysis of more detailed spatial hydrodynamic information. This would be difficult, especially with the present imaging routines. Therefore, it is suggested that fast imaging strategies are attempted such as RARE and EPI. Initially these could be used to simply acquire spin-density images which establish the flow regime and bubbling behaviour in 2D. To gain velocity information these imaging sequences could be combined with propagator measurements, which give the distribution of velocities. This would enable the confident identification of bubbling behaviour in both phases and allow the spatial distribution of bubbling to be mapped.

Additionally, a relatively straightforward modification of the present experiments could made which adapts the single bubble injection system for the fluidised bed for use on the upflow bed. This could be done together with triggered pulse sequences to study the rise behaviour and the nature of bubble transport of controlled injections of gas into the co-current upflow bed. Mechanisms such as the amoeboid or bubble train rise behaviour could be studied and the circumstances by which bubbles travel by either mechanism could be found.

For the trickle bed experiments, similar images could be obtained in beds with larger column-to-particle diameter ratios. Another simple modification would be to use different types of packing, such as Rachig rings, berl saddles or formed catalyst pellets such as trilobes to assess

whether the outcomes of this research are consistent in other forms of packing. A larger experimental matrix which tests the sensitivity of various parameters across a broader range of gas and liquid velocities which traverse different flow regimes would additionally give insight as to how each phases' hydrodynamic behaviour influences regime change. Data such as these could also be acquired in the vertical plane, or in 3D. To assess the extent of temporal behaviour, spatially-resolved propagators would be valuable in informing how the steady trickle state behaves compared to snapshot style images such as those reported here. In order to address the concept of flow maldistribution generally, new technologies such as static mixers, structured packings or modified bed walls could be investigated using the same techniques presented here. In this way, these technological interventions could be assessed in terms of their efficacy at improving flow and material distribution in multiphase reactors.

Regarding the interfacial gas-liquid studies in the trickle bed, the question is posed as to whether phase interactions of any kind could be confidently identified by MRI under more extreme conditions of flow. For this reason, it is recommended that a wetted wall experiment be undertaken under several flow rates of gas and liquid. High spatial resolution velocimetry can be used to identify finer interactions occurring on the scale of the boundary layer, which may thus inform modelling as to whether the boundary layer-scale phenomena are significant or not in the context of trickle beds. Additionally, numerical simulations employing the stochastic distributions of interfacial velocity and shear stresses suggested by the present measurements should be undertaken of the system and conditions presented here, to identify whether improvements in the prediction of pressure drop and performance are obtained. To examine the idea of local interaction in fixed beds further, a full 3D pore-scale analysis could be undertaken of a similar trickle bed system. Here, pore statistics such as connectivity could be assessed spatially, and their relationship with the full shear stress tensor could yield information regarding the physical basis of the lack of interfacial interaction reported in the present data.

In the case of the fluidised bed, primarily the bubble collapse mechanism should be investigated. It would be useful to quantify whether the particle size and shape affects the collapse of the injected bubble. If the bubble could be made to rise reliably through the entire bed without collapse, eruption behaviour and mechanisms could be studied using the techniques presented here. Bubble eruption is an important consideration for the dynamics of the freeboard region and the ejection of catalyst particles. Additionally, using either timed pulses of different durations or multiple nozzles, bubble coalescence and the rise behaviour of

bubble clusters could be studied. Importantly, the effects of nozzle geometry and injection parameters on the injected bubble should be quantified. This should also be done with the addition of a gas reservoir in which the pressure could be held constant, and the volume of injected gas be monitored to allow better comparisons with literature models which predict bubble volume. This would require modifications to the experimental system shown here.

For the velocity imaging of isolated bubbles, it would be advantageous to adjust the properties of the solid phase (either density or particle size) as to generate bubbles which moved both faster and slower than the fluidising fluid in the particle interstices. This would hopefully confirm whether the mechanisms by which gas bypasses the solid phase through bubbles are consistent with previous classical theories about bubble flow. This would chiefly need to be done for a 'slow' bubble as the streamline form imaged in this thesis was consistent. If the bubbles did not collapse up the bed, images in the vertical plane of the rising bubble and how the flow patterns changed with height would additionally be valuable for understanding bubble rise and growth mechanisms. Furthermore, for a more thorough comparison with existing flow theories the MRI images could be used to mesh computational grids into realistic bubble geometries. Solving the equations of fluid flow, or potential flow on these meshes would enable a direct quantitative comparison with the MRI velocimetry results. This would allow the largest areas of discrepancy to be identified, and therefore validate modifications of the original theories due either to spatial void fraction distributions or differences in bubble geometry. Additionally, one of the key demonstrated advantages of the techniques presented in this work for MRI velocity measurements using MRI is the ability to use an MRI-visible gas with potentially any granular medium. This would enable the investigation of practically any Geldart-classified materials. Therefore, other rise behaviours such as 'slow' bubbles could readily be investigated using these methods.

NOMENCLATURE

ABBREVIATIONS

1D, 2D, 3D	one, two or three dimensional
CFD	computational fluid dynamics
MRI	magnetic resonance imaging
NMR	nuclear magnetic resonance
RARE	rapid acquisition with relaxation enhancement
EPI	echo planar imaging

SYMBOLS

U_{mf}	minimum fluidisation velocity	m s^{-1}
U_{mb}	minimum bubbling velocity	m s^{-1}

REFERENCES

[1] Geldart, D. Types of gas fluidization. *Powder Technol.* 1973;7: pp. 285–92.

[2] Davidson, J.F. Symposium on fluidization - discussion. *Trans. Inst. Chem. Eng.* 1961;39: pp. 230–2.

[3] Murray, J.D. On the mathematics of fluidization, Part 2: steady motion of fully developed bubbles. *J. Fluid Mech.* 1965;22: pp. 57–80.

[4] Jackson, R. The mechanics of fluidized beds. Part 2. The motion of fully developed bubbles. *Trans. Inst. Chem. Eng.* 1963;41: pp. T22–30.

[5] Boyce, C.M., Ozel, A., Rice, N.P., Rubinstein, G.J., Holland, D.J., Sundaresan, S. Effective particle diameters for simulating fluidization of non-spherical particles: CFD-DEM models vs. MRI measurements. *AIChE J.* 2017;63: pp. 2555–68.

[6] Lockett, M.J., Davidson, J.F., Harrison, D. On the two-phase theory of fluidisation 1967;22: pp. 1059–66.